



University of Sheffield

Thermal Treatments for the Conditioning of Orphan Nuclear Materials

Liam C. Harnett, MEng (Hons)

A thesis submitted in partial fulfilment of the requirements for the degree of
Doctor of Philosophy

Immobilisation Science Laboratory and HADES Facility

Department of Materials Science and Engineering

University of Sheffield

December 2022

Recipient of EPSRC sponsorship and a studentship as part of an NDA Bursary



Abstract

Spent nuclear materials can become damaged and degraded, presenting a severe radiological hazard and engineering problem. Hence, significant challenges are associated with the handling, long term storage and segregation of this material from the biosphere. The UK inventory of orphan wastes, defined as non-reprocessible and legacy materials, is reviewed. The main UK orphan fuel arisings are from civil operation and development of Magnox, mixed oxide light water, and advanced gas-cooled reactors. Secondary orphan waste materials include cladding from damaged fuel, backfill or containment structures, post irradiation examination waste, and effluent treatment ion exchange materials.

A wide variety of internationally used, immobilisation and disposal methods are critically assessed, as well as novel research wasteforms, to allow for the mapping of appropriate treatment options to respective UK degraded fuel streams. Consideration is also made for other degraded fuel types such as corium and materials damaged during accident scenarios, with assessment of how these could map onto treatment methodologies. A variety of pre-treatment schedules are proposed for each of the orphan nuclear material inventory streams, mapping the chemistry of such streams onto vitrification and hot isostatic pressing as potential thermal treatment and conditioning processes for production of wasteform matrices. The review determined that a large proportion of waste feeds could be treated under controlled conditions to produce glass-ceramics and multiphase-titanate ceramics, as to allow for good compositional flexibility, retention of actinides and fission products, while remaining chemically durable under simulated disposal conditions.

Development of a code for quantitative phase analysis of crystalline and semi-crystalline multi-phase materials was undertaken to permit accessible, rapid analysis of wasteforms during research and development. A suite of phosphate glass and glass-ceramic prototype wasteforms were synthesised and assessed for melt solubility and retention of cerium oxide as a simulant fuel. Use of a base sodium iron phosphate composition and a refractory oxide doped composition, allowed for comparison of the effects on melt behaviour, waste loading capabilities and phase assemblage. The refractory doped glass had less aggressive melt characteristics and retained more simulant waste than the base glass counterpart. Above batched loadings of 16 – 25 mol.% simulant waste, crystallisation of phases occurred, primarily cerium monazite and sodium iron phosphate. Above 34 – 35 mol.% loading of simulant, significant developments of porosity were observed in wasteforms. Quantification of the phase assemblages was carried out with an image analysis code, verified against other quantification techniques. The redox state of iron in the bulk materials was found to be approximately 30%

Fe(II), with X-ray absorption measurements indicating that iron was present in the phosphate glass network as a modifier, partially tetrahedrally coordinated with oxygen. This was supported by a Mössbauer spectroscopy study. Chemical durability experiments showed that the sodium iron phosphate base composition materials were more resistant to leaching than the refractory doped counterparts, although an exception was seen for the 25 mol.% batched simulant waste sample with refractory additions, as it retained more cerium oxide than the base sodium iron phosphate, while maintaining a comparable range of durability which could be indicative of better suitability for long term storage.

Another thermal treatment method was considered for an inorganic caesium ion exchange material. Spark plasma sintering yielded an aluminosilicate glass-ceramic, the rapid processing of which aided in retention of exchanged caesium. An accelerated 28-day chemical durability study was then undertaken for this wastefrom, demonstrating a retention of caesium with some minor alteration and dissolution from the glass phase. The results of this study indicated that this material could be a suitable potential wastefrom for the treatment of inorganic ion exchange media, if consideration is made for large scale processing and quantitative accountancy of caesium retention.

Acknowledgements

That's it – I've finally reached the point of writing my acknowledgements, and I've come to realise the boundless assembly of people to thank for helping to propel me along this unforgettable journey. It really does take a village...

On the more serious notes, this research utilised the HADES/MIDAS facility at the University of Sheffield established with financial support from EPSRC and BEIS, under grant EP/T011424/1. I'm indebted to The EPSRC and Nuclear Decommissioning Authority for the award of my PhD studentship, but I owe my immeasurable gratitude to Neil, Russell, Martin and Ewan for their excellent tutelage, supervision and support throughout the pandemic, a change of PI and your seemingly unending patience.

Lucy, Euan, Lewis, Shaun, Josh, Gaone, Cassandre, Max and Tom, you've all been near constants since the early days, I've really appreciated the times we've shared and trials we have gone through together. Chris, I wouldn't have got off to such a great start if you hadn't been there to give my experimental setups 'the dad look', helped me figure out the little niggles and with percussive maintenance of uncooperative equipment. Thanks to you, I can only ever aspire to be the world's second 'tireddest' man. Laura, I really don't think I would be at this point if you hadn't shown me how to do such world class research in 2018. I think most would struggle to express how much your hard-work, support and understanding ear means to all of us. Colleen, Amber, Clemence and Sarah, thank you for guiding and fast tracking me through the dissolution labs and for your help with getting started in PHREEQC. Dan B, Chris and Lucy, considerable thanks are due for your help with the countless glass melts. Claire, thank you for your support with the IAEA project and our visit to Fukushima, our time with Hao in Fukushima was definitely one of the most memorable experiences of my PhD. Martin, I'm really sorry I couldn't stay awake for the part of one of my beamtime shifts – the earthquake definitely gave us some beans, in all seriousness – thank you for your interminable support while juggling running a lab, getting married and having a baby. To the K02-crew, I know where I need to go if I ever need a good place to passive aggressively talk down to a piece of fitting software or find a great conversation about the work you're all so passionate about. To all the ISL students, academics, and research staff, thank you for putting up with me!

To my parents and family, yes this means I'm not going to be a student any more... Thank you for pushing me to follow my aspirations and fostering my interests in science and engineering. Above all else - Damien, for your help re-learning to code, for your English as a third language skills, for sticking by my side, for always being there and for every moment I have shared with you – thank you.

Contents

Index of acronyms and abbreviations	viii
1. Introduction and Project Scope	1
1.1 Introduction	2
1.2 Research aims and projects	4
1.3 Thesis outline	5
Chapter 1 references	6
2. Literature Survey of UK Orphan Nuclear Materials	9
2.1 Introduction	10
2.1.1 <i>Spent nuclear fuel – typical case</i>	10
2.1.2 <i>Spent nuclear fuel – damaged or degraded case</i>	12
2.2 Taxonomy of UK orphan nuclear materials	14
2.2.1 <i>Magnox clad fuel types</i>	14
2.2.2 <i>Stainless steel clad fuel types</i>	16
2.2.3 <i>Zircaloy clad fuel types</i>	19
2.2.4 <i>Carbide and fuel contaminated materials</i>	20
2.2.5 <i>Ion exchange materials for effluent treatment</i>	21
2.3 Immobilisation of degraded and spent nuclear fuel	22
2.3.1 <i>Dissolution, separation, and re-processing</i>	22
2.3.2 <i>Spent fuel pond storage</i>	22
2.3.3 <i>Dry cask and high integrity container storage</i>	23
2.3.4 <i>Cementation</i>	25
2.3.5 <i>Vitrification</i>	26
2.3.5.a <i>Silicate glasses</i>	27
2.3.5.b <i>Phosphate glasses</i>	29
2.3.5.c <i>Glasses for Zircaloy clad and exotic fuels</i>	30
2.3.6 <i>Ceramic immobilisation</i>	33
2.3.6.a <i>Single phase and use of spark plasma sintering (SPS)</i>	33
2.3.6.b <i>Multi-phase ceramics and use of hot isostatic pressing (HIP)</i>	34
2.3.6.c <i>Glass-ceramics</i>	36
2.4 Comparison of methods summary	40
2.4.1 <i>Concluding remarks</i>	40
Chapter 2 references	44

3. Materials and Methods	57
3.1 Materials and synthesis	58
3.1.1 <i>Oxide solid-state synthesis and batching</i>	58
3.1.2 <i>Alkoxide nitrate synthesis</i>	58
3.1.3 <i>Ion exchange</i>	59
3.1.4 <i>Thermal treatment technologies</i>	59
3.2 Gas pycnometry and density balance measurements	64
3.2.1 <i>Sample preparation and technique</i>	64
3.3 Powder X-ray diffraction	65
3.3.1 <i>Standard pXRD sample preparation and measurement</i>	65
3.3.2 <i>Klug and Alexander quantitative phase analysis</i>	65
3.4 X-ray fluorescence spectroscopy	68
3.4.1 <i>Sample preparation</i>	68
3.4.2 <i>XRF analysis</i>	68
3.5 X-ray absorption spectroscopy (XAS, EXAFS)	69
3.5.1 <i>Sample preparation</i>	71
3.5.2 <i>Synchrotrons and beamlines</i>	71
3.5.3 <i>Fe-K pre-edge analysis</i>	72
3.5.4 <i>Data processing with Athena and Artemis</i>	72
3.6 Simultaneous thermal analysis	73
3.6.1 <i>Thermal analysis method</i>	73
3.7 Mössbauer spectroscopy	74
3.8 Scanning electron microscopy and energy-dispersive X-ray spectroscopy	75
3.8.1 <i>Sample preparation</i>	75
3.8.2 <i>SEM imaging and EDX analysis</i>	76
3.9 Phase analysis of grayscale images	77
3.9.1 <i>Introduction and manual method</i>	77
3.9.2 <i>Computer assisted processing methodology</i>	77
3.10 Product consistency testing	80
3.10.1 <i>PCT-B</i>	80
3.10.2 <i>ICP-OES and post dissolution particle analysis</i>	81
Chapter 3 References	82

4. Sodium Iron Phosphate Glass-Ceramics	84
Summary	85
4.1 Iron-rich orphan nuclear materials	86
4.2 Base compositions and additions	88
4.2.1 <i>Sodium iron phosphate (SIP)</i>	88
4.2.2 <i>Sodium iron phosphate with Al and Si (IPSAS)</i>	88
4.3 Synthesis	93
4.3.1 <i>Glass batching</i>	93
4.3.2 <i>Cursory melts and thermal analysis</i>	93
4.3.3 <i>Glass melt with cast and anneal</i>	94
4.3.4 <i>Frit production for durability testing</i>	94
4.4 Glass melt observations	96
4.5 Archimedes density and molar volume	96
4.6 Powder X-ray diffraction	100
4.6.1 <i>Crystalline phase assemblage</i>	100
4.6.2 <i>LaB₆ spike Rietveld analysis</i>	110
4.7 Scanning electron microscopy	113
4.7.1 <i>Bulk material EDX analysis</i>	113
4.7.2 <i>BSE and EDX analysis of crystalline phases</i>	118
4.7.3 <i>BSE semi-quantitative analysis</i>	123
4.8 Mössbauer spectroscopy	128
4.9 Fe-K edge X-ray absorption spectroscopy	132
4.9.1 <i>Iron valence by pre-edge analysis</i>	132
4.9.2 <i>EXAFS analysis</i>	138
4.10 Chemical durability testing	141
4.10.1 <i>PCT-B testing</i>	141
4.10.2 <i>ICP-OES analysis</i>	142
4.11 Conclusions and further work	149
Chapter 4 references	155

5. Aluminosilicate Glass-Ceramic Materials for Treatment of Spent Radionuclide Ion Exchange Media	154
Summary	155
5.1 Ion specific media and treatment options	157
5.1.1 <i>Fukushima Daiichi disaster</i>	157
5.1.2 <i>Commercial ion-exchange materials</i>	157
5.1.3 <i>Thermal treatment options for spent ion-exchange materials</i>	158
5.2 Synthesis and characterisation	159
5.2.1 <i>As-received material and ion-exchange</i>	159
5.2.2 <i>Spark plasma sintering</i>	159
5.2.3 <i>Bulk characterisation</i>	159
5.3 Chemical durability testing	162
5.3.1 <i>PCT-B testing</i>	162
5.3.2 <i>ICP-OES and ion chromatography analysis</i>	162
5.3.3 <i>Post dissolution powder characterisation</i>	164
5.4 Conclusions and further work	169
Chapter 5 References	170
6. Further discussion and conclusions	173
6.1 Conclusions	174
6.1 Future work	178
Appendix 1. Development of phosphate glass and multi-phase titanate ceramic compositions for thermal treatment of irradiated nuclear fuel residues	179
Appendix 2. Characterisation of sodium iron phosphate glass loaded with simulant nuclear fuel	188
Appendix 3. Characterisation of glass-ceramic wastefoms using quantitative image analysis of electron micrographs	190
Appendix 4. Quantitative image analysis source code	195
Appendix 5. Reactive spark plasma sintering of Cs-exchanged chabazite: characterisation and durability assessment for Fukushima Daiichi NPP clean-up	196

Index of acronyms and abbreviations

(W)AGR	: (Windscale) Advanced Gas-cooled Reactor
AFIC	: Active Furnace Isolation Chamber
AFM	: Atomic Force Microscopy
ALPS	: Advanced Liquid Processing System
ANSTO	: Australian Nuclear Science and Technology Organisation
AVM	: Marcoule vitrification workshop (translation)
BFS	: Blast Furnace Slag
BSE	: Back-Scattered Electron
BVS	: Bond Valence Sum
BWR	: Boiling Water Reactor
CAC-FA	: Calcium Aluminate Cement - with Fly Ash
CIF	: Crystallographic Information File
CS	: Centre Shift
CST	: Crystalline Silico-Titanate
DFR	: Dounreay Fast Reactor
DI	: De-Ionised
DTA	: Differential Thermal Analysis
EDX	: Energy-Dispersive X-ray spectroscopy
EXAFS	: Extended-X-ray Absorption Fine Structure
FCM	: Fuel Containing Materials
FEFF	: Free Energy Force Field
FHP	: Fuel Handling Plant
FP	: Fission Product
FWHM	: Full Width Half Maximum
GDF	: Geological Disposal Facility
GIC	: Graphite Intercalation Compounds
GOF	: Goodness Of Fit
GRG	: Generalised Reduced Gradient
HIP	: Hot Isostatic Press
HLW	: High Level Waste
HUP	: Hot Uniaxial Press
IAEA	: International Atomic Energy Agency
ICV	: In-Container Vitrification
INES	: International Nuclear Event Scale
IPSAS	: Iron Phosphate with Sodium, Alumina and Silica
ISG	: International Simple Glass
ISM	: Ion Specific Media
KBS	: Nuclear fuel safety (translation)
LW	: Line Width
LWR	: Light Water Reactor
MAS-NMR	: Magic Angle Spinning - Nuclear Magnetic Resonance
MCC	: Materials Characterisation Centre
MDF	: MOx Demonstration facility
MOx	: Mixed Oxide (fuel)

MW	: Mixture Windscale
NDA	: Nuclear Decommissioning Authority
NNL	: National Nuclear Laboratory
NPP	: Nuclear Power Plant
NWS	: Nuclear Waste Services
OPC	: Ordinary Portland Cement
PCT	: Product Consistency Test
PDF	: Powder Diffraction File
PFR	: Prototype Fast Reactor
PHREEQC	: pH REdox EQUilibrium in C-language
PIE	: Post Irradiation Examination
POCO	: Post Operational Clean-Out
PUREX	: Plutonium Uranium REdox Extraction
PWR	: Pressurised Water Reactor
pXRD	: powder X-Ray Diffraction
QS	: Quadrupole Splitting
RBMK	: High-power channel reactor (translation)
SARRY	: Simplified Active water Retrieval and Recovery
SEM	: Scanning Electron Microscopy
SGHWR	: Steam Generating Heavy Water Reactor
SIP	: Sodium Iron Phosphate
SIXEP	: Site Ion Exchange Plant
SMP	: Sellafield MOx Plant
SNF	: Spent Nuclear Fuel
SPFT	: Single Pass Flow Through
SPS	: Spark Plasma Sintering
STA	: Simultaneous Thermal Analysis
SYNROC	: SYNthetic ROCK
TGA	: Thermo Gravimetric Analysis
tHM	: tonnes of Heavy Metal
ThORP	: Thermal Oxide Reprocessing Plant
TMI	: Three Mile Island
TRISO	: TRi-structural ISOtropic
UHQ	: Ultra-High Quality (water)
VOC	: Volatile Organic Compound
VTT	: State technical research centre (translation)
WAC	: Waste Acceptance Criteria
WVP	: Waste Vitrification Plant
XANES	: X-ray Absorption Near-Edge Spectroscopy
XAS	: X-ray Absorption Spectroscopy
XPS	: X-ray Photoelectron Spectroscopy
XRF	: X-ray Fluorescence Spectroscopy

1. Introduction and Project Scope

1.1 Introduction

Nuclear power was brought to the centre stage in the latter half of the 20th century, new physics, chemistry, and materials innovations were being developed with great frequency. Reactions between newly separated, highly energetic materials were harnessed for the first time, generating power to meet the growing global needs. Initially there was little consideration for the life cycle of the reactors, fuels, and secondary materials. Since development, internationally operating organisations, bodies, and state agencies have been formed to provide considerable oversight for nuclear installations, storage of nuclear materials and management of waste [1,2].

The UK was an early adopter of nuclear technologies, contributing to some of the developments and improvements of power generation efficiency through its assortment of installation designs: from fuel piles to early Magnox power stations [3], then progressing to the age of advanced gas-cooled (AGR) and fast breeder reactors [4,5], through to the 21st century where pressurised water reactors are set to gradually become the primary fission power source [6]. Through this history of advances and development: materials, systems, and processes have evolved; each component had to be prototyped and tested, often so thoroughly that it could not be used again. This generated a unique stream of orphan nuclear materials, now considered to be waste. During early implementations, any failures or terminated development schemes would also give rise to waste material which did not have a life in the existing nuclear fuel cycles. Such an inventory has remained within interim storage solutions, some for decades, leading in many cases, to a significant degree of further degradation and damage [7]. Secondary materials can be generated through the handling and processing of nuclear fuel, such as the cladding that it can be in persistent contact with, becoming heavily irradiated and activated during reactor operation [8]. The water that passes between fuel channels and cooling systems on nuclear sites can gradually dissolve contaminants, itself becoming a form of waste. To reduce the volume of this contamination, this can be separated and concentrated with water treatment facilities utilising ion exchange materials [9,10]. With this growing volume of waste and long-lived isotopes that pose a radiological risk to our biosphere, simple surface level storage is not adequate. Consideration must be made for making the waste stable for long enough that the radiological hazard can diminish over thousands of years, while reducing the space the material occupies [11].

Thermal treatment technologies have been demonstrated to change the chemical make-up and structure of hazardous materials and high-level waste (HLW), the material streams of which are often very well defined for a particular fuel processing campaign,

treatment facility or decommissioning activity. Thermal treatment has been used for conditioning, consolidating, and immobilising such materials into glass [12], crystalline ceramics [13–15], cements [16–18], polymers [19] and metallic wasteforms [20]. Application of these methods is subject to the condition and composition of the waste feed, and the resulting wasteform should meet desirable properties for safe long-term storage: minimal radiological releases during high activity lifetime, mechanical stability, resistance to damage by self-irradiation, chemical durability in the atmosphere and groundwater conditions that could arise during storage.

1.2 Research aims and projects

This body of research set out to approach the engineering and scientific challenge of applying thermal treatment technologies to UK orphan nuclear materials. Accordingly, at commencement the aims set were:

- To determine what the ‘legacy’ and ‘orphan’ materials are, in the context of the UK civil nuclear sphere through review of archival literature and collaboration with the Nuclear Decommissioning Authority and National Nuclear Laboratory.
- To consider and assess the suitability of a suite of matrices for hosting said orphan materials under proposed UK geological disposal facility (GDF) conditions.
- To synthesise prototype glass, ceramic and glass-ceramic wastefoms.
- To study the formation of different phases under a variety of thermal treatment options.
- To evaluate the thermal behaviour, assemblage, structure, chemistry, and chemical durability of prototypical wastefoms, with consideration of other degradation mechanisms.

With the disruption of the pandemic, a particular focus of scope was made to sodium iron phosphate glass and glass-ceramics for thermal treatment of fuel materials including further aims:

- To study the redox behaviour of iron in the bulk phosphate glass and glass-ceramics using a suite of spectroscopic techniques.
- To develop and validate methodologies for rapid quantitative analysis of multi-phase materials, such that they could be easily implemented in an industrial setting.

1.3 Thesis outline

The review of the UK orphan nuclear material inventory is featured **Chapter 2**, further discussing potential routes for breaking down those material streams into constituent parts for blending or homogenisation. A host of material structures and matrices for immobilisation of nuclear waste are then evaluated, with consideration for coupled thermal treatment techniques, culminating in an overall selection of credible waste feeds, host matrices and treatment options for orphan nuclear materials.

Chapter 3 focuses on the key methodologies used for projects featured in this thesis and PhD research outputs. Material synthesis routes are discussed and described with an overview of the techniques used for thermal treatment, including that of a titanate ceramic material featured in a brief publication, see **Appendix 1**. Characterisation methods are discussed, with explanations of the spectroscopic techniques and chemical durability testing methods used. This chapter also features an outline of the motivation and development for a quantitative image analysis code, using information from electron microscopy images to determine relative phase proportions automatically. This is also featured as a research output in **Appendix 3**, with the latest version of the code available from **Appendix 4**.

Chapter 4 is the primary results and discussion body of work concerning sodium iron phosphate glass and glass ceramics for thermal treatment of nuclear fuel materials. This section features an insight into the behaviour and characteristics of prepared glass melts, the Mössbauer and X-ray absorption spectroscopy (XAS) studies, phase assemblage of prototype wasteforms and applied methods of quantification therein. Additionally, a review of the microstructural developments of crystalline phases is included with a final chemical durability investigation via leaching experiments.

Chapter 5 concerns a project for thermal treatment of a secondary orphan nuclear material, inorganic caesium ion exchange media, as used for water treatment facilities at Sellafield, UK and Fukushima, Japan. A further minor review of organic and inorganic ion exchange materials is included. A resistive heating and pressing method, spark plasma sintering is used, with additional material generated from processing parameters optimised during trials. This material was characterised and prepared for a 28-day accelerated chemical durability study. The work here was featured as a research output article, see **Appendix 5**.

Chapter 6 covers the overall conclusions for project work with reference to research aims and discusses proposed further work.

Chapter 1 references

- [1] D. Fischer, International Atomic Energy Agency - The First Forty Years, 1997.
<https://doi.org/10.01.2003>.
- [2] Nuclear Waste Services Annual Review, 2022.
https://assets.publishing.service.gov.uk/government/uploads/system/uploads/attachment_data/file/1096709/NWS_AnnualReview_FINAL_d.pdf.
- [3] S.E. Jensen, E. Nonbol, Description of the Magnox type of gas cooled reactor, 1998.
https://inis.iaea.org/collection/NCLCollectionStore/_Public/30/052/30052480.pdf.
- [4] E. Nonbøl, Description of the Advanced Gas Cooled Type of Reactor (AGR), Roskilde, Denmark, 1996.
https://inis.iaea.org/collection/NCLCollectionStore/_Public/28/028/28028509.pdf.
- [5] S.E. Jensen, P.L. Ølgaard, Description of the Prototype Fast Reactor at Dounreay, Roskilde, Denmark, 1996.
https://inis.iaea.org/collection/NCLCollectionStore/_Public/28/026/28026107.pdf.
- [6] G. Meyer, E. Stokke, Description of Sizewell B Nuclear Power Plant, Halden, 1997.
<https://researchbriefings.files.parliament.uk/documents/POST-PN-137/POST-PN-137.pdf>.
- [7] IAEA, Survey of wet and dry spent fuel storage, 1999. http://www-pub.iaea.org/MTCD/Publications/PDF/te_1100_web.pdf.
- [8] A. Tasooj, R.E. Einziger, A.K. Miller, Modeling of Zircaloy Stress-Corrosion Cracking: Texture Effects and Dry Storage Spent Fuel Behavior "Modeling of Zircaloy Stress-Corrosion Cracking: Texture Effects and Dry Storage Spent Fuel, 1984.
www.astm.org.
- [9] E. Tusa, R. Harjula, P. Yarnell, Fifteen Years of Operation with Inorganic Highly Selective Ion Exchange Materials, WM'07 Conf. (2007).
[https://web.archive.org/web/20170809103727/https://www.fortum.com/SiteCollectionDocuments/Products and services/WM07_15years_7025.pdf](https://web.archive.org/web/20170809103727/https://www.fortum.com/SiteCollectionDocuments/Products%20and%20services/WM07_15years_7025.pdf).

- [10] M. Herbas, Ion Exchange to cope with decommissioning, University of Manchester, 2018.
https://www.research.manchester.ac.uk/portal/files/78646962/FULL_TEXT.PDF.
- [11] IAEA, Design and Operation of HLW Vitrification and Storage Facilities, Vienna, 1992.
https://inis.iaea.org/collection/NCLCollectionStore/_Public/24/019/24019780.pdf.
- [12] M.T. Harrison, Vitrification of High Level Waste in the UK, *Procedia Mater. Sci.* 7 (2014) 10–15. <https://doi.org/10.1016/J.MSPRO.2014.10.003>.
- [13] S. V Yudintsev, S. V Stefanovsky, M.S. Nikol, S. A, O.I. Stefanovskaya, B.S. Nikonov a, Brannerite, UTi_2O_6 : Crystal Chemistry, Synthesis, Properties, and Use for Actinide Waste Immobilization, *Radiochemistry.* 58 (2016) 289–301.
<https://doi.org/10.1134/S1066362216040019>.
- [14] N. Clavier, N. Dacheux, R. Podor, Synthesis, Characterization, Sintering, and Leaching of-TUPD/ Monazite Radwaste Matrices, *Inorg. Chem.* 45 (2006) 220–229.
<https://doi.org/10.1021/ic051607p>.
- [15] K. Popa, M. Cologna, L. Martel, D. Staicu, A. Cambriani, M. Ernstberger, P.E. Raison, J. Somers, $CaTh(PO_4)_2$ cheralite as a candidate ceramic nuclear waste form: Spark plasma sintering and physicochemical characterisation, *J. Eur. Ceram. Soc.* 36 (2016) 4115–4121. <https://doi.org/10.1016/J.JEURCERAMSOC.2016.07.016>.
- [16] M. Sutton, P. Warwick, A. Hall, Uranium(VI) interactions with OPC/PFA grout, *J. Environ. Monit.* 5 (2003) 922–928. <https://doi.org/10.1039/b308554f>.
- [17] J. Cronin, N. Collier, Corrosion and expansion of grouted Magnox, *Mineral. Mag.* 76 (2012) 2901–2909. <https://doi.org/10.1180/minmag.2012.076.8.05>.
- [18] S.A. Kearney, B. McLuckie, K. Webb, R. Orr, I.A. Vatter, A.S. Yorkshire, C.L. Corkhill, M. Hayes, M.J. Angus, J.L. Provis, Effects of plutonium dioxide encapsulation on the physico-chemical development of Portland cement blended grouts, *J. Nucl. Mater.* 530 (2020) 151960.
<https://doi.org/10.1016/j.jnucmat.2019.151960>.
- [19] R.-S. Juang, T.-S. Lee, Oxidative pyrolysis of organic ion exchange resins in the presence of metal oxide catalysts, *J. Hazard. Mater.* 92 (2002) 301–314.
[https://doi.org/10.1016/S0304-3894\(02\)00025-0](https://doi.org/10.1016/S0304-3894(02)00025-0).

- [20] E.R. Vance, D.S. Perera, S. Moricca, Z. Aly, B.D. Begg, Immobilisation of ^{129}I by encapsulation in tin by hot-pressing at 200 °C, *J. Nucl. Mater.* 341 (2005) 93–96.
<https://doi.org/10.1016/j.jnucmat.2005.01.011>.

2. Literature Survey of UK Orphan Nuclear Materials

2.1 Introduction

‘Orphan’ is a term used here to encompass an inventory of civil-use nuclear materials which do not have a re-processing, treatment, or disposal route following their economically useful lifetime. A large aspect of this is from legacy stores of spent nuclear fuel (SNF), orphaned due to properties such as: unique research designs, degradation, damage (intentional during testing or through failure), abnormal fuel chemistry or burnup conditions. Damaged and degraded orphan fuel presents a severe radiological hazard, hence significant challenges are associated with the handling, long term storage and segregation of this material from the biosphere. Initial scoping of which materials and their relative quantities would qualify for such an inventory proved onerous with the early resources available. A great deal of progress was made partly through talks and meetings with representatives from the UK National Nuclear Laboratory (NNL) and spent fuel management teams. Further information was garnered through review of a 2017 report from the Nuclear Decommissioning Authority (NDA), discussing radioactive materials not reported in the 2016 national inventory [1]. Details on reactor and fuel type design, typical burnups, failure modes and compositions were uncovered through public domain literature review where possible, though due to the nature of the still in-service nuclear technology and redefinition of inventory during end of reprocessing at the time of writing, some information was still restricted. The UK orphan inventory of non-reprocessible and legacy nuclear materials include fissile fuels such as those used in Magnox, mixed oxide, and advanced gas-cooled reactors. A possible approach to finding solutions for treatment and sequestration of these materials, is to review a wide variety of internationally used examples for storage, immobilisation, and disposal methods. A critical assessment of these approaches can allow for the mapping of appropriate treatments to respective UK orphan material streams. Consideration can also be made for other degraded fuel types such as corium (partially melted fuel complexing with cladding and structural components) and materials damaged during accident scenarios such as the Windscale Pile No.1 fire [2] in Sellafield, UK, or further afield in support of international collaboration on remediation of fuel-damage and fuel-melt accidents [3–6]. Inclusion is made for high heat generating secondary orphan wastes such as effluent treatment ion exchange materials, as they too can have a significant radiological inventory but do not have a well-established treatment route.

2.1.1 Spent nuclear fuel – typical case

Fuel materials for nuclear fission typically have a significant content of fissile uranium or plutonium in the form of fuel pellets or bars, these are stacked inside sealed metallic pins or elements, which are welded together to form a fuel assembly [7,8]. During reactor operation and start-up, fuel

assemblies are loaded into a grid pattern with a moderator, poisons, control rods and other components to form the core. After several years of operation in a reactor, the fissile isotopes in the fuel become depleted to the point where burn-up efficiency decreases below a threshold value. Following this, the fuel is now to be considered SNF [7]. In the process of refuelling or defueling, the spent fuel assemblies are carefully removed from the reactor and placed into deep, water-filled cooling ponds [9,10].

Of those currently in operation at the time of writing, 85% of commercial reactors globally are a form of light water reactor (LWR) [11]. In this case, the nuclear fuel is ceramic pellets of uranium dioxide, UO_2 (sometimes with smaller quantities of PuO_2) [12], usually sintered to 1 cm height and 1 cm diameter, see **Figure 2.1.1.A**. These pellets are stacked 4-5 m high and sealed inside fuel pin cladding, which is usually a zirconium alloy (zircaloy) or a type of stainless steel [7]. Fuel pins are manufactured with a narrow gap between the pellets and the cladding walls, this is to allow for the swelling of pellets during reactor operation [13,14]. Microscopic studies of spent fuel samples, considered a form of post irradiation examination (PIE), have been highly informative in describing the development of microstructural features during reactor burn-up. The grains of ceramic UO_2 fuel have a fluorite type crystal structure, hence only some of the actinide fission products (FPs) can successfully substitute uranium in the structure [15–17]. Bubbles of gas form in pores of the ceramic fuel, these are usually the most volatile of FPs such as Kr, Xe and I. Development of metallic alloy precipitates, sometimes termed as ϵ -particles, can be caused by FPs such as Mo, Ru and Rh. Volatile components such as Cs and Tc, migrate to the boundaries between grains, while oxides of Rb, Ba and Nb form near the pellet rim, with some trans-uranic elements

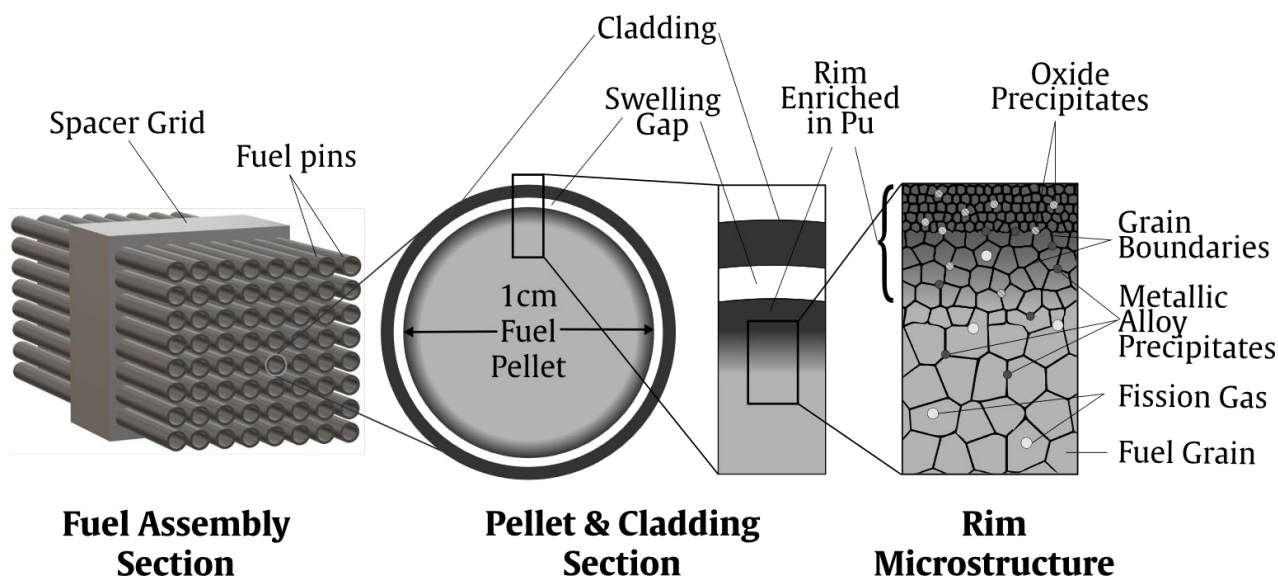


Figure 2.1.1.A – Sketch demonstrating the features of undamaged spent LWR fuel, not to scale. Figure adapted from Shoesmith (2000), Buck et al. (2004) and Bruno et al. (2006) [15–17].

being generated through neutron capture. The geometry of the fuel means that more of the uranium will be ‘burned-up’ near the pellet rim, causing a significant increase in the concentration of Pu in these grains of fuel [15–17].

2.1.2 Spent nuclear fuel – damaged or degraded case

During manufacture, handling, operation and storage, defects can develop in the cladding material. Micron-sized pinholes allow for the release of fission gas, and substantial cladding failures could permit the ingress of air, moisture, and coolant water. Grain boundary precipitates such as Cs or Tc will readily dissolve in contact with water, fouling cooling systems and potentially causing contamination during fuel drying. If temperatures of about 20-50 °C [10] and coolant cover are maintained, the alloy ϵ particles and oxide fuel structures still will corrode, albeit at a significantly slower rate than Cs and Tc precipitates, see **Figure 2.1.2.A**. In-grown actinides present in the fuel can have very long half-lives, for example ^{237}Np has $t_{1/2} = 2,100,000$ years [18], hence damaged spent fuel presents a long-term significant radiological hazard for emission of radionuclides into the environment. Some less common fuel and cladding materials have a significantly higher propensity for oxidation and hydrolysis, having been found to be severely corroded during surveys of pond storage, see **Section 2.2**. These legacy fuel wastes are unsuitable for typical treatments or separation techniques due to a high content of volatile radionuclide species such as Kr, I and Te, which diffuse from the fuel matrix forming gaseous products during heating [19], necessitating additional considerations for off-gas scrubbing systems. Additional unsuitability for treatment and separation can be due to irregular geometries (bent or damaged pins), heavy contamination through corrosion or high contact dose rates. Other legacy materials include novel fuel materials from development research.

Another example of heavily damaged and degraded spent fuel is the material formed during partial core damage and meltdown accidents such as the aforementioned Windscale Pile No.1 in 1957 (Sellafield, UK), Three Mile Island Reactor 2 (Pennsylvania, USA) in 1979, Chernobyl No.4 (Pripyat, Ukraine) in 1986 and Fukushima Daiichi Units 1-3 (Okuma, Japan) in 2011 [2–5]. In all cases, parts of the reactor cores far exceeded standard operating conditions, creating pressures and temperatures whereby fuel and cladding components melted and combined into a heterogeneous multi-phase material which is variously termed corium, lava or fuel-containing material (FCM). In the case of the Chernobyl accident, there were significant breaches of the reactor building by the molten oxide fuel- zirconium cladding mass, subsequently materials such as graphite moderators, shielding concrete and suppression boron were incorporated with the corium[4,20,21]. In contrast, the Windscale pile incident resulted in combustion and melt of uranium metal fuel,

aluminium cartridges and graphite moderator, with further degradation caused by oxidation in air and steam [2,22].

The International Atomic Energy Agency (IAEA) has strictly defined damaged spent fuel as “Any SNF that requires non-standard handling to demonstrate compliance with applicable safety, regulatory or operational requirements” [23]. For this review, non-conforming and non-standard fuel types which also require specialised handling, are considered alongside degraded fuels. In order to meet domestic and international waste acceptance criteria such as chemical durability and radiation tolerance, suitable treatment methodologies need to be determined and used to segregate damaged fuels from causing potential radiological and radiotoxic hazards [24].

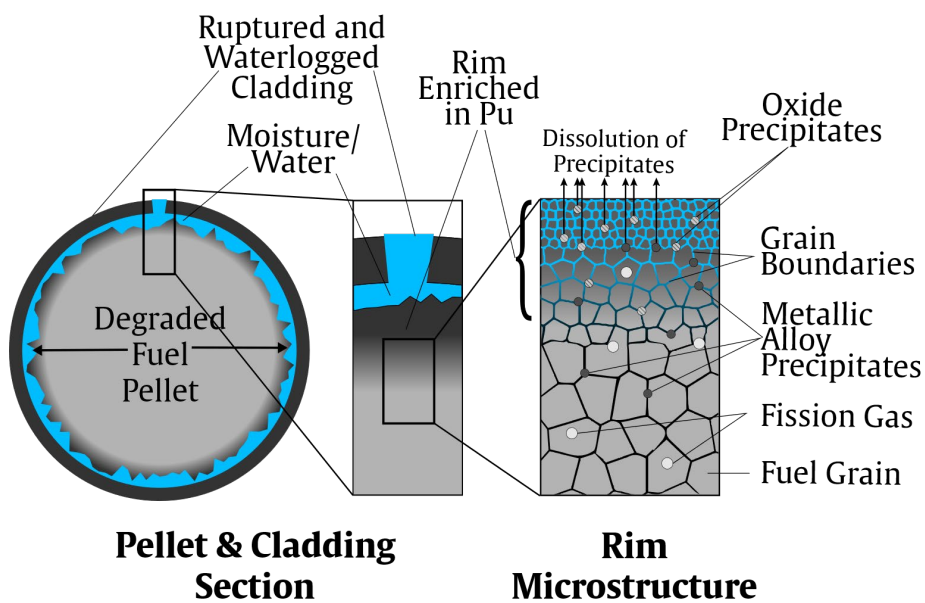


Figure 2.1.2.A - Sketch showing a ruptured cladding section, corroded pellet surface, contamination, and dissolution of FPs. Figure adapted from Shoemith (2000), Buck et al. (2004) and Bruno et al. (2006) [15–17].

2.2 Taxonomy of UK orphan nuclear materials

In line with the IAEA, the UK defines ‘damaged nuclear fuel’ as a situation where an element has a significant nonconformity from the standard fuel pin shape, such as a ruptured cladding. The Office for Nuclear Regulation has recommended that such materials should be managed with specialised handling equipment and isolated from intact fuel [23]. Fuel materials categorised as such may have structural damage (from cutting, processing and post irradiation examination); development of corrosion products (resulting from failed storage containers); unique fuel assembly and alloy designs (including novel fuel chemistries). Henceforth, these materials will be referred to as ‘orphan fuels,’ unless specified otherwise.

2.2.1 Magnox clad fuel types

Building upon the technical knowledge, experience and fissile material accumulated during the early 1950’s by the establishment of the Windscale plutonium piles and UK weapons programmes [2], construction began on the UK’s first commercial nuclear reactors. The first civil facility was Calder Hall, which opened in 1956 with four Magnox reactors, a type of graphite moderated, CO₂ cooled design that uses natural uranium metal in magnesium alloy cans as fuel, see **Figure 2.2.1.A**. Over the following decades a further 22 Magnox reactors were commissioned across the UK, with a combined total capability for 4.2 GW of generation [25].

Magnox orphan fuels fall into two key categories: ex-reactor and legacy inventories, see **Table 2.2.A**. The ex-reactor fuel is currently the most significant component of the inventory, resulting from the operation and decommissioning of Magnox reactors over during their operational lifetimes. These materials are composed of irradiated natural U metal (0.7% ²³⁵U before use) base fuel, clad in Magnox Al 80 (0.7 mol.% Al, 0.01 mol.% Be, Mg balance.) – with geometries of pins and cooling fins varying according to the reactor they were used in, see **Figure 2.2.1.A**. The quantity of this fuel considered as orphan material is dependent on the success of the final reprocessing campaign conducted at Sellafield, but still constitutes tens of tonnes of corroded fuel pins from pond storage [26,27]. Legacy Magnox fuel describes the materials that resulted from the development and optimisation of Magnox technology, the fissile material was the same as used for later ex-reactor fuels, with some experimental Al clad pins made. The stores of legacy Magnox consist of de-clad fuel bars, cutting wastes, deformed cans, see **Figure 2.2.1.B**, scraps in stainless steel cans backfilled with cement and other highly contaminated products from corrosion such as such as UO₂ and Mg(OH)₂ [26–28]. Pre-processing of ex-reactor Magnox to facilitate immobilisation would ideally start by drying and de-cladding followed by chemical dissolution, or total dissolution of fuel and cladding for both ex-reactor and legacy stores. Both routes would

generate a fuel liquor rich in U and small quantities of Pu and FPs, with total dissolution liquors containing Mg from cladding and other storage material contaminants (Ca, Si, Fe, Al). Although it is pyrophoric, metallic uranium can also be processed into uranium oxides prior to a dry-way thermal treatment [29]. The establishment of the Sellafield Magnox reprocessing plant in 1964 has allowed for recovery of Pu from spent fuel using the chemical process plutonium uranium redox extraction (PUREX) [30], with segregation of minor actinide FPs into a high level waste (HLW) stream [31].

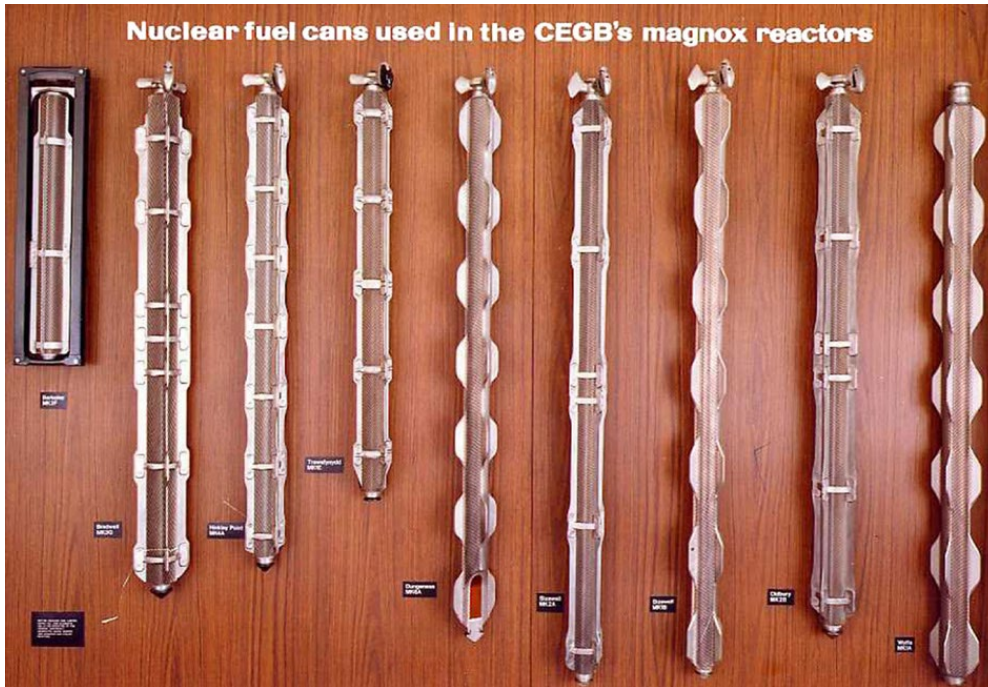


Figure 2.2.1.A – Variations of Magnox fuel can geometries. Figure from Hastings et al. 2007 (*Rights obtained from Elsevier*) [32].

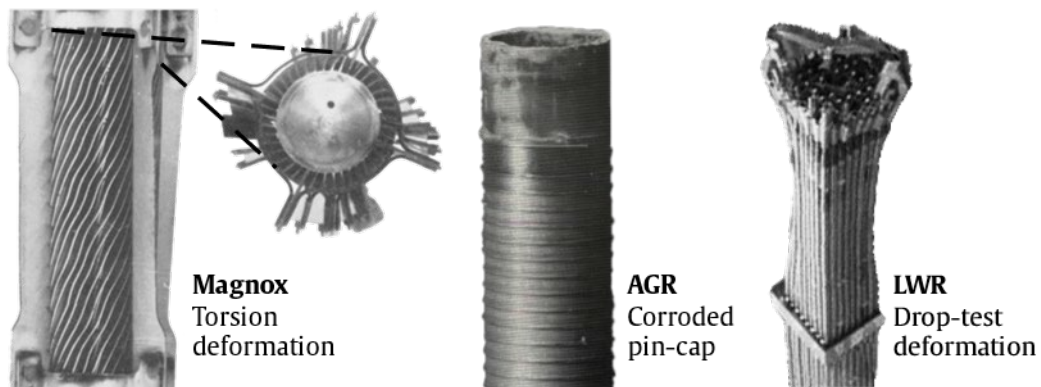


Figure 2.2.1.B - Photographs of damaged fuel examples, from left to right: irradiated Magnox pin with deformed fins from torsion (top and profile view, *Speight, et al. 1966 - reproduced with permission*), slightly corroded AGR fuel pin end-cap (profile view, *Hambley 2016 - reproduced with permission*) and LWR assembly subjected to 5 m drop test (*Tepeco 2013*) [13,52,61].

Table 2.2.A - Approximate UK civil inventory of exotic legacy fuels, defining fuel type in tonnes of heavy metal (tHM) and feasibility (Yes/with significant Caveats/No) of proposed pre-processing options. Applicability for pre-processing was determined using information supplied by UK NNL and the author's opinion.

Residue Type	Approx. Inventory tHM	Pre-processing Route			Property and Chemistry References
		De-clad Fuel	De-clad Fuel (Chemical Dissolution)	Fuel & Cladding (Total Dissolution)	
Magnox					
Ex-reactor	Up to 500	N	C	Y	[26,27]
Legacy	Up to 200	N	N	C	[26–28]
Stainless Steel					
DFR Breeder Material	32	N	C	Y	[8,33]
WAGR	30	Y	Y	Y	[34,35]
PFR MOx	8 &	Y	Y	Y	[35–38]
- Intact & Failed	< 1	N	C	Y	
Zircaloy					
LWR MOx	<100	Y	Y	Y	[39–42]
MOx and PuO ₂ Residues	40	N/A	Y	N/A	[43,44]
SGHWR	4	Y	Y	Y	[40,45]
Carbide & Corium					
Carbide (PFR & WAGR)	2 & < 1	C Y	C Y	Y Y	[1,36,46]
Corium and FCM	N/A	N	N	C	[20,47]

2.2.2 Stainless steel clad fuel types

Following a white paper published in 1964 [48], the advanced gas-cooled reactor (AGR) design was selected for efficiency and safety improvements over Magnox. While still graphite moderated and CO₂ cooled, AGR fuel consists of low enriched uranium oxide ceramic pellets, clad with stainless-steel [49], see **Figure 2.2.2.A**. The first trial of the technology took the form of a Windscale advanced gas-cooled reactor (WAGR) unit constructed c.1963 [50]. A further total of

seven dual unit power stations were constructed across the United Kingdom between 1965-1989, with 10 power reactor units still in an operational condition at the time of writing [51]. A significant quantity of ex-reactor AGR fuels has also undergone some degree of corrosion during medium term storage [52], see **Figure 2.2.1.B**. The Dounreay fast reactor (DFR) programme for breeding of plutonium isotopes was operational between 1959-1977, initially introduced to bridge a technological gap for development of UK reactor technology [53]. The breeder blanket material, while not considered to be fuel, is primarily irradiated natural U metal. Another campaign conducted at the Dounreay site was for the prototype fast reactor (PFR) which operated between 1975-1994. PFR used mixed oxide (MOx) ceramic fuel pellets with a mixture of uranium and plutonium oxides clad with nickel-iron and stainless-steel alloys [37].

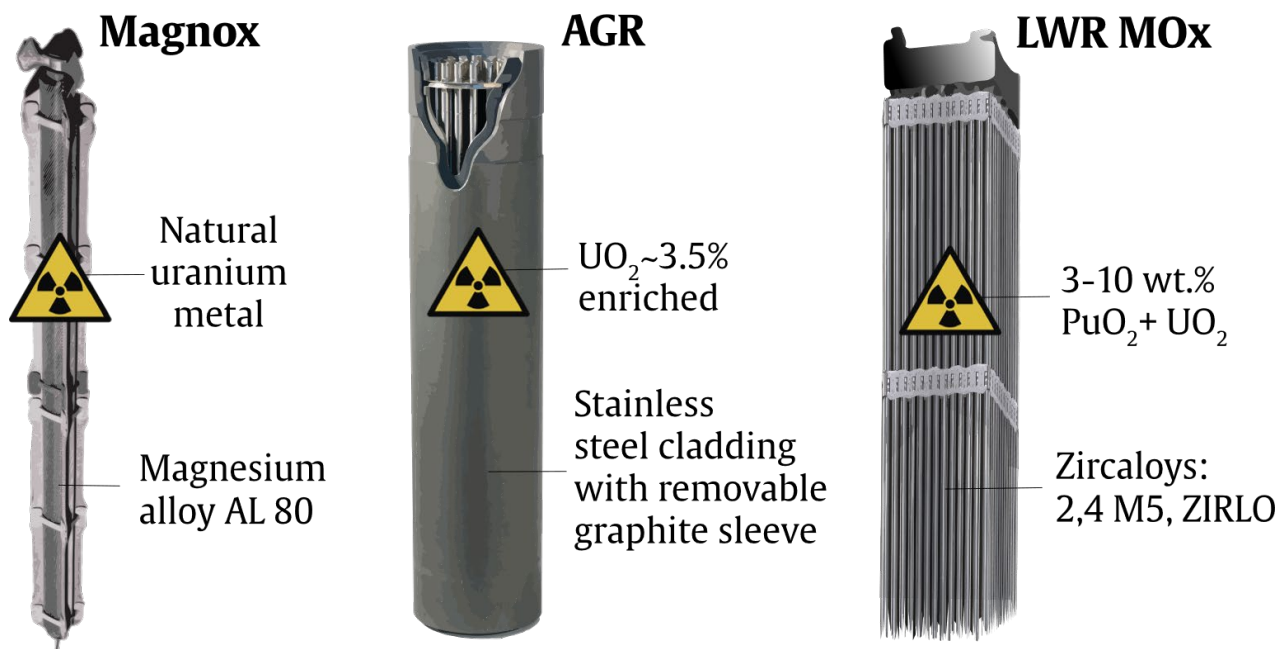


Figure 2.2.2.A - Drawings showing main representative UK orphan fuel types, with cladding and fissile material notes. Figure adapted from the Science Museum Group Collection (1968, c.1982 and 1995) [54–56].

The DFR metallic uranium blanket is made up of pucks with approximate dimensions of 35 mm diameter and 150 mm length, stacked up to ~2.5 m and clad with Type 321 stainless steel [57]. A primary concern with the continued decommissioning of the remaining core, is the blanket material still covered with the molten salt coolant, the status of which has only recently been monitored since operation, see **Figure 2.2.2.B**. While the bulk of spent AGR fuel is considered by the Nuclear Decommissioning Authority (NDA) to be a zero-value asset, some trial materials from WAGR development have already been assigned to the orphan fuel inventory. The

WAGR fuel consists of UO_2 pellets, enriched to 3.5% and 6.0% ^{235}U (annular and cylindrical respectively). Such pellets were clad with austenitic stainless steel (Nb doped, 21.4 mol.% Cr, 23.7 mol.% Ni, Fe bal.). As with Magnox fuels, a variety of WAGR cladding geometries were tested and some fuel pins were even intentionally failed, degrading further in inadequate storage [34,35], see **Figure 2.2.1.B**. A relatively smaller quantity of residual MOx fuel from the PFR programme is made up from annular ceramic UO_2 pellets with 23.1 - 31.8 mol.% PuO_2 , clad with Nimonic PE16 (40.7 - 43.7 mol.% Ni + Co, Fe bal.) and M316 stainless steel (Mo doped, 27.1 - 32.2 mol.% Ni + Cr, Fe bal.) [35,36]. The plutonium content of these assemblies is dependent on the location in the core where they were irradiated and some reaction products may have developed from approximately 1 tonne of heavy metal (tHM) equivalent of corroded material [37]. Most of these stainless-steel type fuels can be de-clad with relative ease to allow for an oxide dry-way process, excluding those which are significantly deformed or corroded and the DFR breeder material. Use of metallic U as a feed, would require the use of an oxidation conversion process to obtain UO_x , although, as with the de-clad Magnox stream, there is a potential hazard with its pyrophoric characteristics [29]. Subsequently, the majority of steel-clad type fuels can otherwise be chemically dissolved with or without cladding, producing either a fuel liquor of U with varying quantities of Pu and FPs, or total dissolution liquors containing significant contaminant inventories of alloy metals (Fe, Cr, Ni, Co and corrosion products) in solution [30].

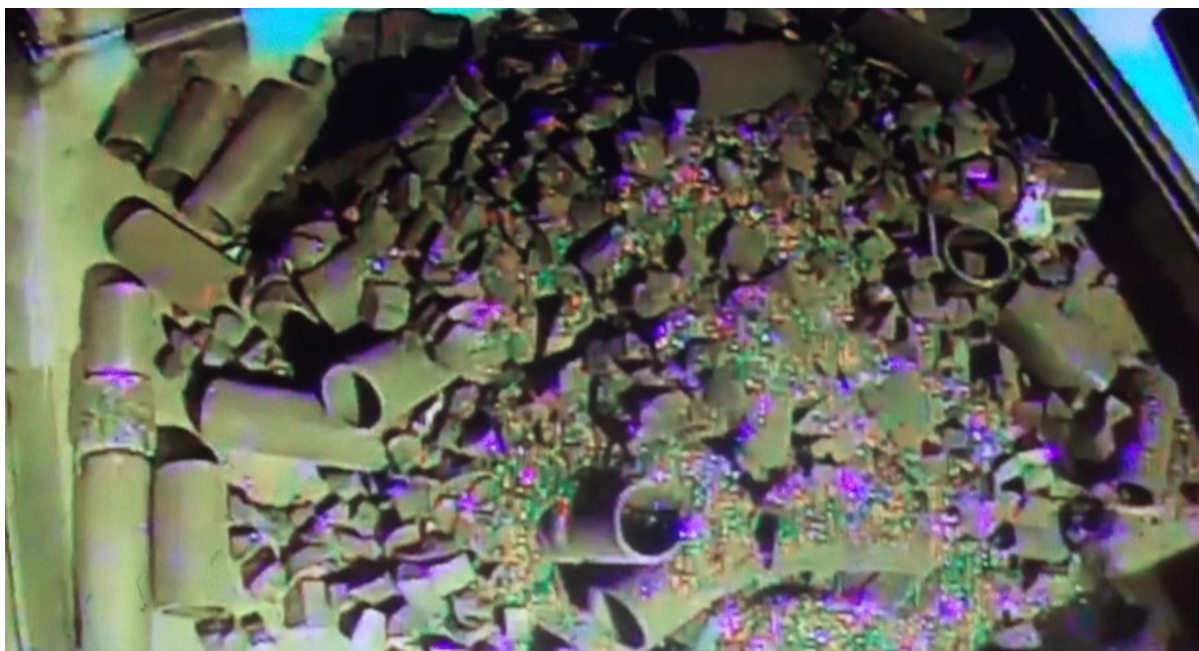


Figure 2.2.2.B – Closed circuit overview of fast reactor MOx bin (*Kay Farmer, DRSL, Reproduced with permission*).

2.2.3 Zircaloy clad fuel types

The most recent UK civil nuclear installation, a dual pressurised water reactor (PWR) generating station at Sizewell B, completed its commissioning phase in 1995, and still stands as the only two completed UK reactors of this type at the time of writing [10,51]. This follows LWR designs which have been widely adopted internationally. Demineralised water is used as a cooling medium and moderator, with fuel consisting of low enriched uranium oxide clad with corrosion-resistant zircaloy-4 [58], see **Figure 2.2.2.A**. International development of MOx technology spurred the construction and commissioning of the Sellafield MOx demonstration facility (MDF) in 1993, which was used to establish a native capability for production of mixed oxide fuels. MDF was shut down between 1999-2000 amid a data falsification enquiry concerning MOx assemblies sent to international customers [39]. A later installation was the Sellafield MOx plant (SMP), which produced its first fuel in 2002. SMP was shut down in 2011 following the Fukushima Daiichi accident, after producing only enough MOx for seven fuel assemblies (calculated for a typical Sizewell B assembly) [59].

Sizewell B and proposed future UK PWR stations have been suggested as a possible avenue for burn-up of separated plutonium and spent fuel feeds via MOx routes, though this necessitates intensive reprocessing and modification of reactors [39]. Spent PWR fuel from the Sizewell B reactors is currently considered to be a zero-value asset, although there is still a notable inventory of unirradiated development and validation materials designated as orphan fuel. Destructive testing and trials for fuel assemblies included drop-tests to verify the integrity of fuel pins, examples of resulting material can be seen in **Figure 2.2.1.B**. Due to the variety of assembly designs that were considered and trialled before MOx production was discontinued, the orphan ceramic fuel pellets arising from LWR MOx have a PuO₂ content varying between 2.9 – 9.8 mol.% with the balance as UO₂. This fuel type constitutes up to 100 tHM, not including the cladding with varying assembly geometries and zirconium alloys: zircaloy-2, -4, M5 and ZIRLO (Zr bal. with < 1.6 mol.% Sn, Fe, Cr, Ni or Nb) [40–42], see **Figure 2.2.2.A**. Fortunately, these materials are unirradiated, and would be suitable for de-cladding prior to conditioning. The presence of a significantly lower quantity of MOx and PuO₂ residues, 40 tHM, has also been grouped here due to the already significant plutonium content of the waste feed. These materials include mixed fuel pellets, scraps, and residues, depleted oxides, UO₂ and PuO₂ ceramics. While not specified with cladding materials, these residues have been largely sourced from Dounreay and SMP, with some contaminated materials from decommissioning activities [43,44].

The steam generating heavy water reactor (SGHWR) was a research reactor at Winfrith, operating between the 1950's – 1990's, which used low enriched uranium fuel with a

deuterated heavy water moderator and a light water secondary coolant loop [45]. Orphan fuel from the Winfrith SGHWR only contributes 4 tHM towards orphan fuels and consists of irradiated low enrichment UO_2 clad with the aforementioned zircaloy-2 (experimental Nb and Ti additions). SGHWR orphan fuels have both 36 and 60 rod configurations with small quantities of PIE waste following surveillance during its operational lifetime [40,45]. The most straightforward pre-processing system for these zirconium clad fuels would be removal of cladding followed by chemical dissolution for a U and Pu rich liquor feed, with minor FP contributions arising from irradiated SGHWR material. In the rare cases where de-cladding is not possible, a significant inclusion of Zr will be present in a full dissolution liquor with corresponding quantities of minor transition metal dopants in solution (Sn, Fe, Cr, Ni, Nb and Ti).

2.2.4 Carbide and fuel containing materials

A very small quantity of carbide fuel was trialled using the PFR and WAGR facilities during their operation, 2 tHM and <1 tHM, respectively [14,37]. These exotic materials were produced in order to support research for high-temperature and accident tolerant fuels. The UK carbide trial fuels have typical chemistries of U_xC_y with some (U, Pu)C used during PFR research. Non-standard annular pellet and spherical geometries were used for the fuel, subsequently clad with M316 stainless steel or SiC [8,38]. In some cases, the carbide fuels form a composite with cladding alloys or Si, this is poorly suited to dissolution processes, with residual SiC from total dissolution proving problematic due to its poor acid solubility. Where carbide materials are clad with stainless steel, dissolution following de-cladding would produce a U and Pu rich liquor with FPs and some residual graphite.

Additionally, it is recognised that the understanding of treatment of material from damaged reactor cores is important to demonstrate suitable methodologies in preparation for the recovery and sequestration of fuel debris from Chernobyl and Fukushima Daiichi reactors. Although the UK only has small quantities of material resulting from a fire within the Windscale Pile 1 in 1957 [2], much can be learned by studying fuel-containing materials, ‘fuel lavas’ or ‘corium’ from previous nuclear accidents, as briefly mentioned in **Section 2.2**. In the USA, Three Mile Island Unit 2 was a PWR that experienced a partial core meltdown in 1979 [60]. In Ukraine, Chernobyl Reactor No. 4 was a graphite moderated UO_2 fuel reactor (RBMK) which completely melted down in 1986 [4]. The most recent loss of coolant accident occurred in Japan and triggered the partial meltdowns of the boiling water reactor (BWR) Units 1-3 and spent fuel damage in Unit 4 at the Fukushima Daiichi power plant in 2011 [61]. In the latter case the base fuel is a uranium oxide, with one of the Fukushima Daiichi cores (Unit 3) loaded with MOx fuel, in all cases, the fuel was

clad with zircaloy. The majority of known FCM is heavily contaminated with cladding-actinide eutectics, neutron arrestors such as boron and reactor vessel structural materials [20,47]. Corium and other FCM presents a significant processing challenge, as de-cladding is not feasible, and a wide gamut of contaminants are present. A liquor resulting from total dissolution of FCM would likely have Ca, Si, Mg, U, Pu, Zr, Fe, Cr, Ni, Al, B, FPs, in solution.

2.2.5 Ion exchange materials for effluent treatment

Liquid effluent waste is a persistent radiological hazard and significant engineering problem that arises during any decommissioning activities of wet nuclear licensed facilities. As such, effluent treatment is prevalent at many nuclear licensed sites in the UK, particularly those in post operational clean out (POCO) and decommissioning phases. Contaminated water and other effluents are pumped through columns of ion-exchange media or reverse-osmosis apparatus, whereby contaminant radionuclides are concentrated onto exchange material or into active liquors. A notable example is the Sellafield Site Ion-Exchange Effluent Plant (SIXEP), which processes feedwater from fuel storage ponds and other plant decommissioning projects. SIXEP uses a series of exchange vessels to reduce effluent concentrations of aqueous strontium and caesium, employing a primary exchange material of a natural aluminosilicate zeolite, clinoptilolite, with an approximate formula $\text{Na}_6\text{Al}_6\text{Si}_{30}\text{O}_{72} \cdot 24\text{H}_2\text{O}$ [62]. This chemistry has an excellent ratio of cations for direct vitrification or sintering to produce high stability phases in glass-ceramic wasteforms, without further additions of base glass, filler or modifiers [63,64].

The UK-Japan collaborative research programme has supported study of such ion exchange materials, with Japanese interests arising from the importance of ion exchange systems for the remediation of Fukushima Daiichi. Since the 2011 earthquake, tsunami and subsequent nuclear disaster, the overwhelming footprint of the decommissioning water treatment facilities and processing waste storage at the Fukushima Daiichi nuclear power plant (NPP) site is one of the issues hindering progression of decommissioning activities. The meagre availability of space has necessitated the dilution of low activity effluents into seawater [65], to allow for storage of more hazardous high activity wastes. Therefore, prompt and significant volume reduction of waste ion specific media into a robust immobilised wasteform is necessary to permit the reclamation of site space for fuel removal activities, while adhering to strict waste acceptance criteria (WAC) for interim to long-term storage [66].

2.3 Immobilisation of degraded and spent nuclear fuel

For over half a century, states using civil nuclear power have amassed these spent fuel elements; the segregation and storage of this SNF is becoming a growing concern due to potential for further degradation, high associated proximity doses and radiological inventories [67,68]. In order to meet the waste acceptance criteria for geological disposal, organisations and governing bodies have been founded to safely manage and treat spent fuels for long-term storage, researching and developing new methods where suitable technologies do not yet exist. There are several key waste performance characteristics that include technological complexity, lifetime durability, chemical solubility for actinides and FPs, radiation tolerance, volume increase and expense.

2.3.1 Dissolution, separation, and re-processing

The UK already has extensive experience of reprocessing, with the opening of the Magnox reprocessing plant in 1964, recovering useful actinides from spent fuel using the chemical PUREX process while separating minor actinide and FPs into an HLW stream for vitrification. The thermal oxide reprocessing plant (ThORP) was built and commissioned between 1978 - 1994 for processing of the newer AGR and LWR oxide fuels using a similar process, working with experience gained from Magnox reprocessing. The ThORP facility ended its last processing campaign in 2018 with the Magnox reprocessing lines closing in 2022 [31,69]. Early closures have been caused by accelerated shutdown and post operational clean-out (POCO) timetables, in the wake of reduced workforces and facility downtimes during the COVID-19 [70]. Some of the most significant components in the UK orphan fuels inventory include highly corroded and contaminated Magnox fuel, meaning further steps would be required to extract the fuel and FPs after total chemical dissolution. Furthermore, many existing facilities and designs for treatment plants do not have adequate handling equipment for these non-standard orphan fuels. As such, only de-cladding of fuel, fuel dissolution and total dissolution will be considered here as potential preparatory processes for production of homogeneous oxide and calcine waste feeds.

2.3.2 Spent fuel pond storage

Although during the past several decades, many states operating civil nuclear facilities have established re-processing campaigns for spent fuel, there is a significant inventory of high burn-up and non-standard spent fuel materials with substantial heat generation and contact dose rates. Much of the industrial experience developed to date has been with wet pond storage, and while the global capacity was increasing in tandem with the development of new civil nuclear installations, the growth has stagnated in the past decade, with an approximate global storage capacity of

200,000 tHM. An IAEA technical document released in 1999, advocated for installation of medium-term wet storage at ‘away from reactor’ facilities, although little consideration was made for supporting storage and transfer of damaged and degraded fuel elements [71]. Poorly engineered pond storage has been a significant source of degraded spent fuel, due to mishandling, corrosion of cladding and interaction with containment materials. In addition, pond storage is not suitable for degraded fuel such as those in the UK orphan stock, or for ruptured fuel, which would lead to accelerated corrosion. Pond storage is also susceptible to accidents such as those at Fukushima Daiichi where active cooling circuits can be a point of failure, after which decay heat evaporates the water, exposing the spent fuel [72]. As such, this technique has little prospect for safe long-term storage of orphan fuel materials.

2.3.3 Dry cask and high integrity container storage

Dry storage of spent fuel materials is subject to stringent requirements such as the heat generation properties of the fuel, cladding and fuel oxidation potential, storage atmosphere and cooling demands. Dry storage typically comprises hermetically sealed storage casks or canisters, where the atmosphere can be controlled to provide an inert or low reactivity gaseous environment.

Several Scandinavian projects for geological disposal have been preparing to implement dry storage canisters for spent fuel assemblies. The nuclear fuel safety-3 (KBS-3) system, **Figure 2.3.3.A**, consists of a cast iron separating grid to hold the dried fuel elements, which is surrounded by a welded copper overpack. These canisters will then be buried in spaced boreholes within the facility and backfilled with bentonite clay. The final barriers are cementitious backfill and up to 500 m of bedrock as a feature of the facilities’ geology. This multi-barrier design has been proposed for repositories in both Olkiluoto, Finland and Forsmark, Sweden, supported by research highlighting low potential for oxidation of the protective copper overpack [73,74]. The low porosity of bentonite buffer materials also serves to retard migration of potentially corrosive ions in impure groundwater [75]. Some work has suggested that over the 100 millennia lifespan of such a facility, the canisters could fail due to copper sulfidation reactions with small quantities of exposed groundwater or stress-corrosion cracking [76], though extensive validation and modelling has indicated that these are extremely low probability failure modes [73,77]. Other potential issues with the KBS-3 system are overpressure and rupture due to evolution of fission gasses. However, ideally any hydrogen and oxygen generation by radiolysis will be limited by absence of residual water via the drying stage [78,79]. Modelled estimates of the longevity of the copper shield are in the 10^5 - 10^6 y range, which means this material is suitable for long-term storage [73,80]. Objectively, some of the most significant drawbacks of this technology are the volume increase of spent fuel waste and

the cost associated with 5 cm thick overpacks of highly pure oxygen-free copper, considered a limited resource by production output [77].

Most geological repositories proposed and designed, such as the Scandinavian KBS concepts, rely on a granitic or basaltic crystalline host bedrock to host high-level nuclear waste and spent fuel. While this ideal geology is available in regions of Northern Ireland, Devon, Gwynedd and Aberdeen, administrative support for siting has wavered following discussions in the mid 2010's [81,82], only re-emerging in the public forum during the early 2020's. A significantly more accessible geology for siting-stage disposal programmes (not only in the UK but other siting countries such as France and Switzerland) is a type of lower strength sedimentary mud-rock, opalinus or argillite, which is enriched with clay particles. This clay material can be hydrated and serves to retard the diffusion of groundwater, providing in effect a hydrological 'cage' for segregation of waste packages [83–85].

Stores of legacy Magnox fuel in the UK have been held for cooling in intermediate dry stores such as those at Wylfa Power Station in Wales. Due to the reactive nature of the magnesium alloy cladding and to prevent oxidation of the metallic uranium fuel, the elements are held within an anoxic carbon dioxide atmosphere with active cooling [86]. Despite the costly measures to maintain an artificial atmosphere and cooling, some issues with ingress of water causing corrosion were highlighted after commissioning of the Wylfa Buffer stores [10], and estimates for the design lifetime of such storage vaults do not extend beyond 100 y [87]. Dry storage of UK orphan fuels in a controlled atmosphere would therefore not be an appropriate long-term solution. Furthermore, with irregular geometries, compositions and heat generation, even de-clad fuel and oxide ceramics would prove difficult to efficiently store and could result in high local dose rates, introduce a significant potential for uncontrolled criticality and require passive or active cooling.

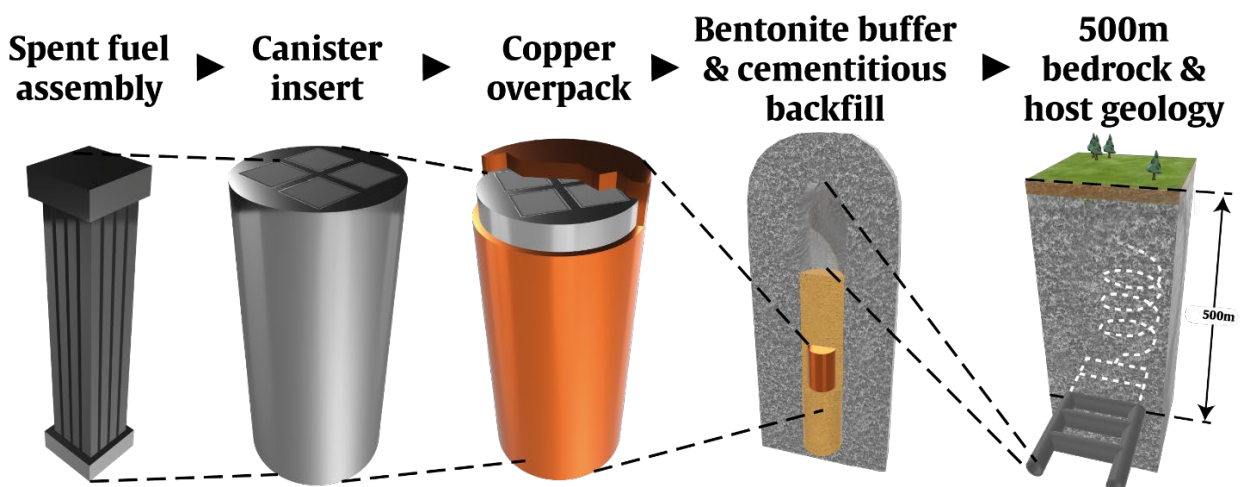


Figure 2.3.3.A – Drawing of simplified KBS-3 concept, not to scale, adapted from *Release-Barriers*, Posiva Oy [74].

2.3.4 Cementation

Historically, significant quantities of fuel wastes have been encapsulated with grout or cement, including the backfilling of legacy Magnox fuel canisters with ordinary Portland cement (OPC), some of which has since failed and corroded, necessitating further conditioning and processing. Greater success has been garnered with lower-level wastes, which are stored in a canister that would be typically backfilled with grout [88]. A recent study conducted with a blended Portland - blast furnace slag (BFS) grout loaded with organic simulant and < 0.5 mol.% PuO_2 , demonstrated that the alpha decay can cause minor alterations in the hydrated cement phases and generate small quantities of hydrogen gas, however further study is required to characterise local phase alterations surrounding PuO_2 particles and there may be limitations for high loadings of plutonium containing materials [89]. With a carefully balanced composition and low radionuclide waste loading, cementitious wastefoms can be designed to buffer the local pH and stabilise over a $10^2 - 10^4$ y time span. However, the models highlighting this only demonstrate this as a chemical equilibrium, in reality the structural properties of the grout would lead to failure much earlier than this, potentially resulting in the release of radionuclides into groundwaters [90]. The disposal lifetime of OPC and even the more durable BFS compositions is inadequate for the proposed orphan nuclear materials, considering the $> 10,000$ -year disposal timeframes required. Thus, while cementation may provide a low-cost, rapidly implementable solution for easier handling of waste and placement in storage, there are potential hazards arising from failure of the cementitious matrix and storage drum. Radiolysis, thermal instability from decay heat and hydrogen generation, all represent significant long and short term factors in the inferior performance of these wastefoms compared to vitreous and ceramic wastefoms [91]; normalised leaching rates for cementitious wastefoms range between $\sim 10^{-1} - 10^3$ g m⁻² d⁻¹ compared to rates as low as $\sim 10^{-3}$ g m⁻² d⁻¹ for some borosilicate glasses [92,93]. The volume increase associated with cement encapsulation is well recognised as an important turning point for consideration of other immobilisation techniques, especially those wastes assigned to space-limited geological disposal. Despite these prevailing issues, OPC is still being considered as a bulking material for European multi-barrier geological disposal concepts [94], with less critical dependencies and lower risk factors associated with corrosion and direct interaction with fuel. While direct disposal, dry storage and cementitious encapsulation of these fuel materials were initially seen as economical and straight forward; their use has been continually contested for deleterious hydrothermal conditions, high volume increases and poor long-term stability [94]. Further work has found that radiation tolerance is poor, and corrosion can be triggered by hydrated cement phases. Consequently, cementitious wastefoms do not provide a viable method for immobilisation of any UK orphan fuel feeds.

2.3.5 Vitrification

Vitrification of radioactive wastes has been promoted as a treatment technique due to its chemical flexibility, process control for some melting technologies, and wastefrom durability [95]. Unlike crystalline materials such as ceramics or quartz, glass structure has no long-range order and is often described as amorphous, see **Figure 2.3.5.A**. Typical glass structure as suggested by the Zachariasen model [96,97], follows formation of a disordered network with several bridging covalent oxygen bonds between ionic centres of Si, P and B, the oxides of which examples of so-called network formers. Alkali cations of elements such as Na, Li and Ca can be added to glass formulations, disrupting bridging oxygen bonds and forming non-bridging oxygen bonds, in effect interrupting the glass network or behaving as so-called network modifiers [96–99].

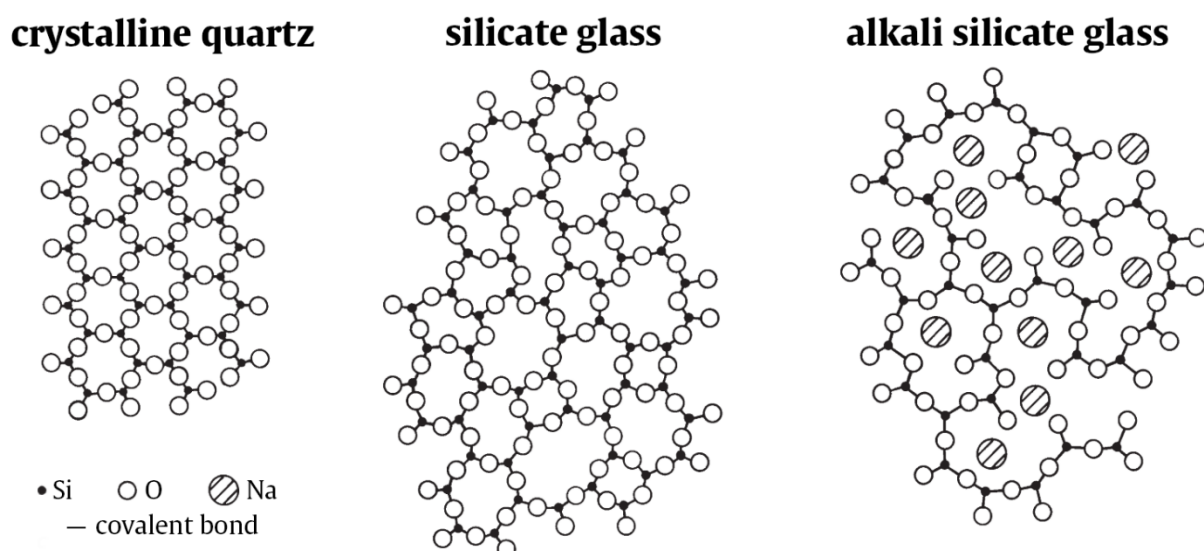


Figure 2.3.5.A – Sketch showing 2-dimensional structures of crystalline silicate quartz, amorphous silicate glass and sodium silicate glass according to the simplified Zachariasen model adapted from *Properties and applications of glass* [96,97].

Through decades of development, coupled with well-established methods adapted from the commercial glass industry, a systematic flow of operations has been established for production of glass wasteforms. For the Sellafield based waste vitrification plant (WVP), high level liquid waste is calcined with a sucrose solution to drive off water and nitrates. The calcined waste is then melted with a glass frit in an induction heated Nicrofer alloy crucible, up to approximately 1050 °C, mixed by sparging with argon gas. Lastly, molten glass is then cast into a canister [100,101], although for some intermediate level waste streams, in-container vitrification (ICV) technologies have been investigated to reduce tertiary wastes [102,103]. In Joule heated ceramic

melter systems, such as that implemented at Savannah River in the US, the homogenised waste can be melted with glass forming additives, enabling adjustment of the glass composition depending on the waste stream [104]. For non-heat generating wastes, post-casting steps such as annealing or slow cooling have also been introduced to optimise the glass structure through reduction of internal stresses, in turn reducing spontaneous fracture potential and diffusion surface area [105]. It is possible to eliminate such steps for high heat generating vitrified waste, as the glass may remain at physically elevated temperatures for decades. Quality assurance, verification and safety assessments of these glass materials are typically carried out using a suite of analytical techniques such as product consistency testing (PCT) [90].

2.3.5.a Silicate glasses

Silicate glasses and borosilicate glasses are attractive matrices for immobilisation of HLW due to their thermal stability, retention of fission products and chemical durability. Excellent durability can be achieved by close control of the composition within a region of immiscibility and rapid quenching [99,108]. WVP uses a slightly modified version of the two-stage French ‘Marcoule vitrification workshop’ (AVM, translated) process, altered due to reflect UK waste streams arising from Magnox reprocessing [86,92], with compositions fixed to include that of Magnox liquor. The wasteform produced has a magnesium borosilicate composition with a base glass with the mixture Windscale (MW) composition, see **Table 2.3.A**. Evidently, this now presents the issue of diminishing Magnox liquor supplies following the cease of reprocessing operations at Sellafield, as well as the costly and hazardous frequent replacement of a Nicrofer melting vessel (previously an Inconel vessel) [100]. Moreover, both AVM and WVP require a fully homogenised waste feed with controlled composition, further reducing throughput and increasing process complexity.

It has been well established that borosilicate systems can produce robust, high durability materials containing daughter FPs and waste elements, although their ability to maintain such desirable properties while supporting high additions of uranium oxide components (UO_x) in the glass matrix is severely limited, and higher melt temperatures in the range of $1150\text{ }^\circ\text{C} - 1500\text{ }^\circ\text{C}$ induce volatilisation of radionuclides such as ^{137}Cs [100,110]. A series of alkali borosilicate glasses produced with a HLW waste feed containing significant inventories of sodium, aluminium and iron oxides, loaded up to approximately 8 mol.% U_3O_8 , were analysed using X-ray absorption spectroscopy. Results indicated that uranyl speciated primarily as U(VI), the U(V) content increasing with larger additions of aluminium oxide [111]. While the uranium component was demonstrated to have been retained in a glass phase, the speciation to hexavalent uranium is not conducive to long term chemical durability as it is easily hydrolysed [112]. Some longer duration PCT- type studies of MW borosilicate glass with 25 wt.% simulated HLW calcine, show a

normalised Si mass loss of $1.05 \times 10^{-3} \text{ g m}^{-2}$ at 28 days and $9.94 \times 10^{-4} \text{ g m}^{-2}$ at 168 days in water [113]. If a new plant for separation were to be commissioned, the corroded and contaminated legacy Magnox element of the inventory would vary too significantly from ideal glass batch chemistry, necessitating a dilution with larger volumes of glass and sacrifice to chemical durability, such as those arising in prototype Butex containing glasses [114]. A sodium borosilicate glass composition known as SON68, is loaded with small additions of Li, Zr, Fe, Mo, Al, Zn, Ca and Nd to simulate HLW. An intermediate glass durability study taking repeat aliquots from the same dissolution vessels of SON68 glass indicated that the normalised loss of Si at 360 days was approximately $8 \times 10^{-5} \text{ g m}^{-2} \text{ d}^{-1}$, achieved via formation of a passivating layer depleted in sodium, lithium and boron [115–117]. Formation of such a layer may be achieved intentionally through corrosion testing prior to long term storage, in-effect pre-forming the passivating layer and increasing in-repository hydrolytic durability. Studies incorporating a high uranium content and simulated HLW calcine into MW glass blends have shown that alkali channels provide a loading capability for U (VI) as uranyl species covalently bonded to oxygen linkages. Nevertheless, UO_3 loading was only around 5 mol.% and the wastefoms had an undesirably high solubility in water [118]. A composition studied by workers in Italy, with a borosilicate base, U2, was incorporated with 1.4 mol.% U_3O_8 at 1200 °C in air. Monolithic glass samples were found to have uranium loss rates of approximately $9 \times 10^{-2} \text{ g m}^{-2} \text{ d}^{-1}$ after 24 days of dissolution, despite the low rate, this is significant as the uranium accounts for a very low molar content in the overall melt [119]. Borosilicate glass solubility for uranium is strongly dependent on the valence state, with the possibility of loading up to 40 wt.% with poor hydrolytic durability U (VI), but only 9 wt.% with U (IV), before crystallising out as UO_2 [120–122].

Alternative glass wastefoms have been trialled through casting of sodium-aluminoborosilicate compositions and processing the glass through a preferential dissolution step, whereby sulfuric acid can be used to partially break down weaker elements of the glass network, leaving a porous silicate matrix. The matrix can be used to host large cations and radioactive waste nuclides such as those prepared with up to 3.5 mol.% Mo_2O_3 simulant [123]. However, little demonstration has shown successful actinide loadings of >10 mol.% waste, furthermore densification and closure of pores to improve hydrolytic durability following waste loading remains a pertinent challenge [99,123]. A method of further improving the hydrolytic durability of such silicate glasses can also be achieved with use of local heating in a ‘flame polishing’ treatment step, whereby the glass surface is heated causing alkali network modifiers such as sodium to volatilise. The result is conversion of several non-bridging oxygen sodium bonds to an appreciably more durable silicate bridging oxygen bond [99,124]. While this may serve as a suitable technique for

commercial glassware and glass products, the introduction of additional processes that risk thermal shock and volatilisation of fission products and actinide species would require additional engineering consideration for off-gas and scrubbing systems [125]. Furthermore, as the method requires access or exposure of the glass product surface, it would not be suitable for in-canister vitrification and direct canister casting wasteforms.

2.3.5.b Phosphate glasses

Initially developed during the 1940's and 1950's, low melting temperature phosphate glasses were later proposed as an alternative to borosilicate glasses for radioactive waste immobilisation [126–128]. However, the corrosive melting conditions caused by early phosphate compositions hindered development, and limited progression since has been largely attributed to the relative absence of industrial experience [128]. Phosphate glasses utilise P and the oxide form of P_2O_5 as the key network former, with simple local structural units of PO_4 . These tetrahedral sub-units form with three bridging oxygen bonds and one of the oxygen-phosphorous bonds as a double bond, to balance the 5+ charge of phosphorous [99,129]. Base phosphate and aluminophosphate glasses have poor solubility for uranium offering no advantage over silicate equivalents [130], however in the domain of nuclear waste glasses, iron additions via iron oxide, Fe_2O_3 are made to phosphate compositions to drastically increase the aqueous durability over simpler phosphate glasses [131]. However, Fe(III) has been demonstrated to behave as a network former with bridging oxygens, while Fe(II) behaves as a network modifier forming non-bridging oxygen bonds [99,132,133].

Recent cursory studies have been undertaken to assess the viability of increasing waste loading of sodium-iron-phosphate glasses through use of small refractory additions and a surrogate cerium oxide waste component [134]. Many of the compositions assessed in this review are of a 40/60 mol.% iron oxide-phosphate system base glass, as their high UO_x loading capabilities out-perform those of equivalent alkali borosilicate, **Table 2.3.A**. A low temperature iron phosphate – with minor alumina and silica additions, named by authors as $PFeUO_x$, formed a homogeneous glass with 3.2 mol.% UO_2 , resulting in a maximum leach rate of $8 \times 10^{-2} \text{ g m}^{-2} \text{ d}^{-1}$ after 7 days under PCT conditions [135,136]. Several further studies have assessed an array of properties for two iron phosphate base glasses, '15% UO_2 ' and 'Sample C', loaded with 15-19 mol.% UO_2 , respectively. Although durability measurements were limited, XAS and Mössbauer analyses indicated a high ratio of Fe (III) present in both samples, which forms significantly less soluble oxygen network bonds than that of Fe (II) [137,138]. Research for immobilisation of Russian high activity wastes has generated some phosphate glass compositions which allowed for high uranium incorporation, a sodium alumina phosphate, SAP 1-7 with 23.9 mol.% UO_3 , and a sodium aluminium iron

phosphate, SAIP 2-7 with 25.0 mol.% UO_3 . PCT and Materials Characterisation Centre (MCC) testing showed that the dissolution rate doubled with the addition of iron, leading to a normalised dissolution rate of $8 \times 10^{-2} \text{ g m}^{-2} \text{ d}^{-1}$ [139,140]. While typically addition of iron has shown to improve durability of phosphate glasses, a possible cause of this effect is the higher molar content of UO_3 for the 2-7 glass may significantly shift melt redox chemistry, further driving oxidation of iron to Fe (III) which forms less durable linkages with the glass network. This is evidenced by devitrification for the higher U content 1-8 and 2-8 glasses in the study. A magnesium phosphate glass study used a base glass frit of oxide constituents and phosphoric acid, these were then melted with simulated HLW calcine, cast, and characterised for durability via MCC-2. The base glass wastefrom had a relatively poor durability leaving a net loss rate of $5 \text{ g m}^{-2} \text{ d}^{-1}$, which improved down to $0.1 \text{ g m}^{-2} \text{ d}^{-1}$ with a 45 wt.% HLW simulant [141]. This glass type may be a promising immobilisation route for legacy Magnox fuel, however further work will be necessary to determine the effects of corrosion products and fuel actinides in the waste feed.

Fully dissolved stainless steel clad fuel materials such as WAGR and those fixed in steel canisters are particularly well suited to iron phosphate glass vitrification, as the high iron content of the pre-processed fuel liquor will stabilise the melt and increase wastefrom chemical durability [131]. FCM could also find a suitable disposition pathway with phosphate glass although the alkali contamination would need to be closely monitored to avoid development of U (VI) which forms highly mobile and soluble ions such as those used during reprocessing [30] and can be more easily hydrolysed than tetravalent uranium [112]. The inclusion of other alloying transition elements may be prohibited if the pre-processed feed is solid: due to the melt temperature difference, a undesirable glass microstructure with alloy or oxide inclusions may develop, leading to potential stress concentration and preferential dissolution [142–144]. Use of cold crucible induction melting may improve the lifetime of refractory and melter materials, as a crucible cooling jacket and skull layer of solidified glass protect the melter. Nonetheless, there is a significantly greater associated financial and technical start-up cost, with potential for continued high-level maintenance and long preheat-startup times [145].

2.3.5.c Glasses for Zircaloy clad and exotic fuels

Zirconia is poorly soluble in oxide glasses, it may therefore be pertinent to attempt separation from feed liquor using a hydro-chlorination process such as Zircex [146], producing a zirconium tetrachloride. Oxidation of the tetrachloride via steam hydrolysis in the reaction vessel, generating zirconium oxide, ZrO_2 . This oxide form, zirconia has shown to improve the chemical durability of French alumino-borosilicate glasses, formed from an inactive calcine melted in an induction vessel.

Low incorporation zirconium glass compositions have been demonstrated with octahedral coordination of Zr^{4+} [147]. Use of such waste glass compositions has only been successfully demonstrated with relatively low quantities of uranium dioxide and zirconia, 0.1 mol.% and 1.5 mol.%, respectively, among an array of FPs and transition metal oxides. A FP stream was calcined at 400 °C, before addition of a glass frit and melting at up to 1150 °C after casting. It should be noted that RuO_2 and a metallic precipitate had devitrified [148]. The poor loading of such a composition indicates that a significant volume increase would result for such fuel feeds as LWR, likely only appropriate for immobilising the minor quantity of zircaloy feed that cannot be de-clad. Despite the relatively low melt temperature, the limited containment of volatile FPs for a high zirconium FCM melt would also not be suitable.

For a separated carbide fuel-cladding feed, the dissolved liquor comprising U, Pu and FPs would be suitable as a minor addition to one of the phosphate glass systems, in effect diluting the effects of contaminant SiC. Alternatively, for the carbide fuel types where SiC cladding is entrained, a method has been studied that utilises oxidation of the silicon via hot nitric acid to form SiO_2 , which is a primary targetable glass former that could be used for borosilicate glass feeds [149]. Metallic wasteforms for cladding and low-intermediate activity metallic wastes are attractive for significant volume reductions. However, for orphan metallic fuels much like the fuels themselves, resulting wasteforms materials have significantly lower relative aqueous corrosion resistance due to generation of galvanic cells, requiring significant alloying of noble metals and therefore require higher melting temperature in excess of 1600 °C [150,151], leading to loss of volatile fission products such as Cs and Tc. Use of hot isostatic pressing as a thermal treatment method for metallic waste has also been considered, with the drive of retaining the inventory of fission products [152], though these techniques are technologically immature. A slightly more mature technology in development for low level waste treatment, plasma vitrification uses the rapid heating effect of a plasma torch to destroy organic matter and rapidly melt waste into a glass-slag material. Unfortunately, much of the development has been made for gasification type non-radioactive waste streams, where much of the byproducts generated are intentionally driven to gaseous phases and vented into the atmosphere [153,154]. Where optimised for low level nuclear waste, dissolution of the network forming boron steadily increased with time within range of reference wasteforms [155], however plasma vitrification still hold significant risk to loss of volatile fission product inventories due to high melting temperatures of 1600-1700 °C [153].

Table 2.3.A -Summary of base waste glass compositions and high UO_x compositions retrieved from literature, oxide components have been calculated to mole % and for all materials the glass/amorphous structure was stated but insufficient diffraction data was included for verification

Sample ID	Nominal (mol.%)											Batch Pre-treatment	Melt conditions	Annealing	Durability	Source
	UO ₂	UO ₃	U ₃ O ₈	P ₂ O ₅	Fe ₂ O ₃	Na ₂ O	B ₂ O ₃	Al ₂ O ₃	SiO ₂	Li ₂ O	MgO					
MW	-	-	-	-	-	12.4	14.5	-	71.3	1.9	-	Rotary calcination with sucrose solution before adding frit	1050 °C in Nicrofer, unknown duration, Ar sparge	Just below T _g for 3h and cool to RT at 0.5 °C/min	27D PCT-B & ICP-OES, ELR: B ~ 10 ⁻² g m ⁻² d ⁻¹ , ELR: Si ~ 10 ⁻² g m ⁻² d ⁻¹	[100,109]
U2	-	-	1.4	-	-	12.3	23.9	-	52.7	9.6	-	"Mixed"	1200 °C, unknown duration, air (inferred)	"Carefully annealed"	24D Powder MCC, 70 °C DI water, (Photospec) NL: U ~ 9 × 10 ⁻² g m ⁻² d ⁻¹	[119]
PFeUOx	7.0	-	-	40.2	23.8	13.8	-	5.6	9.5	-	-	Calcine 700 °C in air for 1h	1250 °C for 2h in air	550 °C and "slow cooling"	"PTC weight loss" ~8 × 10 ⁻² g m ⁻² d ⁻¹	[135,136]
15.0% UO ₂	15.0	-	-	58.7	26.4	-	-	-	-	-	-	"Homogeneous mixture"	1200 °C for 2h in air	450 °C for 3h and slow cool	Unknown, XAS and neutron scattering experiments undertaken	[137]
Sample C	19.0	-	-	48.6	32.4	-	-	-	-	-	-	"Homogeneous mixture"	1200 °C for 2h in air	475 °C for 3h and slow cool	Unknown, XAS and neutron scattering experiments undertaken	[138]
SAP 1-7	-	23.9	-	17.9	-	40.4	-	17.9	-	-	-	Hand milled	Ramp from RT to 1200 °C hold for 1h	-	7D PCT-A/MCC-3 & ICP-AES, NML/NL: U 2.7 × 10 ⁻¹ g m ⁻² / 4 × 10 ⁻² g m ⁻² d ⁻¹	[139,140]
SAIP 2-7	-	25.0	-	17.7	8.9	39.7	-	8.8	-	-	-	Hand milled	4h ramp from RT to 1200 °C hold for 1h	-	7D PCT-A/MCC-3 & ICP-AES, NML/NL: U 5.5 × 10 ⁻¹ g m ⁻² / 8 × 10 ⁻² g m ⁻² d ⁻¹	[139,140]
55M45P OW	-	-	-	45.0	-	-	-	-	-	-	55.0	"Combined"	1250 °C for 2h in air	-	20D MCC-2 & ICP NL: 5 × 10 ² g m ⁻² d ⁻¹	[141]

T_g: glass transition; RT: room temperature; ELR: elemental loss rate; NL: normalised loss

2.3.6 Ceramic immobilisation

Ceramic materials are typically formed from a basis of oxide compounds sintered together to form a monolithic, crystalline body or crystalline powder. The dense and structured nature of these matrices indicate suitability for use as a robust disposition method, whereby radionuclides and other hazardous waste elements are incorporated into the crystalline structure of the wasteform.

2.3.6.a Single phase ceramics and use of spark plasma sintering (SPS)

Single phase zirconolite ($\text{CaZrTi}_2\text{O}_7$) [156] is a titanate ceramic material for which natural forms have been recovered containing significant quantities of U and Th. Zirconolite structure typically follows a pyrochlore derivative of fluorite with TiO_6 and TiO_5 octahedra, while subunit Ca and Zr polyhedra form [157,158]. Substitution of pure actinides or transuranic elements occurs on the zirconium and calcium sites, integrating into the crystalline structure. Reports indicate that zirconolite has been successfully synthesised and loaded with uranium up to a nominal composition of $\text{CaU}_{0.4}\text{Zr}_{0.6}\text{Ti}_2\text{O}_7$ [157]. When the uranium loading ratio was kept low at about 1.4 mol.% and samples were sintered under an argon atmosphere, the oxidation potential was significantly reduced allowing for the targeted formation of the 2M zirconolite polytype, with tetravalent uranium (more electrochemically stable for aqueous durability). At significantly higher loadings above 6.4 mol.% uranium, phase separation is predominant and a pyrochlore type phase developed. It is reportedly not possible to synthesise a loaded single phase pyrochlore from stoichiometric constituents, as segregation of phases occurs with the development of TiO_2 and UO_2 . It is evident from the literature that single phase zirconolite is subject to polytypical formation of secondary and tertiary phases, so additions of FPs and further contaminants would be likely to destabilise the crystalline structure [159]. Certainly, for hot isostatically pressed plutonium immobilisation zirconolite wasteforms have far more favourable leach rates for Zr and $\text{Pu} < 10^{-5} \text{ g m}^{-2} \text{ d}^{-1}$ after 60 days of PCT type dissolution [160,161].

Betafite or $(\text{Ca}, \text{U})_2(\text{Ti}, \text{Nb}, \text{Ta})_2\text{O}_7$, has been considered for high uranium containing wastes because of its natural mineral formation with a pyrochlore type cubic structure [162], samples of which have been dated to be formed 1.4 billion years ago (approximately 2 half-lives of ^{235}U) [163,164]. Average uranium loading achieved in synthetic betafitites was ~25 mol.% uranium. X-ray photoelectron spectroscopy (XPS) confirmed uranium speciation to be a combination of pentavalent and hexavalent ions [165]. The brannerite pyrochlore-type species, $(\text{U}, \text{Pu})\text{Ti}_2\text{O}_6$ is a natural crystalline monoclinic crystalline structure with TiO_6 and UO_6 octahedra [166], that provides a host phase for immobilisation of major SNF component actinides. Experimentally, brannerite has been shown to hold uranium in mixed tetravalent, pentavalent and hexavalent states,

through a charge compensation mechanism dependant on processing conditions and dopant additions [167]. The chemical durability of synthetic uranium containing brannerites has varied greatly in experimental work, with analytical studies conducted using an assortment of dissolution techniques – normalised loss rates for brannerite vary between $\sim 10^{-3} - 10^{-1} \text{ g m}^{-2} \text{ d}^{-1}$ [168].

Monazite (CePO_4) has a phosphate rhabdophane mineral structure with Ce central atoms typically surrounded by up to 8 PO_4 tetrahedral subunits [169]. Single-phase monazite-type ceramic wasteforms have been doped with cerium and molybdenum, which under materials characterisation centre - 1 (MCC-1) test conditions had 28 day leach rates of approximately $2 \times 10^{-3} \text{ g m}^{-2} \text{ d}^{-1}$ for uranium and $\sim 4 \times 10^{-2} \text{ g m}^{-2} \text{ d}^{-1}$ for phosphorus [170]. This improved leach resistance is up to three orders of magnitude greater than that of equivalently loaded borosilicate glasses. Furthermore, monazite can retain these excellent durability properties after complete amorphisation of simulant-loaded crystalline structures by high-fluence irradiation [171], as well as alteration rates that are inversely proportional to temperature (up to $250 \text{ }^\circ\text{C}$) [172]. Natural samples of cheralite, a member of the monazite mineral group, with typical monoclinic structure $\text{Ca,Th}(\text{PO}_4)_2$ have been discovered with high uranium contents (up to $\sim 16 \text{ mol.}\%$) – where the tetravalent thorium has a predisposition to interchange with uranium and mixed lanthanides [173]. Although the cheralite structure has been shown to thermally decompose at high temperatures, a field-assisted spark plasma sintering (SPS) technique has been examined for thermal treatment of actinide wastes, utilising the simultaneous application of uniaxial pressure and direct current. This technique was able to successfully sinter samples, with glovebox apparatus, into high density pellets retaining the monoclinic cheralite structure [173]. Nevertheless, SPS technology is still relatively underdeveloped, especially with regard to production of uranium bearing samples.

Single phase ceramics can be sensitive to compositional changes outside of the main structural exchange components, these materials are therefore best suited to unirradiated, pristine fuels where corrosion products and FPs are absent. Although zirconium cladding could facilitate zirconolite phase development, the alloy dopants that are present in these materials would likely interfere with final phase assemblage, necessitating fine control of waste feed composition. The ideal feed for single phase crystalline materials would be de-clad LWR, low PuO_2 MOx fuels, either in oxide powder or dissolved liquor form.

2.3.6.b Multi-phase ceramics and use of hot isostatic pressing (HIP)

A multiphase titanate ceramic, known as synthetic rock (SYNROC), has been investigated by several nuclear science institutions, in collaboration with international waste research groups [174]. The main phases of SYNROC type-C are partially metamict zirconolite ($\text{CaZrTi}_2\text{O}_7$) [156];

orthorhombic perovskite (CaTiO_3) [175]; monoclinic hollandite ($\text{BaAl}_2\text{TiO}_{16}$) [176] following hot-pressing at $1200\text{ }^\circ\text{C} - 1400\text{ }^\circ\text{C}$ to digest components such as uranium and thorium from the waste stream. The multiphase assemblage, while providing some more preferential reactions with different waste components – e.g. the majority of actinides migrate to zirconolite and perovskite phases – suffers from segregation of crystallites and grain boundary interactions, which can produce wastefoms with thermal and chemical instabilities [177,178]. Zirconolites have been demonstrated via chemical leaching tests to out-perform single-phase brannerite and betafite. Such ceramic phases also provide an attractive dual uptake of Zr as well as actinides [179], therefore allowing for a zirconium rich feed, such as that of LWR MOx and SGHWR.

While these host phases are highly suited to immobilisation of high activity processing wastes, the SYNROC-F variant has more significant promise for treatment of spent fuel. The composition of SYNROC-F is approximately 72.8 mol.% cubic uranium pyrochlore type similar to betafite (CaUTi_2O_7) [180] for disposition of uranium, rare earths and Sr; up to 2.6 mol.% hollandite [$\text{Ba}(\text{Al}, \text{Ti})_2\text{Ti}_6\text{O}_{16}$] for immobilisation of large ionic radius radionuclides like ^{137}Cs ; up to 24.6 mol.% tetragonal rutile or titanium dioxide (TiO_2) [181]. While the pyrochlore type phase has been shown to uptake UO_2 into the structure and favourable PCT-type leach rates of $\sim 10^{-7}\text{ g m}^{-2}\text{ d}^{-1}$ for Cs and $\sim 10^{-8}\text{ g m}^{-2}\text{ d}^{-1}$ for Ca have been observed up to 100 days [182,183], further work may be required to fully understand the effect of FPs, minor actinides and other contaminants on the performance of SYNROC-F. A wet synthesis route following the ‘Sandia process’ constitutes the use of a pre-prepared dry SYNROC precursor (alkoxide nitrate synthesis) material which can be milled into a fine powder before addition to a dissolved liquor waste feed. The resulting material is then calcined before pressing and sintering or sintered using a technique such as hot pressing [184]. This chemical route may prove particularly useful for immobilisation of the de-clad and dissolved pre-processed fuel feed, as the liquor can be incorporated into the precursor calcine, allowing for precise control of waste loading.

Much of the work focusing on immobilisation of some ILW and HLW types has arisen from the Australian National University and Australian Nuclear Science and Technology Organisation (ANSTO), widely credited with the development of the SYNROC suite of titanate multi-phase ceramics. In collaboration with other academic institutions, these multiphase precursors have been shown to produce disposal optimised wastefoms under hot uniaxial press (HUP) and hot isostatic press (HIP) regimes [178,185]. The HIP technique is quite well suited to the conditioning of waste in a glass-ceramic/hybrid waste matrix for the ideal containment or reduction of volatiles; in container processing – reduction of handling; high volume reduction – densification; a batch process style to allow for tailored precursor and frit additions that suit the

waste stream composition and activity. Stainless steel HIP canisters intrinsic to the processing method not only provide a primary level of shielding, but also a containment barrier to prevent vitreous flow during pressing. Use of an active furnace isolation chamber (AFIC) device with the inherent HIP safety features have allowed the certification of some processing apparatus for use of radioactive materials (e.g. depleted UO_2 , $^{238}\text{PuO}_2$ and ThO_2) [186,187]. HIP encapsulation using low melting point metals such as tin for volatile radionuclides has been trialled, although durability, corrosion resistance and development of a galvanic cell is of concern where cladding is included with encapsulated waste or a metallic overpack could make contact [188].

Consideration has also been made for carbide fuels, generating so-called graphite intercalation compounds (GICs) using a combined acidification treatment of sulphuric acid with either hydrogen peroxide or nitric acid. While this has been shown to break down carbide fuels such as tri-structural isotropic (TRISO) particle fuel, the associated volume increase with such acid-GIC processes can be negated using an atmosphere controlled valorisation or gasification process [189]. Immobilisation in organic polymeric matrices has been considered, but such materials are typically subject to radiation induced degradation and is technologically immature [33,190].

2.3.6.c Glass-ceramics

Controlling the crystallisation rate of secondary and tertiary phases in glass materials can result in hybrid or combined so-called glass-ceramic materials. Glass-ceramic wastefoms are promoted in many waste immobilisation reviews for their balance between durability (crystalline phases with bulk actinide inventory), and chemical flexibility in an amorphous phase that can retain much of the remaining excess FPs and minor actinides [191,192]. These properties are not inherent to glass-ceramics, and some promising aluminosilicate compositions, while well characterised for physical properties and initial FP loading characteristics, chemical durability is sometimes overlooked as a key characteristic [193]. With care taken to avoid off-gassing, such a glass-ceramic could prove a potential candidate for direct immobilisation and high volume reduction for inorganic-mineral phase wastes from ion exchange, with high quantities of entrained ^{137}Cs , ^{90}Sr , and ^{60}Co [194].

Work on the artificial synthesis of the brannerite structure from oxide constituents has shown successful replication of brannerite phases and uptake of actinides, however only in very recent years has consideration been made for the addition of a glass phase for chemical flexibility of potential wastefoms. Several investigators have proposed incorporation of sodium borosilicate glass ($\text{Na}_2\text{AlBSi}_6\text{O}_{16}$), to allow for uptake of transuranic elements to crystalline brannerite and re-processing or contaminant chemicals to be incorporated into the glass phase [195,196]. Inherent limitations to quantitative comparison between glass and ceramic phases was hindered by

purported micropores and glass inclusions, although a synthetic brannerite was demonstrated with a uranium static leaching rate for high U glass ceramic of $2.3 \times 10^{-4} \text{ g m}^{-2} \text{ d}^{-1}$ for 7-14 days, using a PCT-type methodology [196]. This ideal durability, chemical flexibility and solubility for uranium mean that brannerite glass-ceramics could prove a suitable host for high-actinide spent fuel feeds such as de-clad irradiated fuel liquor, de-clad irradiated fuel oxides and FCM.

A study into the use of a combined pyrochlore glass-ceramic oxide feed for HIP treatment has been conducted at ANSTO [197]. This work made use of weakly alpha-active europium oxide with other constituents which independently induced development of a $\text{Eu}_2\text{Ti}_2\text{O}_7$ pyrochlore [198] and sodium borosilicate glass, as with the aforementioned brannerite glass-ceramic. Here, europium served as a large ionic radii simulant for spent fuel minor actinides. Glass-ceramic components were introduced to a HIP canister in the ratio of 2:3, respectively, following homogenisation and calcination – before bake-out and hot pressing at $1200 \text{ }^\circ\text{C}$, 100 MPa for 2 hours. The resulting material was tested using an MCC-type static leaching method and the phase separated pyrochlore had a significantly lower dissolution rate to that of the glass elements. After 28 days, boron and silicon normalised loss rates were $\sim 1 \text{ g m}^{-2} \text{ d}^{-1}$ and $\sim 10^{-1} \text{ g m}^{-2} \text{ d}^{-1}$, while the europium normalised loss rate was down at $\sim 2 \times 10^{-5} \text{ g m}^{-2} \text{ d}^{-1}$ [197]. Appropriate adjustments may be made to accommodate high uranium and FP loading using SYNROC-F type titanate precursors, modifying the glass batch components to optimise durability and uptake of minor FPs. With suitable feed preparation, balance of amorphous and crystalline phase contributions, a pyrochlore glass ceramic could provide one of the most flexible host matrices, accepting irradiated fuel liquors, oxide fuel streams, FCM and zirconium contaminated fuel. The addition of zirconium to a pyrochlore glass ceramic feed could be managed by balancing the components necessary to develop minor zirconolite phases alongside the pyrochlore and betafite-types.

Similarly, zirconolite glass-ceramics have been investigated for the immobilisation of plutonium residues – again utilising HIP as the preferred thermal treatment method [158]. Minor quantities of plutonium were added in nitrate form with gadolinium nitrate as a neutron poison. A fluorite-oxide precursor was prepared with small additions of partially oxidised nickel and iron used to buffer charge compensation, in order to control the ratio of Pu (III) and Pu (IV) valence. After homogenisation of precursors, calcination and bake-out, the simulant was HIPed at $1270 \text{ }^\circ\text{C}$, 100 MPa for 2 hours. MCC – type static leaching carried out over 28 days yielded normalised loss for Pu of $5.5 \times 10^{-5} \text{ g m}^{-2} \text{ d}^{-1}$, and B, Si normalised loss rates of $3.1 \times 10^{-1} \text{ g m}^{-2} \text{ d}^{-1}$, $3.2 \times 10^{-1} \text{ g m}^{-2} \text{ d}^{-1}$, respectively. A similar leaching rate for gadolinium indicated that the ceramic zirconolite phase was dissolving congruently and is currently one of the best candidates for keeping Pu sequestered in a tetravalent state. However, with the ease with which metals such as Ni and Fe

can alter the charge balancing behaviour, additional research on zirconolite glass-ceramic materials is necessary to determine suitability for the clad and dissolved-clad pre-processed fuel feeds.

Further development of this technology does however have to take into consideration interactions between the phases of glass-ceramic wasteforms and the welded steel containers, including possible influence on the dissolution and chemical alteration behaviour, though little work has been conducted for SYNROC-F and phosphate glass ceramics. Careful control of the HIP heating, dwell and cooling cycles can facilitate optimal crystallisation of ceramic phases and annealing of glass components – so further study should include a matrix of varied processing parameters [199] and could include some of the other glass-ceramic materials discussed in this section. SPS may also be used for similar multi-phase ceramic and glass-ceramic compositions with significant non-conducting inorganic components. In addition, elucidation of individual and combined phase dissolution properties and irradiation induced degradation is necessary to understand the behaviour of such wasteforms in a geological disposal environment.

Table 2.4.A - Summary of discussed methods, with reference to relative orphan nuclear material loading capability and suitability for emplacement in a geological disposal facility. Noted suitability draws on summary of factors from literature and the authors concluding opinion.

Wasteform	Strengths	Potential Weaknesses	Waste Loading	Suitability for Geological Disposal
Pond Storage	Convenient, visual monitor, no processing	Active cooling, short lifetime, corrosion	Low	Unsuitable
Dry Cask Storage	Can be passively cooled, low cost	Short lifetime, atmosphere dependent, gas generation	Low	Unsuitable
KBS -3 Multi-Barrier	Multiple redundancies, full system	High cost, gas generation, must have geometry conforming fuels	Low	Good
Cementation	Convenient, low cost, industrial waste	Short lifetime, corrosion, significant volume increase	Low	Poor
Borosilicate glass	Well developed, fission product uptake	Poor actinide solubility, durability drop-off and volume increase	Low	Good
Phosphate glass	High actinide uptake, good durability, and accounting for Fe from steel cladding or low Mg quantities	High temperature, uncontained for volatile release, chemistry must negate Fe (II) and U (VI)	Med.	Good
Zirconolite	High actinide uptake, Zr from cladding	Polytype development and chemically inflexible for FPs	High	Good
Betafite	Suitable for alpha active actinide uptake	Chemically inflexible for fission/corrosion products only some alloy components, moderate durability	High	Good
Monazite	Suitable for alpha active actinide uptake	Chemically inflexible for fission/corrosion products, moderate durability	High	Good
Brannerite	Large actinide inventory possible	Chemically inflexible for fission/corrosion products, moderate durability	High	Good
Synroc - F	Phase assemblage, actinides, and FPs	Low TRL, restricted from highly contaminated corium/FCM	High	Good
Brannerite Glass-ceramic	Flexible for large actinide and FP inventory	Low TRL, restricted from highly contaminated corium/FCM, cladding	Med.	Good
Zirconolite Glass-ceramic	Flexible for large actinide, Zr cladding and FP inventory	Low TRL, restricted from highly contaminated corium/FCM	Med.	Good
Pyrochlore Glass ceramic	Flexible for large actinide, FCM, Zr cladding and FP inventory	Low TRL, unable to treat Mg containing waste	Med.	Good

2.4 Comparison of methods summary

2.4.1 Concluding remarks

From the five major initial orphan fuel types, possible pre-processing feed methods have been discussed and assessed, within realistic waste incorporation and feasibility limits. Following this, the preferred thermal treatment options of vitrification and hot isostatic pressing were identified for their ability to ensure that spent fuel and waste materials are fully incorporated into a chemical structure, whether this would result in an amorphous, crystalline or hybrid wastefrom. By the author's critical evaluation of literature, five key host wastefroms have been proposed for the segregation of the UK orphan fuel inventory, see **Table 2.4.A** and **Figure 2.4.1.A**. With a moderate solubility for actinides and iron, phosphate glasses were selected as a suggested wastefrom for their high balance of good base durability and chemical flexibility. For its ability for high actinide and FP loadings, the SYNROC-F multiphase titanate ceramic assemblage was selected, ideal for treatment of de-clad and irradiated oxide fuels or spent fuel calcines. Three glass-ceramic composite materials were chosen for their sheer versatility in potential immobilisation routes for orphan fuel materials, the combination of vitreous and crystalline phase components each balancing incorporation of cladding metals and actinides while maintaining good durability, see **Figure 2.4.1.A**. HIP was selected as the most appropriate thermal treatment of these crystalline and composite host materials, as it offers excellent densification, low temperature processing and batch-style processing, all within hermetically sealed waste packages.

Magnox clad legacy and ex-reactor spent fuels are among some of the most problematic materials for immobilisation due to their age, state of corrosion, high ratio of cladding to fuel, metallic fuel type, ease of rupture and deformation and variety of cladding geometries. A high Mg content liquor of dissolved Magnox fuel has further issues with host matrix compatibility and diminishing potential wastefrom durability. As such, it is recommended that Magnox and other fuel types are de-clad, to improve the downstream incorporation into a wastefrom, where it is possible to do so. Separated Magnox swarf has well demonstrated grouting treatments for moderate timescale storage, although vitrification into an intermediate level waste glass has also been explored [200,201]. De-clad metallic uranium from Magnox or otherwise may prove difficult for dry-way processing, due to the pyrophoric properties of the material [29]. For materials where cladding has been entrained or heavily reacted with the fuel, total dissolution of Magnox will produce a liquor that can be fed, in somewhat dilute quantities to a vitreous wastefrom such as phosphate glass or glass ceramic, see **Figure 2.4.1.A**. In higher Mg concentrations, a glass-ceramic with a glass component of a silicate type - UK MW composition may be more appropriate to improve long-term durability, albeit at the cost of a significant volume increase.

Stainless-steel clad orphan fuels are well suited for phosphate vitrification, as the Fe contribution has been demonstrated to improve glass durability. However, the ratio of ferrous metal to actinides would require dilution in a phosphate glass matrix and addition of iron oxides, significantly increasing waste volume. It is recommended that steel clad residual fuels are de-clad where possible and processed into a high-actinide loading ceramic or glass-ceramic material. It is evident that for heavily contaminated and damaged materials, this will not be possible, so the recommendation is made that this fuel is combined with the steel generated from de-cladding, homogenised through total chemical dissolution and calcination, before incorporation into a phosphate glass wastefrom with significantly higher loading, see **Figure 2.4.1.A**. Phosphate glass compositions are considered in place of iron-borosilicates, due to improved relative loadings of uranium with phosphates and a lesser propensity to form hydrolysable hexavalent uranium [111]. Another possible solution could involve use of a phosphate glass-ceramic, though there has been difficulty with devitrification and targeted phase separation [202]. The continued operation of the UK AGR fleet is expected to have a high probability of generating additional damaged or corroded materials, during defueling, decommissioning and intermediate term storage, contributing to the orphan inventory. It was therefore the intent of the author to explore iron phosphate materials as a potential avenue for immobilisation of iron-rich actinide wastes.

The high Zr content of Zircaloy fuel feeds is deleterious to chemical durability of a vitreous wastefrom, therefore, it is recommended that these materials are de-clad and processed separately. This method is ideal for many of the Zircaloy fuel clad legacy materials, as they have experienced very little or no irradiation, and pose a lesser radiological hazard. However, due care must still be taken with high PuO₂ fuels, and those with a significant ²³⁵U enrichment. Where inclusion of Zr in the pre-processed feed is unavoidable, there is still a high suitability for addition to a zirconolite or pyrochlore glass ceramic host assemblage, as both would allow for the development of crystalline zirconolite, which has been demonstrated to have excellent chemical durability and proliferation resistance [203]. Single phase zirconolite is not recommended for use with these orphan fuels, as it does not have sufficient flexibility for incorporation of cladding alloy additions and FPs, which would likely cause phase separation for high uranium and MOx fuel feeds with experimental cladding, **Table 2.4.A**.

Carbide exotics constitute a very small component of the residual inventory, their use of uncommon materials and geometries, including fuel-cladding composites, make them particularly difficult to feed into a thermal treatment process. As with the other orphan materials, it is recommended that they are de-clad where it is both safe and feasible. Resultant uranium or mixed actinide carbide fuel can then be chemically dissolved, with a more aggressive calcium-

nitric acid dissolution method [204]. Undoubtedly the most contaminated, heterogeneous, and non-standard fuel feed discussed is that resulting from loss of coolant accidents; fuel containing materials and so called 'corium'. De-cladding of corium is often impossible and requires the disturbance and intensive handling of a significant radiological hazard. In order to minimise worker and equipment dose rate, mechanical separation or size reduction was discounted in place of total dissolution as the only recommended pre-processing stage for FCM, at which point it can be appropriately diluted for inclusion into a feed for a zirconolite or pyrochlore glass ceramic. These selections are appropriate for the discussed corium resulting from civil nuclear accidents, for their inclusions of Zircaloy cladding, therefore resulting in a liquor with high Zr content, see **Figure 2.4.1.A**. Alternatives may need to be considered for processing of materials such as the metallic fuel masses generated during the fire of Windscale Pile One [2].

The presence of volatile radionuclides in spent ion exchange adsorbents presents a challenge for intermediate storage, due to high waste volumes and dose rates. The volatility of nuclides such as Cs in their adsorbed form, precludes this type of waste in traditional thermal treatment streams and high temperature vitrification. Instead, a direct sintering approach is suggested as a method to rapidly consolidate and densify the material while in a contained manner, as to retain any nuclide inventory [205], see **Figure 2.4.1.A**. This method could provide advantages for dose rate, and significant volume reduction, where inorganic residues provide intrinsic glass phase network formers such as those required for aluminosilicate and alkali-aluminosilicate materials generated by SIXEP [193,206,207].

While this review covers many different treatment technologies and host matrices, it is by no means exhaustive, with new methods being suggested and developed at the time of writing. There is still a broad scope of research necessary to validate the physical and chemical properties of the discussed wasteforms. It will be pertinent to evaluate the chemical durability, and hydrothermal performance to meet or exceed geological disposal criteria. Suggested work also includes applicability studies using fuel feed simulants for each of the recommended host matrices.

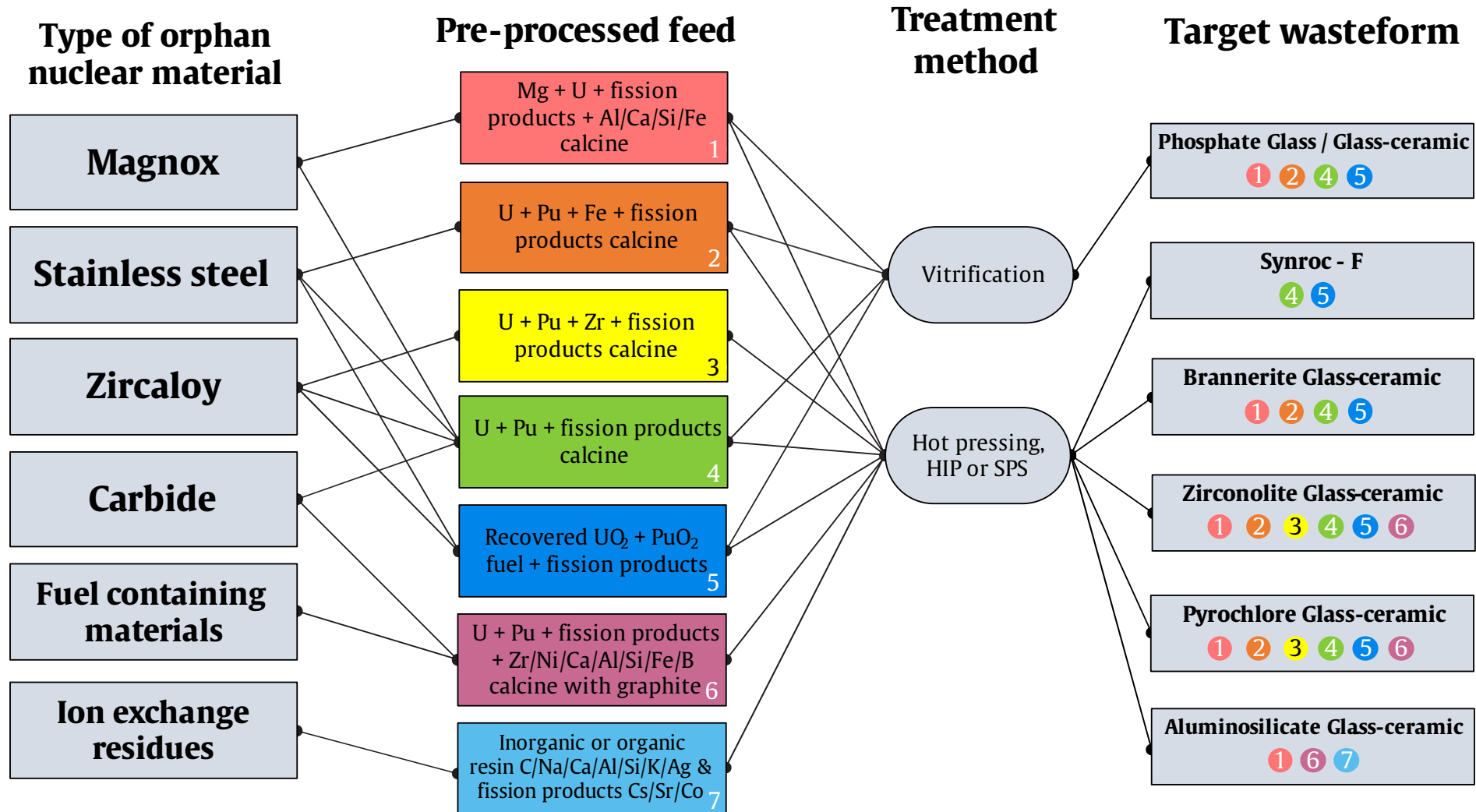


Figure 2.4.1.A - Drawing on the pre-processed feed determinations drawn from **Table 2.2.A** and **Table 2.4.A**, possible treatment methods and target wasteforms were mapped, the colour/number code translates fuel feed types to potential wasteforms, fuel containing materials refer here to the most heavily degraded and heterogeneous fuel forms such as corium

Chapter 2 references

- [1] NDA, Radioactive Wastes in the UK: Radioactive Wastes and Materials not Reported in the 2016 Waste Inventory, 2017. <https://ukinventory.nda.gov.uk/wp-content/uploads/2014/01/2016UKRWMI-Radioactive-wastes-and-materials-not-reported-in-2016-UK-inve....pdf>.
- [2] S. Jones, Windscale and Kyshtym: a double anniversary, *J. Environ. Radioact.* 99 (2008) 1–6. <https://doi.org/10.1016/j.jenvrad.2007.10.002>.
- [3] M.T. Farmer, D.J. Kilsdonk, R.W. Aeschlimann, Corium Coolability Under Ex-Vessel Accident Conditions For LWRs, *Nucl. Eng. Technol.* 41 (2009) 575–602. <https://doi.org/10.5516/NET.2009.41.5.575>.
- [4] A.A. Shiryaev, I.E. Vlasova, B.E. Burakov, B.I. Ogorodnikov, V.O. Yapaskurt, A.A. Averin, A. V. Pakhnevich, Y. V. Zubavichus, Physico-chemical properties of Chernobyl lava and their destruction products, *Prog. Nucl. Energy.* 92 (2016) 104–118. <https://doi.org/10.1016/j.pnucene.2016.07.001>.
- [5] B. Grambow, C. Poinssot, Interactions between Nuclear Fuel and Water at the Fukushima Daiichi Reactors, *Elements.* 8 (2012) 213–219. <https://doi.org/10.2113/gselements.8.3.213>.
- [6] IAEA, Fukushima Nuclear Accident Update Log, (2011) IAEA. <https://www.iaea.org/newscenter/news/fukushima-nuclear-accident-update-log-15>.
- [7] J.R. Lamarsh, A.J. Baratta, Introduction to Nuclear Engineering, 1975.
- [8] IAEA, Development status of metallic, dispersion and non-oxide advanced and alternative fuels for power and research reactors, 2003. http://www-pub.iaea.org/MTCD/Publications/PDF/te_1374_web.pdf.
- [9] D. Hambley, Storage of thermal reactor fuels – Implications for the back end of the fuel cycle in the UK, *EPJ Nucl. Sci. Technol.* 2 (2016) 21. <https://doi.org/10.1051/EPJN/2016014>.
- [10] IAEA, Survey of wet and dry spent fuel storage, 1999. http://www-pub.iaea.org/MTCD/Publications/PDF/te_1100_web.pdf.
- [11] PRIS - IAEA, PRIS - Reactor status reports - Operational & Long-Term Shutdown - By Type, IAEA PRIS. (2020). <https://pris.iaea.org/PRIS/WorldStatistics/OperationalReactorsByType.aspx>.
- [12] C. Burrows, C. Phillips, A. Milliken, The Thermal Oxide Reprocessing Plant at Sellafield-Lessons Learned from 10 Years of Hot Operations and their Applicability to the DOE Environmental Management Program, Tuscon, Arizona, 2006. <https://www.wmsym.org/archives/2006/pdfs/6482.pdf>.
- [13] M. V. Speight, G.F. Hines, G.W. Greenwood, On the origin of torsional deformation in irradiated uranium-magnox fuel elements, *J. Nucl. Mater.* 20 (1966) 126–129. [https://doi.org/10.1016/0022-3115\(66\)90031-6](https://doi.org/10.1016/0022-3115(66)90031-6).
- [14] H. Hughes, R. Hargreaves, AGR Fuel Pin Pellet-Clad Interaction Failure Limits and Activity Release Fractions, 1985. https://inis.iaea.org/collection/NCLCollectionStore/_Public/31/049/31049627.pdf?r=1&r=1.
- [15] D.W. Shoesmith, Chemistry/Electrochemistry of Spent Nuclear Fuel as a Wasteform, in: Uranium Cradle to Grave, 2013. https://www.surface-science-western.com/wp-content/uploads/msc13_shoesmith-1.pdf.
- [16] E.C. Buck, B.D. Hanson, B.K. McNamara, The geochemical behaviour of Tc, Np and Pu in spent nuclear fuel in an oxidizing environment, *Geol. Soc. Spec. Publ.* 236 (2004) 65–88. <https://doi.org/10.1144/GSL.SP.2004.236.01.05>.

- [17] J. Bruno, R.C. Ewing, Spent nuclear fuel, *Elements*. 2 (2006) 343–349. <https://doi.org/10.2113/gselements.2.6.343>.
- [18] IAEA, Generic procedures for assessment and response during a radiological emergency, 2000. http://www-pub.iaea.org/MTCD/Publications/PDF/te_1162_prn.pdf.
- [19] F.C. Iglesia, A.C. Brito, Y. Liu, Fission product release mechanisms and groupings, (1996) 1–22. https://inis.iaea.org/collection/NCLCollectionStore/_Public/30/000/30000524.pdf.
- [20] S. V. Ushakov, B.E. Burakov, S.I. Shabalev, E.B. Anderson, Interaction of UO₂ and Zircaloy during the Chernobyl accident, in: *Mater. Res. Soc. Symp. - Proc.*, Materials Research Society, 1997: pp. 1313–1318. <https://doi.org/10.1557/proc-465-1313>.
- [21] E.B. Anderson, B.E. Burakov, E.M. Pazukhin, High-Uranium Zircon from “Chernobyl Lavas,” *Radiochim. Acta*. 60 (1992) 149–152. <https://doi.org/10.1524/ract.1993.60.23.149>.
- [22] L. Arnold, *Windscale 1957: Anatomy of a Nuclear Accident*, 3rd ed., Macmillan Press Ltd, Basingstoke, 2007.
- [23] IAEA, Management of Damaged Spent Nuclear Fuel, 2009. https://www-pub.iaea.org/MTCD/Publications/PDF/Pub1395_web.pdf.
- [24] IAEA, Basic Principles Objectives IAEA Nuclear Energy Series Technological Implications of International Safeguards for Geological Disposal of Spent Fuel and Radioactive Waste, Vienna, 2010. <http://www.iaea.org/Publications/index.html>.
- [25] M.C. Grimston, W.J. Nuttall, *The Siting of UK Nuclear Power Installations*, 2013. <https://doi.org/10.17863/CAM.5722>.
- [26] S.E. Jensen, E. Nonbol, Description of the Magnox type of gas cooled reactor, 1998. https://inis.iaea.org/collection/NCLCollectionStore/_Public/30/052/30052480.pdf.
- [27] G.T. Higgins, Secondary recrystallisation in magnox AL 80, *J. Nucl. Mater.* 8 (1963) 153–159. [https://doi.org/10.1016/0022-3115\(63\)90030-8](https://doi.org/10.1016/0022-3115(63)90030-8).
- [28] H. Godfrey, Latest understanding of corrosion of Magnox, aluminium and uranium metal wastes in cement, 2017. <https://www.icorr.org/wp-content/uploads/2017/06/cedworkingday2017presentation-hgodfrey-2.pdf>.
- [29] H.B. Peacock, *Pyrophoricity of uranium*, Aiken, SC, 1992. <https://doi.org/10.2172/6783661>.
- [30] W.B. Lanham, T.C. Runion, *PUREX Process for Plutonium and Uranium Recovery*, Oak Ridge, Tennessee, 1949. <https://doi.org/https://doi.org/10.2172/4165457>.
- [31] M. Leafe, End in sight for reprocessing nuclear fuel at Sellafield - Cleaning up our nuclear past: faster, safer and sooner, 2017. <https://web.archive.org/web/20220309001812/https://nda.blog.gov.uk/2017/01/24/end-in-sight-for-reprocessing-nuclear-fuel-at-sellafield/>.
- [32] J.J. Hastings, D. Rhodes, A.S. Fellerman, D. Mckendrick, C. Dixon, New approaches for sludge management in the nuclear industry, *Powder Technol.* 174 (2007) 18–24. <https://doi.org/10.1016/j.powtec.2006.10.015>.
- [33] NDA, Exotic fuels-Dounreay Fast Reactor (DFR) breeder, 2011. https://assets.publishing.service.gov.uk/government/uploads/system/uploads/attachment_data/file/457791/Dounreay_Fast_Reactor__DFR__Breeder_Credible_and_PREFERRED_Options.pdf.
- [34] M. Mignanelli, T. Shaw, Information on Phase Chemistry in UK Spent AGR Fuels, 2009. NNL Report (09) 9834.
- [35] Special Metals, NIMONIC ® alloy PE16, 2004. <http://www.specialmetals.com/assets/smc/documents/alloys/nimonic/nimonic-alloy-pe16.pdf>.

- [36] Thyssenkrupp, Stainless Steel 316 - Data Sheet, Cradley Heath, UK, 2017. <https://www.thyssenkrupp-materials.co.uk/stainless-steel-316-14401.html>.
- [37] S.E. Jensen, P.L. Ølgaard, Description of the Prototype Fast Reactor at Dounreay, Roskilde, Denmark, 1996. https://inis.iaea.org/collection/NCLCollectionStore/_Public/28/026/28026107.pdf.
- [38] Nuclear Decommissioning Authority, Disposability assessment of irradiated PFR carbide fuel, 2011. <https://webarchive.nationalarchives.gov.uk/ukgwa/20211004151355/https://rwm.nda.gov.uk/publication/executive-summary-letter-of-compliance-assessment-report-disposability-assessment-of-irradiated-pfr-carbide-fuel-may-2011/?download>.
- [39] POST, Mixed oxide nuclear fuel (MOx), 2000. <https://researchbriefings.files.parliament.uk/documents/POST-PN-137/POST-PN-137.pdf>.
- [40] C. Whitmarsh, Review of Zircaloy-2 and Zircaloy-4 Properties Relevant to N.S. Savannah Reactor Design, Oak Ridge, Tennessee, 1962. <https://www.osti.gov/servlets/purl/4827123>.
- [41] J.-Y. Park, T.-H. Na, T.-H. Lee, J.-H. Lee, B.-Y. Lee, J.-S. Kim, Effect of applied current on the formation of defect in PWR nuclear fuel rods in resistance pressure welding process, *J. Nucl. Sci. Technol.* 52 (2015) 748–757. <https://doi.org/10.1080/00223131.2014.971900>.
- [42] A. Kecek, K. Tuček, S. Holmström, P. Van Uffelen, Development of M5 Cladding Material Correlations in the TRANSURANUS Code, Luxembourg City, Luxembourg, 2016. <https://doi.org/10.2789/320793>.
- [43] M.A. Simper, Plutonium Management, 2014. <https://www.cneec.group.cam.ac.uk/presentations/NDA13Feb2014.pdf>.
- [44] J. Edwards, P. Sullivan, M. Young, Application of BNFL's Technology for Disposition of Military Plutonium, Vienna, Austria, 1997. https://inis.iaea.org/collection/NCLCollectionStore/_Public/29/046/29046771.pdf.
- [45] D.O. Pickman, J.H. Gittus, K.M. Rose, Fuel for the SGHWR, *Adv. Nucl. Sci. Technol.* 11 (1979) 233–284. <https://doi.org/10.1007/978-1-4613-2862-9>.
- [46] R. Arnott, C. Nixon, B. Hamilton, Nuclear Legacy Advisory Forum, 2010. https://documen.site/downloadFile/presentation-richard-arnott-clive-nixon-bill-hamilton_pdf.
- [47] C. Journeau, D. Roulet, E. Porcheron, P. Piluso, C. Chagnot, Fukushima Daiichi fuel debris simulant materials for the development of cutting and collection technologies, *J. Nucl. Sci. Technol.* 55 (2018) 985–995. <https://doi.org/10.1080/00223131.2018.1462267>.
- [48] Lord Coleraine, The Second Nuclear Power Programme (10 June), Hansard - Parliamentary Speech. (1964). <https://api.parliament.uk/historic-hansard/lords/1964/jun/10/the-second-nuclear-power-programme>.
- [49] E. Nonbøl, Description of the Advanced Gas Cooled Type of Reactor (AGR), Roskilde, Denmark, 1996. https://inis.iaea.org/collection/NCLCollectionStore/_Public/28/028/28028509.pdf.
- [50] IAEA, Ten Years of Nuclear Power, 1964. <https://www.iaea.org/sites/default/files/publications/magazines/bulletin/bull6-3/06304701725.pdf>.
- [51] EDF, UK Nuclear Power Stations: Daily Statuses, (2022). <https://www.edfenergy.com/energy/power-station/daily-statuses>.
- [52] D. Hambley, Spent Fuel Storage Capability, in: CEIDEN Spanish Nucl. Fission Platf., 2016. <https://ceiden.com/wp-content/uploads/2016/03/DH-Fuel-Storage-CIEDEN-2016.pdf>.
- [53] W.J. Carmack, D.L. Porter, Y.I. Chang, S.L. Hayes, M.K. Meyer, D.E. Burkes, C.B. Lee, T. Mizuno, F. Delage, J. Somers, Metallic fuels for advanced reactors, *J. Nucl. Mater.* 392 (2009) 139–50. <https://doi.org/10.1016/j.jnucmat.2009.03.007>.

- [54] Science Museum Group Collection, Magnox fuel cans from Sizewell-A Nuclear Power Station, (1968). <https://collection.sciencemuseumgroup.org.uk/objects/co8233887/magnox-fuel-cans-from-sizewell-a-nuclear-power-station-1968-nuclear-fuel-cans>.
- [55] Science Museum Group Collection, AGR Fuel Element, (1982). <https://collection.sciencemuseumgroup.org.uk/objects/co5473/agr-fuel-element-c-1982-nuclear-fuel-fuel-rods>.
- [56] Science Museum Group Collection, Replica Nuclear Power Station Fuel Assembly, (1995). <https://collection.sciencemuseumgroup.org.uk/objects/co409150/replica-nuclear-power-station-fuel-assembly>.
- [57] L.C. Walters, B.R. Seidel, J.H. Kittel, Performance of Metallic Fuels and Blankets in Liquid-Metal Fast Breeder Reactors, *Nucl. Technol.* 65 (1984) 179–231. <https://doi.org/10.13182/NT84-A33408>.
- [58] G. Meyer, E. Stokke, Description of Sizewell B Nuclear Power Plant, Halden, 1997. <https://researchbriefings.files.parliament.uk/documents/POST-PN-137/POST-PN-137.pdf>.
- [59] M. Forwood, G. Mackerron, W. Walker, Endless Trouble Britain's Thermal Oxide Reprocessing Plant (THORP), 2019. <https://fissilematerials.org/library/rr19.pdf>.
- [60] A.P. Szilagyi, E M Environmental Management Three Mile Island Unit 2 Overview and Management Issues, 2011. https://www.oecd-nea.org/rwm/wpdd/10/documents/13a_3-Mile-Island_Szilagyi.pdf.
- [61] TEPCO, Fuel Removal from Reactor 4 Spent Fuel Pool, 2013. https://photo.tepco.co.jp/library/131030_02e/131030_01-e.pdf.
- [62] J.R. Smyth, A.T. Spaid, D.L. Bish, Crystal structures of a natural and a Cs-exchanged clinoptilolite, *Am. Mineral.* 75 (1990) 522–528. https://rruff.info/doclib/am/vol75/AM75_522.pdf.
- [63] L.C. Harnett, Conditioning of Spent Ion Exchange Materials at the Fukushima Daiichi NPP Site, The University of Sheffield, 2017.
- [64] S.A. Walling, L.J. Gardner, N.C. Hyatt, Characterisation of co-mixed HIP wastefoms for Magnox sludge and clinoptilolite wastes, *IOP Conf. Ser. Mater. Sci. Eng.* (2020). <https://doi.org/10.1088/1757-899X/818/1/012014>.
- [65] TEPCO, Situation of Storage and Treatment of Accumulated Water including Highly Concentrated Radioactive Materials at Fukushima Daiichi Nuclear Power Station (407th Release), 2019. https://www7.tepco.co.jp/wp-content/uploads/handouts_190624_02-e.pdf.
- [66] A. Braun, Application of Ion Exchange Processes for the Treatment of Radioactive Waste and Management of Spent Ion Exchangers, 2002. https://www-pub.iaea.org/MTCD/Publications/PDF/TRS408_scr.pdf.
- [67] C.E. Willingham, Radiation Dose Rates from Commercial PWR and BWR Spent Fuel Elements, Richland, Washington, 1981. https://inis.iaea.org/collection/NCLCollectionStore/_Public/12/642/12642536.pdf.
- [68] S. Pickles, H.J. Powell, Experimental Validation of Irradiated Fuel Inventories Calculated by the Fispin Code Fuels, in: *Nucl. Data Sci. Technol.*, Springer Netherlands, Dordrecht, 1983: pp. 190–195. https://doi.org/10.1007/978-94-009-7099-1_40.
- [69] Sellafield - NDA, End of reprocessing at Thorp signals new era for Sellafield, UK Gov. News. (2018). <https://web.archive.org/web/20181116184144/https://www.gov.uk/government/news/end-of-reprocessing-at-thorp-signals-new-era-for-sellafield>.
- [70] NDA, NDA Annual Report and Accounts 2019/20, HMSO, 2020. https://assets.publishing.service.gov.uk/government/uploads/system/uploads/attachment_data/file/902764/ARAC_2019-20_amended_210720_reduced.pdf.

- [71] G.E. Schweitzer, A.C. Sharber, *An International Spent Nuclear Fuel Storage Facility*, National Academies Press, 2005.
<https://ebookcentral.proquest.com/lib/sheffield/detail.action?docID=3378185>.
- [72] D. Wang, I.C. Gauld, G.L. Yoder, L.J. Ott, G.F. Flanagan, M.W. Francis, E.L. Popov, J.J. Carbajo, P.K. Jain, J.C. Wagner, J.C. Gehin, Study of Fukushima Daiichi Nuclear Power Station Unit 4 Spent-Fuel Pool, *Nucl. Technol.* 180 (2012) 205–215. <https://doi.org/10.13182/NT12-A14634>.
- [73] F. King, M. Kolar, M. Vähänen, C. Lilja, Modelling long term corrosion behaviour of copper canisters in KBS-3 repository, *Corros. Eng. Sci. Technol.* 46 (2011) 217–222.
<https://doi.org/10.1179/18211Y.0000000004>.
- [74] A.H. Svensk, K. Ab, J.A. Svensk, R. Munier, A. Hedin, A.H. Se, J. Andersson, U. Kautsky, L. Morén, J.-O. Näslund, K. Pers, I. Puigdomenech, P. Sellin, J.-O. Selroos, K. Skagius, K. Spahiu, F. Vahlund, L. Werme, Safety assessment for licensing a spent nuclear fuel repository in Sweden, in: 2008. <https://www.researchgate.net/publication/259638600>.
- [75] M. Holmboe, S. Wold, M. Jonsson, Porosity investigation of compacted bentonite using XRD profile modeling, *J. Contam. Hydrol.* 128 (2012) 19–32.
<https://doi.org/10.1016/j.jconhyd.2011.10.005>.
- [76] P. Szakálos, S. Seetharaman, Corrosion of copper canister, (2012).
https://inis.iaea.org/collection/NCLCollectionStore/_Public/43/128/43128053.pdf.
- [77] National Research Council, *A Review of the Swedish KBS-3 Plan for Final Storage of Spent Nuclear Fuel*, National Academies Press, 1984. <https://doi.org/10.17226/19380>.
- [78] D. Cui, J. Low, K. Spahiu, Environmental behaviors of spent nuclear fuel and canister materials, *Energy Environ. Sci.* 4 (2011) 2537–2545. <https://doi.org/10.1039/c0ee00582g>.
- [79] Å. Björkbacka, M. Yang, C. Gasparrini, C. Leygraf, M. Jonsson, Kinetics and mechanisms of reactions between H₂O₂ and copper and copper oxides, *Dalt. Trans.* 44 (2015) 16045–16051.
<https://doi.org/10.1039/c5dt02024g>.
- [80] SKBF/KBS, *Final storage of spent nuclear fuel - KBS-3*, 1983.
https://www.skb.se/publikation/1678004/716_5_KBS-3_Summary.pdf.
- [81] Is it all over for Cumbrian nuclear waste store plans? - BBC News, (n.d.).
<https://www.bbc.com/news/uk-england-21295465>.
- [82] Cumbria rejects underground nuclear storage dump | Nuclear waste | The Guardian, (n.d.).
<https://www.theguardian.com/environment/2013/jan/30/cumbria-rejects-underground-nuclear-storage>.
- [83] P. Marschall, S. Horseman, T. Gimmi, Characterisation of Gas Transport Properties of the Opalinus Clay, a Potential Host Rock Formation for Radioactive Waste Disposal, *Oil Gas Sci. Technol.* 60 (2005) 121–139. <https://doi.org/10.2516/ogst:2005008>.
- [84] Y. Wileveau, K. Su, *In Situ Thermal Experiments Carried Out in Opalinus Clay and Callovo-Oxfordian Claystones*, Lille, 2007. https://www.andra.fr/minisites/lille2007/abstract_lille2007/donnees/pdf/047_048_O_03B_1.pdf.
- [85] A. Zaoui, W. Sekkal, Can clays ensure nuclear waste repositories?, *Sci. Rep.* 5 (2015) 1–5.
<https://doi.org/10.1038/srep08815>.
- [86] J. Morris, S. Wickham, P. Richardson, C. Rhodes, M. Newland, Contingency options for the dry storage of magnox spent fuel in the UK, in: *Proc. Int. Conf. Radioact. Waste Manag. Environ. Remediat. ICEM, ASME*, 2009: pp. 811–816. <https://doi.org/10.1115/ICEM2009-16330>.
- [87] N. Bradley, *Interim Dry Fuel Storage for Magnox Reactors*, 1985.
<https://www.osti.gov/etdeweb/servlets/purl/20109823>.

- [88] M. Sutton, P. Warwick, A. Hall, Uranium(VI) interactions with OPC/PFA grout, *J. Environ. Monit.* 5 (2003) 922–928. <https://doi.org/10.1039/b308554f>.
- [89] S.A. Kearney, B. McLuckie, K. Webb, R. Orr, I.A. Vatter, A.S. Yorkshire, C.L. Corkhill, M. Hayes, M.J. Angus, J.L. Provis, Effects of plutonium dioxide encapsulation on the physico-chemical development of Portland cement blended grouts, *J. Nucl. Mater.* 530 (2020) 151960. <https://doi.org/10.1016/j.jnucmat.2019.151960>.
- [90] R.W.S. J. C. Walton, L. E. Plansky, Models for Estimation of Service Life of Concrete Barriers in Low-Level Radioactive Waste Disposal, (1990) 30–36. <https://doi.org/https://doi.org/10.2172/6548946>.
- [91] D.G. Bennett, R. Gens, Overview of European concepts for high-level waste and spent fuel disposal with special reference waste container corrosion, *J. Nucl. Mater.* 379 (2008) 1–8. <https://doi.org/10.1016/J.JNUCMAT.2008.06.001>.
- [92] M.I. Ojovan, W.E. Lee, S.N. Kalmykov, An introduction to nuclear waste immobilisation, Elsevier, 2019. <https://doi.org/10.1016/C2017-0-03752-7>.
- [93] M. Ojovan, N. Hyatt, eds., Materials for Nuclear Waste Immobilization, MDPI, 2019. <https://doi.org/https://doi.org/10.3390/books978-3-03921-847-9>.
- [94] P. Offermann, Calculation of the Radiolytic Gas Production in Cemented Waste, *MRS Proc.* 127 (1988). <https://doi.org/10.1557/proc-127-461>.
- [95] S. Gin, A. Abdelouas, L.J. Criscenti, W.L. Ebert, K. Ferrand, T. Geisler, M.T. Harrison, Y. Inagaki, S. Mitsui, K.T. Mueller, J.C. Marra, C.G. Pantano, E.M. Pierce, J. V. Ryan, J.M. Schofield, C.I. Steefel, J.D. Vienna, An international initiative on long-term behavior of high-level nuclear waste glass, *Mater. Today.* 16 (2013) 243–248. <https://doi.org/10.1016/j.mattod.2013.06.008>.
- [96] W.H. Zachariasen, The atomic arrangement in glass, *J. Am. Chem. Soc.* 54 (1932) 3841–3851. https://doi.org/10.1021/JA01349A006/ASSET/JA01349A006.FP.PNG_V03.
- [97] H. Rawson, Properties and applications of glass, 2nd ed., Elsevier, 1980. <https://cir.nii.ac.jp/crid/1130282272114191104>.
- [98] B. Grambow, Waste forms for actinides: borosilicate glasses, *ArXiv.* 1904 (2019) 1–21.
- [99] A.K. Varshneya, J.C. Mauro, *Inorganic Glasses*, 2019.
- [100] M.T. Harrison, Vitrification of High Level Waste in the UK, *Procedia Mater. Sci.* 7 (2014) 10–15. <https://doi.org/10.1016/J.MSPRO.2014.10.003>.
- [101] P.D. Wilson, *The Nuclear Fuel Cycle: From Ore to Waste* (Oxford Science Publications), (1996) 344. <https://ebookcentral.proquest.com/lib/sheffield/detail.action?docID=4962953>.
- [102] NDA, *GeoMelt Vitrification of ILW*, 2008. https://webarchive.nationalarchives.gov.uk/ukgwa/20211004151512mp_/https://rwm.nda.gov.uk/publication/executive-summary-letter-of-compliance-assessment-report-geomelt-vitrification-of-ilw-may-2008/?download.
- [103] Billon-Galland C, Crittenden M, Veolia Nuclear Solutions works with Idaho National Laboratory (INL) to Demonstrate New Disposition Path for Radioactive Contaminated Reactive Metal Waste Streams, Palo Alto, California, 2016. <https://www.nuclearsolutions.veolia.com/en/media/press-releases/veolia-nuclear-solutions-works-idaho-national-laboratory-inl-demonstrate-new-0>.
- [104] C.W. Kim, C.S. Ray, D. Zhu, D.E. Day, D. Gombert, A. Aloy, A. Mogu S S-Milankovi C C D, M. Karabulut, Chemically durable iron phosphate glasses for vitrifying sodium bearing waste (SBW) using conventional and cold crucible induction melting (CCIM) techniques, (n.d.). [https://doi.org/10.1016/S0022-3115\(03\)00325-8](https://doi.org/10.1016/S0022-3115(03)00325-8).

- [105] Narayanaswamy O. S., *Glass Science and Technology*, Ford Motor Company, Dearborn, Michigan, 1986. <https://doi.org/10.1016/B978-0-12-706703-2.50008-8>.
- [106] ASTM, *Standard Test Methods for Determining Chemical Durability of Nuclear, Hazardous, and Mixed Waste Glasses and Multiphase Glass Ceramics: The Product Consistency Test (PCT)*, (2014). <https://compass.astm.org/document/?contentCode=ASTM%7CC1285-21%7Cen-US>.
- [107] W.J. Weber, Radiation effects in nuclear waste glasses, *Nucl. Inst. Methods Phys. Res. B.* 32 (1988) 471–479. [https://doi.org/10.1016/0168-583X\(88\)90257-1](https://doi.org/10.1016/0168-583X(88)90257-1).
- [108] C.M. Jantzen, Prediction of Glass Durability as a Function of Glass Composition and Test Conditions: Thermodynamics and Kinetics, *Conf. Adv. Fusion Glas.* Alfred, NY, June 14-17, 1988. (1988).
- [109] A. Riley, S. Walker, N.R. Gribble, Composition Changes and Future Challenges for the Sellafield Waste Vitrification Plant, *MRS Proc.* 1193 (2009) 267. <https://doi.org/10.1557/PROC-1193-267>.
- [110] H. Kamizono, S. Kikkawa, Y. Togashi, S. Tashiro, Volatilization of ^{137}Cs and ^{106}Ru from Borosilicate Glass Containing Actual High-Level Waste, *J. Am. Ceram. Soc.* 72 (1989) 1438–1441. <https://doi.org/10.1111/j.1151-2916.1989.tb07669.x>.
- [111] S. V. Stefanovsky, A.A. Shiryaev, J. V. Zubavitchus, A.A. Veligjanin, J.C. Marra, Valence state and speciation of uranium ions in borosilicate glasses with a high iron and aluminum content, *Glas. Phys. Chem.* 35 (2009) 141–148. <https://doi.org/10.1134/S1087659609020035>.
- [112] F. Endrizzi, X. Gaona, Z. Zhang, C. Xu, L. Rao, C. Garcia-Perez, M. Altmaier, Thermodynamic description of U(VI) solubility and hydrolysis in dilute to concentrated NaCl solutions at $T = 25, 55$ and $80\text{ }^\circ\text{C}$, *Radiochim. Acta.* 107 (2019) 663–678. <https://doi.org/10.1515/RACT-2018-3056/>.
- [113] C.L. Corkhill, N.J. Cassingham, P.G. Heath, N.C. Hyatt, Dissolution of UK High-Level Waste Glass Under Simulated Hyperalkaline Conditions of a Colocated Geological Disposal Facility, *Int. J. Appl. Glas. Sci.* 4 (2013) 341–356. <https://doi.org/10.1111/ijag.12042>.
- [114] D.K. Peeler, K.J. Imrich, D.R. Click, *Magnox:Butex Uranium Bearing Glasses: Physical and Chemical Analysis Data Package*, (2011).
- [115] D. Strachan, J.J. Neeway, L. Pederson, D.K. Schreiber, A. Mitroshkov, Z. Zhu, J. V. Ryan, On the dissolution of a borosilicate glass with the use of isotopic tracing – Insights into the mechanism for the long-term dissolution rate, *Geochim. Cosmochim. Acta.* 318 (2022) 213–229. <https://doi.org/10.1016/J.GCA.2021.12.004>.
- [116] D. Rebiscoul, A. Van der Lee, F. Rieutord, F. Né, O. Spalla, A. El-Mansouri, P. Frugier, A. Ayrál, S. Gin, Morphological evolution of alteration layers formed during nuclear glass alteration: new evidence of a gel as a diffusive barrier, *J. Nucl. Mater.* 326 (2004) 9–18. <https://doi.org/10.1016/J.JNUCMAT.2003.10.015>.
- [117] P. Frugier, S. Gin, Y. Minet, T. Chave, B. Bonin, N. Godon, J.E. Lartigue, P. Jollivet, A. Ayrál, L. De Windt, G. Santarini, SON68 nuclear glass dissolution kinetics: Current state of knowledge and basis of the new GRAAL model, *J. Nucl. Mater.* 380 (2008) 8–21. <https://doi.org/10.1016/J.JNUCMAT.2008.06.044>.
- [118] A.J. Connelly, N.C. Hyatt, K.P. Travis, R.J. Hand, M.C. Stennett, A.S. Gandy, A.P. Brown, D.C. Apperley, The effect of uranium oxide additions on the structure of alkali borosilicate glasses, *J. Non. Cryst. Solids.* 378 (2013) 282–289. <https://doi.org/10.1016/j.jnoncrysol.2013.06.026>.
- [119] G. Calestani, A. Montenero, E. Ferraguti, G. Ingletto, M. Bettinelli, Influence of some oxides on the durability of a borosilicate glass, *J. Non. Cryst. Solids.* 84 (1986) 452–462. [https://doi.org/10.1016/0022-3093\(86\)90809-4](https://doi.org/10.1016/0022-3093(86)90809-4).

- [120] G.B. Schreiber, H D; Balazs, Chemistry of uranium in borosilicate glasses. Pt. 1. Simple base compositions relevant to the immobilisation of nuclear waste, *Phys. Chem. Glas.* 23 (1982) 139–146.
- [121] H.D. Schreiber, The chemistry of uranium in glass-forming melts: Redox interactions of U(VI)-U(V)-U(V)-U(IV) with cerium in aluminosilicates, *J. Non. Cryst. Solids.* 49 (1982) 189–200. [https://doi.org/10.1016/0022-3093\(82\)90118-1](https://doi.org/10.1016/0022-3093(82)90118-1).
- [122] H.D. Schreiber, Chemistry of Uranium in Glass-Forming Melts: Redox Interactions of Uranium with Chromium and Iron in Aluminosilicates, *J. Am. Ceram. Soc.* 66 (1982) 189–200. <https://doi.org/10.1111/j.1151-2916.1983.tb10045.x>.
- [123] T.M. Nik, Preparation and Characterization of Nano porous Silica Glasses for Nuclear waste Immobilization, in: *Conf. Nucl. Sci. Technol.*, 2022: pp. 2–4.
- [124] B.N. Muñoz-Sánchez, M.G. Cabezas, Borosilicate nozzles manufactured by reproducible fire shaping, *J. Mater. Process. Technol.* 261 (2018) 173–183. <https://doi.org/10.1016/j.jmatprotec.2018.06.011>.
- [125] X. Nie, W.W. Chen, Dynamic Equibiaxial Flexural Strength of Borosilicate Glass at High Temperatures, *Exp. Mech.* 52 (2012) 135–143. <https://doi.org/10.1007/s11340-011-9549-1>.
- [126] J.R. Van Wazer, Physical Properties of Solutions of a Sodium Phosphate Glass, *Ind. Eng. Chem.* 41 (1949) 189–194. <https://doi.org/10.1021/IE50469A042>.
- [127] A.E.R. Westman, M.J. Smith, P.A. Gartaganis, The Constitution of The Sodium-acid Phosphate Glasses, 37 (1959) 1764–1775. <https://doi.org/10.1139/V59-256>.
- [128] C.M. Jantzen, Systems approach to nuclear waste glass development, *J. Non. Cryst. Solids.* 84 (1986) 215–225. [https://doi.org/10.1016/0022-3093\(86\)90780-5](https://doi.org/10.1016/0022-3093(86)90780-5).
- [129] B. Richard K, Review: the structure of simple phosphate glasses, *J. Non. Cryst. Solids.* 263–264 (2000) 1–28. <http://www.sciencedirect.com/science/article/pii/S0022309399006201>.
- [130] H.D. Schreiber, G. Bryan Balazs, B.J. Williams, Chemistry of Uranium in Aluminophosphate Glasses, *J. Am. Ceram. Soc.* 65 (1982) 449–453. <https://doi.org/10.1111/j.1151-2916.1982.tb10512.x>.
- [131] S.V. Stefanovsky, O.I. Stefanovsky, S.S. Danilov, M.I. Kadyko, Phosphate-based glasses and glass ceramics for immobilization of lanthanides and actinides, *Ceram. Int.* 45 (2019) 9331–9338. <https://doi.org/10.1016/J.CERAMINT.2018.06.208>.
- [132] X. Yu, D.E. Day, G.J. Long, R.K. Brow, Properties and structure of sodium-iron phosphate glasses, *J. Non. Cryst. Solids.* 215 (1997) 21–31. [https://doi.org/10.1016/S0022-3093\(97\)00022-7](https://doi.org/10.1016/S0022-3093(97)00022-7).
- [133] X. Fang, C.S. Ray, A. Mogu S-Milankovi, D.E. Day, Iron redox equilibrium, structure and properties of iron phosphate glasses, *J. Non. Cryst. Solids.* 283 (2001) 162–172. [https://doi.org/10.1016/S0022-3093\(01\)00416-1](https://doi.org/10.1016/S0022-3093(01)00416-1).
- [134] L. Harnett, M.C. Stennett, E.R. Maddrell, N.C. Hyatt, Development of phosphate glass and multi-phase titanate ceramic compositions for thermal treatment of irradiated nuclear fuel residues, *IOP Conf. Ser. Mater. Sci. Eng.* 818 (2020) 012012. <https://doi.org/10.1088/1757-899X/818/1/012012>.
- [135] D. Russo, D. Rodriguez, N. Grumbaum, C. Gonzalez Oliver, High temperature oxidation and crystallization behavior of phosphate glass compositions, (2003). https://inis.iaea.org/collection/NCLCollectionStore/_Public/35/103/35103669.pdf?r=1.
- [136] D.O. Russo, D.S. Rodríguez, J.M. Rincón L., M. Romero, C.J.R. González Oliver, Thermal properties and crystallization of iron phosphate glasses containing up to 25 wt% additions of Si-, Al-, Na- and U-oxides, *J. Non. Cryst. Solids.* 354 (2008) 1541–1548. <https://doi.org/10.1016/J.JNONCRYSOL.2007.08.044>.

- [137] C.H. Booth, P.G. Allen, J.J. Bucher, N.M. Edelstein, D.K. Shuh, G.K. Marasinghe, M. Karabulut, C.S. Ray, D.E. Day, Oxygen and phosphorus coordination around iron in crystalline ferric ferrous pyrophosphate and iron-phosphate glasses with UO_2 or Na_2O , *J. Mater. Res.* 14 (1999) 2628–2639. <https://doi.org/10.1557/JMR.1999.0352>.
- [138] M. Karabulut, G.K. Marasinghe, C.S. Ray, G.D. Waddill, D.E. Day, Y.S. Badyal, M.-L. Saboungi, S. Shastri, D. Haeffner, A high energy x-ray and neutron scattering study of iron phosphate glasses containing uranium, *J. Appl. Phys.* 87 (2000) 2185. <https://doi.org/10.1063/1.372160>.
- [139] S. V. Stefanovsky, O.I. Stefanovsky, M.I. Kadyko, FTIR and Raman spectroscopic study of sodium aluminophosphate and sodium aluminum-iron phosphate glasses containing uranium oxides, *J. Non-Cryst. Solids.* 443 (2016) 192–198. <https://doi.org/10.1016/j.jnoncrysol.2016.04.031>.
- [140] S.S. Danilov, S.E. Vinokurov, S. V. Stefanovsky, B.F. Myasoedov, Hydrolytic durability of uranium-containing sodium aluminum (iron) phosphate glasses, *Radiochemistry.* 59 (2017) 259–263. <https://doi.org/10.1134/S1066362217030079>.
- [141] T. Okura, T. Miyachi, H. Monma, Properties and vibrational spectra of magnesium phosphate glasses for nuclear waste immobilization, *J. Eur. Ceram. Soc.* 26 (2006) 831–836. <https://doi.org/10.1016/j.jeurceramsoc.2005.07.031>.
- [142] W. Huang, D.E. Day, C.S. Ray, C.W. Kim, A. Mogus-Milankovic, Vitrification of high chrome oxide nuclear waste in iron phosphate glasses, *J. Nucl. Mater.* 327 (2004) 46–57. <https://doi.org/10.1016/j.jnucmat.2004.01.021>.
- [143] W. Huang, D.E. Day, C.S. Ray, C.W. Kim, High temperature properties of an iron phosphate melt containing high chrome nuclear waste, *J. Nucl. Mater.* 346 (2005) 298–305. <https://doi.org/10.1016/j.jnucmat.2005.07.004>.
- [144] A. Carton, C. Rapin, R. Podor, P. Berthod, Corrosion of Chromium in Glass Melts, *J. Electrochem. Soc.* 153 (2006) B121. <https://doi.org/10.1149/1.2165745>.
- [145] D. Gombert, J.G. Richardson, Cold Crucible Induction Melter Technology: Results of Laboratory Directed Research and Development, 2001. <https://doi.org/https://doi.org/10.2172/910987>.
- [146] T.A. Gens, New Developments in Uranium-Zirconium Alloy Fuel Reprocessing, *Nucl. Sci. Eng.* 9 (1961) 488–494. <https://doi.org/10.13182/nse61-a25912>.
- [147] L. Galois, E. Pélegrin, M.-A. Arrio, P. Ildefonse, G. Calas, D. Ghaleb, C. Fillet, F. Pacaud, Evidence for 6-Coordinated Zirconium in Inactive Nuclear Waste Glasses, *J. Am. Ceram. Soc.* 82 (2004) 2219–2224. <https://doi.org/10.1111/j.1151-2916.1999.tb02065.x>.
- [148] L. Galois, G. Calas, G. Morin, S. Pagnet, C. Fillet, Structure of Pd-Te precipitates in a simulated high-level nuclear waste glass, *J. Mater. Res.* 13 (1998) 1124–1127. <https://doi.org/10.1557/JMR.1998.0158>.
- [149] H. Kobayashi, K. Imamura, W.B. Kim, S.S. Im, Asuha, Nitric acid oxidation of Si (NAOS) method for low temperature fabrication of SiO_2/Si and SiO_2/SiC structures, *Appl. Surf. Sci.* 256 (2010) 5744–5756. <https://doi.org/10.1016/j.apsusc.2010.03.092>.
- [150] J. Abraham, D P; McDeavitt, S M; Park, Metal waste forms from the electrometallurgical treatment of spent nuclear fuel, 1996. <https://doi.org/https://doi.org/10.2172/238466>.
- [151] S.M. Mcdeavitt, D.P. Abraham, J.Y. Park, D.D. Keiser, Stainless Steel-Zirconium Waste Forms from the Treatment of Spent Nuclear Fuel, (1997) 29–32. <https://doi.org/10.1007/BF02914763>.
- [152] E. Maddrell, Hot isostatically pressed wastefoms for future nuclear fuel cycles, *Chem. Eng. Res. Des.* 91 (2013) 735–741. <https://doi.org/10.1016/J.CHERD.2012.11.004>.

- [153] C.C. Tzeng, Y.Y. Kuo, T.F. Huang, D.L. Lin, Y.J. Yu, Treatment of radioactive wastes by plasma incineration and vitrification for final disposal, *J. Hazard. Mater.* 58 (1998) 207–220. [https://doi.org/10.1016/S0304-3894\(97\)00132-5](https://doi.org/10.1016/S0304-3894(97)00132-5).
- [154] Z. Jie, C. Liu, D. Xia, G. Zhang, Microwave plasma torches for solid waste treatment and vitrification, *Environ. Sci. Pollut. Res.* 30 (2023) 32827–32838. <https://doi.org/10.1007/s11356-022-24523-2>.
- [155] C.A. Utton, R.J. Hand, P.A. Bingham, N.C. Hyatt, S.W. Swanton, S.J. Williams, Dissolution of vitrified wastes in a high-pH calcium-rich solution, *J. Nucl. Mater.* 435 (2013) 112–122. <https://doi.org/10.1016/J.JNUCMAT.2012.12.032>.
- [156] W. Anthony, R. Bideaux, K. Bladh, M. Nichols, Handbook of Mineralogy - Zirconolite, Chantilly, Virginia, 2005. <http://www.handbookofmineralogy.org/pdfs/zirconolite3o.pdf>.
- [157] E.R. Vance, G.R. Lumpkin, M.L. Carter, D.J. Cassidy, C.J. Ball, R.A. Day, B.D. Begg, Incorporation of uranium in zirconolite ($\text{CaZrTi}_2\text{O}_7$), *J. Am. Ceram. Soc.* 85 (2002) 1853–1859. <https://doi.org/10.1111/j.1151-2916.2002.tb00364.x>.
- [158] Y. Zhang, D.J. Gregg, L. Kong, M. Jovanovich, G. Triani, Zirconolite glass-ceramics for plutonium immobilization: The effects of processing redox conditions on charge compensation and durability, *J. Nucl. Mater.* 490 (2017) 238–241. <https://doi.org/10.1016/j.jnucmat.2017.04.015>.
- [159] T.J. White, R.L. Segall, J.L. Hutchison, J.C. Barry, Polytropic behaviour of zirconolite, *Proc. R. Soc. London. A. Math. Phys. Sci.* 392 (1984) 343–358. <https://doi.org/10.1098/rspa.1984.0035>.
- [160] Y. Zhang, M.W.A. Stewart, H. Li, M.L. Carter, E.R. Vance, S. Moricca, Zirconolite-rich titanate ceramics for immobilisation of actinides - Waste form/HIP can interactions and chemical durability, *J. Nucl. Mater.* 395 (2009) 69–74. <https://doi.org/10.1016/j.jnucmat.2009.09.019>.
- [161] L.R. Blackburn, D.J. Bailey, S.K. Sun, L.J. Gardner, M.C. Stennett, C.L. Corkhill, N.C. Hyatt, Review of zirconolite crystal chemistry and aqueous durability, *Adv. Appl. Ceram.* 120 (2021) 69–83. <https://doi.org/10.1080/17436753.2021.1877596>.
- [162] W. Anthony, R. Bideaux, K. Bladh, M. Nichols, Handbook of Mineralogy - Betafite, cha, 2001. <http://www.handbookofmineralogy.org/pdfs/betafite.pdf>.
- [163] S.A. McMaster, R. Ram, F. Charalambous, M.I. Pownceby, J. Tardio, S.K. Bhargava, Synthesis and characterisation of the uranium pyrochlore betafite $[(\text{Ca,U})_2(\text{Ti,Nb,Ta})_2\text{O}_7]$, *J. Hazard. Mater.* 280 (2014) 478–486. <https://doi.org/10.1016/J.JHAZMAT.2014.07.062>.
- [164] E. Browne, J.K. Tuli, Nuclear Data Sheets for A = 235, *Nucl. Data Sheets.* 122 (2014) 205–292. <https://doi.org/10.1016/J.NDS.2014.11.002>.
- [165] S.A. McMaster, R. Ram, N. Faris, M.I. Pownceby, J. Tardio, S.K. Bhargava, Uranium leaching from synthetic betafite: $[(\text{Ca,U})_2(\text{Ti,Nb,Ta})_2\text{O}_7]$, *Int. J. Miner. Process.* 160 (2017) 58–67. <https://doi.org/10.1016/J.MINPRO.2017.01.011>.
- [166] W. Anthony, R. Bideaux, K. Bladh, M. Nichols, Handbook of Mineralogy - Brannerite, Chantilly, Virginia, 2005. <http://www.handbookofmineralogy.org/pdfs/brannerite.pdf>.
- [167] D.J. Bailey, M.C. Stennett, B. Ravel, D. Grolimund, N.C. Hyatt, Synthesis and characterisation of brannerite compositions $(\text{U}_{0.9}\text{Ce}_{0.1})_{1-x}\text{M}_x\text{Ti}_2\text{O}_6$ ($\text{M} = \text{Gd}^{3+}, \text{Ca}^{2+}$) for the immobilisation of MOx residues, *RSC Adv.* 8 (2018) 2092–2099. <https://doi.org/10.1039/c7ra11742f>.
- [168] S. V Yudintsev, S. V Stefanovsky, M.S. Nikol, S. A, O.I. Stefanovskaya, B.S. Nikonov a, Brannerite, UTi_2O_6 : Crystal Chemistry, Synthesis, Properties, and Use for Actinide Waste Immobilization, *Radiochemistry.* 58 (2016) 289–301. <https://doi.org/10.1134/S1066362216040019>.
- [169] N. Clavier, R. Podor, N. Dacheux, Crystal chemistry of the monazite structure, *J. Eur. Ceram. Soc.* 31 (2011) 941–976. <https://doi.org/10.1016/J.JEURCERAMSOC.2010.12.019>.

- [170] B.. Sales, C.. White, L.. Boatner, A comparison of the corrosion characteristics of synthetic monazite and borosilicate glass containing simulated nuclear defense waste, *Nucl. Chem. Waste Manag.* 4 (1983) 281–289. [https://doi.org/10.1016/0191-815X\(83\)90053-0](https://doi.org/10.1016/0191-815X(83)90053-0).
- [171] A. Meldrum, L.A. Boatner, R.C. Ewing, Displacive radiation effects in the monazite-and zircon-structure orthophosphates, (1997). <https://doi.org/doi/10.1103/PhysRevB.56.13805>.
- [172] G.R. Lumpkin, Ceramic Waste Forms for Actinides, *Elements.* 2 (2006) 365–372. <https://doi.org/10.2113/gselements.2.6.365>.
- [173] C. Gramaccioli, T. Segalstad, A uranium-and thorium-rich monazite from a south-alpine pegmatite at Piona, Italy, 1978. https://www.researchgate.net/publication/255927182_A_uranium-and_thorium-rich_monazite_from_a_south-Alpine_pegmatite_at_Piona_Italy.
- [174] A. Ringwood, S. Kesson, Immobilization of high-level wastes in SYNROC titanate ceramic, 1979. <https://www.osti.gov/servlets/purl/5869621>.
- [175] W. Anthony, R. Bideaux, K. Bladh, M. Nichols, Handbook of Mineralogy - Perovskite, Chantilly, Virginia, 2005. <http://www.handbookofmineralogy.org/pdfs/perovskite.pdf>.
- [176] W. Anthony, R. Bideaux, K. Bladh, M. Nichols, Handbook of mineralogy - Hollandite, 2005. <http://www.handbookofmineralogy.org/pdfs/hollandite.pdf>.
- [177] R.C. Ewing, W. Lutze, High-level nuclear waste immobilization with ceramics, *Ceram. Int.* 17 (1991) 287–293. [https://doi.org/10.1016/0272-8842\(91\)90024-T](https://doi.org/10.1016/0272-8842(91)90024-T).
- [178] A.E. Ringwood, S.E. Kesson, N.G. Ware, W. Hibberson, A. Major, Immobilisation of high level nuclear reactor wastes in SYNROC, *Nature.* 278 (1979) 219–223. <https://doi.org/10.1038/278219a0>.
- [179] A.N. Nikoloski, R. Gilligan, J. Squire, E.R. Maddrell, Chemical stability of zirconolite for proliferation resistance under conditions typically required for the leaching of highly refractory uranium minerals, *Metals (Basel).* 9 (2019). <https://doi.org/10.3390/met9101070>.
- [180] S. Iwata, K. Cenzual, $\text{Ca}_{1.25}\text{U}_{0.75}\text{Ti}_2\text{O}_7$ (CaUTi_2O_7) crystal structure, 2016. https://materials.springer.com/isp/crystallographic/docs/sd_1225266.
- [181] W. Anthony, R. Bideaux, K. Bladh, M. Nichols, Handbook of mineralogy - Rutile, 2005. <http://www.handbookofmineralogy.org/pdfs/rutile.pdf>.
- [182] A.E. Ringwood, Disposal of high-level nuclear wastes: a geological perspective, *Mineral. Mag.* 49 (1985) 159–176. <https://doi.org/10.1180/minmag.1985.049.351.04>.
- [183] P.H.W. Atkins, M.S.D. Read, J.A. Hriljac, Ceramic Materials for the Immobilisation of High Level Radioactive Waste, 2016. <https://core.ac.uk/download/pdf/71999411.pdf>.
- [184] G.T. Stevens, K.G. Watson, A. Bellrose, Microstructural Aspects of SYNROC from Sandia Precursor, 1987. <https://apo.ansto.gov.au/dspace/handle/10238/799>.
- [185] R.B. Rozsa, C.L. Hoenig, Synroc processing options, Livermore, CA, 1981. <https://doi.org/10.2172/6088646>.
- [186] F.W. Clinard, L.W. Hobbs, C.C. Land, D.E. Peterson, D.L. Rohr, R.B. Roof, Alpha decay self-irradiation damage in ^{238}Pu -substituted zirconolite, *J. Nucl. Mater.* 105 (1982) 248–256. [https://doi.org/10.1016/0022-3115\(82\)90381-6](https://doi.org/10.1016/0022-3115(82)90381-6).
- [187] F.W. Clinard, D.L. Rohr, R.B. Roof, Structural damage in a self-irradiated zirconolite-based Ceramic, *Nucl. Instruments Methods Phys. Res. Sect. B Beam Interact. with Mater. Atoms.* 1 (1984) 581–586. [https://doi.org/10.1016/0168-583X\(84\)90127-7](https://doi.org/10.1016/0168-583X(84)90127-7).

- [188] E.R. Vance, D.S. Perera, S. Moricca, Z. Aly, B.D. Begg, Immobilisation of ^{129}I by encapsulation in tin by hot-pressing at $200\text{ }^\circ\text{C}$, *J. Nucl. Mater.* 341 (2005) 93–96. <https://doi.org/10.1016/j.jnucmat.2005.01.011>.
- [189] F. Guittonneau, A. Abdelouas, B. Grambow, HTR fuel waste management: TRISO separation and acid-graphite intercalation compounds preparation, *J. Nucl. Mater.* 407 (2010) 71–77. <https://doi.org/10.1016/j.jnucmat.2010.09.026>.
- [190] H. Wilski, The radiation induced degradation of polymers, *Int. J. Radiat. Appl. Instrumentation. Part. 29* (1987) 1–14. [https://doi.org/10.1016/1359-0197\(87\)90054-3](https://doi.org/10.1016/1359-0197(87)90054-3).
- [191] A. Minaev, S. Oziraner, N. Prokhorova, The use of glass-ceramic materials for the fixation of radioactive wastes, in: *Ceram. Nucl. Waste Manag., TIC - USDoE, 1979*: pp. 229–232. <https://www.osti.gov/servlets/purl/5869621>.
- [192] J.S. McCloy, S. Schuller, Vitrification of wastes: from unwanted to controlled crystallization, a review, *Spec. Issue S1. 354* (2022) 121–160. <https://doi.org/10.5802/crgeos.111>.
- [193] M.D. Kaminski, C.J. Mertz, M. Ferrandon, N.L. Dietz, G. Sandi, Physical properties of an aluminosilicate waste form for cesium and strontium, *J. Nucl. Mater.* 392 (2009) 510–518. <https://doi.org/10.1016/j.jnucmat.2009.04.020>.
- [194] T.A. Vereshchagina, S.N. Vereshchagin, N.N. Shishkina, N.G. Vasilieva, L.A. Solovyov, A.G. Anshits, Microsphere zeolite materials derived from coal fly ash cenospheres as precursors to mineral-like aluminosilicate hosts for ^{135}Cs , ^{137}Cs and ^{90}Sr , *J. Nucl. Mater.* 437 (2013) 11–18. <https://doi.org/10.1016/j.jnucmat.2013.01.343>.
- [195] M.C. Dixon Wilkins, E.R. Maddrell, M.C. Stennett, N.C. Hyatt, Synthesis and characterisation of high ceramic fraction brannerite (UTi_2O_6) glass-ceramic composites, *IOP Conf. Ser. Mater. Sci. Eng.* 818 (2020). <https://doi.org/10.1088/1757-899X/818/1/012018>.
- [196] Y. Zhang, L. Kong, I. Karatchevtseva, R.D. Aughterson, D.J. Gregg, G. Triani, Development of brannerite glass-ceramics for the immobilization of actinide-rich radioactive wastes, *J. Am. Ceram. Soc.* 100 (2017) 4341–4351. <https://doi.org/10.1111/jace.14975>.
- [197] Y. Zhang, Z. Zhang, T. Wei, L. Kong, Y.J. Kim, D.J. Gregg, Pyrochlore glass-ceramics fabricated via both sintering and hot isostatic pressing for minor actinide immobilization, *J. Am. Ceram. Soc.* (2020). <https://doi.org/10.1111/jace.17119>.
- [198] A. Nag, P. Dasgupta, Y.M. Jana, D. Ghosh, A study on crystal field effect and single ion anisotropy in pyrochlore europium titanate ($\text{Eu}_2\text{Ti}_2\text{O}_7$), *J. Alloys Compd.* 384 (2004) 6–11. <https://doi.org/10.1016/j.jallcom.2004.03.133>.
- [199] I.W. Donald, B.L. Metcalfe, R.N.J. Taylor, Review: The immobilization of high level radioactive wastes using ceramics and glasses, 1997. <http://citeseerx.ist.psu.edu/viewdoc/download?doi=10.1.1.628.229&rep=rep1&type=pdf>.
- [200] J. Cronin, N. Collier, Corrosion and expansion of grouted Magnox, *Mineral. Mag.* 76 (2012) 2901–2909. <https://doi.org/10.1180/minmag.2012.076.8.05>.
- [201] P.K. Abratis, F.R. Livens, J.E. Monteith, J.S. Small, D.P. Trivedi, D.J. Vaughan, R.A. Wogelius, The kinetics and mechanisms of simulated British Magnox waste glass dissolution as a function of pH, silicic acid activity and time in low temperature aqueous systems, *Appl. Geochemistry.* 15 (2000) 1399–1416. [https://doi.org/10.1016/S0883-2927\(99\)00118-3](https://doi.org/10.1016/S0883-2927(99)00118-3).
- [202] A. Bohre, K. Avasthi, V.I. Pet'kov, Vitreous and crystalline phosphate high level waste matrices: Present status and future challenges, *J. Ind. Eng. Chem.* 50 (2017) 1–14. <https://doi.org/10.1016/j.jiec.2017.01.032>.

- [203] Nikoloski, Gilligan, Squire, Maddrell, Chemical Stability of Zirconolite for Proliferation Resistance under Conditions Typically Required for the Leaching of Highly Refractory Uranium Minerals, *Metals (Basel)*. 9 (2019) 1070. <https://doi.org/10.3390/met9101070>.
- [204] D.V. Zverev, S.N. Kirillov, K.N. Dvoeglazov, A.Y. Shadrin, M.V. Logunov, A.N. Mashkin, O.V. Schmidt, L.V. Arsenkov, Possible Options for Uranium-carbide SNF Processing, *Procedia Chem.* 7 (2012) 116–122. <https://doi.org/10.1016/j.proche.2012.10.021>.
- [205] Z.A. Munir, U. Anselmi-Tamburini, M. Ohyanagi, The effect of electric field and pressure on the synthesis and consolidation of materials: A review of the spark plasma sintering method, *J. Mater. Sci.* 41 (2006) 763–777. <https://doi.org/10.1007/s10853-006-6555-2>.
- [206] NDA, Waste Stream: Magnox-Secondary Ion Exchange Resin (Cs-Treat), 2016. <https://ukinventory.nda.gov.uk/wp-content/uploads/sites/18/2017/03/9B85.pdf>.
- [207] T.-Y. Chen, J.A. Hriljac, A.S. Gandy, M.C. Stennett, N.C. Hyatt, E.R. Maddrell, Thermal Conversion of Cs-exchanged IONSIV IE-911 into a Novel Caesium Ceramic Wasteform by Hot Isostatic Pressing, *MRS Proc.* 1518 (2013) 67–72. <https://doi.org/10.1557/opl.2013.202>.

3. Materials and Methods

3.1 Materials and synthesis

3.1.1 Oxide solid-state synthesis and batching

All glass-ceramics, melts and a selection of ceramic products were prepared using inorganic reagents, batched to fulfil calculated molar ratios within the experimental matrices. Oxide components were primarily used, in addition to ammonium dihydrogen phosphate as $\text{NH}_4\text{H}_2\text{PO}_4$ (98% ACS, Alfa Aesar) for phosphorus sources in the glass-ceramic materials. Other substitutions for oxides such as sodium carbonate Na_2CO_3 (98%, Alfa) were made in order to improve reactivity of melts and pellets prior to sintering. Ceria, CeO_2 (99.5%, Alfa) additions were used as an inactive trial simulant for UO_2 , as its fluorite structure can provide suitable analogue behaviours prior to approval of active material trials [1]. Batches were homogenised with between 0 – 45 mol.% CeO_2 as simulated spent fuel. Oxide precursors for ceramics were batched on a molar basis before homogenising with a Fritsch Pulverisette 23 mini-mill, ZrO_2 grinding bowl and media. This was carried out to reduce particle size and increase reactivity before uniaxial compression into 10 mm \varnothing pellets (1 ton load for 60 seconds) and sintering at temperature in air atmosphere.

3.1.2 Alkoxide nitrate synthesis

An alkoxide-nitrate synthesis method was used to generate the reactive titanate precursors for SYNROC-F type multiphase ceramic experiments as discussed in one of the PhD project research outputs, see **Appendix 1**. Reagents were sourced from the following: $\text{Ca}(\text{NO}_3)_2 \cdot 4\text{H}_2\text{O}$ (99%, Acros Organics); $\text{Ba}(\text{NO}_3)_2$ (99%, Fluorochem); $\text{Ce}(\text{NO}_3)_3 \cdot 6\text{H}_2\text{O}$ (99%, Sigma); $\text{Al}(\text{OH})_3$ (98%, Acros); $\text{C}_{12}\text{H}_{28}\text{O}_4\text{Ti}$ (96%, Fluorochem). Nitrate components were dissolved in an excess of warm de-ionised water, with the simulant waste added as a cerium nitrate for co-precipitation and ease of homogenisation. Separately, a mixture of stock isopropyl alcohol and aluminium hydroxide were agitated before complexing with an equal volume of titanium isopropoxide. The resulting complex was then shear mixed for 5 minutes with the dissolved nitrates to ensure rapid and homogenous precipitation, see **Figure 3.1.2.A**. The slurry was dried before calcining for 12 hours at 600 °C; the resulting powder was ball milled using a mini-mill, and pressed into 10 mm \varnothing pellets, before sintering for 1 hour at a range of temperatures 1000 °C – 1300 °C.

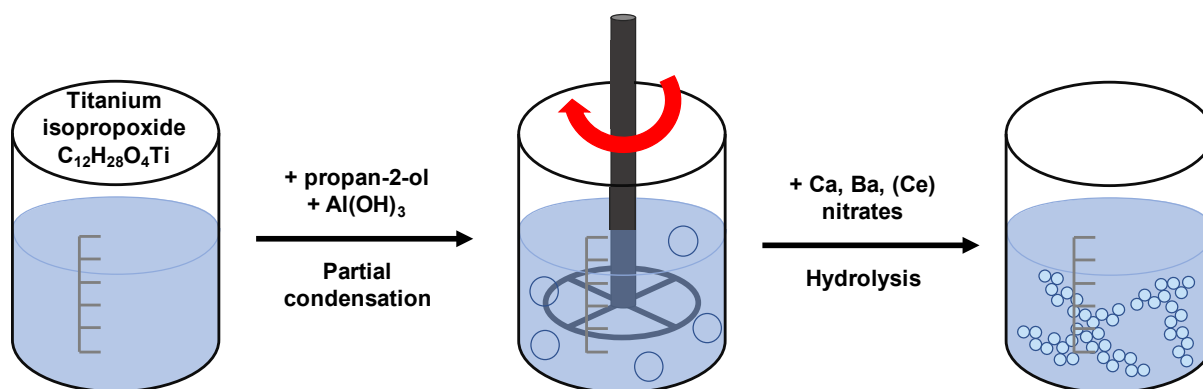


Figure 3.1.2.A – Diagram showing laboratory scale process of alkoxide-nitrate synthesis, reactants are shear-mixed together for 5 minutes

3.1.3 Ion exchange

The following provides a brief summary of the sample preparation technique used, more comprehensive accounts can be found in a subsequent paper [2]. A natural source of chabazite was used to simulate KURIONs caesium ion exchange material. Its composition was 70 ± 2 wt.% Chabazite (Verdi - Zeover), 18 ± 5 wt.% volcanic glass with auxiliary components (< 5 wt.% each) of feldspar, pyroxenes, biotite and philipsite. Material was exchanged with a 0.1 M $^{133}\text{CsNO}_3$ solution (Arcos 99%) in a teflon vessel for 24 hours, turned continuously using a roller-mill. After rinsing twice with 1 L of de-ionised (DI) H_2O , filtration and removal of the subsequent liquor, the exchanged material was dried for 24 hours at 95°C in air. This in effect, provided a material analogous to spent inorganic caesium ion-exchange material, as found in SIXEP and Fukushima Daichi effluent treatment facilities. Cs exchange was verified by Energy Dispersive X-ray spectroscopy and X-ray fluorescence

3.1.4 Thermal treatment technologies

3.1.4.a Glass melting

Precursors batched to target glass at 10 g and 150 g were melted under air-atmosphere in a BRF 15/5-2416 (Elite Thermal Systems Ltd) furnace and a clean alumina crucible, leaving adequate volume for foaming and self-stirring effects to safely occur without any excursion. The melt constituents were held for 6 hours at 300°C for a calcination-decomposition step, before 2 hours at a melt temperature of 1250, 1350 or 1450°C . Monolithic glass samples were then quenched onto a pre-heated steel plate, before annealing at 550°C for 4 hours in air. After the annealing period elapsed, the samples were slow cooled to room temperature at $1^\circ\text{C}/\text{minute}$. For chemical durability experiments, glass frit was produced by water quenching the glass from the molten state.

3.1.4.b Furnace sintering and cold pressing

A BRF 15/5-2416 (Elite Thermal Systems Ltd) chamber furnace was used, with air atmosphere, to sinter compacts and compressed pellets of titanate ceramics at temperature. Clean alumina furnace ware was used, with some platinum foil employed as a barrier for the most reactive ceramic precursors, when sintered at high temperature for the longer durations.

A high temperature pellet trial was carried out to refine the temperature range for development of crystalline cerium pyrochlore in the multiphase titanate ceramic materials, also allowing for the identification of other crystallographic phase transitions over the applied temperature range (600 – 1300 °C). Seven 1.00 g pellets were pressed, using prepared pyrochlore precursor powder. Cylindrical 10mm aperture dies and a manual hydraulic press (Specac) were used in all instances. A 1 ton load was applied for 60 seconds, to form the pellet, before the sample was gently removed using the die punch in the pellet press. A set of digital callipers and a laboratory balance were used to take measurements of the pellets before and after pressing. Three diameter and height measurements were taken for each pellet for the purposes of calculating a rudimentary average. Visual observations and scaled photographs were taken before and after sintering. In some experiments, fragments of the pellets were milled for XRD analysis.

Sintering was undertaken using a clean alumina crucible, sintering one pellet at each temperature: 600 °C, 1000 °C, 1100 °C, 1200 °C and 1300 °C. The furnace was ramped to temperature at 5°C/min, once at temperature, a pellet was loaded and temperature held for 35 minutes (5 minutes for temperature stabilisation after loading the sample and 30 minutes for thermal treatment), before removal for sample cooling (quenched in air) and furnace ramp to the next temperature, see **Figure 3.1.4.A**.

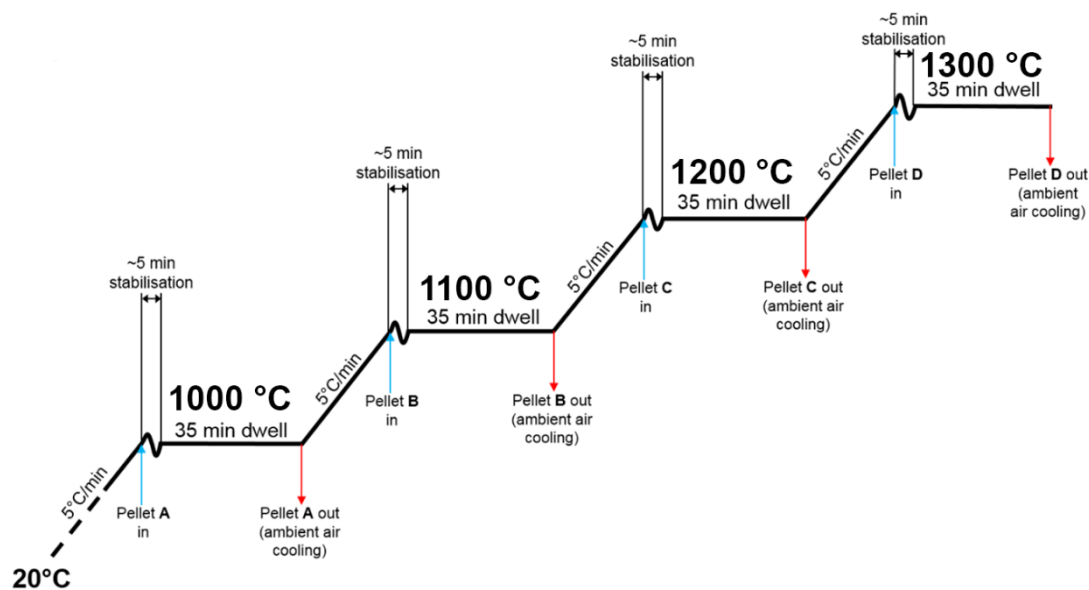


Figure 3.1.4.A – Temperature-time profile displaying the furnace heating schedule, with pellets exposed to temperatures between 1000 °C and 1300 °C.

3.1.4.c Spark plasma sintering

Spark Plasma Sintering (SPS) is a relatively novel sintering technique that operates on the principle of a Joule heating effect via a very high applied current. This is usually coupled with a uniaxial pressure, which facilitates mass-transport and grain growth. The sample powder is contained inside a conductive graphite die, allowing the simultaneous application of heat and pressure. High performance components in the SPS chamber allow for rapid heating rates and near-theoretical densities for the final pellet product.

SPS die preparation is a key stage of the process that is necessary to ensure the sample can be contained and monitored during sintering. The Cs-exchanged chabazite tuff was prepared by calcining in an air-atmosphere chamber furnace (Elite Thermal Systems Ltd) at 300 °C for 12 hours, this was done to remove residual water and reduce the chance of entrainment of steam bubbles. Once calcined, the exchange media was milled manually with a pestle and mortar and sieved with a 212 μm steel mesh. A 20 mm aperture graphite die was cleaned and loaded in the following arrangement: a base graphite punch, two layers of graphite paper discs, 3 g of calcined sample were then loaded and levelled off, two further graphite paper discs were placed above the sample and a graphite top punch, with a cavity for insertion of a monitoring thermocouple, was used to seal the die pack, see **Figure 3.1.4.B**. The

assembled die was then placed into a pellet press and 1 ton of uniaxial load was applied for 5 minutes to compress and stabilise the sample. The punches were then removed and checked for sample leakage before re-insertion, one at a time.

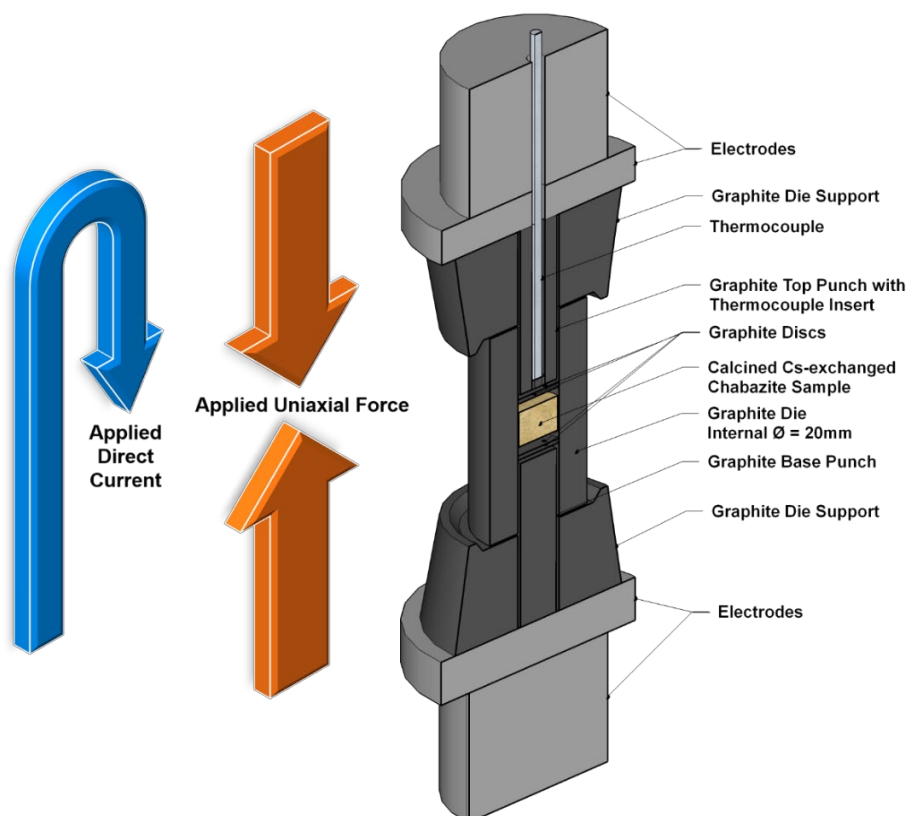


Figure 3.1.4.B – Cross-section sketch of the internal components of SPS vacuum chamber, indicating location of graphite die assembly and sample compact.

Samples were processed using an HP-D 25 SPS system (FCT Systeme GmbH). Using the data from the previous characterisation and analysis, the selected processing parameters were ramped to 1000 °C or 1100 °C, at 50 °C/min under an argon atmosphere with dwell times of 10 or 30 minutes, simultaneously under the application of uniaxial pressure of 15 MPa or 50 MPa. Ensuring that the SPS chamber was clean, and the appropriate gas flow and electrical checks were complete, the ends of the die package were surrounded by graphite die posts and loaded into the chamber, as demonstrated in **Figure 3.1.4.C (a)**. The assembly was covered with a graphite jacket, acting to reduce the overall temperature differential between the die and surrounding components. With the chamber sealed, see **Figure 3.1.4.C (b)**, thermocouples were lowered into the cavity of the top die punch, final safety checks were carried out and the processing parameters adjusted. A series of purge cycles were initiated with

a double vacuum cycle, purging with argon gas, removing any residual gases that could affect the sintering process. The voltage was then ramped to gradually reach the target heating rate of 50 °C/min, simultaneously the pressure exerted on the punches was increased to match the heating rate so that the required pressure was achieved at the same time as temperature, see **Figure 3.1.4.C (c-e)**. Once sintering was completed, the die was left to cool at a natural rate, removed from the chamber, as seen in **Figure 3.1.4.C (f)** and the pellet was removed using a manual press. As the soft graphite paper became slightly entrained in the surface of the pellet, residual graphite was removed by manual grinding with SiC papers. Small quantities of the actual samples were removed in the process, to ensure that no graphite was entrained into the sintered material, which would have contaminated the composition for any chemical analysis. Final measurements of the pellet were recorded before sectioning for characterisation.

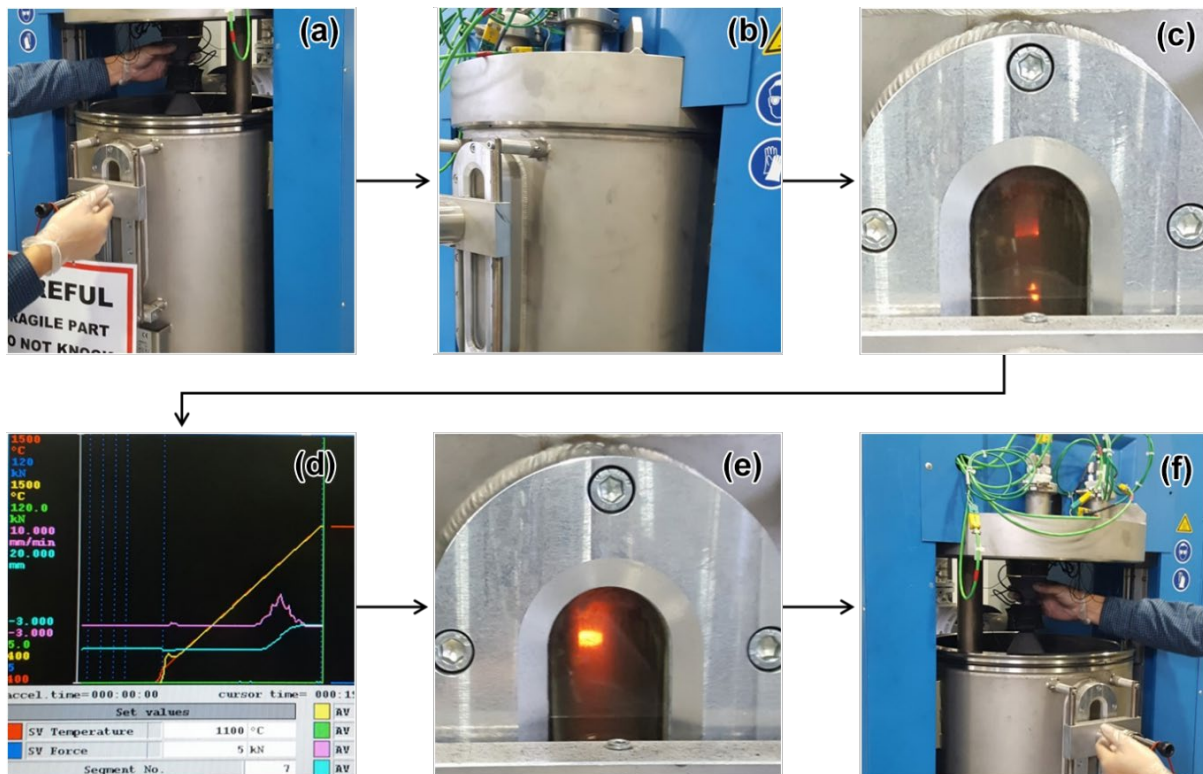


Figure 3.1.4.C – Flow diagram for the SPS process; (a) loading of the die; (b) sealing, purging and evacuating of the chamber; (c) voltage is increased to ramp the temperature at 50°C/min; (d) displacement, pressure, temperature and time are monitored by the system; (e) target temperature and uniaxial pressure is reached and held for the dwell time; (f) after the sample has cooled, it is removed and pressed out of the die.

3.2 Gas pycnometry and density balance measurements

Gas pycnometry is a density measurement technique which relies on the principles of gas displacement to calculate the volume of a powder/other irregular geometry sample. Sample density can then be calculated using the mass of the sample. A density balance is a modified laboratory balance, operating on the Archimedes water displacement method, which measures the specific weight of a solid sample in air and then in a fluid of known density and temperature. These two values were then used to calculate the density according to **Equation 3.2.A**.

$$\rho = \frac{A}{A - B} \cdot (\rho_0 - \rho_L) + \rho_L$$

Equation 3.2.A – Formula for density calculation; ρ = sample density;
 A = sample weight in air; B = sample weight in fluid; ρ_0 = density of air; ρ_L
 = density of fluid

3.2.1 Sample preparation and technique

A Micrometrics AccuPyc II 1340 gas pycnometer was used with a 1 cm³ sample cell for the majority of powder samples and later in the project, a 0.1 cm³ cell for the Spark Plasma Sintered samples, due to the lower sample volume. Sample material was manually milled into a fine powder using a pestle and mortar. Sample cells were loaded to about 70% of the total apparent internal volume of the cell. Helium gas was used to ensure sample pores were being quickly filled with gas and purge cycles were employed so that the solid material would be the only medium for displacement. 10 purge cycles and 10 measurement cycles were taken so that a suitable average and standard deviation could be calculated. The purge fill pressure was set to 86.2 kPa per cycle with an end equilibrium rate of 3.4 kPa per minute.

Density balance measurements of glass monoliths and sintered pellet fragments were taken using an Archimedes (Mettler Toledo) balance, calibrated with water as a liquid at a measured laboratory temperature. Each fragment was measured in both mediums five times, to allow for determination of an average and deviation.

3.3 Powder X-ray diffraction

Powder based X-ray diffraction (pXRD) was used throughout this project for identification of phase assemblage, structural changes and to complement chemical analysis techniques such as XRF and Energy Dispersive X-ray spectroscopy. The principle of X-ray diffraction operates on constructive interference of diffracted X-rays according to Bragg's law, allowing for inference of information about atomic spacings and crystal lattice features.

3.3.1 Standard pXRD sample preparation and measurement

The granular nature of sintered powders and geometries of monoliths and pellet samples necessitated the manual pulverisation of samples into a fine powder using an agate pestle and mortar, before XRD measurements were carried out. The diffractometer used was a Bruker D2 PHASER with a LYNXEYE detector, Ni filtered Cu (K_{α} $\lambda = 1.5418 \text{ \AA}$) radiation and a zero-background sample holder. The holder was loaded with sample and levelled off with a glass slide, before insertion into the diffractometer. Diffraction patterns were collected between $5^{\circ} < 2\theta < 50^{\circ}$ with a step size of $0.02^{\circ} 2\theta$ and dwell time of one second per step. Slit fluorescence conditions, and a longer step dwell time of 3 seconds per step were used for glass and glass-ceramic samples, to assist with identification of any minor Bragg peaks from the onset of crystallisation. The DIFFRAC.EVA software package and the PDF databases were used for phase identification and analysis.

3.3.2 Klug and Alexander quantitative phase analysis

A set of trial measurements were conducted for rapid phase quantification, using several adapted methods as discussed by Klug and Alexander [3]. Fully amorphous phosphate glass, cerium (IV) oxide (99.9%) and prepared cerium phosphate (monazite) standard powders were used in controlled mixtures, for measurements under Ni filtered Cu (K_{α} $\lambda = 1.5418 \text{ \AA}$) in the Bruker D2 Phaser diffractometer. 99% purity α - Al_2O_3 was used where an internal standard was called for, at a 20 wt.% addition. Mixture component absorption coefficients were calculated using the HEPHAESTUS software from the Demeter package [4], assuming theoretical densities [5]. Crystalline phases were found to have the following absorption coefficients for Cu K- α radiation at 8040 eV :

- $\text{CePO}_4 \quad \bar{\mu}X^* = 232.62 \text{ cm}^2\text{g}^{-1}$
- $\text{CeO}_2 \quad \bar{\mu}Y^* = 302.02 \text{ cm}^2\text{g}^{-1}$
- $\text{Al}_2\text{O}_3 \quad \bar{\mu}S^* = 31.64 \text{ cm}^2\text{g}^{-1}$

The method describing mixtures of N components ($N > 2$); $\mu_{I^*} \neq \mu_{M^*}$, whereby mixture components do not have the same absorption coefficients, was used to generate some calibration lines. For component J in a matrix, analysed with an internal standard, S – calibration performed keeping the standard weight fraction, x_S constant, **Equation 3.3.A** was used for sample fraction determination.

$$x_J = \frac{k'}{1 - x_S} \times \frac{I_{iJ}}{I_{kS}} = k \times \frac{I_{iJ}}{I_{kS}}$$

Equation 3.3.A – Where x_J is the component weight-fraction, k is a constant, I represents integrated peak area both of component J in the matrix and the standard, S .

Powder mixtures were batched and finely milled, before homogenising manually in a pestle and mortar and placing in a small zero-background holder. Diffraction data was collected at a selection of characteristic Bragg peaks, a step size of $0.02^\circ 2\theta$ with up to 8 seconds per step. CMPR software was used for peak fitting under a General Public License Subroutine Fortran Translator (GPLSFT) code [6], integrating peak area allowing for subsequent calculation of peak ratios and linear calibration lines, see **Figure 3.3.2.A**. Measured peak ratios of unknown mixtures can be compared to the calibration lines, with component fraction found at the intercept. While relatively simple and quick to prepare samples once a calibration curve has been established, the consistency of output results departed significantly from the other trialled phase quantification techniques: Rietveld full pattern refinement and image based quantitative analysis.

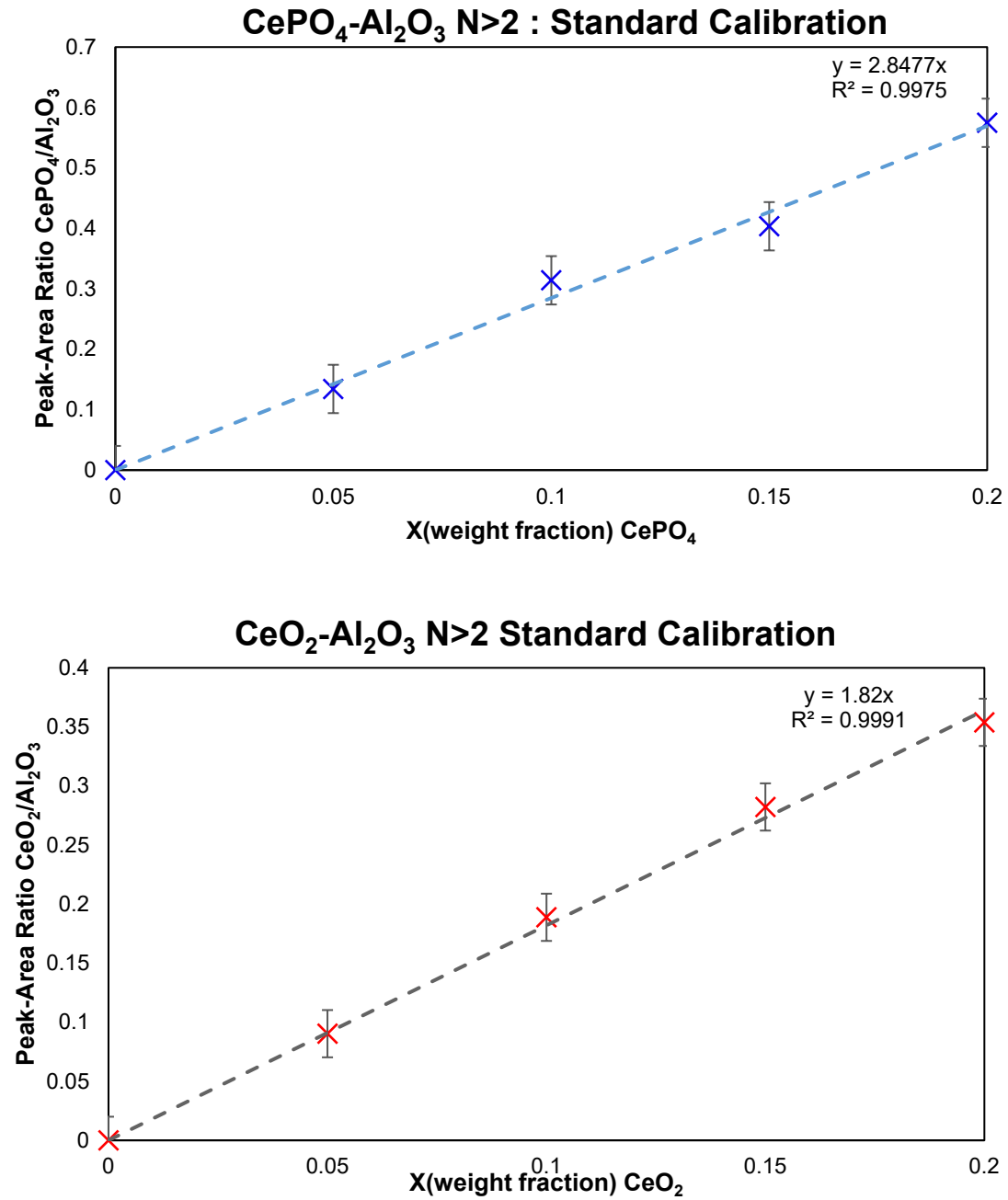


Figure 3.3.2.A – Mixture calibration lines for selected peak ratios with internal standard; monazite as CePO₄ (top), and cerium oxide as CeO₂ (bottom).

3.4 X-ray fluorescence spectroscopy

X-ray Fluorescence Spectroscopy (XRF) is a characterisation technique for quantitative chemical analysis, which utilises the fluorescence associated with the electron vacancy filling, from X-ray displacement. The unique electron structure of every element means that each will fluoresce, with identifiably characteristic energies when electrons fall into the lower energy levels of shells closest to the nucleus. K, L and M (innermost electron shells) spectral lines are chosen as the primary source for quantification of these fluorescence events. XRF was utilised in this study to verify elemental composition of ion exchange material, while also permitting the quantification of the caesium exchange and retention.

3.4.1 Sample preparation

XRF beads (disc-shaped) were prepared using a heated flux, to produce a monolith meeting the requirements of the XRF spectrometer. Milled sample powder was sieved to ensure all particles were $< 212\mu\text{m}$, 1g of this powder was then combined with 10g of lithium tetraborate flux (Sigma Aldrich, 99.995% Purity) for a 1:10 sample-to-flux ratio. These components were placed into a platinum crucible and manually mixed thoroughly. The crucible was placed into an automatic electric Claisse LeNeo™ Fluxer, for fusion at temperatures up to 1065 °C, producing a homogeneous glass bead.

3.4.2 XRF analysis

The analysis of the glass bead samples by XRF, was carried out using a PANalytical Zetium spectrometer under vacuum with a Rh X-ray tube operating at 50kV and 30mA. For each sample, three full spectrum scans were run using the full standardless elemental programme (approx. 20 minutes per scan), so an average could be obtained, and any outlying trace elements could be identified.

3.5 X-ray absorption spectroscopy (XAS, XANES, EXAFS)

X-ray Absorption Spectroscopy (XAS) is a characterisation technique that can be used to further understand the electronic structure of bulk materials. A tuneable X-ray beam is directed at the sample, measuring the beam intensity before and after transmission through the sample, allowing for determination of net absorption. The excitation of electrons in the sample has characteristic absorption spectra, with well defined 'edge' features at a specific energy depending on the element and oxidation states, for example, Fe-K edge work probes the interaction with a 1s electron orbital. Several XAS studies were conducted for Fe-K edge, and Ce-L₂, Ce-L₃ edge spectra, probing the pre-edge features as well as X-ray absorption near edge structure (XANES) and extended x-ray absorption fine structure (EXAFS) regions, see **Figure 3.5.A**.

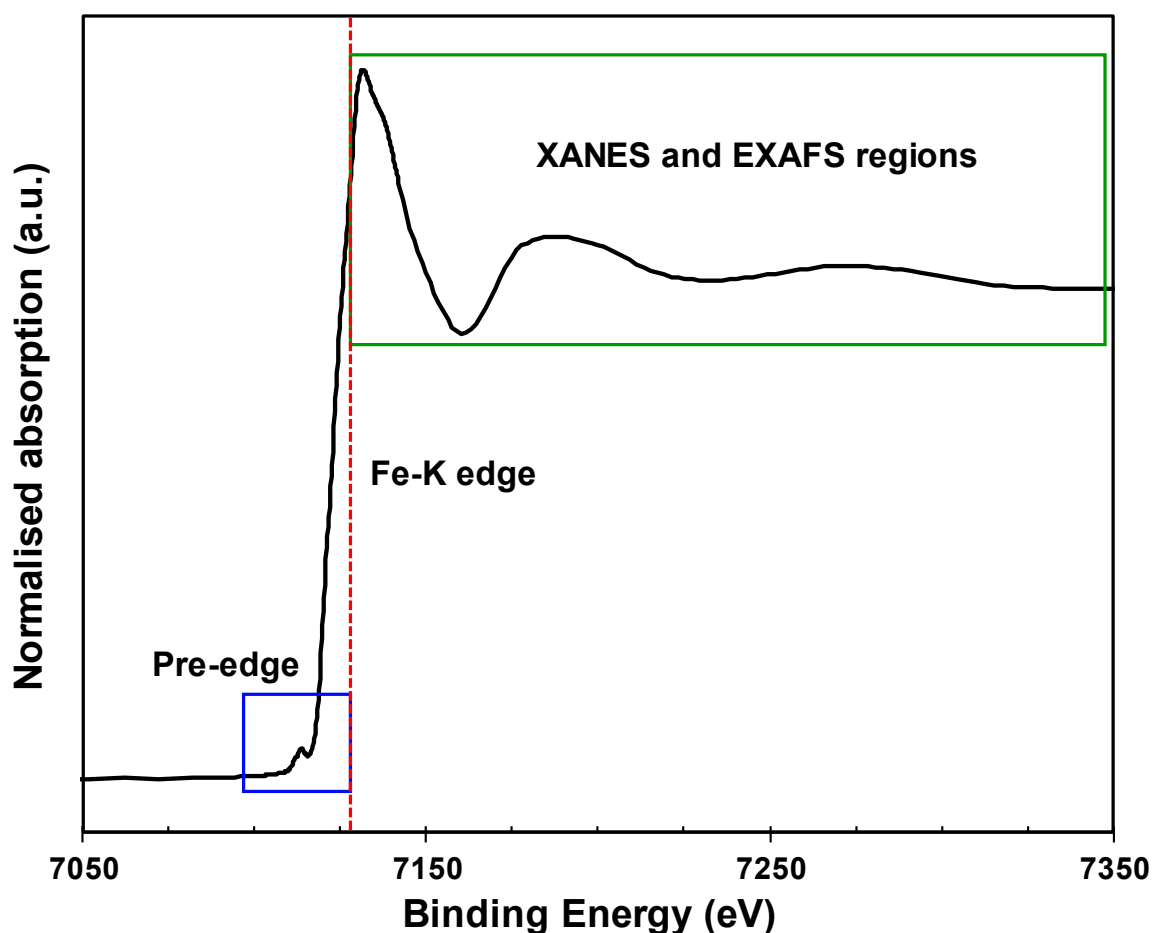


Figure 3.5.A – X-ray absorption spectra for the Fe-K edge of an iron phosphate glass, indicating marked regions of interest for analyses

Pre-edge features and shoulders can be studied to determine electronic structure and oxidation state of the absorber species (as an average for a bulk material). EXAFS data represents the oscillations of photoelectrons ejected from the absorber atoms, allowing for modulation of the absorption spectra by calculation of the sum of probability contributions from physical and thermal effects of scattering events with nearest neighbouring atoms, according to **Equation 3.5.A**.

$$\chi(k) = S_0^2 \sum_i N_i \frac{f_i(k)}{kD_i^2} e^{\frac{-2D_i}{\lambda(k)}} e^{-2k^2\sigma_i^2} \sin(2kD_i + \delta_i(k))$$

Equation 3.5.A – EXAFS equation, where $k = \frac{2\pi}{\lambda}$ is the wavenumber, λ as the wavelength of ejected photoelectrons, χ is a factor of absorption modulation, S_0^2 is the amplitude reduction factor (element dependant constant usually 0.7-1.0), i subscript denotes different scattering possibilities or pathways, the degeneracy N results from the grouping of similar neighbours. A component $\frac{f_i(k)}{kD_i^2}$ represents the spherical proportionality constant (considering isotropic spread of spherical waves, decreasing scattering probability with the square of distance or ‘scattering length’ from absorbers). The exponent $e^{\frac{-2D_i}{\lambda(k)}}$ relates the mean free path of photoelectrons, $\lambda(k)$ to the scattering length and therefore core-hole lifetime, as with greater scattering length, a core-hole may decay before a photoelectron can return. An isotropic term usually defined as the Debye-Waller factor, $e^{-2k^2\sigma_i^2}$ is used to account for disorder induced by thermal vibration and static disorder in the structure, σ^2 representing the mean square radial displacement due to this disorder. Atoms in the sample can alter the phase of photoelectron waves, this is introduced using a phase shift parameter, $\delta_i(k)$. With the factor D_i denoting the scattering length, this is typically half of the total distance travelled by a photoelectron (for single and multiple scattering paths) [7].

The majority of measurements were conducted in transmission mode, whereby the energy of X-rays was measured on incidence to the sample and after transmission, permitting simple calculation of the absorbance, see **Figure 3.5.B**.

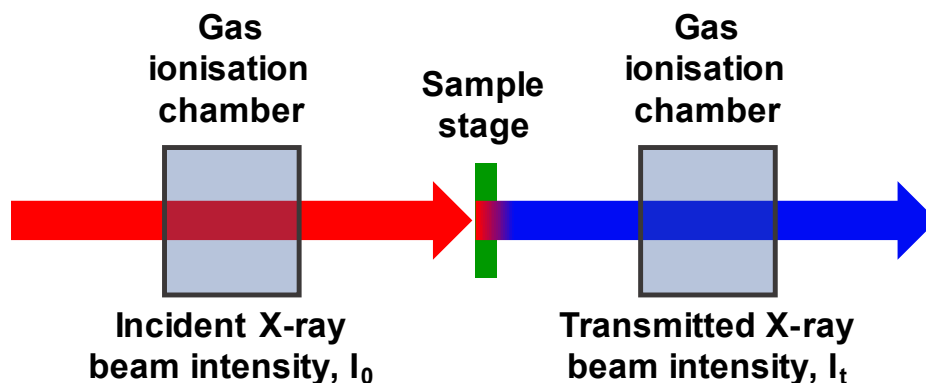


Figure 3.5.B – Transmission mode experimental set-up for X-ray absorption spectroscopy.

3.5.1 Sample preparation

The uniformity, thickness and concentration of absorber atoms exposed to the X-ray beam are all key factors in ensuring collection of well resolved XAS data. For transmission samples, a fine powder was milled and diluted with solid polyethylene glycol, before homogenisation and pressing under low force into a pellet. The ratio of sample to bulking agent was optimised using HEPHAESTUS calculations as to maximise the absorbance step before and after the edge [4]. This also involves balancing a number of absorption lengths that permits transmission, while still being thick enough to allow for a statistically significant number of photons to be absorbed, producing a good signal to noise ratio. For fluorescence measurements, monoliths were ground to have 2 parallel sides, polishing the beam facing side to mitigate surface effects.

3.5.2 Synchrotrons and beamlines

The primary synchrotron facilities used were the BL-27B beamline at KEK-Photon Factory, Tsukuba Japan (see **Appendix 2**), and the 6-BM beamline at NSLS-II, Brookhaven, New York, USA. Initial Fe-K measurements were conducted at BL-27B, with further Fe-K, Ce-L2, Ce-L3 and fluorescence measurements conducted at 6-BM. The Photon Factory synchrotron ring operates at 2.5 GeV, with a top-up mode to maintain beam current, the beamline utilised a double crystal Si(111) monochromator and is specified to reach up to fluxes of 10^{11} photons s^{-1} . This station featured gas flow ionisation chambers as detectors and an active material handling area. The 6-BM beamline at NSLS-II featured both Si(111) and Si(311) monochromators, focusing and harmonic rejection optics. These monochromators are specified to achieve photon fluxes of 2×10^{12} photons s^{-1} and 4×10^{11} photons s^{-1} , respectively. 6-BM also featured gas-flow ionisation chamber detectors.

3.5.3 Fe-K pre-edge analysis

Baseline pre-edge analysis of Fe-K edge XAS data was conducted by fitting a background spline, applying a normalisation function, and fitting two Lorentzian contributions, each at different absorbance energies. The centroid position of these features was used to analyse the iron oxidation state, with reference to data from iron containing standards, while the intensity and integrated area corresponded to the coordination environment. As the Fe-K edge data was collected from a bulk sample, the result obtained represented an average oxidation state and coordination for all iron in the sample [8].

3.5.4 Data processing with Athena and Artemis

Data manipulation and analysis was conducted using free software packages from the Demeter system. Reduction of data, application of a background function, merging, calibrations, and normalisations were conducted using the ATHENA package. Corrections such as de-glitching, and self-absorption were also achieved via ATHENA. The ARTEMIS package permitted probing of the EXAFS region through techniques such as *k*-weighting, application of Fourier transforms and modelling of spectra to fit EXAFS regions using free energy force field (FEFF) calculations and crystallographic information files (CIF) [4].

3.6 Simultaneous thermal analysis

Simultaneous Thermal Analysis (STA) is an analytical technique for combining the simultaneous use of Thermogravimetric Analysis (TGA), and Differential Thermal Analysis (DTA). TGA is a thermal analysis method that monitors and measures the mass change of a sample as a function of temperature ramp and/or time-period. This technique is particularly pertinent for water losses and off-gasses, as the measured mass will measurably decrease during these events. DTA acts as another technique for thermal analysis, whereby the temperature of the sample is directly measured by a thermocouple during heating and compared against a reference sample (alumina), which is heated simultaneously. Phase changes to the sample during the heating cause temperature fluctuations in the material due to latent heat absorption or emission and can be detected as a deviation from the temperature profile of the reference sample.

3.6.1 Thermal analysis method

The DTA element is conducted using data obtained through differential heat flow, allowing for assessment of the onset of glass transition temperature, T_g and crystallisation temperature T_c , which can be coupled with a multiple-heat cycle method, whereby the thermal history of a glass sample can be removed.

This study used a Netzch STA, TG 449 F3 Jupiter analyser, samples were heated and cooled at 5 °C per minute. Thermal analysis of base sodium iron phosphate glass samples was conducted in two runs, where the temperature was ramped to 1350 °C, to a typical melt temperature, before slow cooling to room temperature. Argon was used as an inert purge gas and an alumina pan was employed as the reference sample. Measurements were taken every 0.01 minutes (0.6 seconds).

3.7 Mössbauer spectroscopy

Mössbauer spectroscopy is a technique probing the electronic structure and local environment of iron atoms by studying the recoil of nuclei under irradiation. Through the conservation of momentum, atomic nuclei can recoil during absorption or emission of a γ -photon. For this emission from the nuclei to occur, the incident γ -photon energy must be greater than the excitation threshold for photoelectron emission. Nuclei in solids can lose energy to recoil interactions in ‘phonon packets’, when this phonon energy is = 0, these are termed as ‘recoil-free’ events. ^{57}Fe Mössbauer spectroscopy utilises the 14.4 keV transition and interaction between atoms of ^{57}Fe , accounting for approximately $\sim 2\%$ isotopic abundance. This isotope is generated in an excited state through the electron capture decay from a ^{57}Co source, **Figure 3.7.A**. This method can be used to determine isomer shift, quadrupole splitting effects and magnetic Zeeman splitting effects [9].

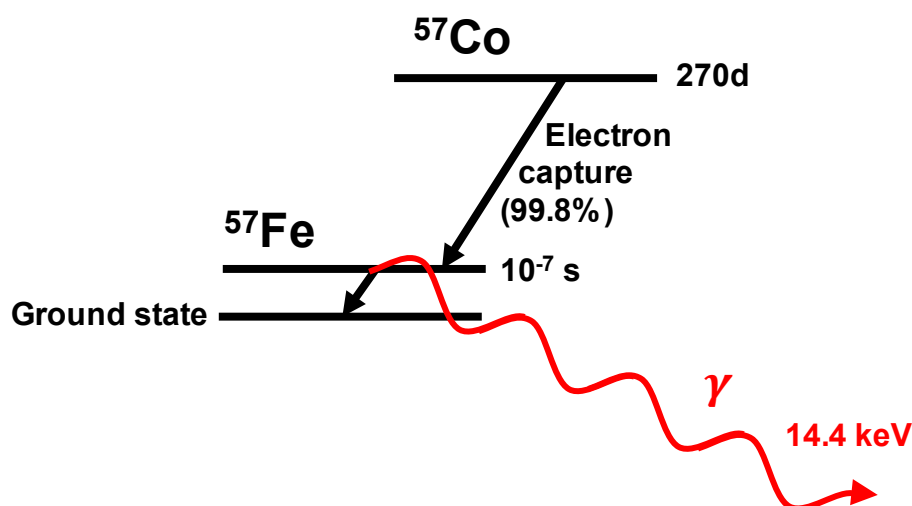


Figure 3.7.A – Simplified diagram showing ^{57}Co undergoing electron capture, and de-excitation of ^{57}Fe to emit a characteristic 14.4 keV gamma ray.

To maximise the signal-noise ratio for spectroscopic data, the doppler effect is employed by continually oscillating either the source, sample, or detector. A WissEL Mössbauer spectroscope, with a ^{57}Co source in a Rh matrix was used, spectra were collected at ambient room temperature for dilute powder samples, targeting 10,000 counts between a velocity range of -5 to $+5$ mm s^{-1} . An α -iron foil was used as the calibration standard and a scan of the standard was performed before each sample run. Fitting was achieved using the Recoil software suite was used to fit paramagnetic Lorentzian doublets [10].

3.8 Scanning electron microscopy and energy-dispersive X-ray spectroscopy

Scanning Electron Microscopy (SEM) is a high-resolution imaging method that instead of using visible light as in optical microscopes, which is limited by the wavelength of light, uses magnetic lenses to raster electrons across a sample surface. The wavelength of the incident electrons, generated from an electron gun, is 4 – 5 orders of magnitude smaller than that of visible light (e.g., 4×10^2 nm for visible violet light and 4×10^{-3} nm for an electron beam). The interactions between the higher energy electrons and the atoms of the sample can cause elastic scattering (scattering instances where the electrons penetrate several hundred nm into the material and are deflected back out to the sample surface for detection), which when detected by the microscope are used to generate an image. The use of this effect is known as Back-Scattered Electron imaging (BSE). The immediate and local atomic numbers of the sample atoms influence the degree of electron scattering, this is used to give a so called ‘Z contrast’ in a BSE image.

With an increased accelerating voltage, the beam of electrons can penetrate further into the sample surface. At about 15kV, the electrons have enough energy to excite the electrons of the innermost shells of sample atoms (K, L or M shells). This excitation, followed by a de-excitation, releases energy in the form of characteristic X-rays allowing for elemental chemical analysis. This technique is known as Energy-Dispersive X-ray spectroscopy (EDX), and compositional images can be generated when the high energy beam is rastered across the surface. However, these extremely sensitive, electron-based imaging methods necessitate specific sample preparation, so that the surface is pristine and conductive. A non-conductive sample will lead to charge-up of electrons, which can cause image artefacts and damage the sample/instrument.

3.8.1 Sample preparation

Flat faces and fracture surfaces of monolithic samples were cold-mounted using an EpoxiCure-2 (Buehler) resin-hardener mix in a 4:1 ratio. Where necessary, larger pellet and glass coupon samples were sectioned using an IsoMet Low Speed Saw (Buehler), fitted with a diamond blade submerged in IsoCut Fluid (Buehler) prior to cold-resin mounting. After 48 hours cure-time, the samples were demoulded and ground using gradually finer grade SiC papers (240-600 grit): 57, 48, 40, 35 and 26 μm grit. This was followed by polishing each sample with graded MetaDi (Buehler) monocrystalline diamond suspensions (6, 3 and 1 μm) with

individual polishing cloths. Samples were manually manipulated on an Automet Grinder-Polisher (Buehler) to reach a 1 μm final surface finish.

To make the mounted samples conductive, they were coated with an atomic-scale layer of carbon, using an Automatic Carbon Coater (Agar Scientific). The mounted samples were placed in a vacuum chamber, accompanied by sharpened graphite electrodes. After evacuating the chamber, a voltage was applied to the electrodes for 5 seconds, vaporising the graphite, depositing a thin carbon layer onto the sample surfaces. To ensure efficient conduction between the sample surface and SEM mounting stub, lines of Electrodag 1415 (Agar Scientific) conductive paint were applied to allow electrons to flow between the top and base of the sample.

3.8.2 SEM imaging and EDX analysis

Imaging was conducted using a Hitachi TM3030 bench-top SEM, fitted with a tungsten filament with a digitally controlled stage. Samples were secured on the SEM stub using a cross-strip of carbon tape, adjusting the stub height to ensure optimal working distance. Once under vacuum, a 15kV electron beam was used to generate images under the BSE setting. Micrographs were taken at low magnifications of $\times 80 - \times 250$ to provide an overview of a representative area of the sample (Note: higher magnifications were used for regions of interest). Elemental EDX analysis was performed using a Quantax 70 (Bruker) EDS system with a silicon drift detector. Scans of 600 seconds were conducted under 15kV and EDX modes, at lower magnification to permit semi-quantitative bulk analysis and review of phase distribution, and higher magnification for regions of interest. Spot analysis for phase identification was conducted using a high count-rate spot size with an average taken of five points on each phase, allowing for calculation of average composition. Due to poor detector performance for lighter elements ($Z < 11$) and oxygen ($Z = 8$), molar compositions are calculated from normalised ratios and oxide compositions.

3.9 Phase analysis of grayscale images

3.9.1 Introduction and manual method

Quantitative phase analysis is key to the development of glass ceramic nuclear wasteforms. In addition to presenting us with relative phase ratios, it can allow for inference of material properties as a sum of their constituent crystalline and glassy phases. Some of the most regularly implemented phase quantification techniques have centred around X-ray diffraction-based Rietveld and pattern refinement methods. While these can provide useful additional information on material structure and phase assemblage, there are some inherent limitations such as the necessity to use an internal standard to quantify amorphous phases. Moreover, many refinement techniques require a starting model and structural understanding of the material [11,12]. Micrographic image analysis is used in research areas such as cementitious materials, as it can be particularly well exploited to measure pore sizes efficiently and determine aggregate size distribution [13]. Quantitative phase analysis by electron micrograph thresholding across contrast regions has been reported in the literature [14], though in this example, the technique was facilitated by proprietary-hard-coded microscope software with limited flexibility and user parametrisation. The current work aims to provide an open-source, fast and lightweight image analysis tool to complement common characterisation techniques for glass ceramics.

3.9.2 Computer assisted processing methodology

The developmental stages of this methodology are outlined in the publication of a project research outputs, **Appendix 3**. The prototypical glass ceramic wasteform material used in this study was from a suite of sodium-iron-phosphate compositions. Base glass composition was doped with additions of alumina and silica to melts and loaded with cerium oxide as a redox active fluorite surrogate for spent fuel. The primary composition used for initial tests consisted of component oxides and ammonium dihydrogen phosphate, loaded with 34 mol.% CeO₂ and melted at 1250 °C before casting and annealing for 4 hours at 550 °C, henceforth, identified as IPSAS 34 mol.% CeO₂, 1250 °C. Glass ceramic monolithic samples were sectioned, cold resin mounted and polished to a 1 µm mirror finish and carbon coated to reduce surface charge. BSE images were collected using a Hitachi TM3030 instrument, as described in **Section 3.8.2**. Concurrent analysis by pXRD and EDX allowed for confirmation of phase assemblage. Image acquisition parameters were set to medium brightness and high contrast, with fine adjustments made, per sample, to maximise the contrast in grey values between the individual phases. The

phase proportions can be delineated, as delimited by regions with different grey values, or BSE contrast, a factor influenced by the atomic number of the species in each phase. The free, open-source image processing software ImageJ, was used as a base platform in the Fiji package [15]. The package utilises JavaScript-based functions and macros to assist with automation of various post-processing tasks. This work resulted in coding of a script, see **Appendix 4**, which will facilitate a quantitative-phase analysis methodology. An initial routine uses sample surface BSE images collected at a range of magnifications to measure particle size to pixel count ratios and smallest-feature statistics. The routine is followed by selection of an optimum magnification, such that small crystallites ($> 5 \mu\text{m}$) are properly resolved. A low-magnification broad micrograph of the material surface was collected, allowing overlay of a coordinate grid, a pseudo-random number generator was then used to select cells of the grid in order to collect sample micrographs at the desired magnification, **Figure 3.9.2.A**.

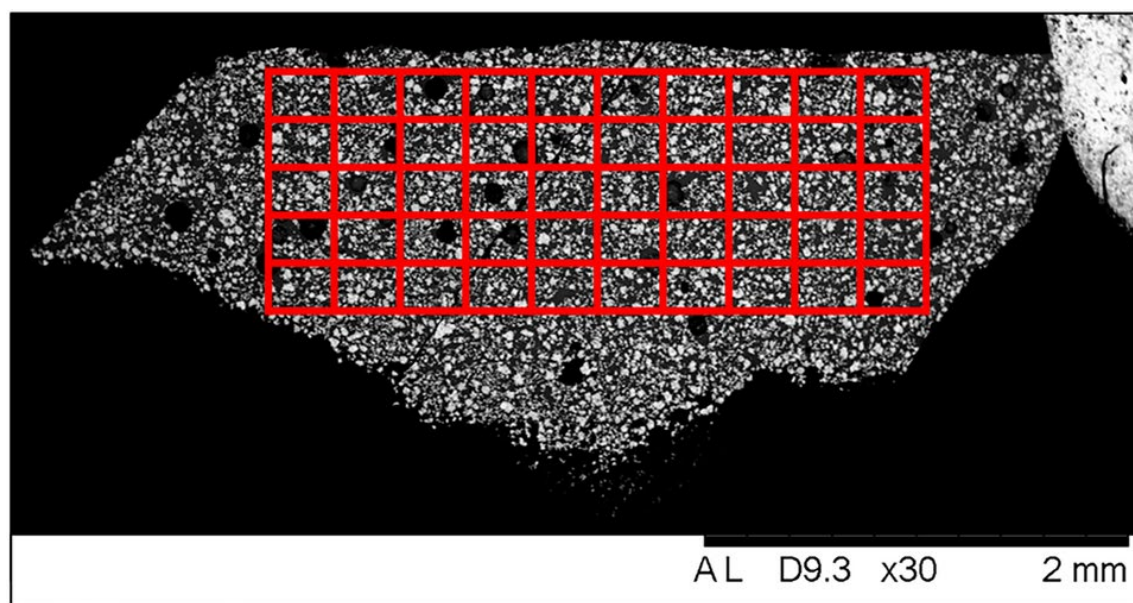


Figure 3.9.2.A - Broad-overview BSE of IPSAS 34 mol.% CeO₂, 1250 °C, with coordinate grid overlay

During following stages of the code development, image-scale calibration was unnecessary, as phase quantities were determined by ratio of pixel counts. The script analyses a histogram of grey values represented in the sample BSE, then calculating the points at which minima of intensity can be found. The peak intensities between such points were then used to represent the discrete phases, the areas for which were determined by thresholding between

pairs of minima and counting the number of pixels remaining, **Figure 3.9.2.B (a)**. Ratios of these areas were then used to infer relative phase quantities.

Following the processing of a first image, the remaining image set from a sample can be quickly processed to strengthen the measurement statistics. The user is given option to manually exclude mis-identified phases such as mounting material or pores, see **Figure 3.9.2.B (b)**, and can also generate a representative figure to accompany phase quantity statistics for publication. The version of the script, Phase Analysis of Grayscale ImagesS (PAGIS) supplied with this thesis can delineate 2–6 individual phases.

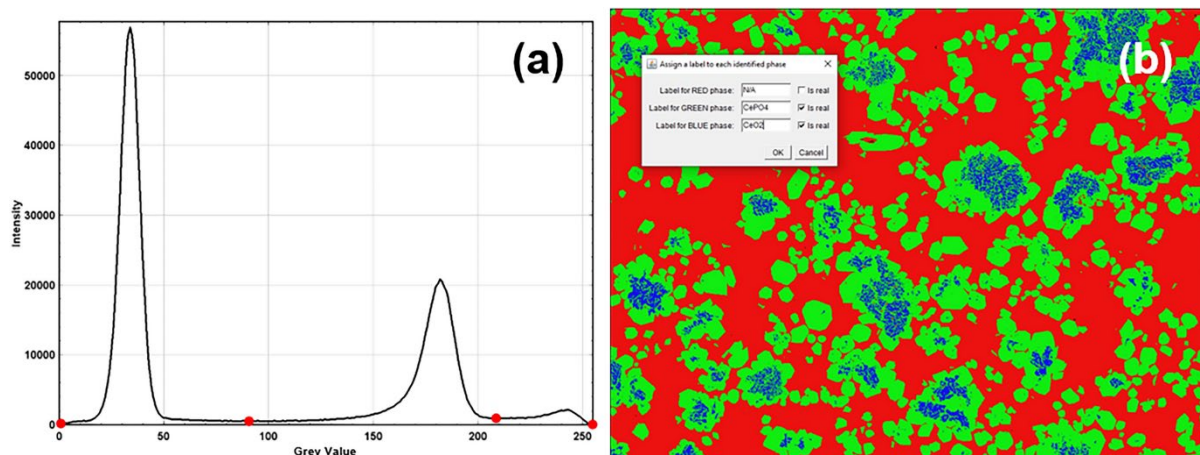


Figure 3.9.2.B - (a) Grey value histogram for IPSAS 40 wt% CeO₂, 1250 °C, (b) phase labelling and exclusion

3.10 Product consistency testing

Product consistency testing (PCT) is an American Society for Testing and Materials standard method to assess aqueous chemical durability of solid samples under accelerated laboratory conditions. Particulate material is sealed in a container with a solution and allowed to react over a defined period before the post-dissolution material and aliquots of solution can be studied. The PCT-B methodology [16], was used in line with standard short-medium term durability assessment, and to allow for comparison with literature studies.

3.10.1 PCT-B

Samples were pulverised using a large manual percussion mortar and sieved to retain a particle size fraction of between 75 – 150 μm . The resulting powder was thoroughly washed using several litres of propan-2-ol and an ultrasonic bath. The durability study was undertaken using approximately 1 g of powder with 9 mL of UHQ water as a leachate, to yield a powder - solution SA/V value of 1200 m^{-1} .

As the analysis techniques used for leachate analysis are highly sensitive to compositional contaminants in the ppb-ppt (parts per billion or trillion) range, an intensive cleaning regime was necessary to adequately prepare the test vessels. 15 mL PTFE (Teflon) pots were rinsed initially with de-ionised water, before soaking in a 1% DECON 90 solution (KOH, decon[®]) for 16 hours. The vessels were then rinsed twice with de-ionised water to remove the residual DECON 90 solution, before soaking in a 1% HNO_3 (ACS 70%) solution made with UHQ (ultra high quality, 18.2 M Ω) water for a further 16 hours. Three further rinses with UHQ water were carried out before each pot was loaded with approximately 10-12 mL of UHQ water, sealed and weighed. The loaded pots were then each weighed before holding in an oven at 90 °C for 16 hours. After removal and cooling, vessels were re-weighed, and masses compared against initial data to evaluate the seal quality and retention of solution – pots with > 5% evaporative losses were removed from service. The final confirmation of the cleaning process was the use of pH indicator paper to validate the solution as being within a relatively neutral pH of 5 – 7. Three sample pots and two blanks (pots with water, but no sample) for each time duration (1, 3, 7, 14, 21 and 28 days) were held at 90 °C in an oven to accelerate any chemical alteration. The blank samples provide a control to register any contamination associated with vessel degradation and leachate preparation, while triplication allows for calculation of average and assessment of experimental error. Sub-samples of the solutions were taken at each time-point, passed through a 0.2 μm mesh syringe filter before

measuring with a pH meter (Mettler Toledo). Ionic species were kept in solution by acidification with HNO₃ (VWR 67-69%).

3.10.2 ICP-OES and post dissolution particle analysis

Solution aliquots were analysed by ICP-OES (inductively coupled plasma with optical emission spectroscopy) using a Thermo Fisher iCAPDuo 6300. Measurements of Cs content were also carried out by ion chromatography (Thermo Scientific ICS 1100).

Powder samples from some time points, especially day 28 at the end of the studies, were further characterised, first by pXRD, see **Section 3.3.1** and an assessment of morphology, alteration layers and local chemical composition was conducted using SEM / EDX, see **Section 3.8.2**.

Chapter 3 References

- [1] M.C. Stennett, C.L. Corkhill, L.A. Marshall, N.C. Hyatt, Preparation, characterisation and dissolution of a CeO₂ analogue for UO₂ nuclear fuel, *J. Nucl. Mater.* 432 (2013) 182–188. <https://doi.org/10.1016/J.JNUCMAT.2012.07.038>.
- [2] L.C. Harnett, L.J. Gardner, S.-K. Sun, C. Mann, N.C. Hyatt, Reactive spark plasma sintering of Cs-exchanged chabazite: characterisation and durability assessment for Fukushima Daiichi NPP clean-up, *J. Nucl. Sci. Technol.* (2019) 1–11. <https://doi.org/10.1080/00223131.2019.1602484>.
- [3] H. Klug, L. Alexander, *X-ray Diffraction Procedures: For Polycrystalline and Amorphous Materials*, 2nd Edition, 1974. <https://doi.org/https://doi.org/10.1002/xrs.1300040415>.
- [4] B. Ravel, M. Newville, ATHENA, ARTEMIS, HEPHAESTUS: Data analysis for X-ray absorption spectroscopy using IFEFFIT, *J. Synchrotron Radiat.* 12 (2005) 537–541. <https://doi.org/10.1107/S0909049505012719>.
- [5] K. Mathew, C. Zheng, D. Winston, C. Chen, A. Dozier, J.J. Rehr, S.P. Ong, K.A. Persson, Data descriptor: High-throughput computational X-ray absorption spectroscopy, *Sci. Data.* 5 (2018). <https://doi.org/10.1038/SDATA.2018.151>.
- [6] B.H. Toby, CMPR – a powder diffraction toolkit, *J. Appl. Crystallogr.* 38 (2005) 1040–1041. <https://doi.org/10.1107/S0021889805030232>.
- [7] S. Calvin, XAFS For Everyone, 2013. <https://doi.org/10.1201/b14843>.
- [8] M. Wilke, F. Farges, P.E. Petit, G.E. Brown, F. Martin, Oxidation state and coordination of Fe in minerals: An Fe K-XANES spectroscopic study, *Am. Mineral.* 86 (2001) 714–730. <https://doi.org/10.2138/am-2001-5-612>.
- [9] Y. Yoshida, G. Langouche, eds., *Mössbauer Spectroscopy*, Springer Berlin Heidelberg, Berlin, Heidelberg, 2013. <https://doi.org/10.1007/978-3-642-32220-4>.
- [10] P.A. Bingham, R.J. Hand, S.D. Forder, Doping of iron phosphate glasses with Al₂O₃, SiO₂ or B₂O₃ for improved thermal stability, *Mater. Res. Bull.* 41 (2006) 1622–1630. <https://doi.org/10.1016/J.MATERRESBULL.2006.02.029>.
- [11] X. Orlhac, C. Fillet, P. Deniard, A.M. Dulac, R. Brec, Determination of the crystallized fractions of a largely amorphous multiphase material by the Rietveld method, *J. Appl. Crystallogr.* 34 (2001) 114–118. <https://doi.org/10.1107/S0021889800017908>.
- [12] S. Kemethmüller, A. Roosen, F. Goetz-Neunhoeffler, J. Neubauer, Quantitative analysis of crystalline and amorphous phases in glass-ceramic composites like LTCC by the rietveld method, *J. Am. Ceram. Soc.* 89 (2006) 2632–2637. <https://doi.org/10.1111/j.1551-2916.2006.01113.x>.
- [13] M.A. Saghiri, H. Kazerani, S.M. Morgano, J.L. Gutmann, Evaluation of mechanical activation and chemical synthesis for particle size modification of white mineral trioxide aggregate, *Eur. Endod. J.* 5 (2020) 128–133. <https://doi.org/10.14744/EEJ.2020.84803>.

- [14] J. Crum, V. Maio, J. McCloy, C. Scott, B. Riley, B. Benefiel, J. Vienna, K. Archibald, C. Rodriguez, V. Rutledge, Z. Zhu, J. Ryan, M. Olszta, Cold crucible induction melter studies for making glass ceramic waste forms: A feasibility assessment, *J. Nucl. Mater.* 444 (2014) 481–492. <https://doi.org/10.1016/J.JNUCMAT.2013.10.029>.
- [15] J. Schindelin, I. Arganda-Carreras, E. Frise, V. Kaynig, M. Longair, T. Pietzsch, S. Preibisch, C. Rueden, S. Saalfeld, B. Schmid, J.Y. Tinevez, D.J. White, V. Hartenstein, K. Eliceiri, P. Tomancak, A. Cardona, Fiji: An open-source platform for biological-image analysis, *Nat. Methods.* 9 (2012) 676–682. <https://doi.org/10.1038/NMETH.2019>.
- [16] ASTM, Standard Test Methods for Determining Chemical Durability of Nuclear, Hazardous, and Mixed Waste Glasses and Multiphase Glass Ceramics: The Product Consistency Test (PCT), (2014). <https://compass.astm.org/document/?contentCode=ASTM%7CC1285-21%7Cen-US>.

4. Sodium Iron Phosphate Glass- Ceramics

Summary

A series of glass and ceramic type host systems have been investigated for potential conditioning of disposition of high loading streams, with some chemical flexibility for incorporation of iron-rich calcines arising from total dissolution or oxide separation of nuclear fuel. A base sodium iron phosphate composition was studied with addition of fluorite structured CeO_2 as a fuel simulant. Materials were synthesised within a matrix of melting temperatures and fuel simulant loading, to allow for the study of phase formation. A set of secondary compositions were synthesised with additions of Al_2O_3 and SiO_2 to the glass batch, in an effort to passivate the aggressive nature of phosphate glass melts. Samples were characterised for phase assemblage and composition by powder X-ray diffraction and electron microscopy; cerium monazite, $\text{Ce}(\text{PO}_4)$ was the primary crystalline phase at high loadings. An investigation of iron valence and local structure was carried out by Mössbauer spectroscopy and X-ray absorption spectroscopy, with the iron redox behaviour trending slightly, resulting in wasteforms containing more Fe(III) than Fe(II). Some evaluation of chemical durability was undertaken with a series of PCT-B tests conducted for a selection of the produced phosphate materials, allowing for assessment of dissolution behaviour for the two base compositional variants.

4.1 Iron-rich orphan nuclear materials

Though undamaged stainless-steel clad fuel pins are routinely being separated from the graphite sleeves and transferred into slotted cans at the Sellafield Fuel Handling Plant (FHP), ThORP reprocessing of this fuel is no longer possible with the termination of such activities. The state of much of the legacy damaged AGR, WAGR and DFR breeder residual orphan materials preclude separation and fuel pin disassembly prior to disposal. Further arisings of iron-rich spent fuel feeds are also likely, following longer than design-life storage of AGR fuel following de-fuelling and decommissioning activities, with the last UK AGR reactors scheduled to be shut down for the final time in 2028 [1]. Much of these materials have already degraded to a point where they have required re-packaging, although no long-term storage or disposal assignment has been made at the time of writing. With no further operation of Magnox type reactors or production of Magnox fuels, following the final campaigns of Magnox reprocessing, stainless steel-clad orphan materials are likely to become one of the larger components of the UK orphan nuclear material inventory (encompassing WAGR, AGR, DFR breeder and PFR MOx materials). If a thermal treatment method is established for damaged and legacy steel containing fuel and orphan streams, it may provide an alternative option to direct disposal of the future inventory of un-damaged AGR spent fuel. Dismantling of fuel pins has historically been somewhat routine in the UK, with well understood engineering and technological complexity [2]. All such activities would still need to be undertaken via remote operation in a hot-cell facility, due to the activity of long-lived fission product radionuclides. Unfortunately, with the shutdown of all reprocessing operations, nuclear workforce attrition is likely in this specialisation, which may also give rise to future difficulties de-cladding fuel. Use of total acid dissolution of the damaged nuclear material, including cladding, is likely to produce the most homogeneous waste feed, when compared with mechanical size reduction. With some mechanism of drying and calcination, such as employment of a rotary calciner, a pre-processed solid waste feed rich in uranium and iron can be produced.

When considering vitrification as a thermal treatment for such a stream, borosilicate compositions do not typically have good actinide loading capabilities, which would drive a large increase in waste volume. Phosphate based glass compositions have been developed with greater solubility for actinides such as uranium, though hydrolytic durability of P – O – P bonds is poor. Addition of iron to a base phosphate glass has been demonstrated to replace some of these bonds for P – O – Fe(II/III) bonds, significantly improving the chemical durability of the material [3,4]. Phosphate glasses can have quite aggressive melting characteristics and have been shown to corrode crucible materials and melter components, even over short glass-making campaigns [5], so further glass batch additions should be considered to help improve thermal stability of glass-melts, prolong melter lifetime, and reduce more hazardous melt-foaming characteristics.

4.2 Base compositions and additions

4.2.1 Sodium iron phosphate (SIP)

The addition of sodium, while a network modifier, to phosphate and iron phosphate glasses is one such avenue that has been demonstrated to improve thermal stability of glass as well as contributing to enhanced dissolution resistance and was further investigated here [6,7]. All batching reagents used were from Alfa Aesar stock, with stated purities and molar composition for the base sodium iron phosphate (SIP). Batching ratios were calculated with respect to oxide equivalents for each reagent in the following base ratio: 59 mol.% P_2O_5 , 30 mol.% Fe_2O_3 and 11 mol.% Na_2O , as indicated by the 0 mol.% simulant loaded compositions listed in **Table 4.2.A**. The batch chemicals were ammonium dihydrogen phosphate, $NH_4H_2PO_4$ (98%); iron oxide, Fe_2O_3 (95%); sodium carbonate, Na_2CO_3 (98%). This base composition was selected following a review of basic sodium iron phosphate glasses, with similar compositions indicating potential for high loading of actinides, retained favourably during chemical durability studies [8–10]. Ceria, CeO_2 (99.5%) additions were used as an inactive trial simulant for UO_2 , prior to demonstration through active trials. Ceria shares a fluorite structure with UO_2 , as well as a large cationic radius and it has been demonstrated to behave as an active redox couple in surrogate nuclear waste forms [11,12]. It should however be noted that the redox behaviour of cerium is not directly analogous to that of uranium, while cerium forms Ce(III) and Ce(IV), uranium will typically speciate to U(IV), U(V) or U(VI) [12]. In addition, the relative density of ceria is 30% lower than its uranium counterpart, which is likely to lead to slightly different melt characteristics. These features should be considered when interpreting redox analyses and equivalency for predicting the behaviour of uranium bearing compositions. The density discrepancy may have a lesser effect due to significant self-stirring effects and bubbling caused by ammonia evolution during early stages of the melting process. Additions of this surrogate fuel were made to the pre-batched base SIP composition, up to 45 mol.%.

4.2.2 Sodium iron phosphate with Al and Si (IPSAS)

Additional studies have also indicated improved melt stability and refractory lifetime with silica and alumina additions to phosphate glass melts [8,9]. Work conducted on a similar base glass also parametrised the addition of Al_2O_3 , SiO_2 and B_2O_3 , with findings indicating that such oxides have a significant advantage with respect to thermal characteristics listed from most impactful to least impactful. However, this was not without sacrifice to glass formability and melt solubility [13]. Further work with cursory dissolution profiling of a metaphosphate base glass that contained large alumina additions has shown no significant impact on the chemical durability, as compared to reference iron phosphates [14]. As such, a trial with small alumina and silica additions, to passivate

melt characteristics, assess any change in simulant fuel solubility, and to permit determination of the initial chemical durability with reference to the SIP base compositions. Again, batching reagents used were from Alfa Aesar stock, with stated purities and molar composition for the base iron phosphate sodium aluminosilicate (IPSAS). Batching ratios were calculated with respect to oxide equivalents for each reagent in the following base ratio: 61 mol.% P_2O_5 , 18 mol.% Fe_2O_3 , 9 mol.% Na_2O , 8 mol.% SiO_2 and 4 mol.% Al_2O_3 , see **Table 4.2.A** for IPSAS batched compositions and synthesis conditions. In addition to the reagents as used for SIP base materials, Alfa SiO_2 (99%) and Al_2O_3 (99%) were used. To allow for near comparisons with SIP samples, IPSAS compositions were batched for loadings of up to 43 mol.% ceria simulant waste.

Table 4.2.A - Batch compositions for samples synthesised to molar ratios, measured bulk average EDX compositions, including glass and crystalline phases, are in brackets. Compositions are tabulated against melt temperature, average density by Archimedes measurement and crystalline phases as detected via powder X-ray diffraction. All measurements were conducted with samples annealed at 550 °C.

*Decreases attributed to foaming and slag incorporation. [†]pXRD crystalline phases: monazite, ceria, NFP = sodium iron phosphate. ^{††}majority amorphous with too few minor Bragg peaks to identify.

Sample ID	Batched and (Measured EDX) Composition by Oxides ± 1.0 (mol.%)						Temperature Melt (°C)	Average Density (g cm ⁻³)	XRD Crystalline Phases [†]
	P ₂ O ₅	Fe ₂ O ₃	Na ₂ O	SiO ₂	Al ₂ O ₃	CeO ₂			
SIP_0_1250	58.5 (55.0)	30.3 (23.9)	11.2 (15.6)	0.0 (0.9)	0.0 (4.5)	0.0 (0.0)	1250	2.970 \pm 0.013	amorphous
SIP_4_1250	56.1 (56.7)	29.1 (22.2)	10.7 (13.7)	0.0 (1.0)	0.0 (4.8)	4.1 (1.8)	1250	3.010 \pm 0.011	amorphous
SIP_8_1250	53.7 (53.8)	27.8 (25.5)	10.2 (12.4)	0.0 (0.8)	0.0 (3.8)	8.2 (3.7)	1250	3.180 \pm 0.009	amorphous ^{††}
SIP_16_1250	48.7 (52.0)	25.3 (25.6)	9.3 (13.6)	0.0 (0.9)	0.0 (3.4)	16.7 (4.5)	1250	3.160 \pm 0.024	monazite
SIP_25_1250	43.5 (48.0)	22.6 (28.1)	8.3 (10.2)	0.0 (0.5)	0.0 (2.3)	25.6 (10.9)	1250	3.610 \pm 0.021	monazite, ceria, NFP
SIP_35_1250	38.1 (45.3)	19.7 (19.4)	7.3 (10.6)	0.0 (0.8)	0.0 (2.3)	34.9 (21.7)	1250	3.290 \pm 0.010	monazite, ceria, NFP
SIP_45_1250	32.4 (41.3)	16.8 (18.2)	6.2 (11.1)	0.0 (0.8)	0.0 (0.2)	44.6 (28.4)	1250	3.410 \pm 0.013	monazite, ceria, NFP

SIP_0_1350	58.5 (51.0)	30.3 (28.9)	11.2 (11.1)	0.0 (0.6)	0.0 (8.3)	0.0 (0.0)	1350	2.870 \pm 0.019	amorphous
SIP_4_1350	56.1 (53.5)	29.1 (25.5)	10.7 (9.6)	0.0 (1.2)	0.0 (8.4)	4.1 (1.7)	1350	2.968 \pm 0.033	amorphous
SIP_8_1350	53.7 (51.8)	27.8 (26.2)	10.2 (10.0)	0.0 (1.2)	0.0 (7.5)	8.2 (3.3)	1350	3.078 \pm 0.013	amorphous ^{††}
SIP_16_1350	48.7 (49.3)	25.3 (27.0)	9.3 (11.0)	0.0 (1.4)	0.0 (6.6)	16.7 (4.6)	1350	3.144 \pm 0.009	monazite, NFP
SIP_25_1350	43.5 (47.9)	22.6 (27.1)	8.3 (11.6)	0.0 (0.8)	0.0 (6.1)	25.6 (6.5)	1350	3.180 \pm 0.036	monazite, ceria, NFP
SIP_35_1350	38.1 (42.8)	19.7 (29.7)	7.3 (12.4)	0.0 (0.7)	0.0 (6.2)	34.9 (8.2)	1350	3.236 \pm 0.027	monazite, ceria, NFP
SIP_45_1350	32.4 (38.2)	16.8 (15.3)	6.2 (10.8)	0.0 (9.1)	0.0 (9.1)	44.6 (17.5)	1350	2.523 \pm 0.026	monazite, ceria, NFP

Sample ID	Batch and (Measured EDX) Composition by Oxides ± 1.0 (mol.%)						Temperature Melt ($^{\circ}\text{C}$)	Average Density (g cm^{-3})	XRD Crystalline Phases [†]
	P ₂ O ₅	Fe ₂ O ₃	Na ₂ O	SiO ₂	Al ₂ O ₃	CeO ₂			
SIP_0_1450	58.5 (52.0)	30.3 (26.3)	11.2 (9.7)	0.0 (1.3)	0.0 (10.7)	0.0 (0.0)	1450	2.880 \pm 0.032	amorphous
SIP_4_1450	56.1 (50.6)	29.1 (25.4)	10.7 (11.2)	0.0 (1.5)	0.0 (9.4)	4.1 (1.9)	1450	3.085 \pm 0.007	monazite, NFP
SIP_8_1450	53.7 (48.7)	27.8 (29.2)	10.2 (8.9)	0.0 (0.9)	0.0 (8.1)	8.2 (4.2)	1450	3.153 \pm 0.011	monazite, NFP
SIP_16_1450	48.7 (46.4)	25.3 (27.8)	9.3 (9.3)	0.0 (0.9)	0.0 (8.7)	16.7 (6.8)	1450	3.253 \pm 0.008	monazite, ceria, NFP
SIP_25_1450	43.5 (46.2)	22.6 (26.9)	8.3 (9.5)	0.0 (1.5)	0.0 (8.7)	25.6 (7.2)	1450	3.388 \pm 0.019	monazite, ceria, NFP
SIP_35_1450	38.1 (33.5)	19.7 (21.9)	7.3 (9.4)	0.0 (1.0)	0.0 (25.0)	34.9 (9.2)	1450	3.494 \pm 0.009	monazite, ceria, NFP
SIP_45_1450	32.4 (38.0)	16.8 (14.6)	6.2 (9.9)	0.0 (1.0)	0.0 (10.0)	44.6 (26.5)	1450	3.406 \pm 0.012	monazite, ceria, NFP

IPSAS_0_1250	61.1 (55.7)	18.1 (19.7)	9.3 (10.0)	7.2 (8.1)	4.3 (6.6)	0.0 (0.0)	1250	2.790 \pm 0.017	amorphous
IPSAS_4_1250	58.8 (57.7)	17.4 (17.3)	9.0 (9.4)	6.9 (7.4)	4.1 (6.3)	3.8 (1.9)	1250	2.840 \pm 0.021	amorphous
IPSAS_8_1250	56.4 (54.5)	16.7 (16.9)	8.6 (10.2)	6.7 (7.8)	3.9 (6.1)	7.7 (4.4)	1250	2.930 \pm 2.928	amorphous
IPSAS_16_1250	51.4 (56.2)	15.2 (13.3)	7.8 (9.2)	6.1 (8.2)	3.6 (5.6)	15.9 (7.5)	1250	3.150 \pm 0.046	amorphous ^{††}
IPSAS_25_1250	46.1 (50.1)	13.7 (16.2)	7.0 (9.3)	5.5 (7.1)	3.2 (9.6)	24.5 (7.6)	1250	3.380 \pm 0.006	monazite, ceria
IPSAS_34_1250	40.6 (50.4)	12.0 (14.4)	6.2 (9.2)	4.8 (7.4)	2.8 (4.5)	33.5 (14.1)	1250	3.400 \pm 0.028	monazite, ceria, NFP
IPSAS_43_1250	34.8 (44.9)	10.3 (14.6)	5.3 (11.1)	4.1 (6.5)	2.4 (3.9)	43.0 (19.0)	1250	2.840 \pm 0.022	monazite, ceria, NFP

Sample ID	Batch and (Measured EDX) Composition by Oxides ± 1.0 (mol.%)						Temperature Melt ($^{\circ}\text{C}$)	Average Density (g cm^{-3})	XRD Crystalline Phases [†]
	P ₂ O ₅	Fe ₂ O ₃	Na ₂ O	SiO ₂	Al ₂ O ₃	CeO ₂			
IPSAS_0_1350	61.1 (53.0)	18.1 (18.3)	9.3 (7.9)	7.2 (8.0)	4.3 (12.7)	0.0 (0.0)	1350	2.752 \pm 0.006	amorphous
IPSAS_4_1350	58.8 (55.3)	17.4 (15.7)	9.0 (7.9)	6.9 (7.3)	4.1 (12.2)	3.8 (1.6)	1350	2.930 \pm 0.039	amorphous
IPSAS_8_1350	56.4 (52.9)	16.7 (17.0)	8.6 (8.7)	6.7 (7.9)	3.9 (9.7)	7.7 (3.9)	1350	2.965 \pm 0.006	amorphous
IPSAS_16_1350	51.4 (51.9)	15.2 (15.4)	7.8 (9.0)	6.1 (7.5)	3.6 (8.8)	15.9 (7.3)	1350	3.121 \pm 0.010	amorphous
IPSAS_25_1350	46.1 (48.7)	13.7 (15.3)	7.0 (8.9)	5.5 (7.2)	3.2 (8.6)	24.5 (11.3)	1350	3.280 \pm 0.012	monazite, ceria
IPSAS_34_1350	40.6 (48.2)	12.0 (14.2)	6.2 (9.4)	4.8 (7.4)	2.8 (8.0)	33.5 (12.9)	1350	3.372 \pm 0.020	monazite, ceria, NFP
IPSAS_43_1350	34.8 (37.5)	10.3 (15.3)	5.3 (11.1)	4.1 (9.2)	2.4 (9.2)	43.0 (17.7)	1350	2.683 \pm 0.048	monazite, ceria, NFP

IPSAS_0_1450	61.1 (53.8)	18.1 (14.9)	9.3 (8.1)	7.2 (8.0)	4.3 (15.2)	0.0 (0.0)	1450	2.737 \pm 0.011	amorphous
IPSAS_4_1450	58.8 (52.3)	17.4 (14.9)	9.0 (9.4)	6.9 (8.3)	4.1 (13.0)	3.8 (2.1)	1450	2.858 \pm 0.007	amorphous
IPSAS_8_1450	56.4 (52.3)	16.7 (15.1)	8.6 (8.1)	6.7 (7.5)	3.9 (13.7)	7.7 (3.3)	1450	2.843 \pm 0.041	amorphous
IPSAS_16_1450	51.4 (50.0)	15.2 (14.7)	7.8 (8.9)	6.1 (7.5)	3.6 (11.0)	15.9 (8.0)	1450	3.095 \pm 0.006	monazite, NFP
IPSAS_25_1450	46.1 (50.1)	13.7 (17.5)	7.0 (8.2)	5.5 (8.0)	3.2 (8.3)	24.5 (7.9)	1450	3.279 \pm 0.044	monazite
IPSAS_34_1450	40.6 (42.9)	12.0 (15.7)	6.2 (9.4)	4.8 (9.5)	2.8 (10.6)	33.5 (11.9)	1450	3.345 \pm 0.014	monazite, NFP
IPSAS_43_1450	34.8 (41.1)	10.3 (14.2)	5.3 (7.6)	4.1 (7.7)	2.4 (5.3)	43.0 (24.1)	1450	2.779 \pm 0.012	monazite, ceria, NFP

4.3 Synthesis

4.3.1 Glass batching

Hygroscopic reagents were dried overnight at up to 180 °C to reduce the moisture content of batch constituents prior to weighing. With the base compositions batched to the SIP or IPSAS base molar ratios, simulant loaded samples were prepared with further addition of ceria powder, as a relative molar addition up to 45 mol.%. Following addition of each reagent to a container, the mixture was manually stirred and homogenised. Batching was performed immediately prior to calcination, decomposition pre-melting and glass melt steps, in order to avoid any detrimental reactions with moist atmosphere. Batch sizes started at 10 g target glass for broad matrix compositions, up to 100 g for chemical durability frits and casting of fluorescence measurement monoliths.

4.3.2 Cursory melts and thermal analysis

A small series of base sodium iron phosphate glass melts were melted in mullite crucibles in an air atmosphere chamber furnace, for 1 hour at 1250 °C, before casting was attempted. It was found that for the SIP base glass melt, the immediate ramp to temperature at 5 °C per minute caused excessive foaming over the crucible edges, into secondary containment, and there was significant degradation of crucible walls which led to failure during attempted casting. Even with pre-heated casting plates and moulds, successfully cast coupons would crack and shatter if they were not loaded into an annealing oven within 30 seconds of casting. It was also noted that under the initially proposed melting conditions, solubility for simulant fuel at higher loadings was poor in both SIP and IPSAS glass melts, with cast products containing unincorporated reagents and slag.

Fundamental thermal analyses of base glasses were conducted under argon atmosphere, samples of pre-cast base glass frit were ramped through the transition temperatures, up to 1350 °C. DTA data were calculated as a first derivative and normalised to the region of interest, before an exponential smoothing function was applied to minimise the interference of thermocouple noise. Both SIP and IPSAS base glasses demonstrated DTA endothermic minima after the onset of T_g , and exothermic peaks at T_c , **Figure 4.3.A**. With T_g onset occurring at approximately 467 °C for SIP glass, it was noted as being lower than typical glasses in the range of 480 – 550 °C for iron phosphate and sodium iron phosphate glass ceramic compositions [15–17]. However, the IPSAS exhibited a higher T_g onset at 490 °C, with this difference attributed to the intentional addition of alumina and silica refractory oxides in the batch. An annealing temperature was proposed as 550 °C, which while above the transition of base glasses, was likely to be in the realm of transition points for the higher loaded glasses. If the annealing temperature was too low, there may have been some unwanted crystallisation. Slow cooling was employed to allow flexibility for higher simulant-loaded melt compositions with greater T_g , as would be expected for waste loaded glass. Further modifications to the thermal treatment schedule were made following this.

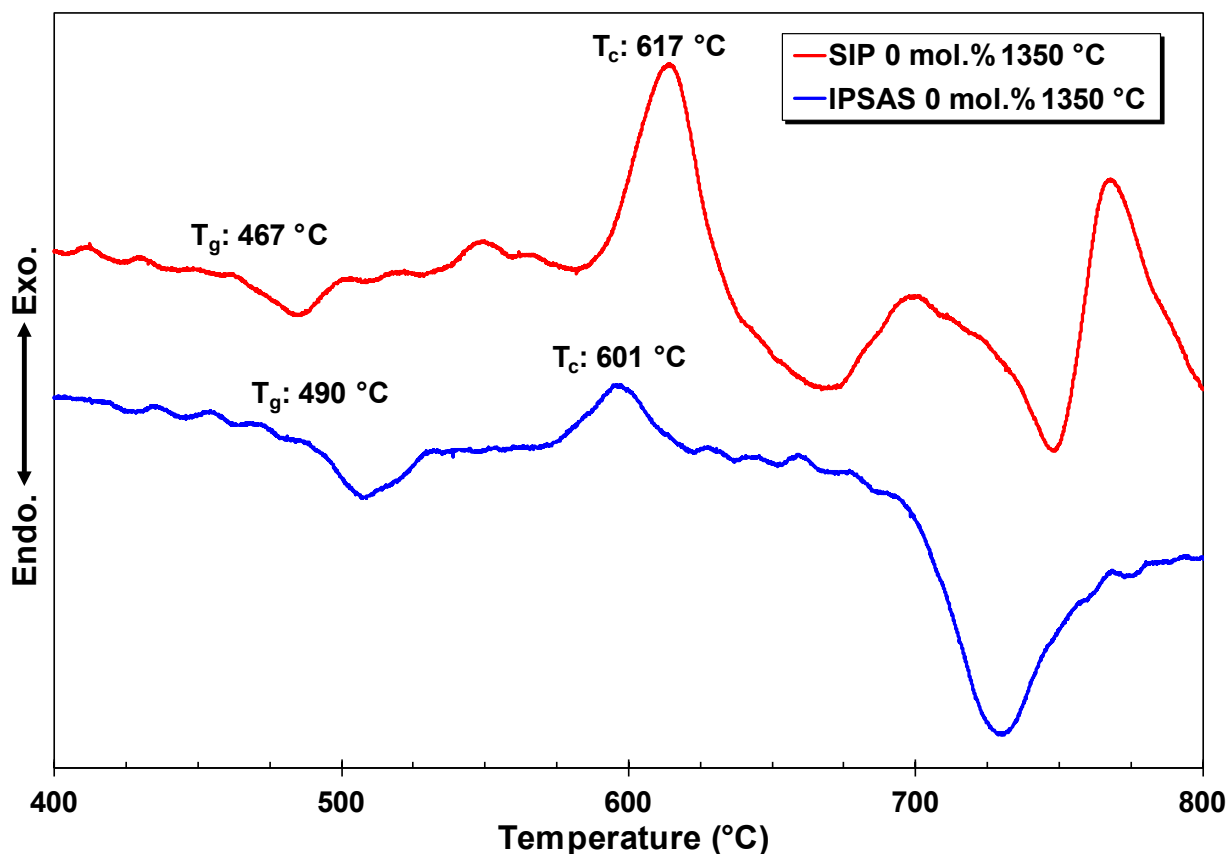


Figure 4.3.A – Differential thermal analysis traces of unloaded SIP and IPSAS base glass frits, with glass transition onsets, T_g , and crystallisation temperatures, T_c , marked. DTA was collected at a ramp rate of 5 °C min^{-1} under flowing argon.

4.3.3 Glass melt with cast and anneal

Pre-calcined alumina crucibles were used for the remainder of the study, and all melts were allowed to dwell at 300 °C for 6 hours to allow for calcination and steady decomposition of the ammonium dihydrogen phosphate precursor. Following melts were carried out under air atmosphere in a chamber furnace, with melt temperatures held for 2 hours prior to casting. Melting temperatures of 1250 °C , 1350 °C and 1450 °C were selected to provide an additional thermal variable. Monoliths cast onto preheated steel plates were then loaded into an annealing furnace held at 550 °C for 4 hours before slow cooling through T_g to room temperature at 1 °C per minute . Under these conditions, the base glass compositions were found to be fully homogenous by pXRD.

4.3.4 Frit production for durability testing

Glass frit was prepared for chemical durability tests by pouring molten glass, immediately after removal from the melt furnace, into a double-contained steel bucket filled with water. Care was taken to reduce the pour height within safely outside the range of any evolved steam and the water. The water instantly quenched the glass droplets into fine beads and particles, though the buckets were left to cool completely for 30 minutes before further handling.

4.4 Glass melt observations

Melt viscosity during pouring increased significantly with higher simulant waste loadings, as is typical with substantial additions of refractory materials like ceria. In all melt series, with the exception of SIP 1450 °C compositions, melt behaviour followed a consistent trend of decreasing viscosity with increasing temperature. The highest simulant waste loaded melts exhibited evidence of foaming, with some annealed monoliths featuring a porous structure. At lower melt temperatures, some high loading samples featured a minor slag layer (adhered to the crucible or secondary containment). The SIP 1450 °C series experienced a substantial degree of foaming and produced aggressive melts, as such it was not possible to properly pour and cast the highest simulant loaded samples, so crucibles were moved from a furnace at melt temperature to an annealing furnace at 550 °C, as to act as a quench before allowing for an annealing period and slow cooling. These samples were mechanically recovered from crucibles following cooling.

4.5 Archimedes density and molar volume

The average monolith density of the glass or glass ceramic monoliths was determined via Archimedes measurements. As with melt viscosity, the density generally increases with ceria loading, however, this behaviour was not entirely linear, and all series exhibited a degree of decrease in measured densities at loadings above 34 - 45 mol.%, see **Figure 4.5.A**. The most marked decreases were found at 45 mol.% simulant loading of SIP melted at 1350 °C and for all of the IPSAS 43 mol.% loaded series. The general increase for all series was attributed to the increased incorporation of cerium, retention of some high density undigested ceria, CeO_2 , 7.19 g cm^{-3} and crystallisation of monazite, $\text{Ce(PO}_4\text{)}$ 5.21 g cm^{-3} [18,19]. However, the highest loadings under these conditions were extending far beyond the melt solubility limits, overcoming the lower relative additions of passivating alumina and silica to form more aggressive melts, in turn, generating porous materials with incorporated foam and slag. Inclusion of these intermediate slag phases and higher porosity drove the average Archimedes density down, such cases are marked with open symbols, **Figure 4.5.A**. The peak density for SIP series was 3.61 g cm^{-3} , 1250 °C melt loaded to 25 mol.% simulant and the peak for IPSAS series was 3.40 g cm^{-3} , 1250 °C melt loaded to 34 mol.% simulant. These values are in line with similar iron phosphate glasses featured in literature, such as a caesium oxide and barium oxide loaded composition, IPCs45Ba5 , with a density of 3.639 g cm^{-3} [17].

Molar volumes for the glass and glass-ceramic samples in the as-annealed condition, were calculated using the Archimedes density data and the molar mass found by bulk semi-quantitative EDX analysis, discussed further in **Section 4.7.1**. As these data are derived from EDX analysis, they are presented with a caveat here that due to poor detection of characteristic X-rays for

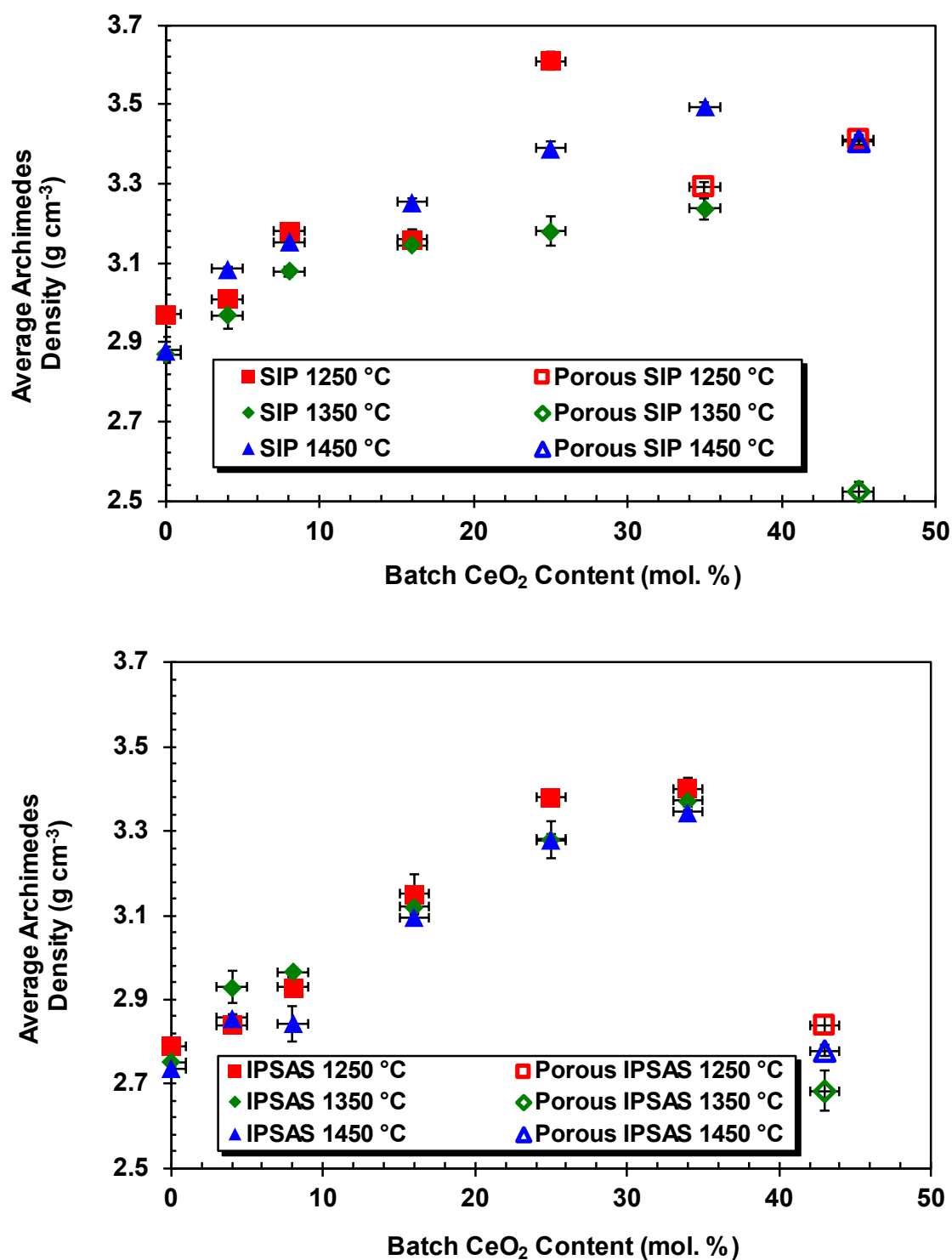


Figure 4.5.A – Plots of average density for monoliths as measured by Archimedes method, SIP compositions (top) and IPSAS compositions (bottom) respectively. Unfilled symbols indicate highly porous samples. Error bars may be obscured by datapoint symbols.

light elements ($Z < 11$), including oxygen, so any oxygen content was inferred using molar ratios of oxide forms for other detected elements, normalised to a sum of the remaining constituents. Furthermore, the methodology for determining average composition by EDX analysis is heavily dependent on selection of representative sampling locations on a monolithic surface, which was more prohibitive for highly porous samples. The combination of these factors and uncertainties led to a greater combined error and therefore calculated molar volume, as represented in **Figure 4.5.B**. In both compositional series SIP and IPSAS, it can be noted that the molar volume remains approximately consistent up to the onset of crystallisation at 16 – 25 mol.% simulant waste loading, with SIP melts converging between $70 - 85 \text{ cm}^3 \text{ mol}^{-1}$ and IPSAS melts within a range of $80 - 90 \text{ cm}^3 \text{ mol}^{-1}$. With higher simulant loadings at the onset of crystallisation and beyond, an approximately exponential upwards trend emerges, driven primarily by drop-off in sample densities with increased porosity, as marked by open symbols. With reference to data points before the development of significant porosity, the apparent trend was approximately linear, due to the bulk molar mass increasing at a faster rate than the increasing density. In the most pronounced example, the SIP 1250 °C melt series, the bulk molar mass was almost doubled from $210 - 400 \text{ g mol}^{-1}$ between simulant waste loadings of 0 – 45 mol.% CeO₂ respectively. Conversely, for the same series, the density only increases by approximately 15% from lowest to highest loading. The most notable departures from the trends in molar volume, such as the IPSAS 25 mol.% loaded sample melted at 1250 °C, can be primarily attributed to the equivalent differences in measured Archimedes density, though in this particular case the effect was more pronounced because of a lower-than-expected bulk cerium content, therefore lower molar mass. This could indicate that the IPSAS 25 mol.% simulant loaded 1250 °C melt sample experienced cerium containing slag formation which may have adhered to the crucible during casting, or separation of large crystallites of cerium rich monazite.

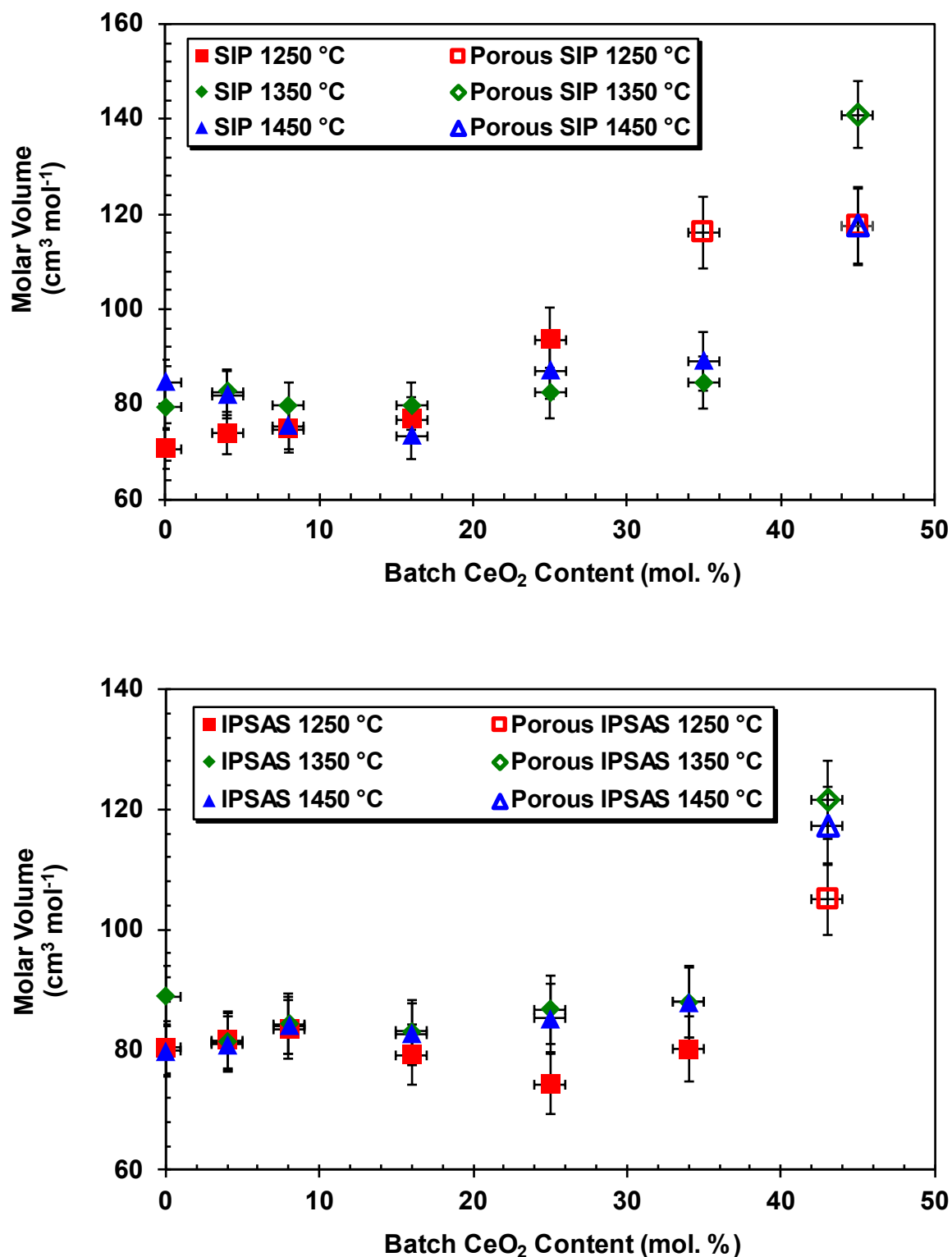


Figure 4.5.B – Plots of molar volume, as calculated using Archimedes density and molar mass from EDX analysis, SIP compositions (top) and IPSAS compositions (bottom) respectively. Unfilled symbols indicate highly porous samples. Error bars may be obscured by datapoint symbols.

4.6 Powder X-ray diffraction

The amorphous nature and phase assemblage of samples in this study were determined using finely milled powder samples, as measured with an X-ray diffractometer in a modified setup to amplify even minor Bragg peaks indicative of crystallisation, see **Section 3.3.1**. Here, pXRD also provides an avenue for comparison of any crystalline phases between the melt series. Fully amorphous samples, as indicated by the XRD column of **Table 4.2.A**, were those as defined by a high noise floor and a moderately intense feature with a continuous distribution of diffraction between 15 – 40 $2\theta^\circ$. Here, the data have been analysed using Bruker DIFFRAC.EVA and peak matching was achieved with the PDF-4+ database [20].

4.6.1 Crystalline phase assemblage

The SIP series melted at 1250 °C remained largely X-ray amorphous up to 25 mol.% loadings of simulant material, though some very minor Bragg peaks were detected for monazite at 16 mol.% addition, see **Figure 4.6.A**. The crystalline phases identified, in order of majority of Bragg peaks and intensities detected were: cerium monazite, $\text{Ce}(\text{PO}_4)$ (PDF #83-6052); undigested ceria, CeO_2 (PDF #78-0694); sodium iron phosphate, $\text{NaFe}(\text{P}_2\text{O}_7)$ (PDF #23-0680) [20]. This was representative of all melt series discussed here, with such crystalline phases identified and matched with a high degree of confidence. The most intense Bragg peaks for cerium monazite were found for the 45 mol.% loading sample, with the (021), (002) and $(21\bar{2})$ peaks as the most prominent instances. Similarly for ceria, undigested crystalline remnants were detected at higher loadings of 25 – 45 mol.%, however, decreases in intensities for the ceria (020) and (220), peaks were noted where the simulant loading increased from 35 – 45 mol.%. This was likely due to the more energetically favourable crystallisation of cerium monazite over formation of amorphous cerium bearing phases, with greater crystallisation being driven by increased loading of simulant fuel. Sodium iron phosphate was only found for samples with 25 mol.% or greater loading, though an apparent shift of symmetry can be observed, with the sodium iron phosphate $(11\bar{1})$, (111) and (012) Bragg peaks for 25 mol.% loaded SIP 1250 °C absent in that of the 35 – 45 mol.% series counterparts. Sodium iron phosphate was still detected in these samples, through identification of the (200), (022) and $(22\bar{2})$, reflections. A number of additional reflections were also observed at 14.10° and 16.40° , for 35 – 45 mol.% samples, although not statistically representative enough to match with a very high degree of confidence, the peak parameters agree well with those of the (020) and (200) reflections for a sodium iron phosphate polytype $\text{NaFe}_3\text{P}_3\text{O}_{12}$ (PDF #78-0784). An intermediate phase represented by Bragg peaks at 20.4° and 25.8° for 25 – 35 mol.% loaded materials covers a partial match for the (100) and (012) reflections for iron phosphate $\text{Fe}(\text{PO}_4)$ (PDF #84-0876) [20].

The SIP 1350 °C melt series demonstrated similar behaviour for phase formation and crystallisation, with 0 – 8 mol.% samples remaining X-ray amorphous, see **Figure 4.6.B**. This series

did however experience the onset of crystallisation of monazite and secondary phases at lower loadings than that of the 1250 °C series, with the 16 mol.% sample exhibiting low intensity monazite (110), (002), (021) and (21 $\bar{2}$) peaks (PDF #83-6052) [20]. Another key difference in the lower temperature series was the overall decrease in Bragg peak intensities for the crystalline phases, where the simulatant loading increases from 35 – 45 mol.%. As this effect was very well pronounced, broadly across the diffractogram without a significant emergence of an X-ray amorphous feature, this suggests a cause related to the measurement conditions. Diffraction studies with powders smaller than 1 μm , have found peak broadening as a function of structure factor, since such smaller particles and single crystallites will typically have lower mass, they will not attenuate collimated X-rays as strongly as larger particles for an identical measurement volume. In this study, the diffraction powders were not sieved, and some may have been milled to contain a proportion of $< 1 \mu\text{m}$ particles. Powder samples with single crystallites can be affected more severely by preferred grain orientation, with some larger crystallites on the order of 10 – 50 μm developing in some samples [21–23]. The emergence of (111), (020) and (220) Bragg peaks for crystalline ceria (PDF #78-0694), progresses at simulatant loadings beyond 25 mol.% with those of the higher loadings exhibiting such reflections with greater intensity. Another commonality was the symmetry shift behaviour for sodium iron phosphate $\text{NaFe}(\text{P}_2\text{O}_7)$ (PDF #23-0680), with (11 $\bar{1}$), (111) and (012) reflections only present in the diffractogram for 25 mol.% loading, and other reflections attributed to the same phase at higher loadings. Peaks that can be attributed, with a lower degree of confidence, to another sodium iron phosphate polytype $\text{NaFe}_3\text{P}_3\text{O}_{12}$ (PDF #78-0784) and iron phosphate $\text{Fe}(\text{PO}_4)$ (PDF #84-0876), also agree with the SIP 1250 °C series [20].

The diffractograms for SIP 1450 °C series melts show crystallisation and secondary phase incorporation at even lower simulatant loadings, with the only fully X-ray amorphous sample being the unloaded base glass, see **Figure 4.6.C**. The majority crystalline phase for higher loading samples was again monazite (PDF #83-6052), with a primary (021) reflection. With the 45 mol.% simulatant loaded material, the remaining undigested ceria (PDF #78-0694), was predominantly represented by the (111) and (020) reflections. There was a very significant development of crystalline sodium iron phosphate, $\text{NaFe}(\text{P}_2\text{O}_7)$ (PDF #23-0680) [20], onset at 4 mol.% simulatant addition, with pronounced (11 $\bar{1}$) and (012) reflections. In further support of sodium iron phosphate as an intermediate phase, the increase of simulatant loading in this series aligns with a steady increase of detected crystalline monazite and ceria, with a decrease of intensity for primary sodium iron phosphate peaks. As with the other SIP melt series, minor reflections present in fully and partially crystalline samples can be attributed with lower confidence to $\text{NaFe}_3\text{P}_3\text{O}_{12}$ (PDF #78-0784) and $\text{Fe}(\text{PO}_4)$ (PDF #84-0876) [20].

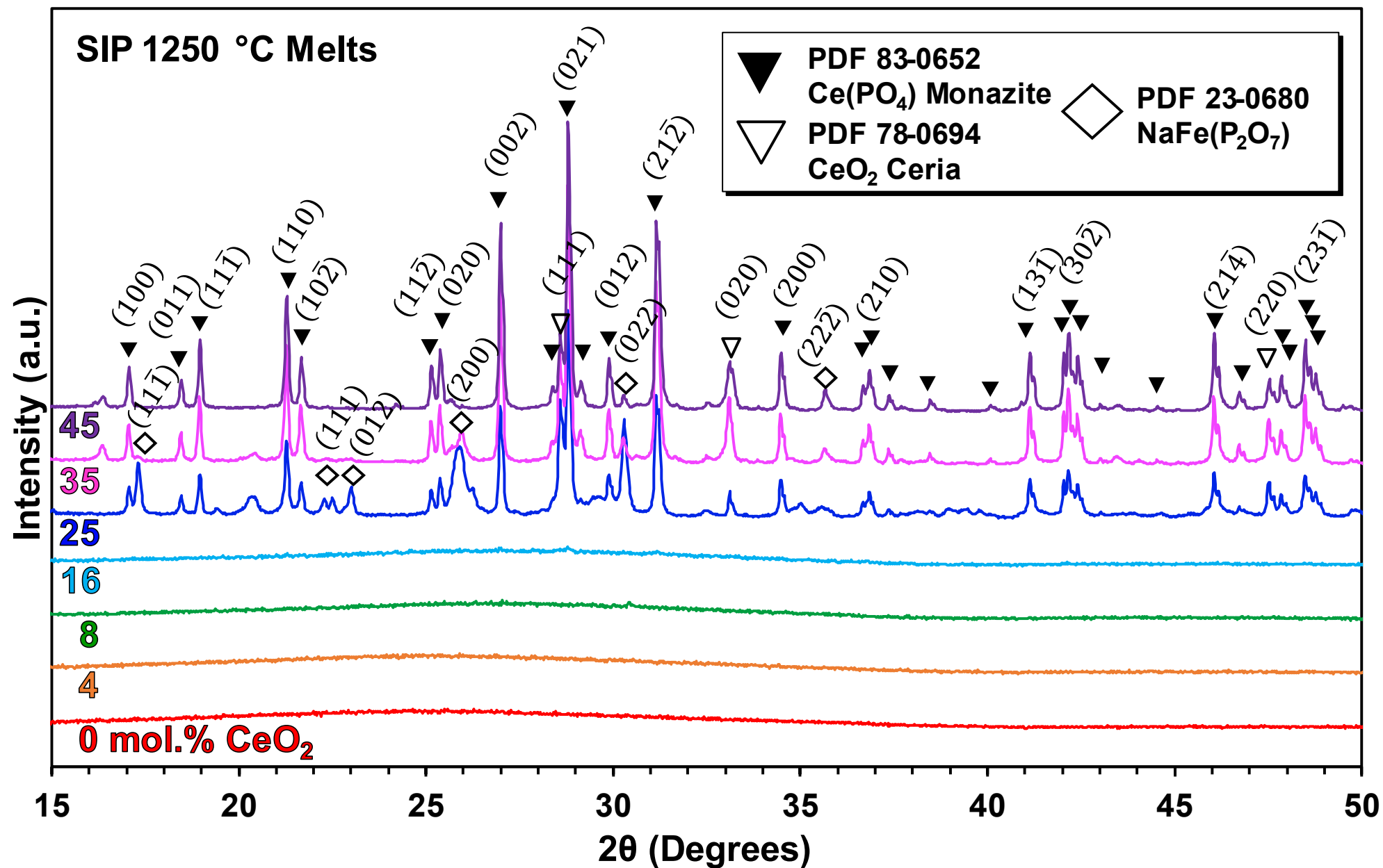


Figure 4.6.A - Indexed X-ray diffractograms for semi-crystalline series of SIP melts at 1250 °C, the PDF cards used are indicated in the legend, with the molar batch loading of ceria fuel simulant between 0 – 45 mol.%, as indicated, bottom to top, respectively.

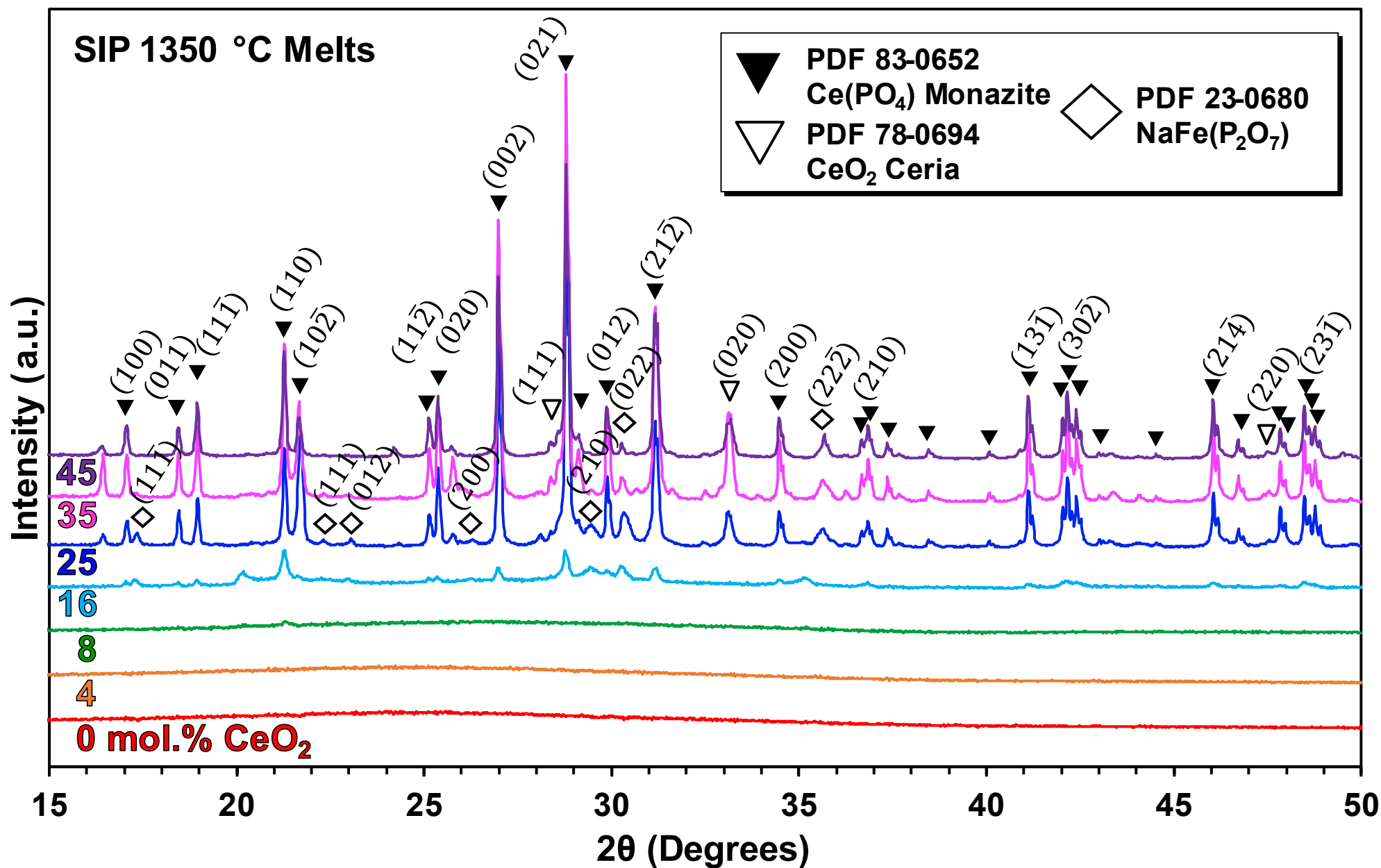


Figure 4.6.B - Indexed X-ray diffractograms for semi-crystalline series of SIP melts at 1350 °C, the PDF cards used are indicated in the legend, with the molar batch loading of ceria fuel simulant between 0 – 45 mol.%, as indicated, bottom to top, respectively.

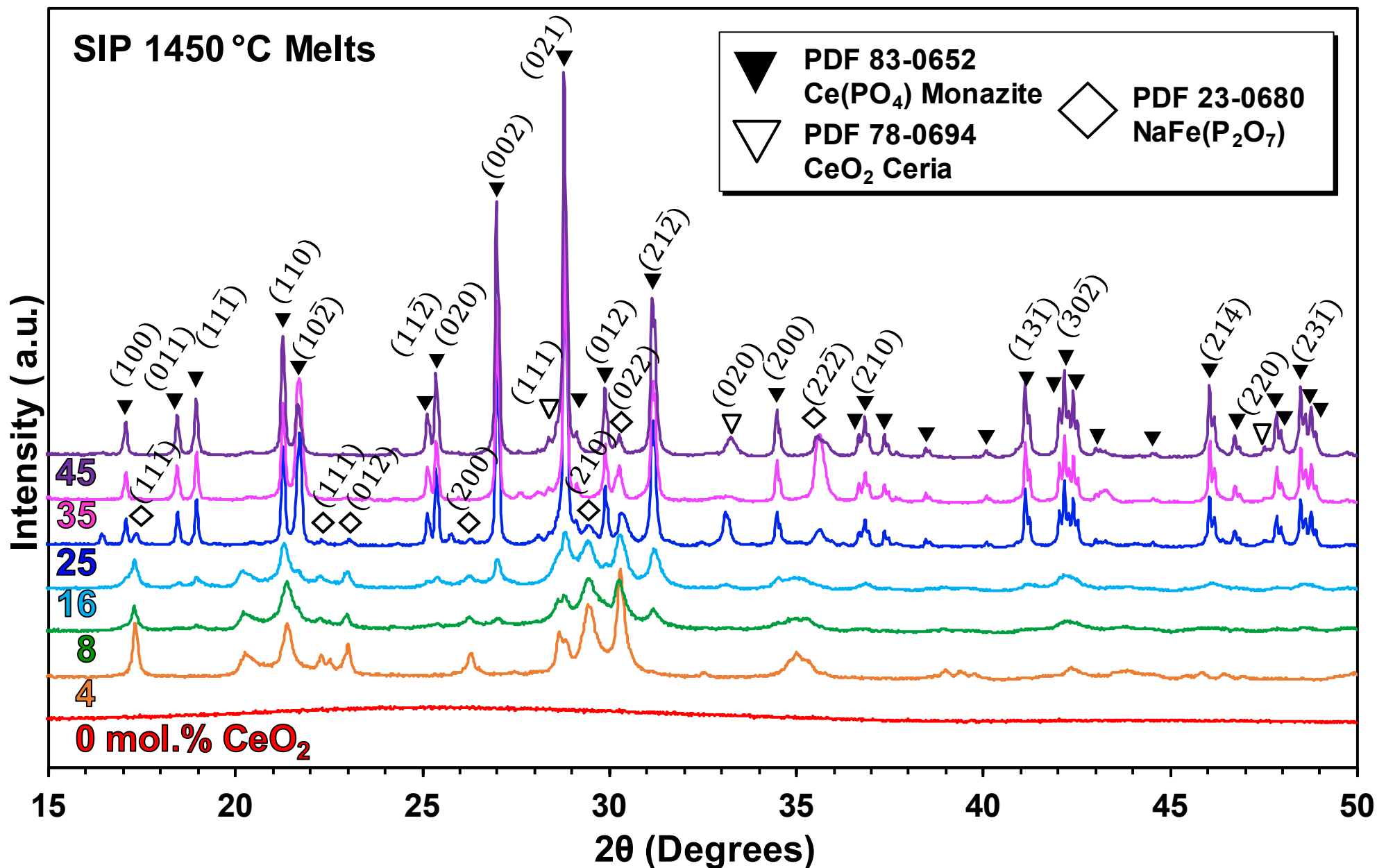


Figure 4.6.C - Indexed X-ray diffractograms for semi-crystalline series of SIP melts at 1450 °C, the PDF cards used are indicated in the legend, with the molar batch loading of ceria fuel simulant between 0 – 45 mol.%, as indicated, bottom to top, respectively.

For the IPSAS melt series', the primary crystalline phases identified agreed with that of the SIP series. In order of decreasing reflection intensities, the crystal phases detected were: cerium monazite, $\text{Ce}(\text{PO}_4)$ (PDF #83-6052); undigested ceria, CeO_2 (PDF #78-0694); sodium iron phosphate, $\text{NaFe}(\text{P}_2\text{O}_7)$ (PDF #23-0680) [20]. IPSAS 1250 °C series melts exhibited pristine glass phase assemblages for up to 16 mol.% additions of simulant, as demonstrated by the X-ray amorphous nature of the diffractograms presented in **Figure 4.6.D**. For the high loading samples > 25 mol.% simulant waste, the primary crystalline phase was monazite, demonstrated by the intense (021), $(21\bar{2})$ and (002) reflections. A significant quantity of undigested ceria remains in most of the partially crystalline samples, increasing up to the 43 mol.% loaded material, evident by the intense feature present at the ceria (PDF #78-0694) (111) reflection. In comparison to the SIP compositional variant melted at the same temperature, see **Figure 4.6.A**, the detection of matched sodium iron phosphate, $\text{NaFe}(\text{P}_2\text{O}_7)$ (PDF #23-0680) was significantly more truncated in the IPSAS series. Crystalline sodium iron phosphate was represented by the minor (111), (012) and (022) reflections in the 34 mol.% material, with only the lower confidence assignment of (200) and (022) reflections made for 43 mol.% loading. Additionally, Bragg peaks associated with secondary phases such as a sodium iron phosphate polytype $\text{NaFe}_3\text{P}_3\text{O}_{12}$ and iron phosphate $\text{Fe}(\text{PO}_4)$, were not detected in any of the IPSAS 1250 °C series melts. This coupled with the more consistent densification behaviour of the IPSAS materials, suggests that the small additions of refractory oxides act to reduce the generation and incorporation of slag and (otherwise demonstrated in SIP series melts as inclusion of more secondary phase material) [20].

For the IPSAS 1350 °C melt series, the resulting materials again remained single phase glass up to 16 mol.% simulant loading, as represented by the X-ray amorphous feature centred at approximately 24.0° , see **Figure 4.6.E**. The majority crystalline phase in high simulant waste loaded samples was cerium monazite (PDF #83-6052) with a primary (021) reflection. Undigested ceria (PDF #78-0694) was detected as present only in low levels, as compared to IPSAS 1250 °C series melts, as represented by the minor (111) and (020) peaks, suggesting that the higher melt temperature allows for greater incorporation of cerium into the glass phase for this composition. Sodium iron phosphate $\text{NaFe}(\text{P}_2\text{O}_7)$ (PDF #23-0680) was detected at even lower intensities for 34 – 43 mol.% simulant waste loaded samples, matched to the (022) and $(02\bar{2})$ reflections, again here as supporting evidence for reduced formation and incorporation of intermediate phases with IPSAS compositions. There were also very minor peaks found at approximately 16.0° for the 43 mol.% loaded material, this may be attributed, with lower confidence match to a sodium iron phosphate polytype $\text{NaFe}_3\text{P}_3\text{O}_{12}$ (PDF #78-0784) [20].

In the IPSAS 1450 °C melt series, the formation of primary glass phase was consistent at simulant loadings of up to 8 mol.%, as represented by broad X-ray amorphous features, see **Figure 4.6.F**. The onset of crystallisation appeared for 16 mol.% loaded sample, with very low intensity detections attributed to monazite (PDF #83-6052) ($10\bar{2}$) and (021), with another lower confidence designation of crystalline sodium iron phosphate $\text{NaFe}(\text{P}_2\text{O}_7)$ (PDF #23-0680), from the ($02\bar{2}$) peak. At 25 mol.% loadings and above, the development of crystalline phase assemblages followed the characteristic pattern as seen with the other IPSAS melt series', with a significant majority of the intense Bragg peaks matched to monazite, with a primary (021) reflection increasing in intensity with simulant loading. Undigested ceria (PDF #78-0694) was retained in small quantities at the highest 34 – 43 mol.% loadings, as represented by the (111) and (020) peaks. Similarly, inclusion of low intensity peaks associated with sodium iron phosphate $\text{NaFe}(\text{P}_2\text{O}_7)$ (PDF #23-0680) at these higher loadings, aligns with the crystallisation behaviour of the other IPSAS melt series. The most notable example of sodium iron phosphate detection in the IPSAS 1450 °C melts was the broad feature representing the ($02\bar{2}$) reflection for 43 mol.% simulant loading. While the phase formation characteristics of this series are largely in agreement with other IPSAS series', the higher melting temperature may have led to more aggressive melting conditions, causing crystallisation of the intermediary sodium iron phosphate for the lower loading 16 mol.% composition. This is further supported by the Archimedes data, see **Figure 4.5.A**, as while not porous, the IPSAS 1450 °C 16 mol.% sample did not agree with the linear trend of density increase with simulant loading.

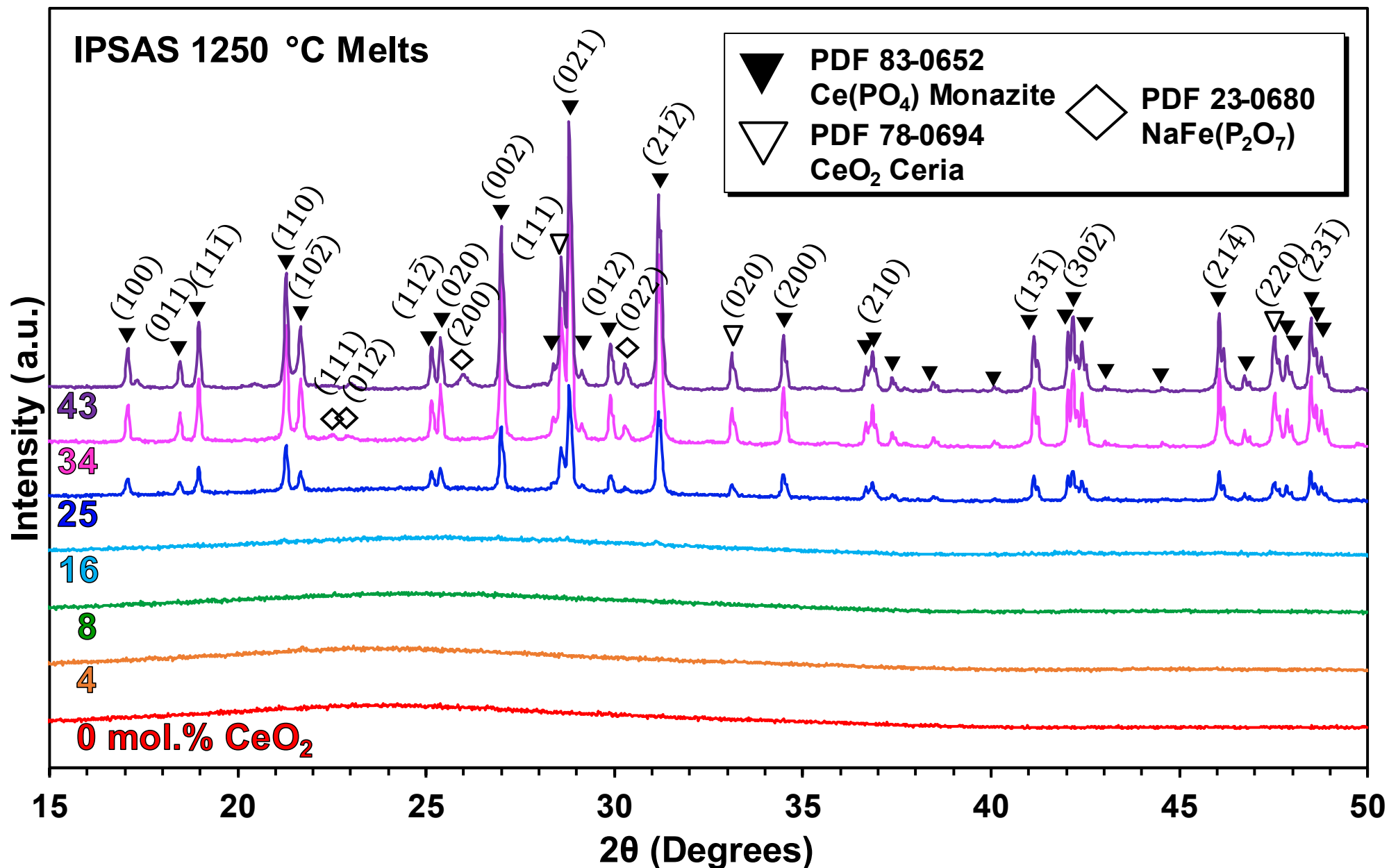


Figure 4.6.D - Indexed X-ray diffractograms for semi-crystalline series of IPSAS melts at 1250 °C, the PDF cards used are indicated in the legend, with the molar batch loading of ceria fuel simulant between 0 – 43 mol.%, as indicated, bottom to top, respectively.

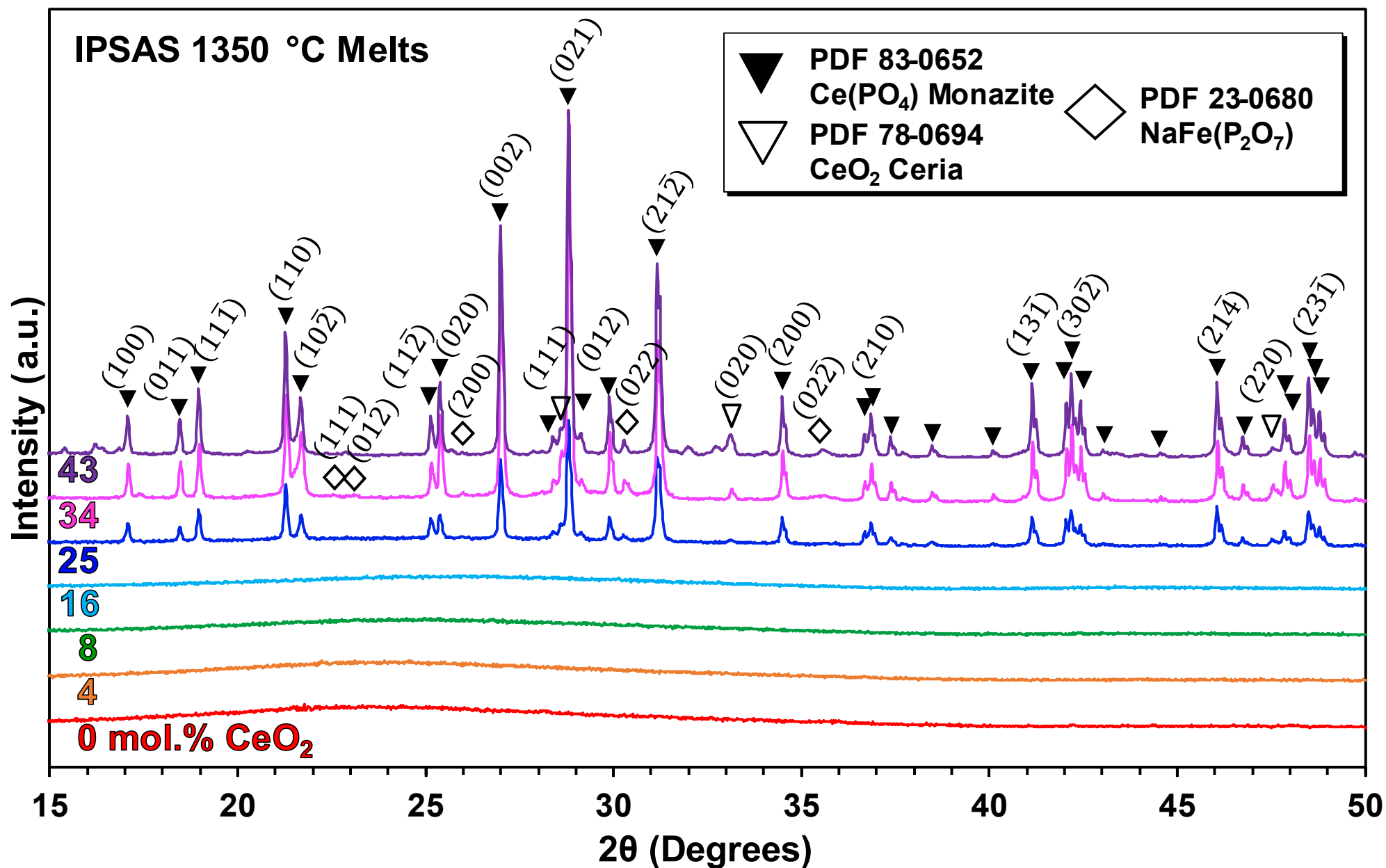


Figure 4.6.E - Indexed X-ray diffractograms for semi-crystalline series of IPSAS melts at 1350 °C, the PDF cards used are indicated in the legend, with the molar batch loading of ceria fuel simulant between 0 – 43 mol.%, as indicated, bottom to top, respectively.

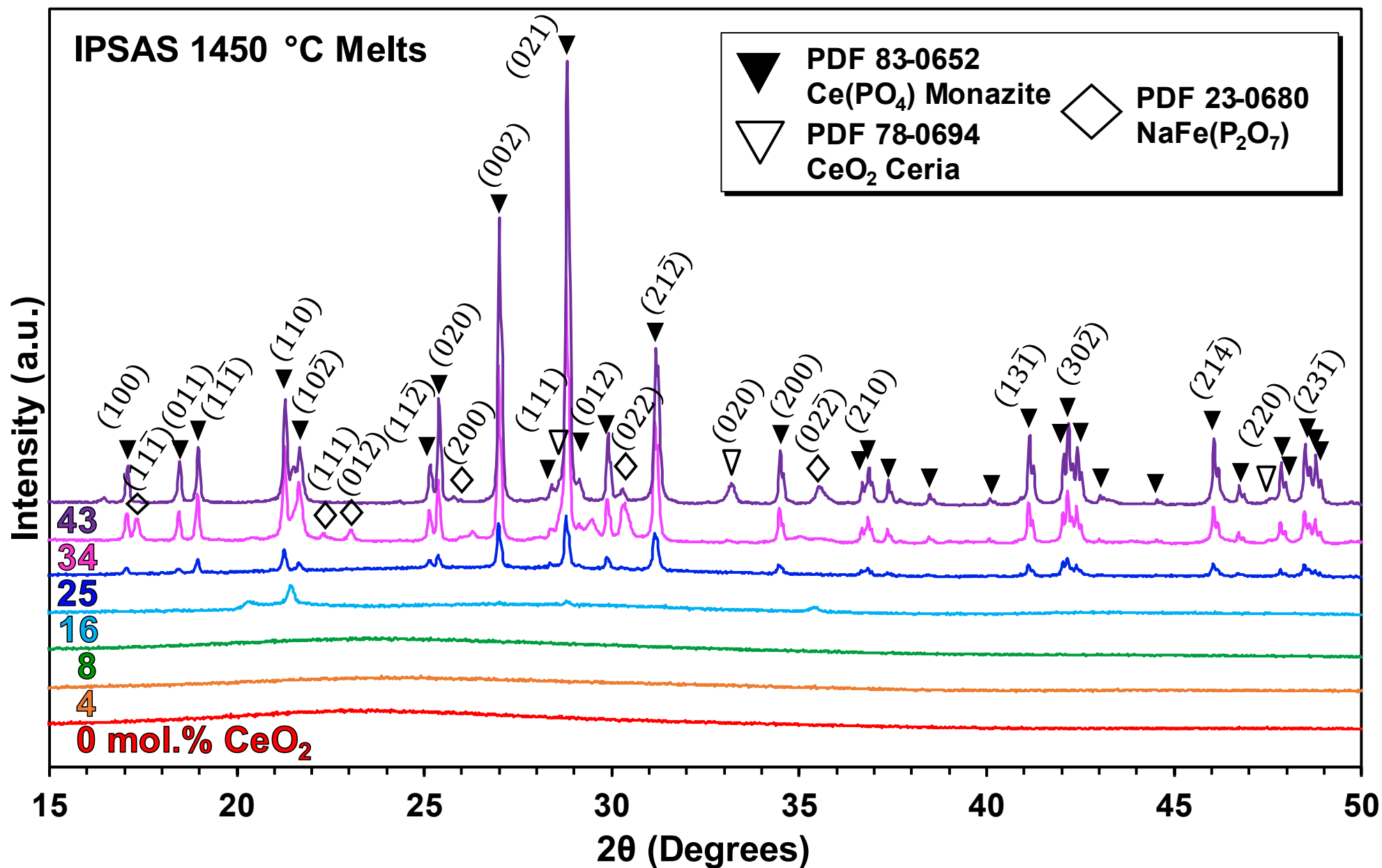


Figure 4.6.F - Indexed X-ray diffractograms for semi-crystalline series of IPSAS melts at 1450 °C, the PDF cards used are indicated in the legend, with the molar batch loading of ceria fuel simulant between 0 – 43 mol.%, as indicated, bottom to top, respectively.

4.6.2 LaB₆ spike Rietveld analysis

Quantification of relative phase proportions was attempted using spike-Rietveld analysis. Typical Rietveld analysis does not permit quantification of any amorphous fractions, without addition of a known quantity of standard material with known diffraction properties. The IPSAS 25 mol.% loaded sample melted at 1350 °C was selected for this work as it demonstrated a relatively simple phase assemblage containing glass, cerium monazite and undigested ceria, and with respect to diffraction data: sharp, well-defined peaks were resolved for crystalline phases with a still notable X-ray amorphous feature pertaining to the glass phase, at about 15 – 35°. Selected for its known and standardised properties, a ~10 wt.% addition of LaB₆ (NIST 660C) spike was added and homogenised with test sample powder, using a pestle and mortar. Data were collected with the same diffractometer conditions, though over a range of 10° – 70° 2θ. A 10 term polynomial Chebyshev background function was first fitted using TOPAS6 software, before the assemblage was modelled using ideal structures of cerium monazite, fluorite-structured ceria, and LaB₆, as obtained from literature CIFs [24–26]. With initialisation of thermal parameters and instrument settings, Bragg peaks were fitted as Pearson VII shape functions, see **Figure 4.6.G**. A realistic fit was obtained by ensuring the linear regression did not progress beyond the number of independent variables, and all fitting parameters were set to converge with refinement halting where $\delta\chi^2 < 0.00001$.

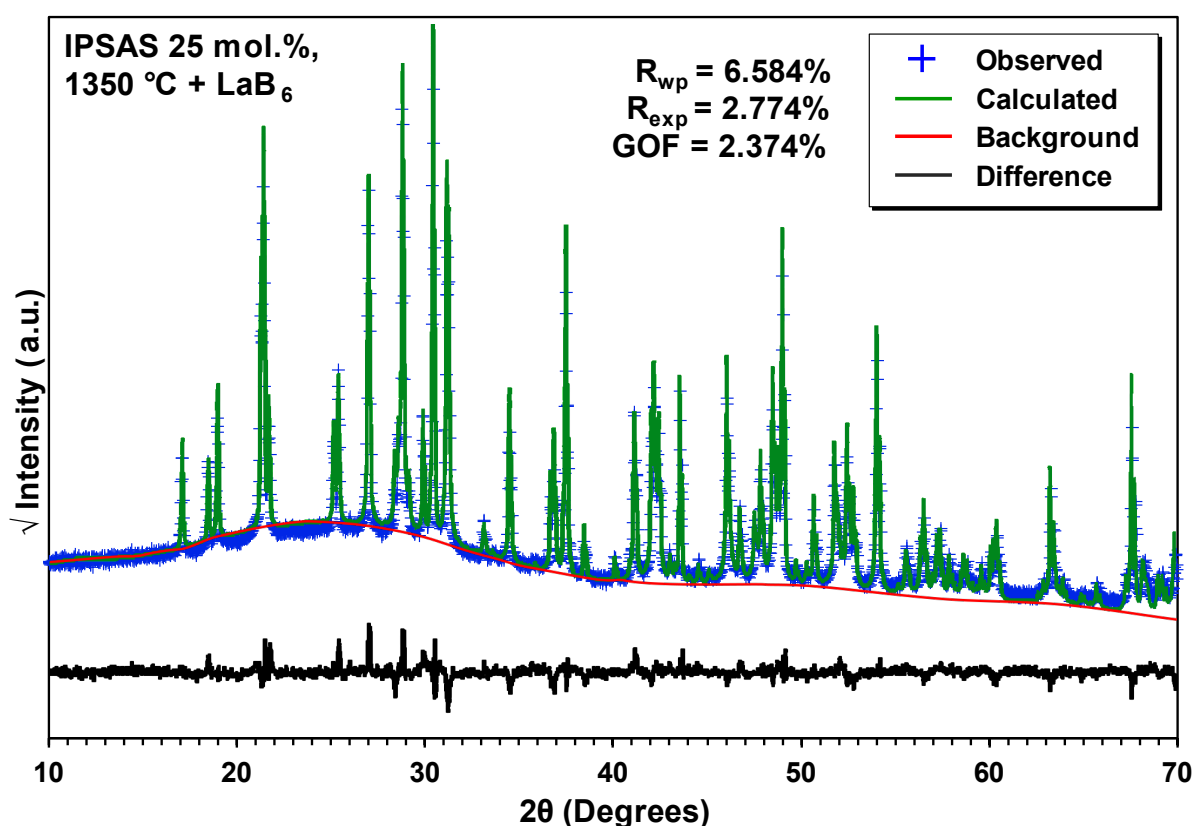


Figure 4.6.G - LaB₆ -spiked X-ray Rietveld analysis for IPSAS 25 mol.% simulant sample melted at 1350 °C. A starting assemblage and structure was modelled using analysis reported in **Figure 4.6.E**. Fitting statistics are marked.

Although an adequately low weighted profile R-factor (R_{wp}) of 6.584 % was found, when applied into ratio of squares with the theoretical minimum possible expected R-factor (R_{exp}), this resulted in R_{wp}^2 approximately 5.6 greater than the value of R_{exp}^2 , higher than the ideal ratio of < 4 . The goodness of fit (GOF) parameter, also referred to as χ^2 , was well below a maximum value of 10 % and very close to the ideal case of 2 %. While not all fitting statistics were securely within typically accepted ranges, analysis proceeded with this fit as the differences between observed and calculated values were minimal and the statistics were reasonably close to an ideal fit. The difference spectrum (black trace) indicated a good agreement of the background fit with some over- and under-fitting of some primary Bragg peaks for LaB_6 and cerium-monazite, though these are in proportion to the relative intensity of the observed data. Using HEPHAESTUS calculations of mass-attenuation coefficients of the crystalline phases and the base glass and the corrected addition of LaB_6 standard spike, weight fractions of phases present in the original un-spiked sample could then be calculated. For crystalline phases the sample was found to contain: 31.80 ± 0.27 wt.% cerium monazite and 1.41 ± 0.13 wt.% undigested ceria, leaving 66.79 ± 0.30 wt.% fraction of amorphous or glass material.

While with a reasonable degree of prior knowledge of a specific samples phase assemblage, it is possible to refine a model to one set of diffraction data, there are many undesirable aspects to this methodology. This diffraction-based method of quantitative phase analysis requires long measurement times, provides little flexibility for samples containing unknown phases, phases with polytypical structures, crystallites exhibiting isomorphism, preferred orientation, and offers only limited repeatability and reliability of fitting. Results can be heavily dependent on sample preparation techniques, diffractometer conditions, and user fit interpretation as has been noted in a number of international round-robin diffraction studies, with large spreads of results for identical samples, mixtures and methods [27–29].

Integrated Bragg peak area quantification methods were attempted, as outlined in **Section 3.3.2**, though they were ultimately unsuccessful for consistently calculating the phase assemblage in these materials. As the composition of the amorphous glass fraction changed with the overall batch composition, particularly with respect to cerium content, the absorption coefficient of the glass fraction also changed, causing unpredictable degrees of X-ray attenuation. Calibration lines were produced using mixtures of standards, including 0 mol.% IPSAS glass melted at 1350 °C, with a consistent absorption coefficient.

4.7 Scanning electron microscopy

4.7.1 Bulk material EDX analysis

Bulk semi-quantitative EDX analysis was used as a technique to verify the composition of monolithic samples in the as-annealed state. EDX points were taken at five locations on the sample surfaces and then data was averaged, with points re-selected if the standard deviation was too high for any one element, see **Figure 4.7.A**. As with molar volume, EDX data are presented with the caveat of poor detection of light elements ($Z < 11$) such as oxygen. Compositions were calculated from normalised molar oxide content. Pores, pore boundaries and sample edges were avoided as points for analysis, as to mitigate any deleterious effects of the beam interacting with an incomplete volume and to ensure a representative area of sample was covered. Care was taken for the higher simulant waste loaded samples, as these had a higher typical distribution of microstructural pores, zones of heterogeneous incorporated slag and larger crystallites. Fully amorphous glass samples were confirmed with pristine polished surfaces in BSE images, with no crystallisation. The onset of crystallisation as found by pXRD for 4 – 25 mol.% CeO₂ materials melted at 1350 °C, was reflected by the formation of angular crystallites typically ranging diameter of 5 – 50 µm, distributed throughout the glass matrix and well defined by BSE phase contrast.

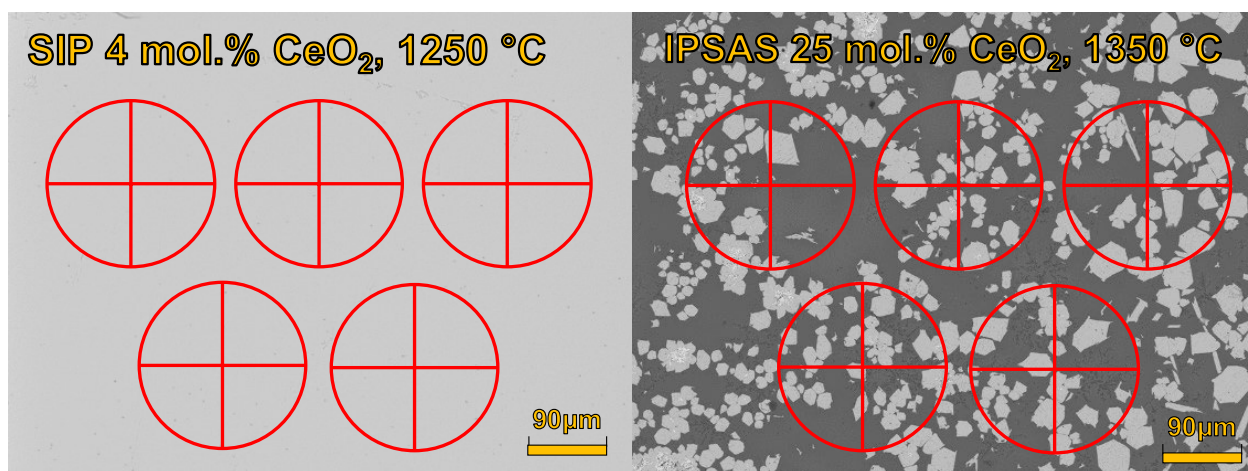


Figure 4.7.A – Back Scattered Electron micrographs for SIP 4 mol.% CeO₂ melted at 1250 °C (left) and IPSAS 25 mol.% CeO₂ melted at 1350 °C (right), with markers indicating zones for collection of EDX spectra.

The inferred molar content of primary glass constituents: P₂O₅, Fe₂O₃ and Na₂O (as oxides), did not remain within entirely consistent ratios to one another in all glass series, with the most variability arising in the SIP melt series, see bracketed values in **Table 4.2.A**. The batched base SIP glass targeted a molar oxide ratio of P₂O₅, Fe₂O₃ and Na₂O of 6 : 3 : 1, which was consistent with fully amorphous SIP compositions melted at 1350 – 1450 °C, up to the onset of crystallisation at 16 – 25 mol.% simulant loadings, whereby the ratios shifted closer to 4 : 2 : 1, respectively.

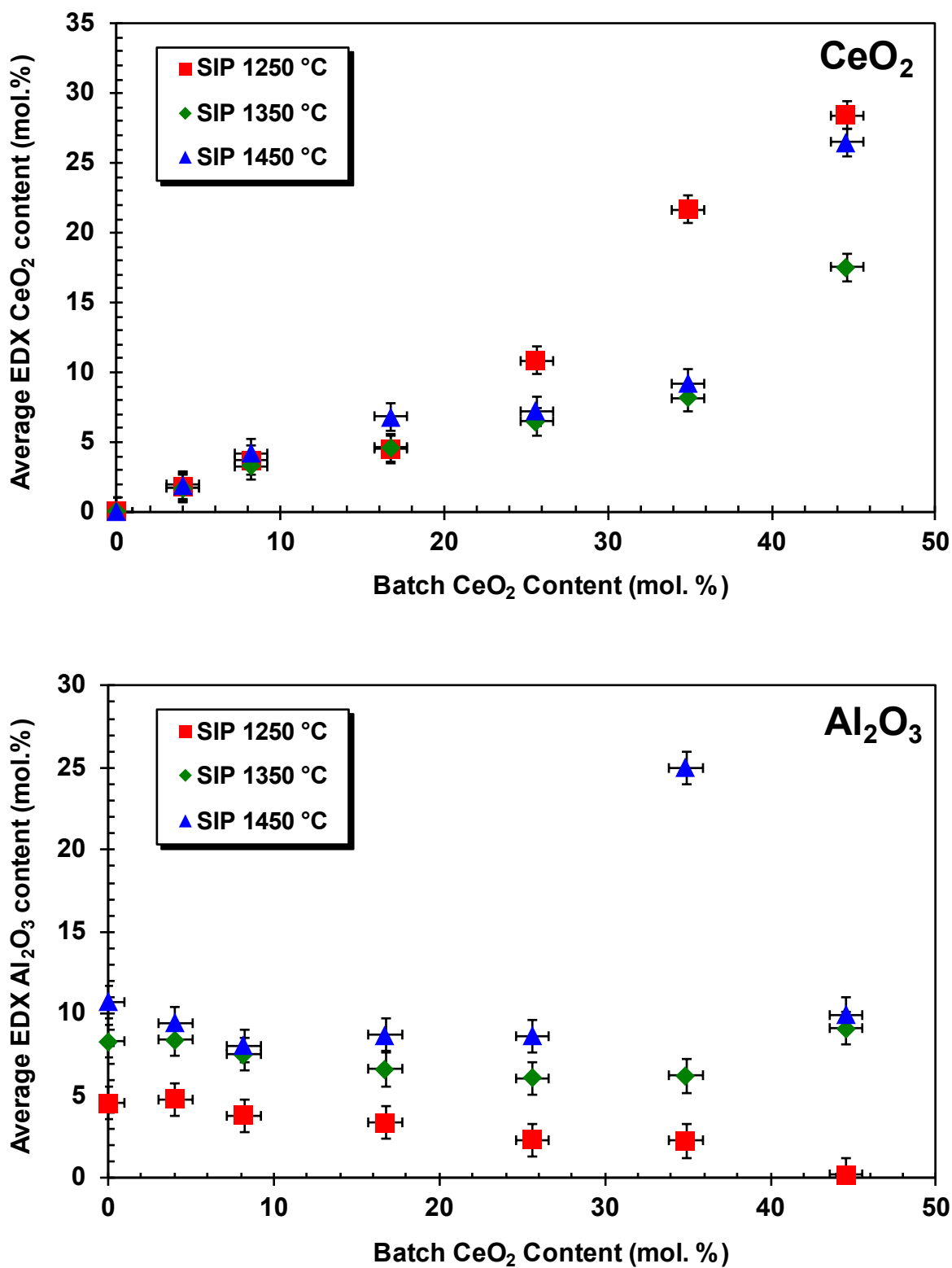


Figure 4.7.B – Plots of average measured molar content as a function of batched CeO_2 content in all SIP melt series. Data measured via EDX analysis and converted to oxides, CeO_2 (top) and Al_2O_3 (bottom).

Calculated molar ratios (as inferred through EDX measurements) significantly departed from those targeted with batch compositions, particularly with respect to CeO_2 content, as demonstrated in a plot of batched to measured composition, see **Figure 4.7.B**. Where in an ideal case with full incorporation of ceria, the relationship would be perfectly linear and equal for all SIP and IPSAS melt series. This effect is ascribed to crystallisation of larger crystallites of cerium rich monazite and retention of more refractory cerium species in un-incorporated slag which adhered to melt crucibles during casting. The apparent difference between batched Ce content and measured content, could also be attributed to the higher density of ceria as compared to the other glass melt constituents, so if the effect of self-stirring is diminished remnant ceria is likely to reside at the base of the crucible. As the compositions were measured by EDX, calibration of the system may have also been a factor in variable detections of Ce. For the SIP series melts, the 45 mol.% loaded sample melted at 1250 °C retained the highest quantity of ceria at 28.4 mol.%, still only ~0.6 times the target composition. The 1250 °C SIP melt series did provide a more linear increase in measured ceria content over the entire batched loading range, while the 1350 – 1450 °C melt series followed an approximate linear trend up to 35 mol.% simulant loading.

With the higher temperature SIP series, the development of high porosity led measured ceria content to depart from this initial trend, with a sharp increase. While the batch content for all SIP materials did not include any SiO_2 , up to 1.5 mol.% of trace silica was detected across the series, with the Si $\text{K}\alpha 1$ peak signal only marginally above the noise floor of the spectrum (0.20 cps/eV and 0.25 cps/eV, respectively). This inclusion can be attributed to minor contamination of crucibles and furnaces with small quantities of silica naturally present as a contaminant in less pure reagents and alumina crucibles. A single clear exception is that of the silica content in the SIP sample loaded with 45 mol.% simulant waste and melted at 1350 °C, where measured bulk silica content was 9.1 mol.%. A review of the EDX maps revealed that silicon was not concentrated in localised structures and phases, but relatively evenly distributed across the sample surface. Although care was taken to prepare SIP and IPSAS samples separately for microscopy, this instance is likely to have resulted from some contamination during surface polishing. The spike of detected silica here explains the decrease in expected value of ceria content as compared to the highest loaded 1250 °C and 1450 °C counterparts. SIP base material batches also omitted use of any Al_2O_3 , however as the crucible material, it was expected that some incorporation would occur with the more corrosive melts. In the SIP 1250 °C melt series, the low simulant loaded glasses 0 – 4 mol.% had the highest measured alumina content of 4.5 mol.% and 4.8 mol.% following a linear decrease with additional ceria loading, see **Figure 4.7.B**. This suggests that the addition of CeO_2 is itself behaving as a refractory material at 1250 °C, passivating the melting conditions and reducing dissolution of the crucible. For the SIP 1350 – 1450 °C melt series, the alumina content remained within a relatively

consistent range 6.1 – 10.7 mol.%, with the exception of SIP 35 mol.% simulant melted at 1450 °C, where a peak value of 25.0 mol.% alumina was found, above even the highest concentrations added to IPSAS series batches. It is suggested that a weaker feature or piece of corroded crucible may have been incorporated into the melt at the high temperature, evidenced by the concentration of aluminium into the matrix phases of the monolithic sample. This was not entirely conclusive, as with many of the high temperature melts, the crucible failed shortly after casting and rapid cooling, so could not be retrieved for thorough analysis. Between the 1250 – 1450 °C series, the overall alumina content increased with temperature, as the higher temperatures induced more corrosive melt characteristics.

The IPSAS base glass had targeted a molar ratio for the P_2O_5 , Fe_2O_3 and Na_2O primary structural constituents, of approximately 6 : 2 : 1, which remained largely consistent across all IPSAS melt series and between all simulant loadings, see the unbracketed compositions as listed in **Table 4.2.A**. As with the SIP equivalent series, the measured CeO_2 content of IPSAS melts departed significantly from the batched target content. The increase did remain relatively linear with batch composition across all temperatures, with greater deviation following the onset of crystallisation at 25 mol.% loading, see **Figure 4.7.C**. The greatest retention of ceria was found for the IPSAS 43 mol.% simulant loaded sample, with a measured value of 24.1 mol.%, reflecting the ~0.6 ratio of the ideal expected value. As with SIP series melts, low incorporation of ceria is expected to result from unincorporated slag phases containing ceria and separation of large cerium monazite crystals which could not be adequately covered by the EDX sampling methodology. Measured silica content was found to remain within a consistent range of 6.1 – 9.5 mol.%, and alumina experienced a small overall decrease within the range of 3.9 – 15.2 mol.%, see **Figure 4.7.C**. The greatest alumina incorporation was for the 0 mol.% ceria 1450 °C melt, this in part may be due to the absence of passivating ceria and result from degradation at the higher temperature. Across the overall scope of the IPSAS series, alumina content decreased with greater simulant loading and increased with greater melting temperatures. The IPSAS 1250 °C sample loaded with 25 mol.% simulant falls out of line with this apparent trend, with a greater alumina content than expected, this may similarly be due to a smaller quantity of fractured crucible inclusion, as compared with SIP 35 mol.% simulant melted at 1450 °C.

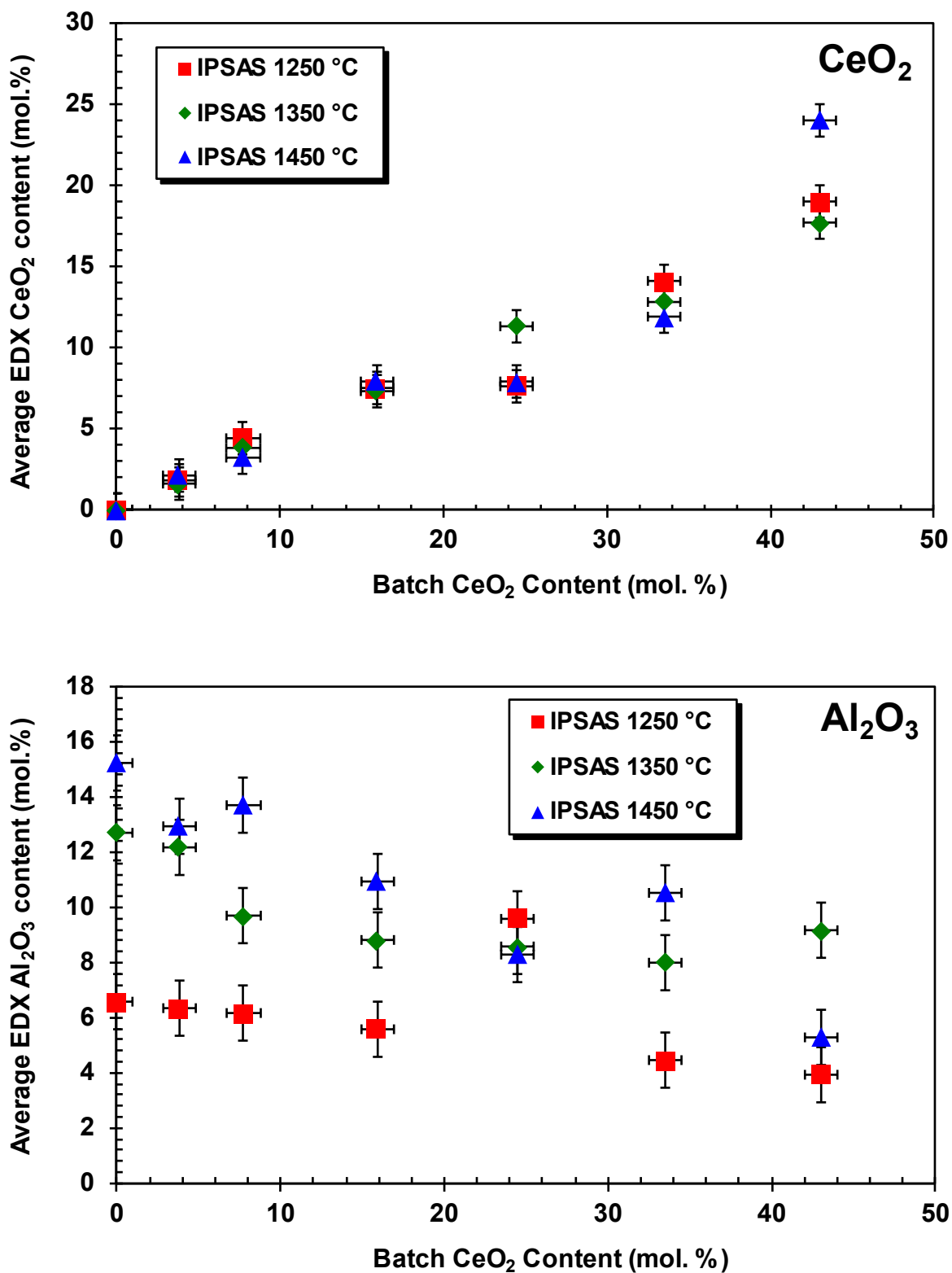


Figure 4.7.C – Plots of average measured molar content as a function of batched CeO₂ content in all IPSAS melt series. Data measured via EDX analysis and converted to oxides, CeO₂ (top) and Al₂O₃ (bottom).

4.7.2 BSE and EDX analysis of crystalline phases

As with the X-ray diffractograms collected for the fully amorphous samples, the back-scattered electron micrographs demonstrated the pristine polished section surface, with no crystallisation and only minor surface texture as remnant from mechanical polishing preparation. Part of the casting for IPSAS 0 mol.% loaded glass melted at 1350 °C was quenched and not annealed, see **Figure 4.7.D**. Dendritic crystallites of an aluminium phosphate phase separated from the matrix, however the small crystallite widths of 2 – 4 µm prevented accurate definition of stoichiometry by EDX analysis. The pristine surface of annealed glass in **Figure 4.7.D** was characteristic of all fully amorphous glass samples, with no porosity, very little surface texture and feature definition.

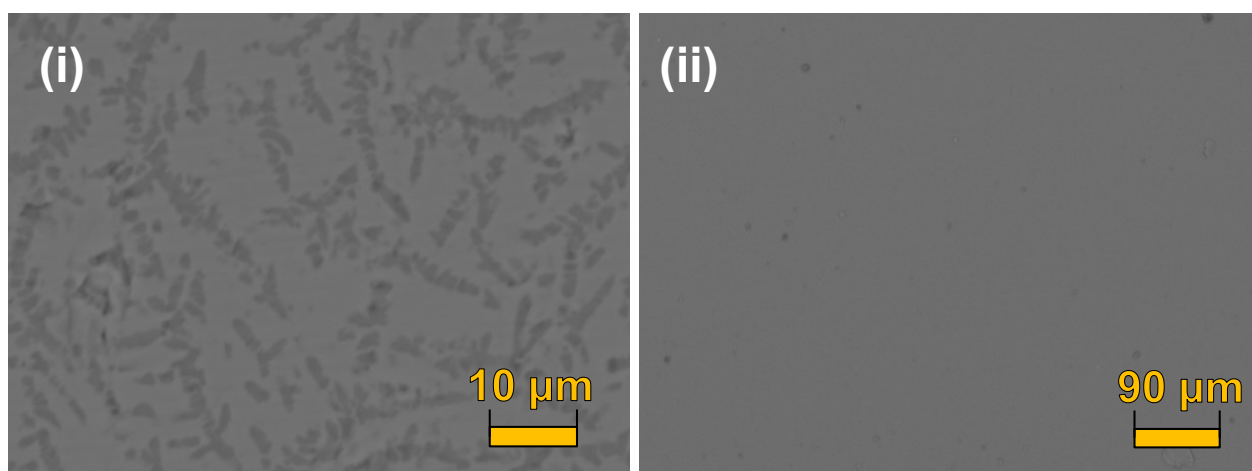


Figure 4.7.D – Back Scattered Electron Micrographs of IPSAS 0 mol.% CeO₂ glasses melted at 1350 °C, un-annealed showing some crystallisation of aluminium phosphate (i) and annealed, fully amorphous (ii)

The most typical morphology of monazite crystallites for the higher simulant loaded samples, was that of a faceted structure developing around grains of undigested ceria in a core-shell type formation, see **Figure 4.7.E**. As in this example for IPSAS material loaded with 16 mol.% simulant and melted at 1250 °C, the phase with brightest contrast and highest detected proportion of cerium was confirmed to match the stoichiometric ratio for cerium oxide, and featured an irregular surface texture and phase boundary, apparent as a nucleation point for crystalline cerium monazite. The bright grey phase with the second highest detected proportion of cerium was depleted in all other elements with exception to phosphorus and oxygen, here all found to be present in an approximate stoichiometric ratio to that of cerium monazite. The morphology of this phase was characteristically angular and faceted, often exhibiting the core-shell microstructure with undigested ceria. The dark grey matrix phase was the majority component for the lower and moderately simulant loaded samples and was found in agreement with the X-ray amorphous features measured using pXRD, denoting the glass phase. The glass phase was rich in phosphorus and sodium, in

comparison to the primary crystalline phases, though cerium content of this glass was not uniform in the presence of crystallites. With crystallisation, and oversaturation of the glass melt, cerium remains concentrated in the undigested grains and with the formation of monazite. Glass in proximity of 0 – 20 μm to the crystallites was slightly depleted in cerium as compared to the bulk glass, in a gradient with the lowest concentration being at the glass-crystallite boundary. For the IPSAS 16 mol.% loaded 1250 $^{\circ}\text{C}$ melt sample, the calculated loading at the boundary was 6.6 mol.% of ceria loaded into the glass phase, while the bulk glass outside of this range was calculated to have an average loading of 7.6 mol.% ceria.

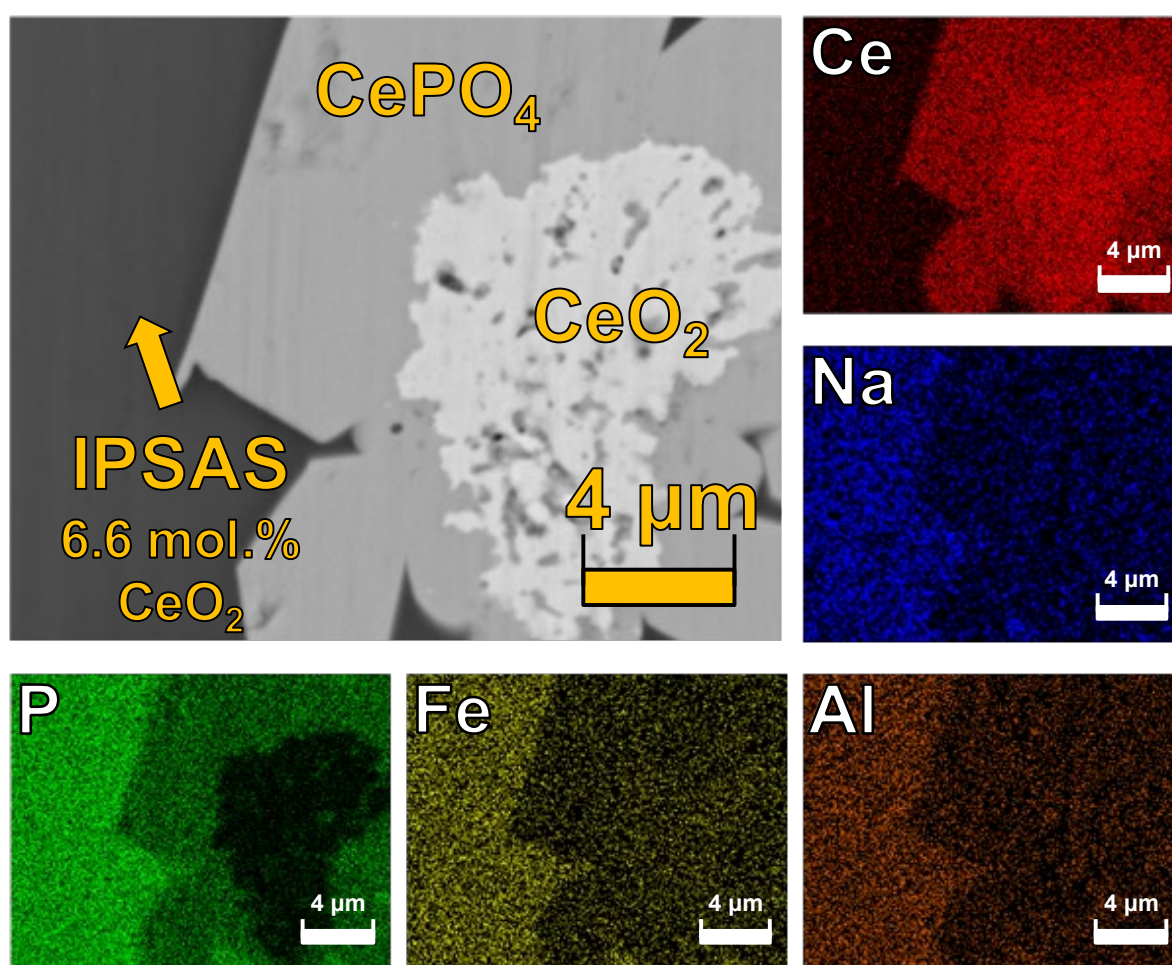


Figure 4.7.E – Backscattered Electron micrograph (top left) of IPSAS 16 mol.% simulant loaded material melted at 1250 $^{\circ}\text{C}$, demonstrating a representative core-shell type formation of monazite around a grain of ceria. The elemental EDX maps for marked species are also presented to the right and bottom edges.

Some secondary crystalline phases developed in samples such as IPSAS 34 mol.% melted at 1350 $^{\circ}\text{C}$, evolving small local concentrations of sodium iron phosphate and some small quantities of apparent sodium aluminium iron phosphate, see **Figure 4.7.F**. The EDX compositions of these small crystallites was difficult to reliably measure due to their size and therefore an overlap of interaction volume with the surrounding phases occurred, with the magnifications and detector

used. It can however be noted that the higher local concentrations of detected aluminium in the Al EDX map overlap with that of the small 2 – 6 μm , dark, angular crystallites, with petal-like growth directions from a central nucleation point. While crystalline sodium iron phosphate was also detected via pXRD, the aluminium rich phase was not, as was reflected by the very sparsely distributed crystallites that were few in number. This region of interest was not representative of the entire IPSAS 34 mol.% simulant loaded 1350 $^{\circ}\text{C}$ melt, though it does demonstrate the greater digestion of ceria into glass and crystalline phases at the higher melt temperature, as represented by the very narrow white remnants of a CeO_2 grain, still following a characteristic core-shell formation of monazite around the ceria. A key difference that was representative of the bulk sample, is the depleted quantity of cerium in the glass phase, here approximated to 1.5 mol.%. No larger areas of separated glass were accessible at the sample surface to measure a bulk glass composition, the surface featured a substantial crystalline content, mostly cerium monazite, where it becomes more energetically favorable for cerium to partition into ordered structures.

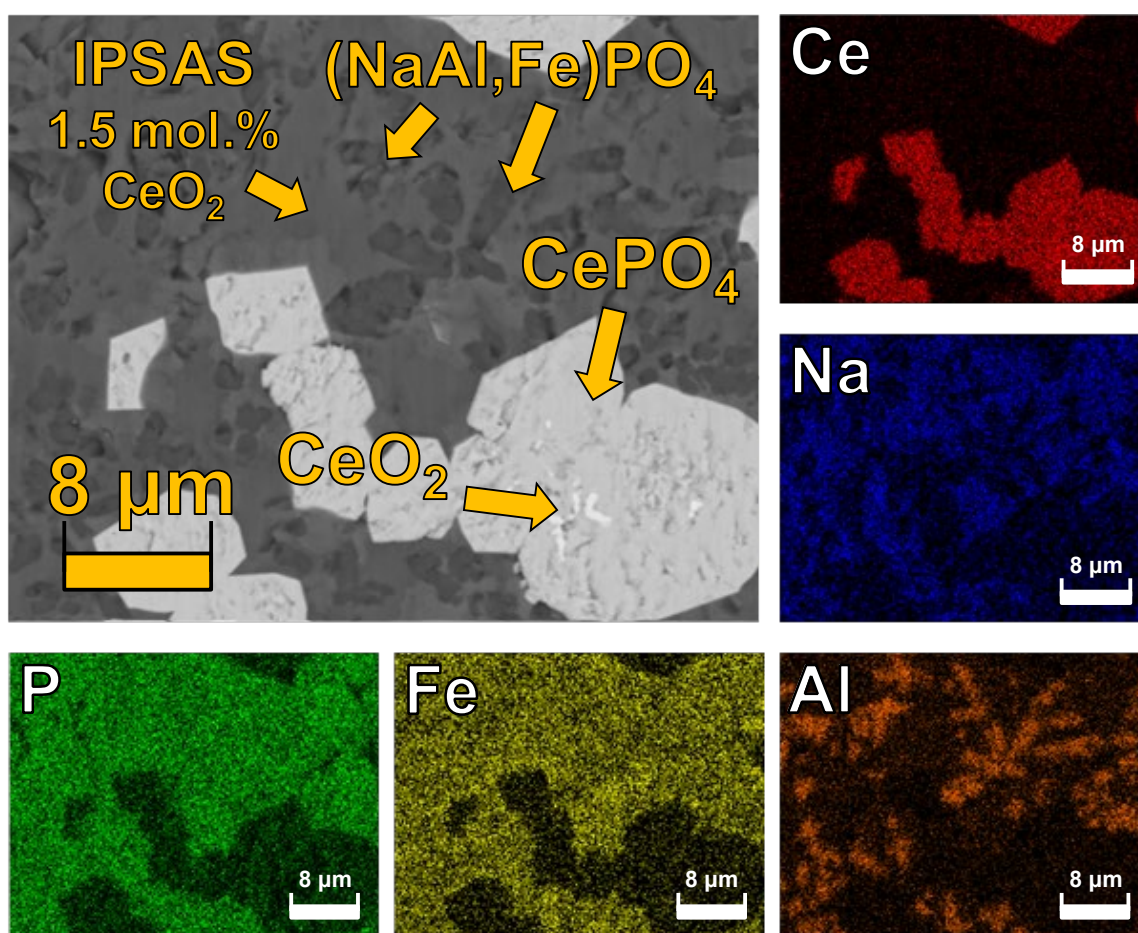


Figure 4.7.F - Backscattered Electron micrograph (top left) of IPSAS 34 mol.% simulant loaded material melted at 1350 $^{\circ}\text{C}$, demonstrating formation of minor secondary crystalline phase. The elemental EDX maps for marked species are also presented to the right and bottom edges.

SIP loaded with 35 mol.% and melted at 1450 °C demonstrated retention of the high aluminium concentrations (25 mol.% overall) in the amorphous glass phase, see **Figure 4.7.G**. Cerium monazite remains the primary crystalline phase, represented by the light grey angular particles, with some sparse sodium iron phosphate micro-crystallites distributed throughout the glass matrix. With such a significant development of crystalline monazite, the glass phase is depleted of cerium content, as indicated by the marked region with a measured ceria content of approximately 2.2 mol.%. Iron is primarily concentrated in the glass phase, though some local concentrations can be observed at the sodium iron phosphate sites. The SIP 35 mol.% loaded sample melted at 1450 °C, features a minor development of porosity (left side of BSE micrograph) and some cracking across the surface. While this indicates a degree of mechanical instability, several samples experienced minor fractures during the multi-stage grinding and polishing process.

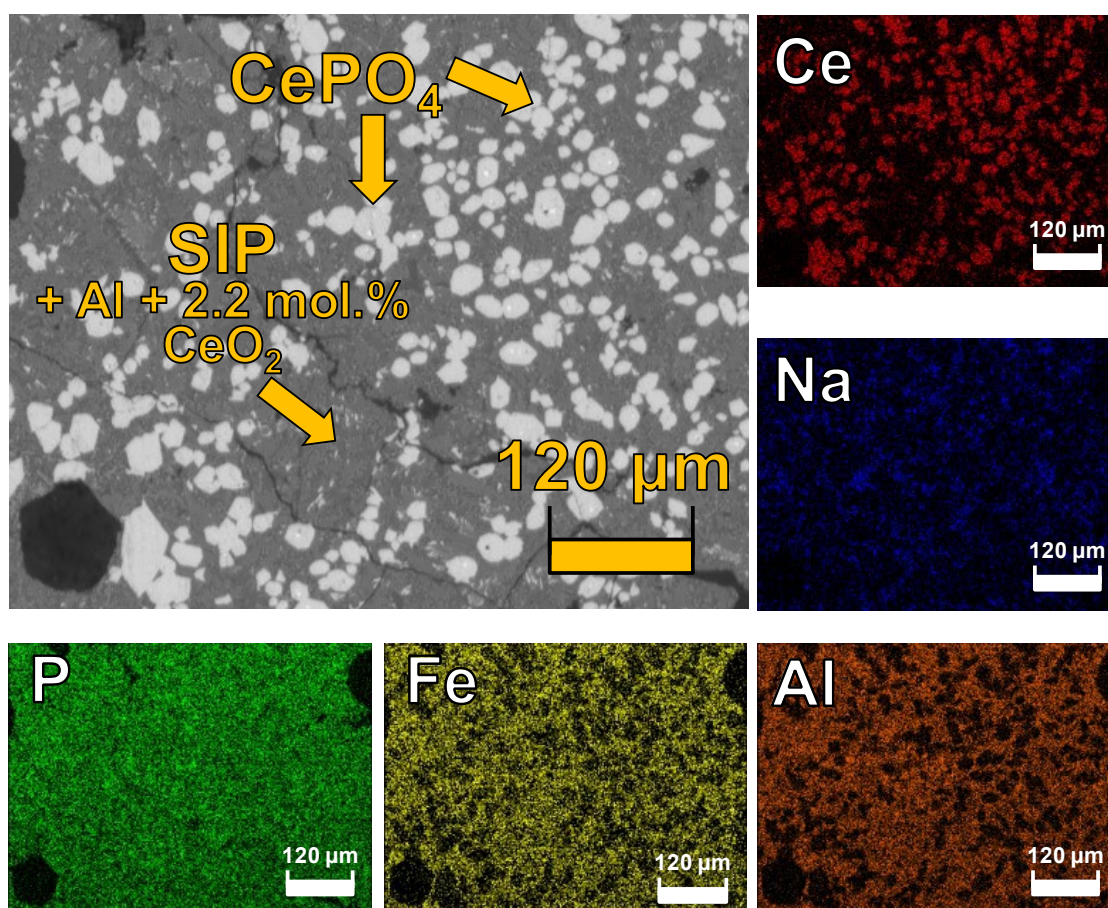


Figure 4.7.G – Back Scattered Electron micrograph (top left) of SIP 35 mol.% simulant loaded material melted at 1450 °C, showing broad scale separation of monazite and Al rich amorphous phase depleted in Ce. The elemental EDX maps for marked species are also presented to the right and bottom edges

Samples identified as having experienced a development of high porosity, bear characteristic resemblance to the microstructure of the SIP 35 mol.% simulant waste loaded sample melted at 1250 °C, **(i) Figure 4.7.H**, with some pores larger than 500 µm in diameter and the majority ranging between 100 – 250 µm in diameter. While the evolution of ammonia gas during early melting stages can cause foaming and bubble development, in the later stages of the glass melting schedule, redox effects between the oxide constituents of the glass melt could also lead to evolution of gaseous oxygen in the presence of cerium [30–32]. The brighter appearance of pixels in the non-porous regions represents cerium monazite and undigested ceria in the core-shell arrangement, with a relatively low proportion of amorphous glass phase and crystalline sodium iron phosphate.

Acquisition of bulk EDX composition was hindered by separation and aggregation of larger crystallites of cerium monazite for several samples, leaving local surface regions with artificially elevated measured ceria content, such as in SIP 16 mol.% simulant loaded material melted at 1450 °C, see **(ii) Figure 4.7.H**. Monazite crystallites with diameter 40 – 80 µm form in local regions, leaving a sparse web of dendritic monazite structures in the remaining glass matrix, such that the bulk area local to the dendrites has a lower measured molar ceria content, as compared to the larger aggregates. In such examples, care was exercised to include analysis points to account for a sufficiently representative region of the bulk material.

The dendritic monazite structures were of a characteristic monazite cross or ‘cruciform’, crystallite morphology, as can be observed for a high magnification micrograph of SIP 16 mol.% simulant loaded sample melted at 1350 °C, see **(iii) Figure 4.7.H**. Evolution of the cruciform morphology has been well documented in literature for monazites, though the dendritic arrangements is more typical of secondary phases also forming as polymorphs for sodium phosphate and sodium iron phosphate materials [14,33]. Due to their small relative size with widths of 2 – 4 µm, it was not possible to extract a precise EDX composition of the cruciform crystallites, but the morphology, bright phase contrast, a strong detection of cerium and phosphorous in the broad scale EDX map was indicative of cerium monazite.

The development of cruciform monazite dendrites occurred in SIP and IPSAS series, primarily following the onset of crystallisation at batch loadings above 16 – 25 mol.% CeO₂. The IPSAS 25 mol.% simulant loaded material melted at 1450 °C is one such example demonstrating the broader scale of dendritic structures, see **(iv) Figure 4.7.H**. As the only primary crystalline phase for the IPSAS 25 mol.% simulant sample melted at 1450 °C, identification as cerium monazite also agreed well with the pXRD study, see **Section 4.6.1**.

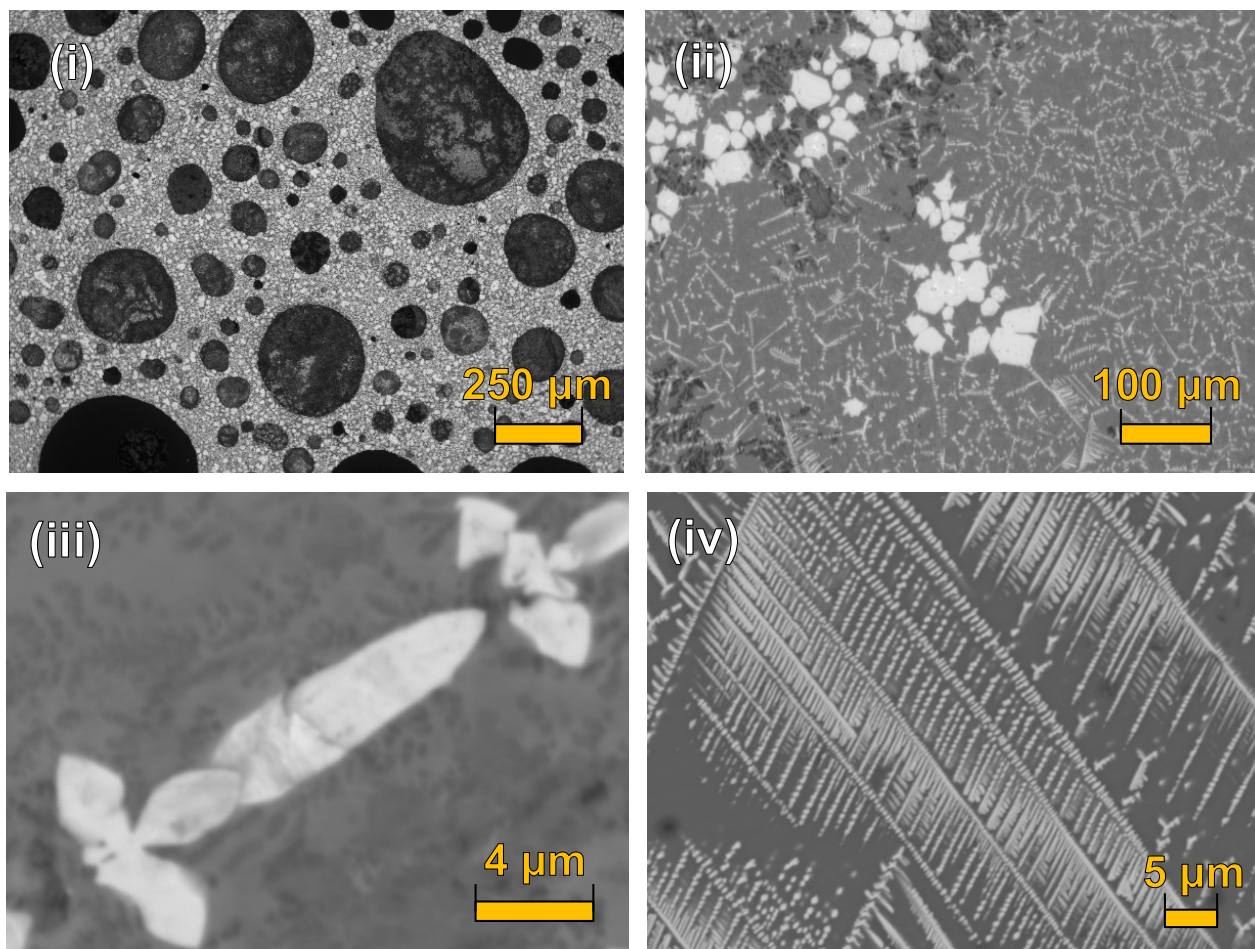


Figure 4.7.H - Back-scattered electron micrographs demonstrating high porosity SIP_35_1250 (i); aggregation of large monazite crystallites SIP_16_1450 (ii); high magnification of cruciform monazite crystallite SIP_16_1350 (iii); dendritic monazite cruciform morphology IPSAS_25_1450 (iv).

4.7.3 BSE semi-quantitative analysis

Using the code and computer driven method as outlined in **Section 3.9.2**, a small study was conducted with the most heavily crystallised monolithic samples, as prepared for SEM. These were selected due to their heterogenous, multiphase assemblage, and well-defined crystallisation, with all phases differing in atomic weight and therefore exhibiting an optimal degree of phase contrast. Materials loaded with 43 mol.% simulant were not selected for analysis with this method, due to their highly porous microstructure. 25 BSE micrographs were collected in a pseudo-random sampling fashion across the sample surface, with the code employed to delineate the separate phases and quantify the relative average area ratios using pixel counting. High simulant loaded SIP materials were not analysed using this method as there was very poor phase contrast between crystalline sodium iron phosphate and the glass matrix phase, such that the histogram peaks would have a significant overlap.

With the aforementioned ideal characteristics in high simulant loaded IPSAS samples where no sodium iron phosphate crystallised, three well-defined grey value histogram peaks were demarcated for the glass (darkest), cerium monazite, and undigested ceria (brightest) phases, with clear distributions of grey values and no peak overlaps, see **Figure 4.7.I**. The characteristic core-shell microstructure of crystalline cerium monazite forming around undigested ceria grains can be identified by the green and blue phases as marked in the phase colour map.

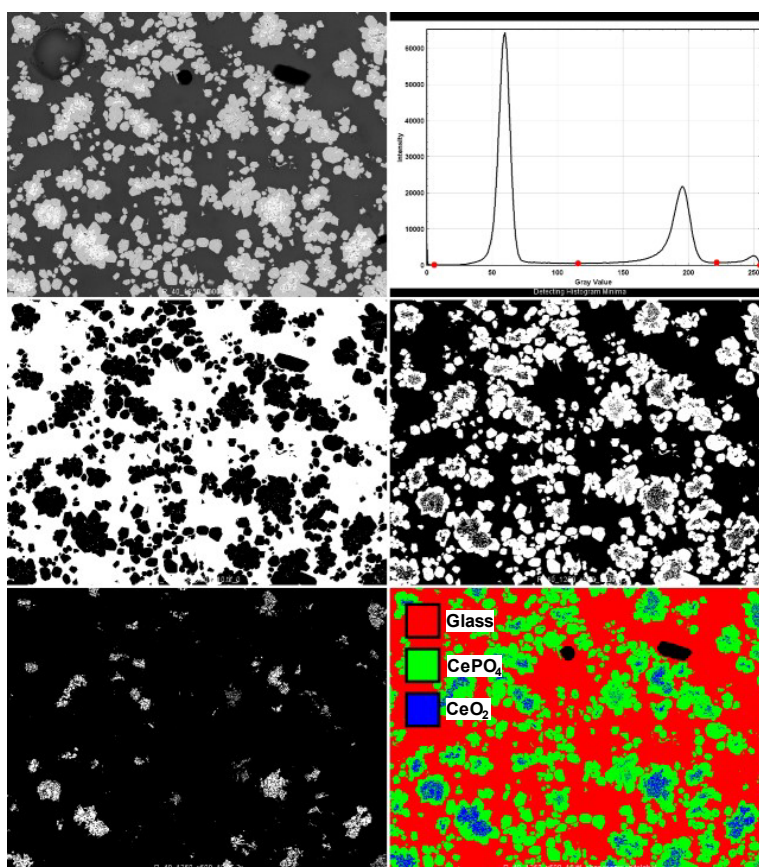


Figure 4.7.I – Single image phase-by-phase semi-quantitative areal analysis for IPSAS 34 mol.% loaded material melted at 1250 °C. Top left – original BSE image, top right – histogram, middle left – glass phase, middle right – monazite, bottom left – ceria, bottom right – phase colour map.

IPSAS 25 mol.% simulant loaded sample melted at 1450 °C was exhibiting formation of dendritic monazite cruciform crystallites, see (iv) **Figure 4.7.H**, and no other crystalline phases. However, due to the small width of the dendrites, it was necessary to collect BSE images at higher magnifications in order to resolve all features. The pseudo-random sampling method still followed, covering a grid area representative of the entire sample surface. During analysis, it was noted that the monazite peak for the grey value histogram was relatively broad, between values of 148 – 226, see **Figure 4.7.J**. The peak corresponding to the glass phase was sharp and well defined.

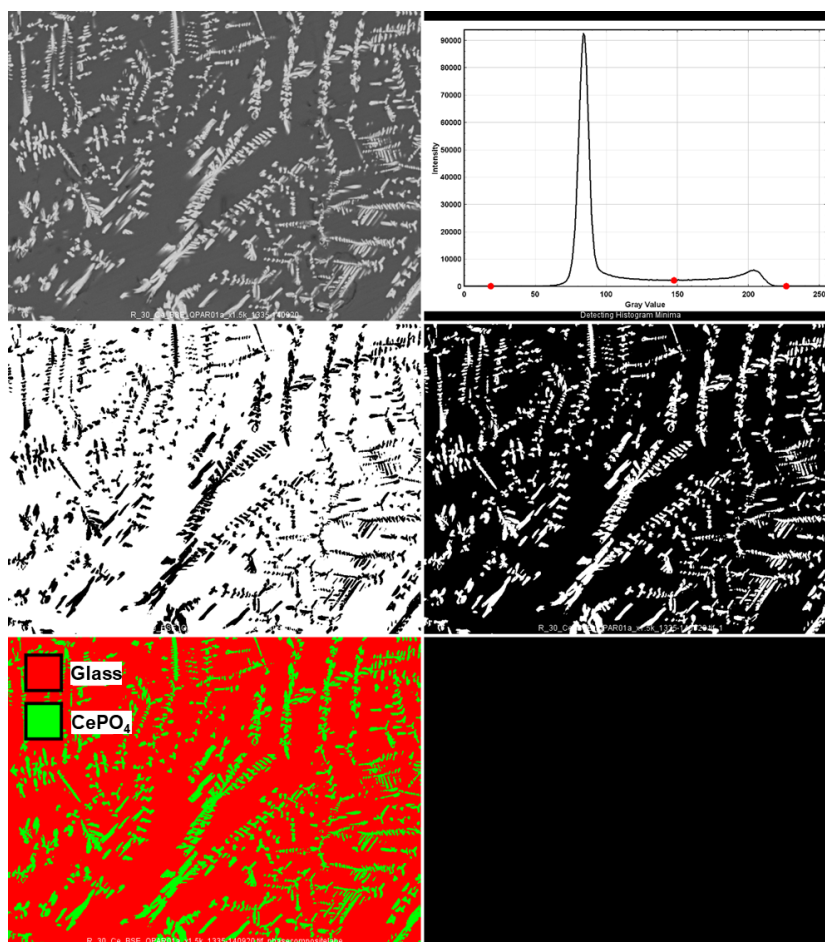


Figure 4.7.J – Single image phase-by-phase semi-quantitative areal analysis for IPSAS 25 mol.% loaded material melted at 1450 °C. Top left – original BSE image, top right – histogram, middle left – glass phase, middle right – monazite, bottom left – phase colour map.

The most challenging assemblages to measure using the image-based quantification method, were those containing sodium iron phosphate. With very small crystallite sizes of 2 – 8 μm , a dark contrast of grey values, close to that of the glass phase and the accompany significantly larger crystallites of monazite, it was not adequately recognised as a discrete phase by the first generation of code. A middle-high magnification was selected as a compromise, as to not let the larger monazite crystallites occlude representative regions, but still allow for determination of the sodium iron phosphate phase. It was also necessary to revise the histogram analysis code to manage cases such as these, with slight contrast overlap. A more sophisticated approach was taken to allow definition of the number of phases present in the sample image set, histogram minima pins were permanently applied to the lowest and maximum grey values, and the minima calculating function was adjusted to analyse the first derivative of the raw histogram data. Application of the revised code is demonstrated for the IPSAS 34 mol.% simulant loaded composition melted at 1350 °C, see

Figure 4.7.K. It can be noted that the narrow, low intensity grey value histogram peak attributed to sodium iron phosphate has some overlap with the distribution of the glass phase peak, reducing the confidence with which measurements can be reported, though it is beyond the full width at half maximum in this example. The undigested ceria phase is represented by a sharp spike at the maximum grey value end of the histogram. This is attributed to the saturation of the microscope BSE detector following the adjustment of gain and contrast to resolve the sodium iron phosphate phase. As ceria is the constituent with the brightest phase contrast, this saturation has no significant impact on analysis, since the ceria area pixels are still counted, just with a majority at a maximum grey value of 255.

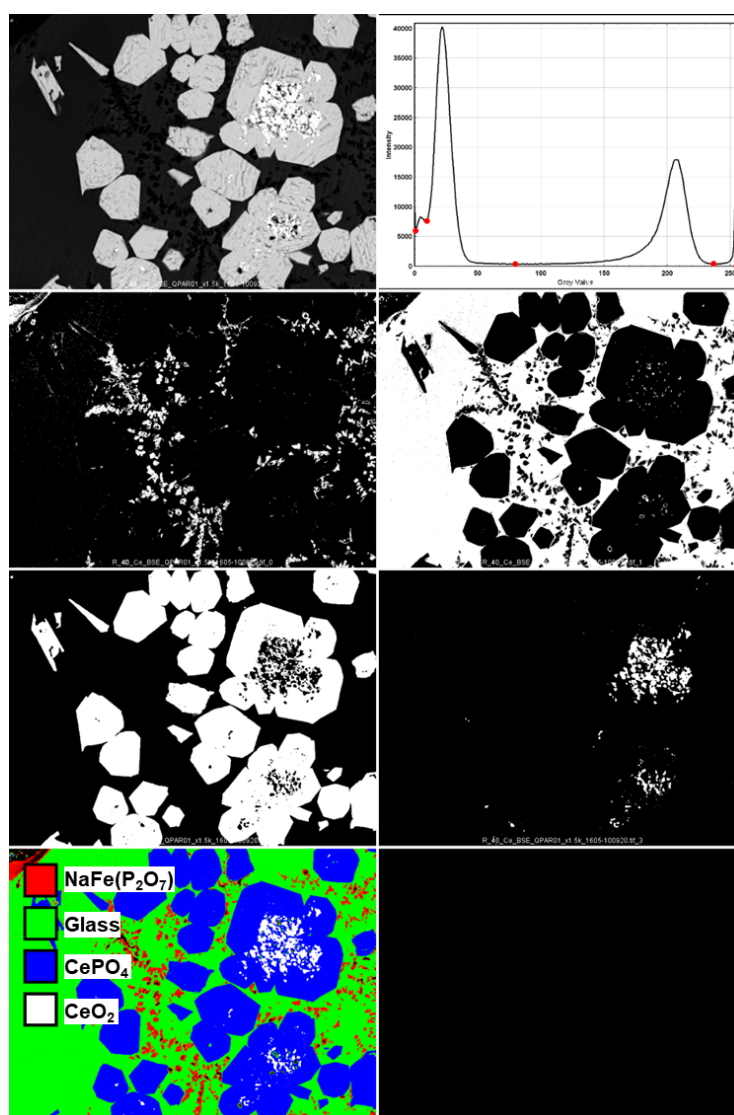


Figure 4.7.K - Single image phase-by-phase semi-quantitative areal analysis for IPSAS 34 mol.% loaded material melted at 1350 °C. From left to right and top to bottom: Original BSE image, histogram, NaFe(P₂O₇), glass phase, monazite, ceria, phase colour map.

Results calculated from the average area measurements by pixel counting, reflected the relative phase assemblages, with only IPSAS 34 mol.% melted at 1350 °C and 1450 °C featuring the fourth phase as secondary crystallised sodium iron phosphate, see **Table 4.7.A**. Glass constituted the majority phase by assumed volume, in all cases apart from those where sodium iron phosphate crystallised. Cerium monazite was the majority crystalline phase across the series, apart from IPSAS 34 mol.% simulant melted at 1350 °C, where sodium iron phosphate formed a larger majority by volume. Undigested ceria was present as the minor crystalline phase in all samples except for IPSAS 25 mol.% loaded simulant melted at 1450 °C, where the ceria was totally incorporated. As a comparison to the spike Rietveld pXRD based quantification method, **Section 4.6.2**, the measurement of IPSAS 25 mol.% sample melted at 1350 °C was assessed. It should be noted that the Rietveld method calculates a weight percentage for phases present, while the image-based method results in a volumetric assemblage. As the glass phase composition and density varies with composition and processing conditions, and the density of powder used for diffraction is not equivalent to that of a monolith, the comparison will remain between wt.% and vol.%. The inferred assemblage here was 64.9 vol.% glass, 34.5 vol.% cerium monazite and 0.6 vol.% undigested ceria, agreeing well with the results from Rietveld analysis, the measured assemblage constituted 66.8 wt.% glass, 31.8 wt.% cerium monazite and 1.4 wt.% ceria.

Table 4.7.A – Results for measurement of the most crystalline samples of IPSAS melt series, with the relative phase proportions presented as average volume %, derived from the average area % measurements collected by the analysis code.

Sample ID	Glass vol.%	Ce(PO ₄) vol.%	CeO ₂ vol.%	NaFe(P ₂ O ₇) vol.%
IPSAS_25_1250	77.1	21.0	1.9	0.0
IPSAS_34_1250	57.9	37.7	4.4	0.0
IPSAS_25_1350	64.9	34.5	0.6	0.0
IPSAS_34_1350	46.8	29.7	0.4	23.1
IPSAS_25_1450	67.7	32.3	0.0	0.0
IPSAS_34_1450	30.4	49.7	0.2	19.7

4.8 Mössbauer spectroscopy

Mössbauer spectra were obtained for the 0 mol.%, 8 mol.% and 25 mol.% variants of both SIP and IPSAS samples that were melted at 1350 °C, as these were the samples selected for all further spectroscopic analysis and chemical durability testing, due to their coverage of the compositional matrix. The Recoil software suite was used for fitting of spectra, applying a method adapted from Bingham et.al, whereby broad paramagnetic Lorentzian doublets are combined, four fit for the Fe²⁺ valence state and four for the Fe³⁺ valence state [13,34]. An example fit of SIP glass loaded with 0 mol.% CeO₂ and melted at 1350 °C can be seen in **Figure 4.8.A**, whereby the cumulative contributions of all paramagnetic doublets form a calculated model that satisfies the features of observed spectra well. All six Mössbauer spectra were collected and fitted in the same manner, the relative stacked plots for which can be seen in **Figure 4.8.B**. The relative intensities of the primary spectral features remained largely consistent, though the addition of greater ceria loadings resulted in reduction of absorption and a lower signal to noise ratio. Furthermore, the IPSAS 25 mol.%, 1350 °C sample was measured with slight increases in line width of the moderate intensity feature in the centre of spectra, and a significant broadening of primary features.

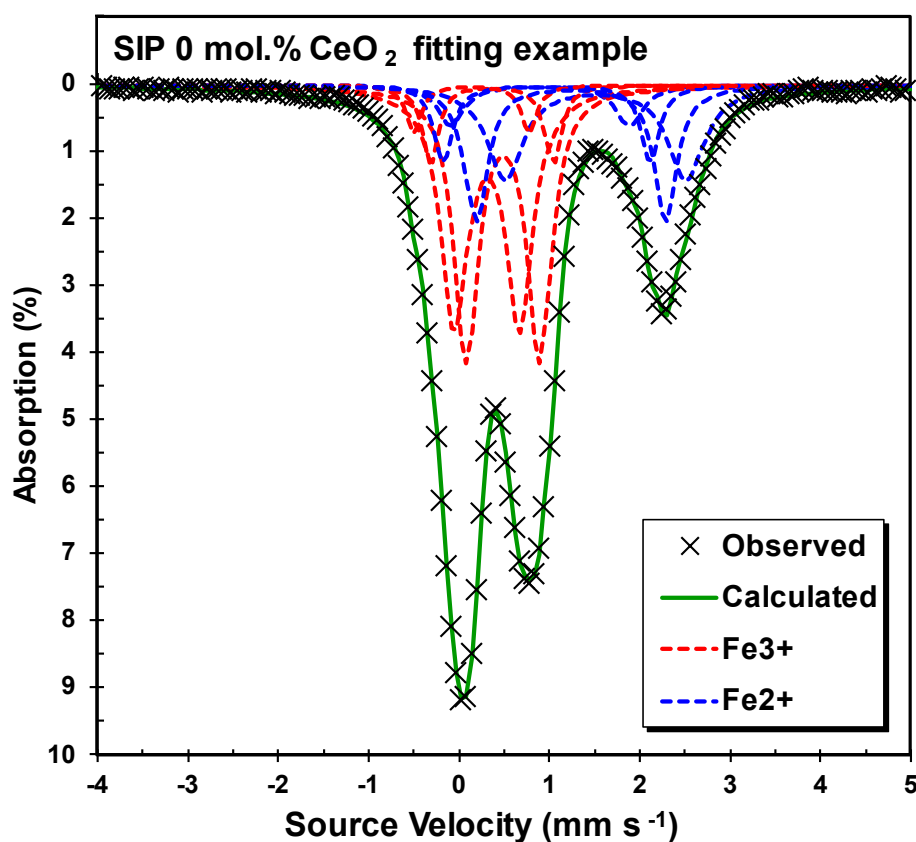


Figure 4.8.A – Example fit of Mössbauer spectrum of SIP_0_1350, showing eight doublets fit, one set of four for each of Fe²⁺ and Fe³⁺ contributions (dashed lines), with the total calculated fit (green)

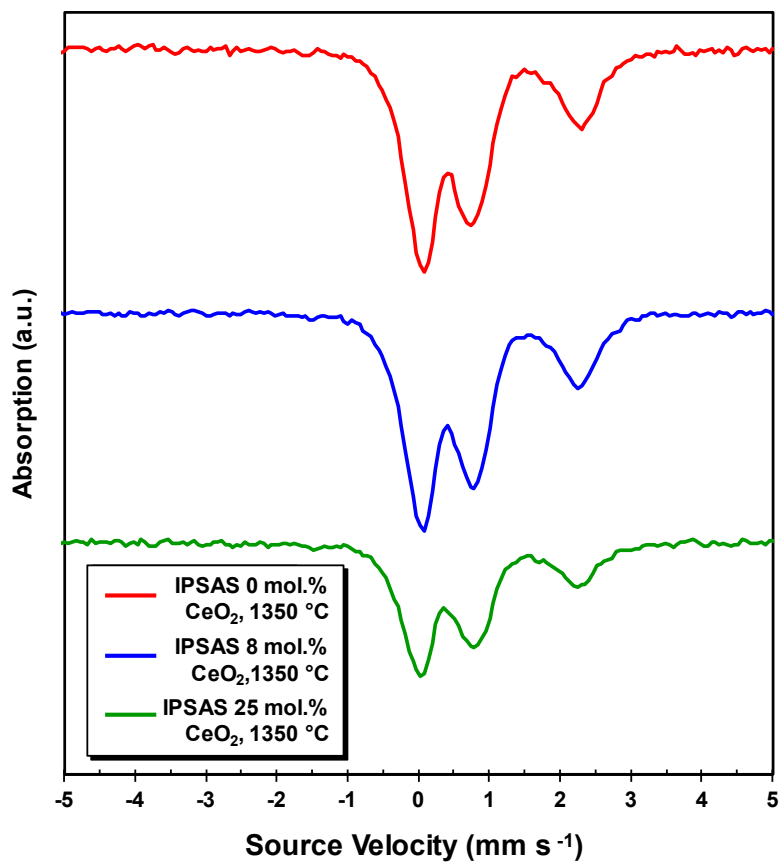
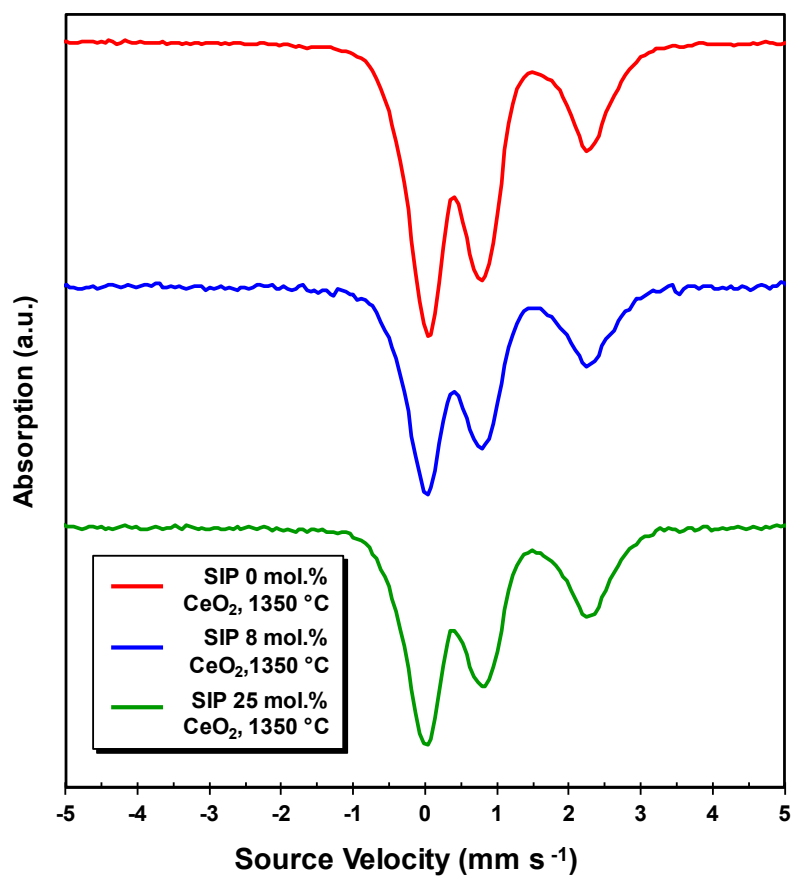


Figure 4.8.B – All folded Mössbauer spectra for SIP (top) and IPSAS (bottom) compositions measured.

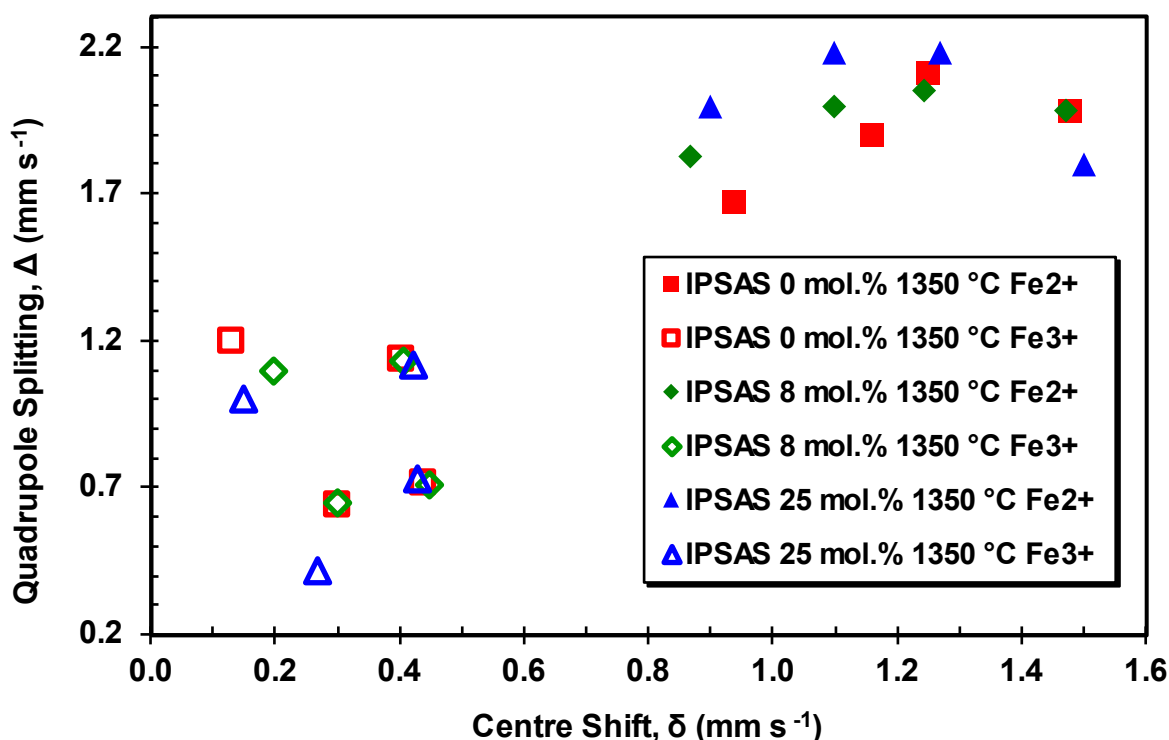
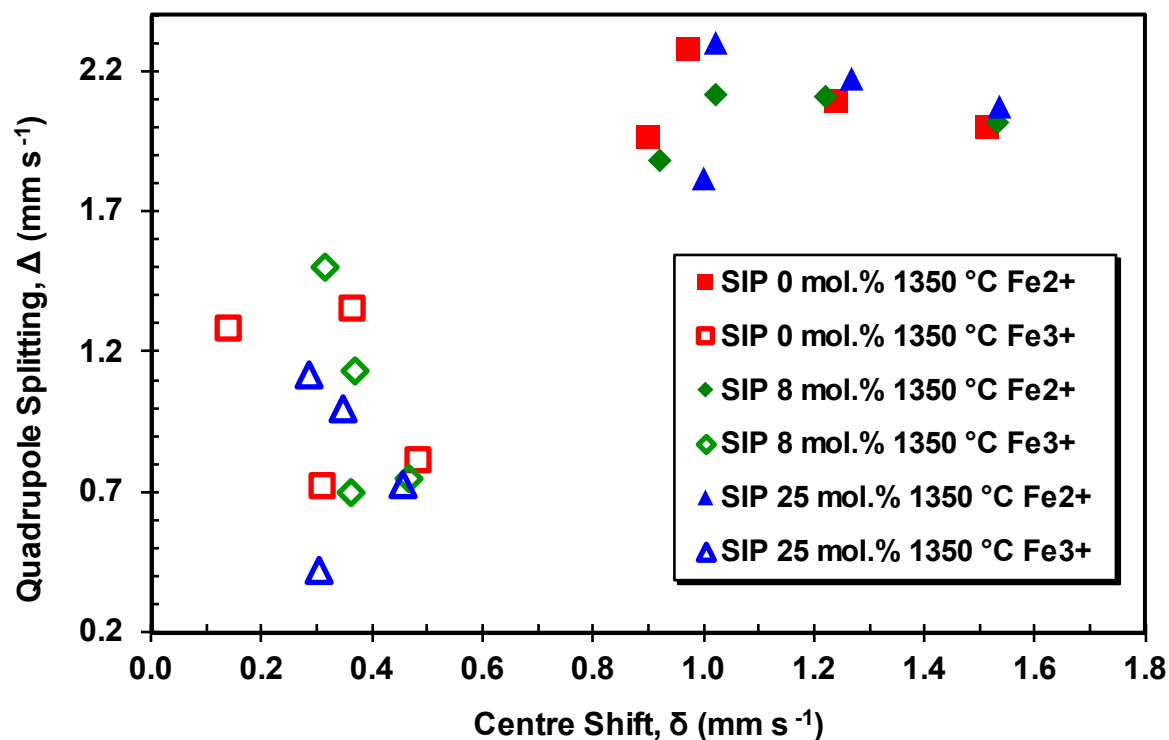


Figure 4.8.C – Plots showing the regions of centre shift vs quadrupole splitting for SIP (top) and IPSAS (bottom) samples, as assigned to the Fe²⁺ (shaded symbols) and Fe³⁺ (open symbols) valence states.

The doublet centre shift (CS, δ), quadrupole splitting (QS, Δ), and line width (LW, Γ) parameters for each valence state were measured, with assignment to valence state

informed by literature values obtained for iron containing minerals [35]. Plots of individually area weighted doublets, with CS as a function of QS, verified the assignment of features to such reported Fe²⁺ local regions (high CS 0.87 – 1.53 mm s⁻¹; high QS 1.67 – 2.30 mm s⁻¹) and Fe³⁺ local regions (low CS 0.13 – 0.49 mm s⁻¹; low QS 0.42 – 1.50 mm s⁻¹) [13,17,36–38], see **Figure 4.8.C**. With each region of doublets combined using area weighted averages, relative area assigned to each valence state could be combined to calculate an overall Fe²⁺/ΣFe ratio in each sample, see **Table 4.8.A**. Consideration was made for the recoil-free fraction ratio at room temperature, comparing the rigidity of bonds surrounding Fe³⁺ centres to that of Fe²⁺, a typical value established for sodium iron phosphate glasses of approximately 1.3 was used [13,36,39,40]. However, the exact fraction can only be confirmed with a temperature dependant study, and redox assessment should be made with reference to other techniques such as XAS. The corrected Fe²⁺/ΣFe redox values did not exceed 32% Fe²⁺ and experienced an overall slight increase with the batched addition of simulant waste loading, agreeing with literature for doped iron phosphate glasses [41,42]. The redox value of IPSAS loaded with 25 mol.% simulant waste, melted at 1350 °C is reported with lower confidence due to the noisier and more attenuated spectrum obtained, see **Figure 4.8.B**.

Table 4.8.A – Tabulated summary of area weighted Mössbauer spectra fitting parameters, with Fe²⁺/ΣFe redox ratio corrected for a recoil free fraction ratio of 1.3.

Sample ID	CS, δ (mm s ⁻¹) ±0.02	QS, Δ (mm s ⁻¹) ±0.02	LW, Γ (mm s ⁻¹) ±0.02	Area (%) ±2	Site	Fe ²⁺ /ΣFe ±1 (%)
SIP_0_1350	0.38	0.84	0.16	70	Fe ³⁺	23
	1.27	2.07	0.20	30	Fe ²⁺	
SIP_8_1350	0.36	0.90	0.17	64	Fe ³⁺	28
	1.28	2.05	0.18	36	Fe ²⁺	
SIP_25_1350	0.37	0.92	0.15	60	Fe ³⁺	31
	1.20	2.12	0.18	40	Fe ²⁺	
IPSAS_0_1350	0.37	0.86	0.15	62	Fe ³⁺	29
	1.28	1.97	0.19	38	Fe ²⁺	
IPSAS_8_1350	0.38	0.86	0.15	66	Fe ³⁺	26
	1.26	2.00	0.18	34	Fe ²⁺	
IPSAS_25_1350	0.37	0.81	0.17	59	Fe ³⁺	32
	1.24	2.05	0.20	41	Fe ²⁺	

4.9 Fe-K edge X-ray absorption spectroscopy

The SIP and IPSAS 0 mol.%, 8 mol.% and 25 mol.% ceria loaded glass samples melted at 1350 °C were measured at Fe-K edge using the NSLS-II 6BM beamline, Brookhaven, New York, to probe the iron valence and local structure via scattering of Fe 1s electrons, as per **Section 3.5**. Data were collected using step-sizes of 0.2 eV at the pre-edge (7108 – 7112 eV), edge (7112 – 7124 eV) and near-edge (7124 – 7160 eV) regions of the spectra; step size of 1.0 eV beyond these ranges for the extended fine-structure. Data were selected from these ranges for pre-edge deconvolution, see **Figure 4.9.A**, and EXAFS analysis.

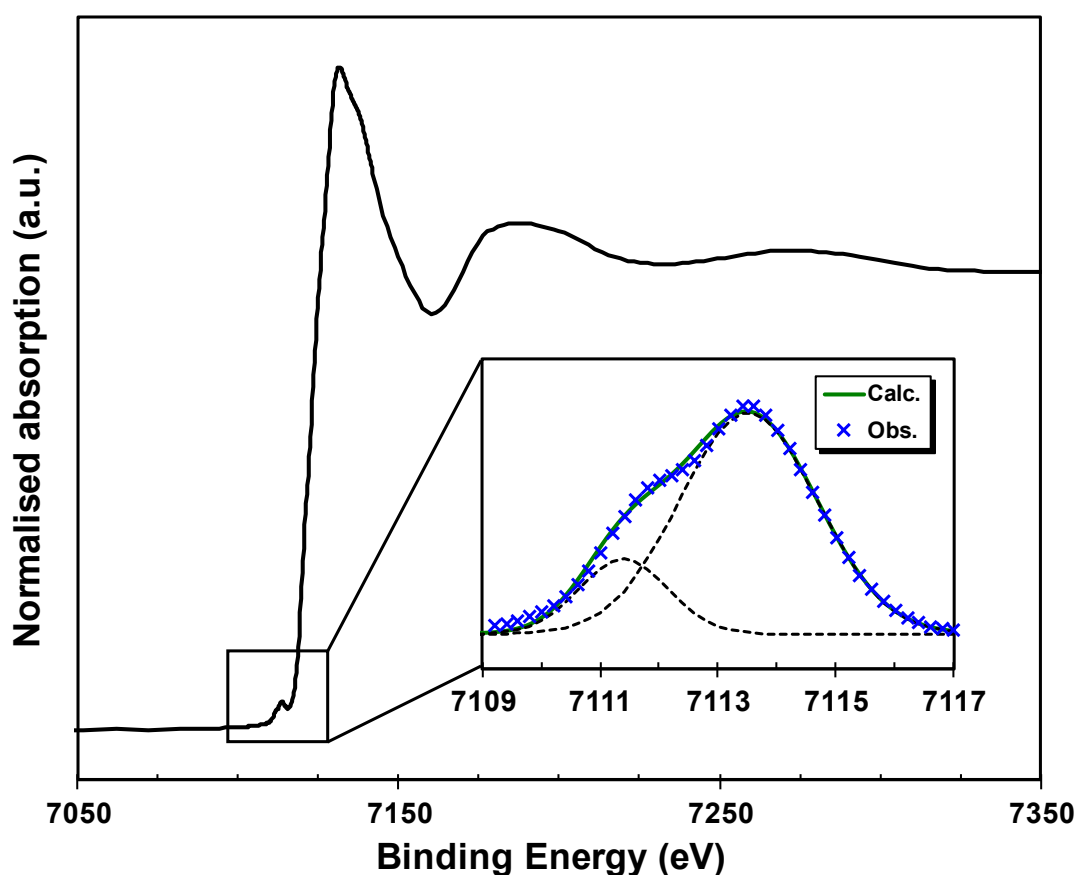


Figure 4.9.A – Location of the Fe-K pre-edge feature at 7109 – 7117 eV (inset) for IPAS 0 mol.% glass melted at 1350 °C, with example background-corrected fit.

4.9.1 Iron valence by pre-edge analysis

A clear pre-edge feature could be observed in all SIP and IPSAS spectra, with two distinct maxima at approximately 7112.1 eV and 7113.6 eV. For pre-edge fitting, a region of interest was selected between 7108 – 7118 eV, see **Figure 4.9.A**, to cover the entirety of the line shape. The feature position and shape remained relatively consistent across each compositional series, though the

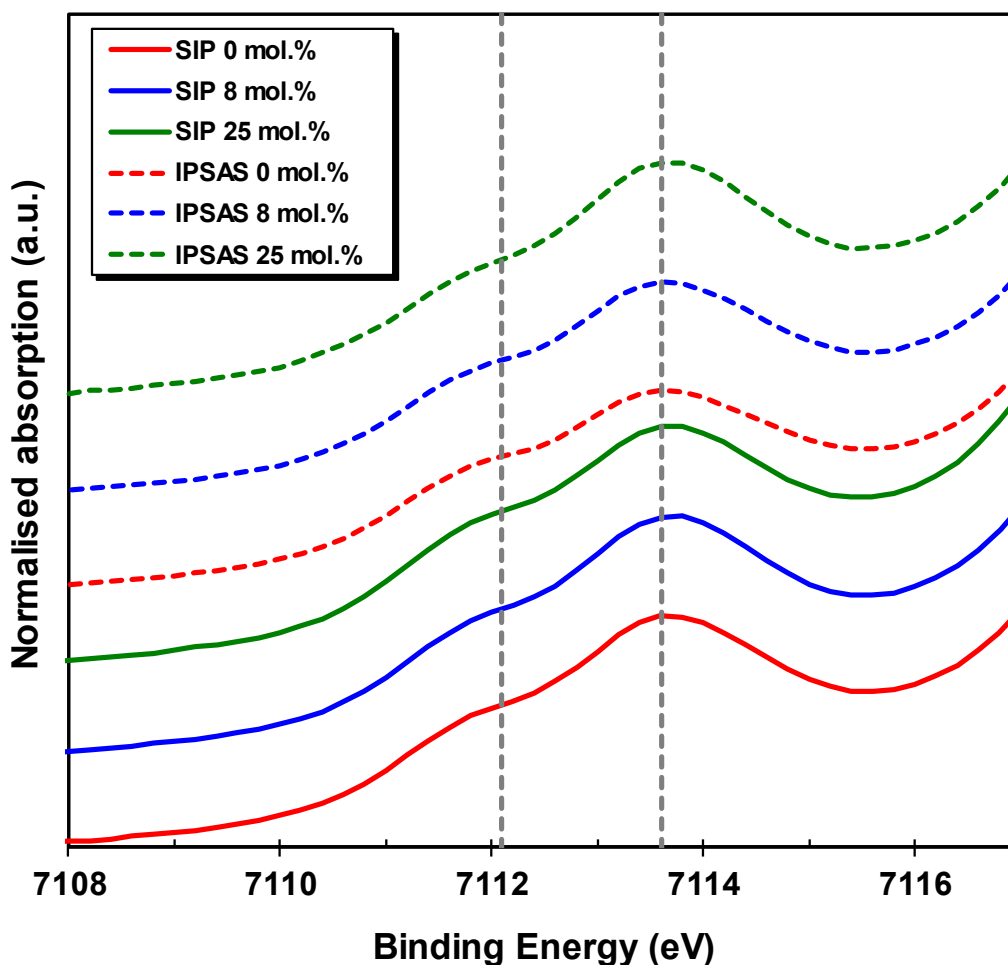


Figure 4.9.B – SIP and IPSAS 1350 °C melt series pre-edge stack, showing the deconvolution peak locations and slight shifts across the series (dashed grey lines). SIP data are presented in continuous coloured lines, with IPSAS data in dashed coloured lines.

IPSAS pre-edge features were notably less intense with a shift of the first pre-peak to a slightly lower binding energy, **Figure 4.9.B**. With the pre-peaks lying on the start of the rising Fe-K edge, it was necessary to fit a background as the leading edge of a Lorentzian peak aligned with the Fe-K edge. This was subtracted from the raw data, see **Figure 4.9.C**, before two pre-peak contributions were fitted using generalised reduced gradient (GRG) non-linear method, constrained to the pre-edge region, and optimising the fit for minimisation of the χ^2 parameter, see **Figure 4.9.C**. The area under each pre-peak was integrated, then used to weight the overall pre-edge feature centroid position.

Four spectroscopic standards were also measured at the NSLS-II 6BM beamline; two for Fe(II) or Fe²⁺ (iron carbonate as FeCO₃ and staurolite as [Fe,Mg]₂Al₉Si₄O₂₃); two for Fe(III) or Fe³⁺ (iron phosphate as FePO₄ and aegirine as NaFeSi₂O₆). The pre-edge features of these spectra were also fitted, as to allow for plotting of the centroid position as a function of total integrated

intensity, with Fe(II) and Fe(III) centroids at 7112.1 eV and 7113.5 eV adapted from a method by Wilke et.al [43], see **Figure 4.9.D**. Greater Fe(III) content means there is less charge associated with the iron atoms, therefore less screening is experienced by the inner electron shells. This results in a feature shift to a higher absorption energy. The FeCO₃ and staurolite standards were found to have a pre-edge centroid in very close proximity (within 0.09 eV) of the median Fe(II) line as proposed by Wilke et al., with the FePO₄ and NaFeSi₂O₆ standards also found with centroids close to the literature Fe(III) median (within 0.14 eV). This larger 1.6 eV spread between the Fe²⁺ standards and Fe³⁺ standards is due to the configuration and properties of the synchrotron and beamline used, independent of those used to obtain literature values. As pure standards with iron in each valence state, a high confidence is still held that pre-edge features with centroids closer to the 7112.0 – 7112.1 eV range contain a greater proportion of Fe(II) and those closer to the 7113.5 – 7113.6 eV range contain more Fe(III). The SIP and IPSAS centroid data fell within a very discrete range of 7113.0 ± 0.1 eV. The magnified region inset to **Figure 4.9.D**, shows the relative centroid positions for all measured samples. For SIP wastefoms melted at 1350 °C a very small increase of integrated intensity arises with increased loading of ceria simulant, with the centroid position shifting to a lower binding energy with respect to greater simulant loadings. The IPSAS series shows a more substantial approximate upward trend of integrated intensity, as the waste loading is increased. Contrary to that of the SIP materials, the centroid position of the IPSAS series shifted to higher energies with greater simulant loading.

The individual pre-peak parameters are listed in **Table 4.9.A**, for all samples and standards measured with reference to overall feature centroid position and area. Calculation of the Fe²⁺/ΣFe ratio was permitted using valence standard lines. While the average valence results as found via XAS measurements did not agree with those found by Mössbauer spectroscopy, the narrow range of results, whereby the average iron valence changes only slightly within the melt series, was reflected well. In agreement with the Mössbauer study **Table 4.8.A**, the SIP series experienced a redox shift to greater Fe²⁺ content at higher loadings, with the 0 mol.% simulant base glass found to have a slightly reduced Fe²⁺ content. The highest Fe²⁺ content was achieved with the SIP 25 mol.% sample. The IPSAS series average valences as determined by XAS followed the general decreasing Fe²⁺ trend with increasing loading, as found via Mössbauer spectroscopy for IPSAS 0 mol.% and 8 mol.% simulant loadings. However, while this trend did not continue for the IPSAS 25 mol.%, as determined through the Mössbauer study, the XAS pre-edge measurement indicated that the lowest Fe²⁺ content was achieved at this higher loading.

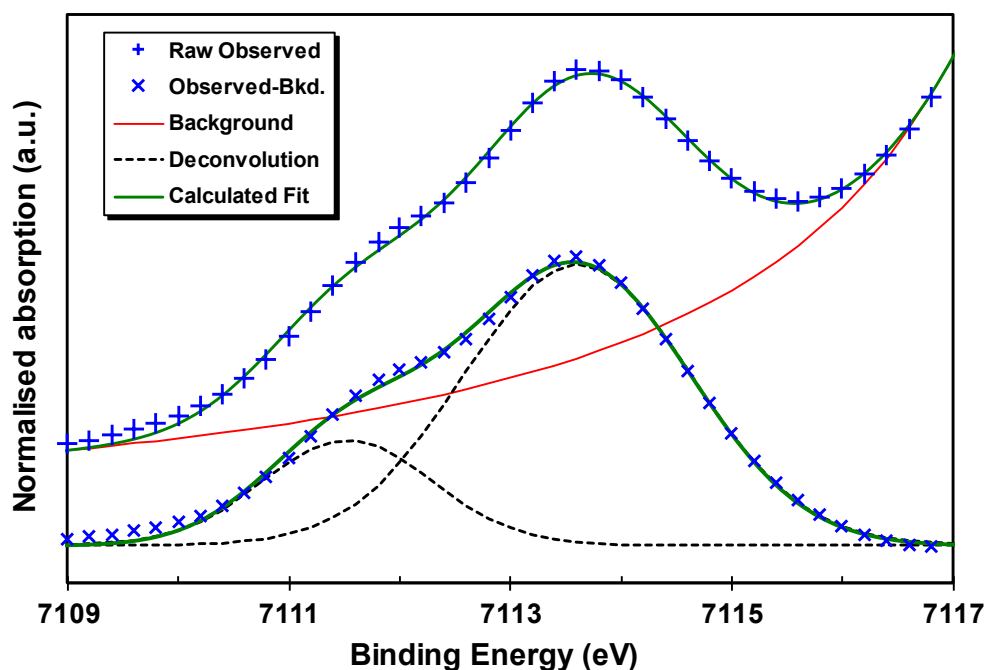


Figure 4.9.C – Example pre-edge fitting for SIP 0 mol.% 1350 °C glass, showing full process from background subtraction to fit of devolved contributions.

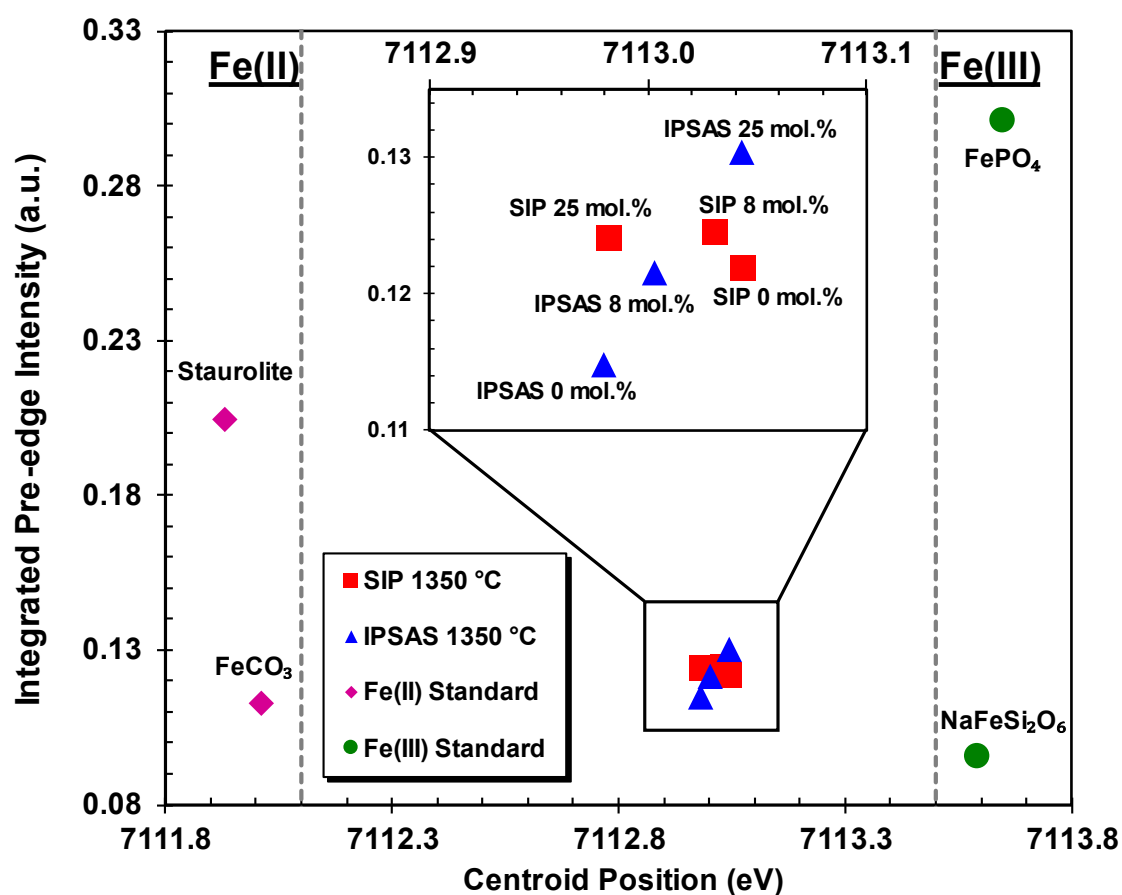


Figure 4.9.D – Pre-edge fitting parameter summary, in adapted method of Wilke et al. (grey dashed lines), pre-edge fitting was also applied to data for Fe(II) and Fe(III) reference standards as to allow for delineation of Fe(II) and Fe(III) regions. A magnified region of the data associated with SIP and IPSAS pre-edge fits is inset.

Table 4.9.A – Tabulated results for each pair of deconvoluted pre-edge peaks, including the measured Fe(II) and Fe(III) standards. Data is presented with weighted pre-edge centroid and Fe(II) ratio, as obtained using the valence standard lines. χ^2 did not exceed 0.01.

Sample ID	Peak parameters				Combined Area	Centroid (eV)	χ^2	Fe ²⁺ / Σ Fe (%)*
	Height (a.u.)	Position (eV)	FWHM (eV)	Area (a.u.)				
SIP_0_1350	0.0138	7111.53	0.7715	0.0267	0.1219	7113.04	0.00003	33
	0.0370	7113.61	1.0256	0.0951				
SIP_8_1350	0.0146	7111.53	0.7631	0.0278	0.1244	7113.03	0.00003	34
	0.0384	7113.60	1.0031	0.0966				
SIP_25_1350	0.0159	7111.56	0.7619	0.0304	0.1240	7112.98	0.00003	37
	0.0372	7113.59	1.0034	0.0937				
IPSAS_0_1350	0.0109	7111.40	0.7523	0.0206	0.1147	7112.98	0.00005	37
	0.0322	7113.52	1.1639	0.0941				
IPSAS_8_1350	0.0112	7111.34	0.7483	0.0210	0.1214	7113.00	0.00005	35
	0.0353	7113.53	1.1335	0.1004				
IPSAS_25_1350	0.0119	7111.33	0.7755	0.0231	0.1303	7113.04	0.00007	32
	0.0397	7113.56	1.0781	0.1072				
FeCO ₃ Standard	0.0246	7111.20	0.7023	0.0433	0.1126	7112.01	0.00003	100
	0.0233	7112.87	1.1860	0.0693				
Staurolite Standard (Fe,Mg) ₂ Al ₉ Si ₄ O ₂₃	0.0689	7111.44	0.6893	0.1190	0.2045	7111.93	0.00008	100
	0.0383	7112.80	0.8910	0.0855				
FePO ₄ Standard	0.0118	7111.38	0.8125	0.0240	0.3545	7113.60	0.00137	0
	0.1586	7113.77	0.8313	0.3305				
Aegirine Standard NaFeSi ₂ O ₆	0.0218	7112.85	0.9588	0.0524	0.0959	7113.59	0.00003	0
	0.0240	7114.27	0.7246	0.0436				

*Iron redox condition is quoted here as a calculated value, though it is recognised that the coordination environment strongly effects measured intensity. In text the information has been used to rank the relative redox conditions.

4.9.2 EXAFS analysis

A study of the EXAFS region for the Fe-K edge data was conducted to evaluate the first shell single scattering paths for X-ray photoelectrons, and to permit further discussion of the local structure and static disorder surrounding the central iron absorber atoms. Care was taken to not over-interpret the fitting results with the limited data available for these primarily amorphous compositions, focusing only on the first set of Fe – O nearest-neighbour single scattering paths. As the primary structure was non-crystalline, tabulated crystallographic data from literature for a combined Fe(II), Fe(III)NaSi₂O₇ aegirine structure [44] was applied to a FEFF calculation, as per the methods and software discussed in **Section 3.5.4**. The calculation utilised iron as the central absorber for the -K edge, initiated with a large cluster size of 8 Å, and a maximum path length of 6 Å. Initial fits of the first two nearest neighbour paths were applied to crystalline standards measured at the beamline, as to permit refinement of a realistic value for the amplitude parameter, S_0^2 . This value was taken forward and fixed for analysis of amorphous samples, with a representative path length selected from the first set of oxygen single scattering paths generated by the FEFF calculation. The coordination number was allowed to vary, with restraints placed on maximum deviation of the fitted scattering path and edge position. A Fourier transform was parameterised to calculate the fit to the data as arranged by $\chi(k)$, representing the number of degrees of freedom for the EXAFS dataset, with a Hanning window [45] between k values of 3 – 11 Å⁻¹, as to cover enough independent points for the number of variables to be calculated. Another Hanning window was applied to fit the data within real-space, $|\chi(R)|$ as a function of radial distance, within the range of the first scattering paths between 1.20 – 2.85 Å. Finally, a bond valence sum (BVS) was calculated following the fit, to aid in assessment of the physical properties of such a local structure [46,47], as per **Equation 4.9.A** and **Equation 4.9.B**.

$$V_x = \sum s_{xy}$$

Equation 4.9.A – Total bond valence for atom x , V_x , as a sum of the valence for each bond s , between atom x and other core-shell atoms, y . In the work here, the sum represents a factor of the coordination number for the first shell Fe – O bonds.

$$s_{xy} = \exp\left(\frac{R_{xy}' - R_{xy}}{b}\right)$$

Equation 4.9.B – The valence for each bond s_{xy} is obtained by taking the exponent of the difference between the tabulated ideal bond length R' , and fitted bond length R (Å), as divided by a tabulated parameter b , usually equal to 0.37 Å.

An example fit showing the application of a fit for the first set of core shell oxygen single scattering paths is shown in **Figure 4.9.E**, showing good agreement within the first scattering paths up to a radial distance of 2.3 Å. The features beyond this radial distance likely represent the first Fe – P, Fe – Fe and Fe – O – P scattering paths [48], though fitting these with high confidence was limited due to the weaker potentials associated with these greater distances and the increase in number of fitting variables such paths would introduce without being able to increase the number of independent points. The higher waste loading SIP and IPSAS series wastefoms were less concentrated in iron, as such, these absorption samples were prepared with a larger cross-section to permit absorption of comparable number of iron centres. However, this led to a slight attenuation of data in the EXAFS region, as reflected by poorer misfit parameters obtained for the high waste loading samples, see **Table 4.9.B**. Iron centres were found to have a coordination between that of tetrahedral and octahedral, with a slight favourability for a tetrahedral configuration.

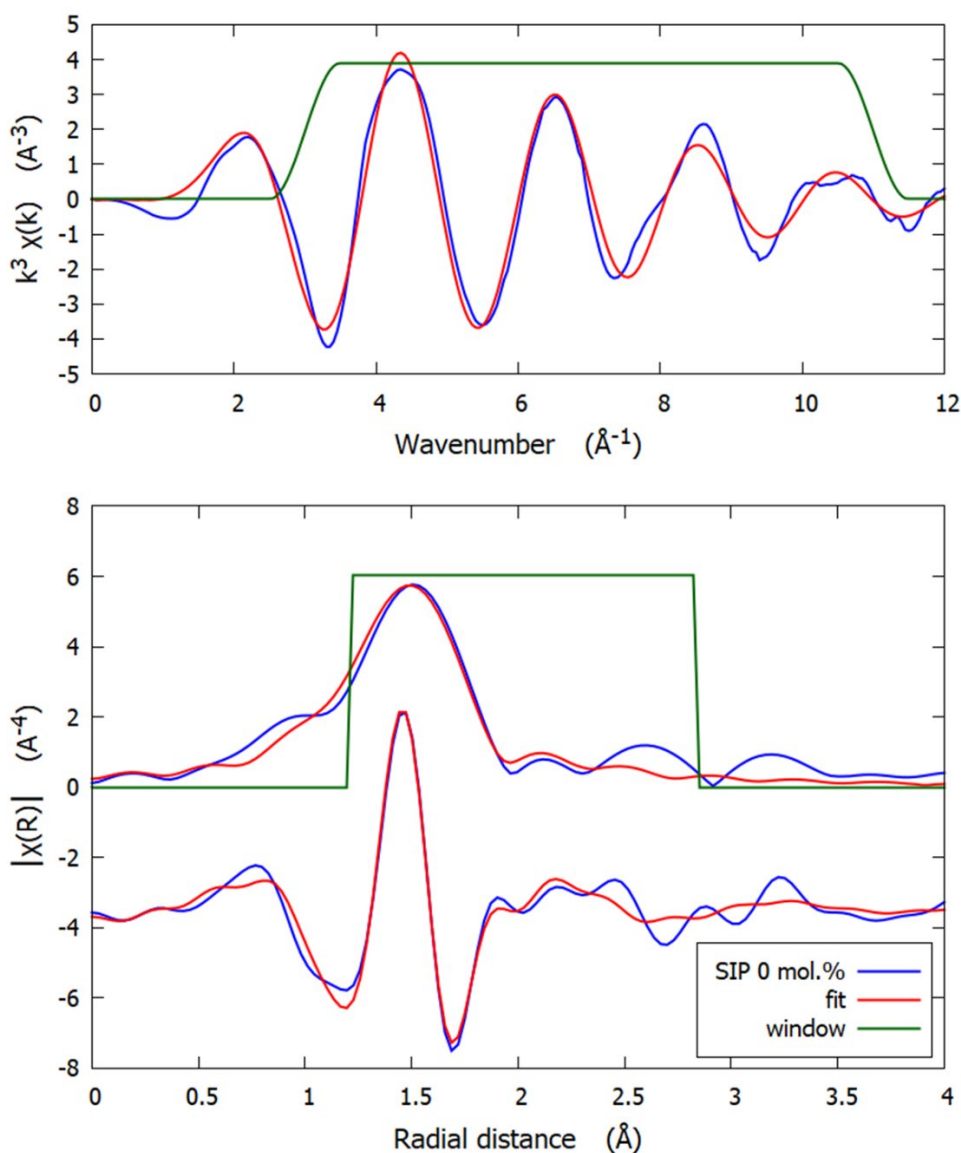


Figure 4.9.E – Example fit for the SIP 0 mol.% simulant glass melted at 1350 °C, showing the $\chi(k)$ Fourier transform (top) and radial distance of $|\chi(R)|$ (bottom).

Table 4.9.B – Tabulated results of Fe-K EXAFS region analysis, where E_0 is the shift in the position of the edge, S_0^2 is the amplitude parameter used for fitting, CN O_1 is the refined coordination number for the first shell oxygen single scattering path, $\sigma^2 O_1$ represents the mean square radial displacement or thermal parameter, R O_1 is the refined path length, a bond valence sum for this first shell of oxygen scatterers is included, and the statistical misfit R-factor was calculated. Errors are bracketed.

Sample ID	E_0 (eV)	S_0^2	CN O_1	$\sigma^2 O_1$ (Å)	R O_1 (Å)	BVS	R-factor
SIP_0_1350	-0.4 (2.2)	0.9	4.8 (0.8)	0.010 (0.003)	1.95 (0.01)	2.71	0.018
SIP_8_1350	-2.1 (2.6)	0.9	4.9 (0.9)	0.011 (0.003)	1.94 (0.02)	2.80	0.021
SIP_25_1350	-2.8 (2.7)	0.9	4.7 (1.0)	0.012 (0.003)	1.95 (0.02)	2.63	0.022
IPSAS_0_1350	0.7 (1.9)	0.9	5.2 (0.8)	0.009 (0.002)	1.96 (0.01)	2.82	0.015
IPSAS_8_1350	-3.0 (2.2)	0.9	4.8 (0.8)	0.009 (0.002)	1.96 (0.02)	2.63	0.018
IPSAS_25_1350	-4.6 (2.4)	0.9	4.6 (0.8)	0.010 (0.002)	1.94 (0.02)	2.65	0.019

The values for oxygen coordination are however reported with a significant error. The IPSAS series was found to have similar values for oxygen coordination, although IPAS 0 mol.% simulant waste loaded glass had a coordination number indicating that the local structure was more favourable to an octahedral configuration. The most tetrahedrally coordinated wastefoms were found to be the SIP 25 mol.% simulant sample and the IPSAS counterpart. Bond length for first shell oxygen scatterers was very consistent across the SIP and IPSAS series, all at 1.95 Å, within error. The bond valence sums gave reported values which fell within the same range of iron valence as found by Mössbauer spectroscopy and Fe-K pre-edge analysis, ranging between 20 – 37 % $Fe^{2+}/\Sigma Fe$ for the SIP series and 18 – 37 % $Fe^{2+}/\Sigma Fe$ for that of the IPSAS series. However, these values are reported with lower confidence than the ratios found via Mössbauer and pre-edge analysis methods, as the fits do not account for the effects of other scattering paths on the iron bond valence. With iron presence in the glass phase, the typical substitution of the P – O – P linkages for bridging oxygens is expected with Fe – O bonds and Fe – O – P bonds [48–50]. While conclusive evidence for the phosphorous to oxygen double scattering path was not obtained, the evidence of an oxygen coordination that is not typical of iron oxide crystal structures is indicative of first shell substitution, with oxygen configuration varying with the valence of substituted iron centres.

4.10 Chemical durability testing

The six samples of 0 mol.%, 8 mol.% and 25 mol.% simulant loaded SIP and IPSAS materials from spectroscopic studies were carried forward through for chemical durability testing. Sufficient quantities of glass were fritted, crushed, sieved, and washed, as per **Section 3.10.1** so that a consistent comparative calculated surface area to volume ratio of 1200 m^{-1} could be maintained throughout the experimental series.

4.10.1 PCT-B testing

PCT dissolution vessels were weighed and measured before and after each step of the preparation and dissolution experiment, as to verify the integrity of the vessel seals during heating and accelerated dissolution. During each sampling stage, aliquots taken from dissolution vessels were probed for pH, with an average of all triplicate series see **Figure 4.10.A**. The SIP sampling aliquots buffered to pH 5.8 – 6.0 over the course of the experiments, though it should be noted that a differently calibrated pH probe had to be used for day 3 sampling of SIP, so all average pH values were artificially reduced to 5.5 – 5.6 at this time point, including the control blank samples. IPSAS 0 – 8 mol.% simulant waste loaded sampling aliquots buffered to pH 2.0 – 2.1, indicating a significant change in solution chemistry and generation of protonating ions and acidic species as the experiment progressed. The IPSAS 25 mol.% simulant loaded sample aliquots buffered to a pH of 3.8 – 4.0, still strongly acidic, but indicating a lesser change in solution chemistry may have occurred. The use of a non-standard pH probe did also have the same effect on reducing the average aliquot pH for IPSAS samples for day 3. Due to the log scale nature of pH measurements, correcting data against the control sample blanks was not possible, they are simply used for reference here.

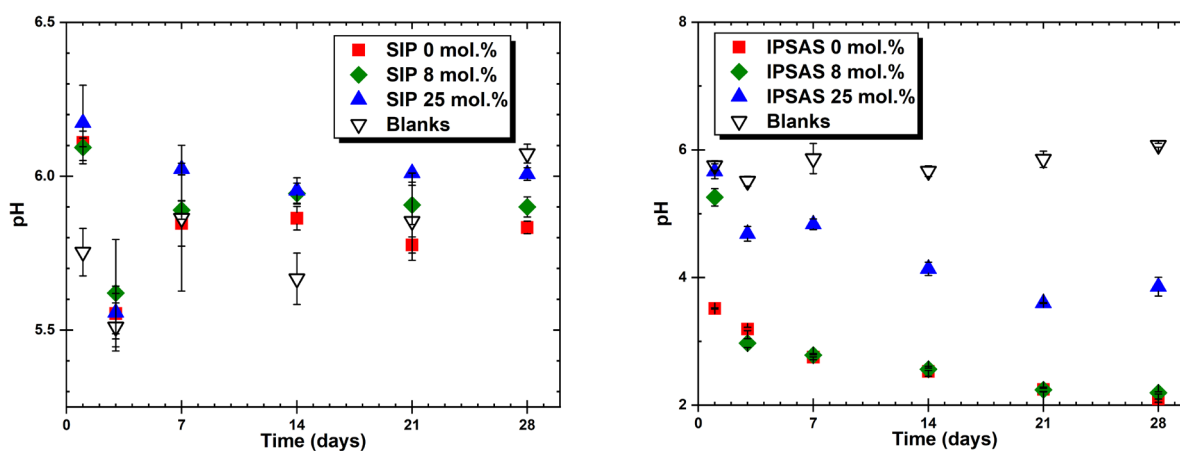


Figure 4.10.A – Plots of average pH at each sampling time point for SIP (left) and IPSAS (right) PCT-B aliquots. pH of control blank samples is shown with open symbols. In all cases, the error bars represent the standard deviation from each triplicate set.

4.10.2 ICP-OES analysis

Aliquots were prepared and analysed for elemental release, as per **Section 3.10.2**, and the spectrometer detector was calibrated against elemental concentration standards during measurements. For SIP glass, the releases of cerium, iron, phosphorous, sodium and aluminium were measured, additionally silicon release was measured for IPSAS glass, as it was not present in any meaningful concentrations in either the SIP batch, as-cast materials or in the UHQ dissolution media. Spectrometer signal for each primary elemental line was converted to mass concentration as a function of volume, by using calibration standards of known concentrations which were measured at the same time as sample aliquots. The resulting concentrations were corrected against the elemental releases in control blank samples and to the volume of solution as measured into the dissolution vessels. This data was then normalised with respect to the specific surface area as calculated from powder geometry, the mass fraction of each element present in the original sample (as measured by EDX see bracketed values in **Table 4.2.A** and **Section 4.7.1**), per the loss calculation, see **Equation 4.10.A**.

$$NL_{(x)} = \frac{C_{(x)} \times V_{sol}}{A_G \times m_{(x)}}$$

Equation 4.10.A – Normalised mass loss (NL) equation for element x , where $C_{(x)}$ is the concentration of element x in a known volume of solution, V_{sol} . The original powder sample surface area is calculated from geometric assumptions, A_G and the mass fraction of element x is $m_{(x)}$. Dissolution rate, $D_{(R)}$ can also be found by dividing the change in (NL) by the time period.

Normalised mass loss data for SIP 0 – 25 mol.% simulant loaded 1350 °C melts are presented in **Figure 4.10.B**. General trends of release rate from day 0 – 1 and beyond indicated that minimal fines were present with the prepared powders. The cerium concentrations, **Figure 4.10.B (a)**, were at zero or below the spectrometer detection limit for all aliquots of SIP and IPSAS 0 mol.% simulant samples, so they are not included in the plots. Cerium loss only reached detectable levels after 7 days of dissolution, with peak cerium dissolution rates found after 21 days, registering $1.2 \times 10^{-4} \text{ g m}^{-2} \text{ d}^{-1}$ for SIP with 8 mol.% loading of simulant and $2.0 \times 10^{-5} \text{ g m}^{-2} \text{ d}^{-1}$ for that of the 25 mol.% loaded sample. Due to a small amount of evaporative loss at this time point, the concentration of cerium present could have been artificially increased, these maximum rates for SIP 8 – 25 mol.% loaded simulant are however comparable to a base iron phosphate glass loaded with 8 mol.% ceria, $5.0 \times 10^{-5} \text{ g m}^{-2} \text{ d}^{-1}$ [50].

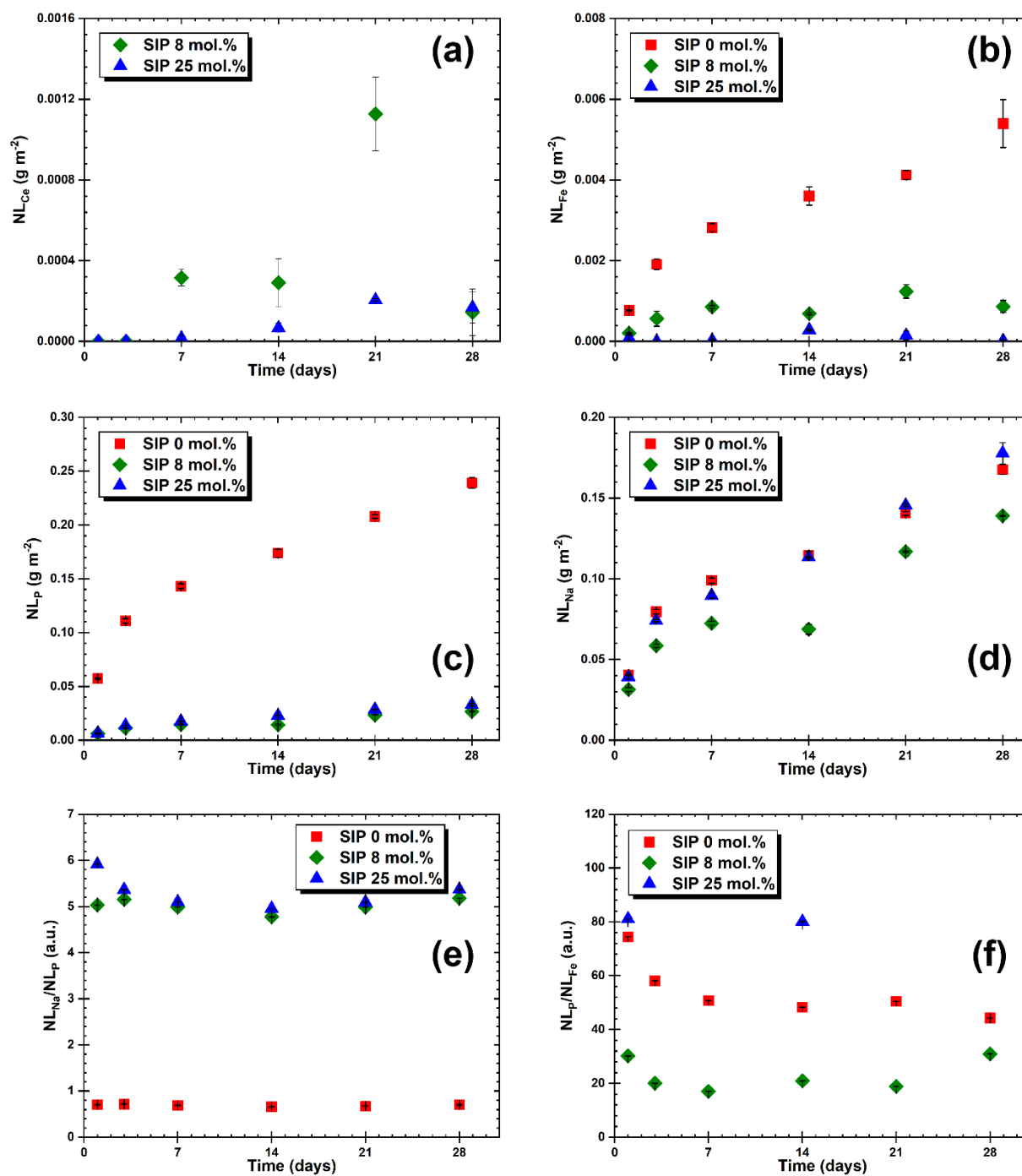


Figure 4.10.B - Calculated normalised mass-loss results from ICP-OES of SIP dissolution aliquots for elemental release of: cerium (a), iron (b), phosphorous (c), sodium (d), unitless ratio of sodium to phosphorous release (e), and unitless ratio of phosphorus to iron release (f). The change of loss scale should be noted, and smaller error bars may be occluded by datapoint symbols.

It should be noted that while the SIP 8 and 25 mol.% samples were batched with the relative proportions of ceria, the thermally treated product was found to only have 3.3 mol.% and 6.5 mol.% ceria, by EDX analysis. The literature example did not include measurement of the as-cast composition, though did use a greater SA/V ratio of 2000 m^{-1} , where 1200 m^{-1} was used for this

study. A general trend was observed for SIP wasteforms, as represented by the release rate of iron, phosphorus and, to a lesser extent, sodium, see **Figure 4.10.B (b-d)**, indicating that the bulk glass phase has likely experienced congruent dissolution. The SIP 0 mol.% loaded simulant experienced the most significant loss of primary network formers phosphorus and iron. A residual rate could be calculated from the data obtained between days 7 and 28, where iron was lost at a rate of $1.2 \times 10^{-4} \text{ g m}^{-2} \text{ d}^{-1}$, higher than an equivalent iron phosphate base glass, whereby the residual iron loss rate was found to be $3.5 \times 10^{-5} \text{ g m}^{-2} \text{ d}^{-1}$ [50]. Iron loss was substantially lower for the higher waste loadings of SIP at 8 – 25 mol.%, though the behaviour was not consistent enough over a reasonable range to calculate a residual rate with high confidence. Releases of the other primary network former, phosphorous, followed a very similar pattern, with SIP 0 mol.% simulant demonstrating a residual rate of $4.6 \times 10^{-3} \text{ g m}^{-2} \text{ d}^{-1}$, with SIP 8 mol.% simulant stabilising at $5.9 \times 10^{-4} \text{ g m}^{-2} \text{ d}^{-1}$ and SIP 25 mol.% at $7.4 \times 10^{-4} \text{ g m}^{-2} \text{ d}^{-1}$. An iron phosphate composition prepared for immobilisation of technetium, with a similar P_2O_5 ratio to SIP and IPSAS samples, achieved a comparable phosphorous release rate of $8.3 \times 10^{-3} \text{ g m}^{-2} \text{ d}^{-1}$ [51]. It should be noted that the aforementioned glass was prepared for a SA/V value of 1790 m^{-1} , whereas the present study has used 1200 m^{-1} . The dissolved phosphorous may form species such as phosphoric acid, this is evidenced for the more acidic pH for the SIP 0 mol.% simulant sample with greater phosphorous release, as compared to the SIP 8 – 25 mol.% counterparts. The ratio of NL_{Na}/NL_P and NL_P/NL_{Fe} , see **Figure 4.10.B (e-f)**, show the correlation in loss rates between these species, further evidencing support for the congruent dissolution of the glass phase. It should be noted that due to iron concentrations for SIP 25 mol.% simulant being below the detection limit for sampling days 3, 7, 21 and 28, only the day 1 and day 14 NL_P/NL_{Fe} ratios are presented.

As with the SIP dissolution experiments, the IPSAS samples did not experience a large jump in loss rate between day 0 – 1, indicating minimal presence of fines, see **Figure 4.10.C**. All elements measured for the IPSAS series: Ce, Fe, P, Na, Si, and Al largely followed a similar proportional trend of increasing loss with longer residence time, again indicating that dissolution of the primary glass phase containing all such elements was occurring. For IPSAS 8 mol.% simulant loaded glass, cerium release was accelerated, see **Figure 4.10.C (b)**, with a day 7 – 28 residual rate of $5.3 \times 10^{-4} \text{ g m}^{-2} \text{ d}^{-1}$. While this is lower than that of the SIP 8 mol.% loaded equivalent sample, the rate calculated for SIP cerium loss is instantaneous, and reported with lower confidence. The higher loading IPSAS 25 mol.% sample was observed to have substantially lower cerium losses, though the behaviour was not consistent enough at such low detections as to permit high confidence in calculation of a residual rate. It should also be noted that the IPSAS wasteforms contained a significantly higher proportion of ceria, as compared to the SIP series, with the 25 mol.% loaded materials found to contain 11.3 mol.% and 6.5 mol.%, respectively.

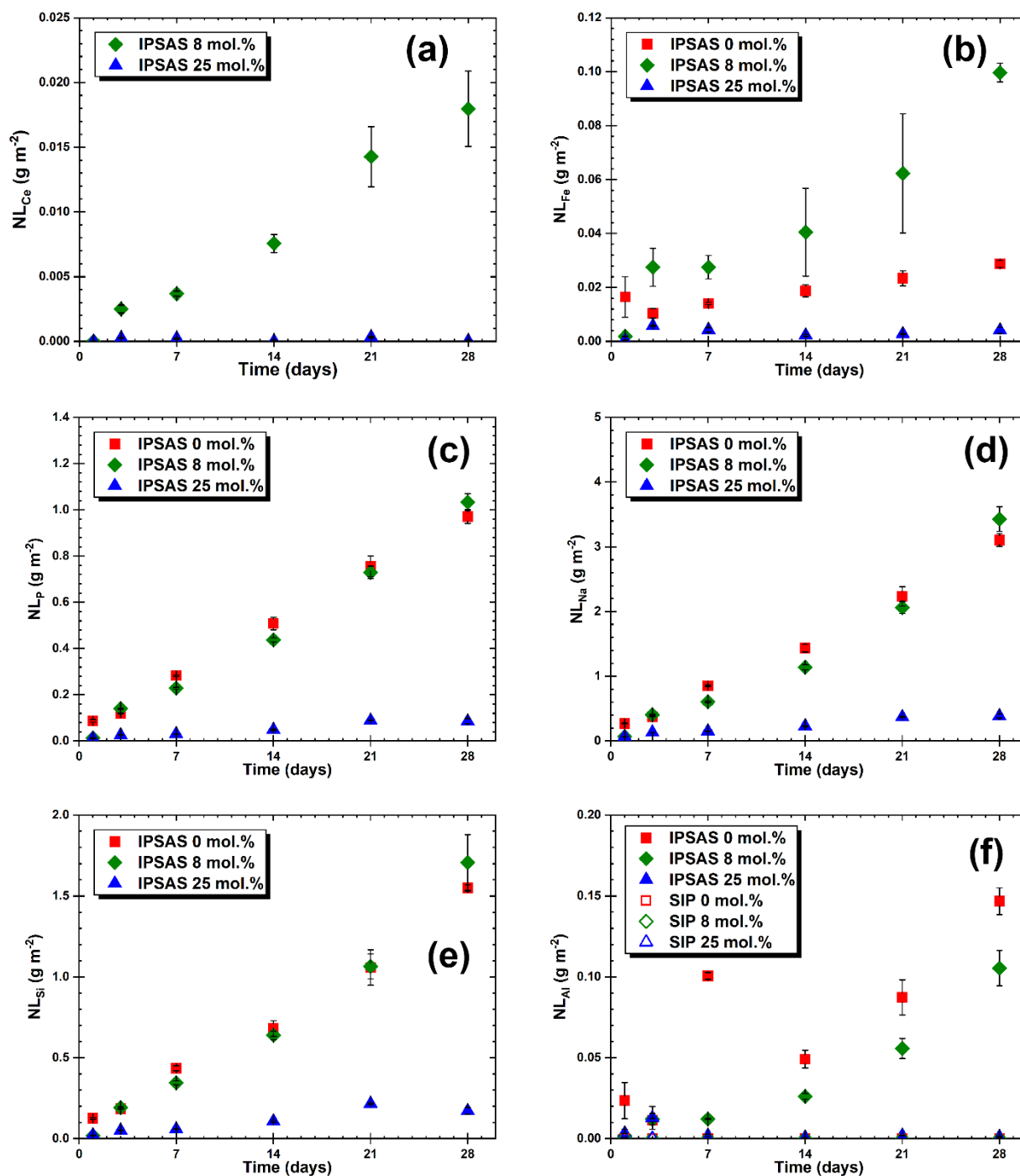


Figure 4.10.C - Calculated normalised mass-loss results from ICP-OES of IPSAS dissolution aliquots for elemental release of: cerium (a), iron (b), phosphorous (c), sodium (d), silicon (e), and aluminium – also showing relative SIP mass-losses (f).

The change of loss scale should be noted, and smaller error bars may be occluded by datapoint symbols.

The dissolution rate of iron was highest for the IPSAS 8 mol.% simulant aliquots, at $3.4 \times 10^{-3} \text{ g m}^{-2} \text{ d}^{-1}$, more than an order of magnitude greater than iron phosphate glasses reported in literature [50,51], see **Figure 4.10.C (b)**. The IPSAS 0 mol.% and 25 mol.% simulant wastefoms

have substantially lower iron residual rates of $7.0 \times 10^{-4} \text{ g m}^{-2} \text{ d}^{-1}$ and $1.4 \times 10^{-4} \text{ g m}^{-2} \text{ d}^{-1}$, respectively. As with the other elemental releases for the IPSAS series, the phosphorous loss was generally greater than that of the SIP counterparts, see **Figure 4.10.C (c)**. The IPSAS 25 mol.% simulant loaded samples, were found to have a phosphorous residual leaching rate of $2.6 \times 10^{-3} \text{ g m}^{-2} \text{ d}^{-1}$, still within a lower range of other phosphate glass systems [51]. Conversely, IPSAS 0 – 8 mol.% ceria glasses experienced much higher release rates of phosphorous: $3.3 \times 10^{-2} \text{ g m}^{-3} \text{ d}^{-1}$ and $3.8 \times 10^{-3} \text{ g m}^{-3} \text{ d}^{-1}$, respectively. This is well reflected in the IPSAS series pH measurements, whereby evolution of significant quantities of phosphoric acid drove the pH to a more acidic extreme, as compared to the 25 mol.% simulant, see **Figure 4.10.A**. The pattern as also observed for the sodium loss rate, **Figure 4.10.C (d)**, is evidence for a much poorer chemical durability of the glass phase in the IPSAS 0 – 8 mol.% wastefoms. SiO_2 was added in the IPSAS glass batches and confirmed to be present at 7.2 – 8 mol.% in the as-cast material, it was expected that some significant silicon loss would be detected for the IPSAS series dissolution experiments. The silicon loss rate for IPSAS 0 mol.% simulant aliquots were $5.3 \times 10^{-2} \text{ g m}^{-2} \text{ d}^{-1}$, with that of the 8 mol.% counterpart only slightly higher, see **Figure 4.10.C (e)**. A silicon residual leaching rate of $5.3 \times 10^{-3} \text{ g m}^{-3} \text{ d}^{-1}$ was obtained for IPSAS 25 mol.% ceria material, comparable to a ceria loaded borosilicate composition for HLW immobilisation, which had a silicon leaching rate of $\sim 8 \times 10^{-3} \text{ g m}^{-2} \text{ d}^{-1}$, with a powder SA/V value of 1300 m^{-1} [52]. Though aluminium had combined into the glass melt as a result of crucible corrosion, the SIP series had not been intentionally loaded with alumina in the glass batch and as such, the as-cast material had a lower aluminium content. It was apparent that the aluminium of the SIP series was present in a more resistant phase than the equivalent IPSAS series, as the signal for aluminium was at or near the detection limit for all SIP samples, see **Figure 4.10.C (f)**. This effect was also replicated for the IPSAS 25 mol.% simulant aliquots, while the silicon loss rates for IPSAS 0 – 8 mol.% ceria loaded samples were far greater. A spike in aluminium release was found at d 7 for IPSAS 0.% simulant, though this is attributed to some minor contamination during the sampling stage.

The NL_{Na}/NL_P and NL_P/NL_{Fe} and NL_{Si}/NL_{Al} ratios for IPSAS glasses were also plotted, see **Figure 4.10.D**. These indicate a strong correlation between the dissolution rates of glass network formers for IPSAS 0 – 8 mol.% simulant glasses, while the 25 mol.% counterpart does not appear to be experiencing dissolution with such congruence. However, it should be noted that the ratios featuring iron and aluminium losses may be discounted, as the IPSAS 25 mol.% simulant material had several datapoints at or near the detection limit. If only referring to the NL_{Na}/NL_P ratio, the 25 mol.% wasteform does appear to experience congruent dissolution of the primary glass phase.

The combined overall normalised losses and instantaneous dissolution rates were calculated for each series, see **Figure 4.10.E**. The SIP wasteforms experienced the lowest mass losses, with an apparent initial leaching rate of $9.9 \times 10^{-2} \text{ g m}^{-2} \text{ d}^{-1}$ for the 0 mol.% sample, down to a residual rate of $8.5 \times 10^{-3} \text{ g m}^{-2} \text{ d}^{-1}$. SIP with 25 mol.% simulant waste was observed to have

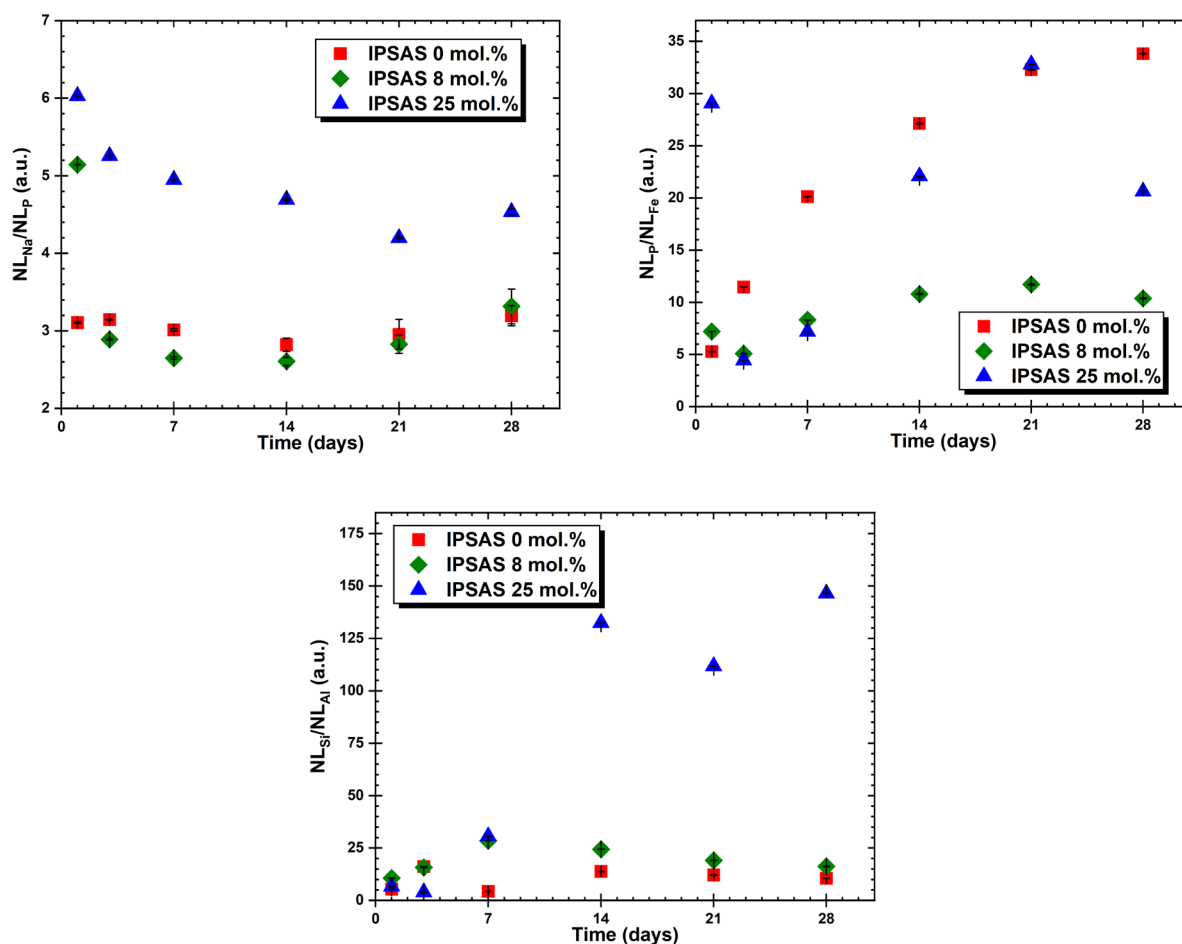


Figure 4.10.D - Calculated ratios of mass-loss results from ICP-OES of IPSAS dissolution aliquots for: unitless ratio of sodium to phosphorus release (left), unitless ratio of phosphorus to iron release (right), and unitless ratio of silicon to aluminium release (bottom).

an initial dissolution rate of $4.6 \times 10^{-2} \text{ g m}^{-2} \text{ d}^{-1}$, later reducing to a combined residual leaching rate of $5.3 \times 10^{-3} \text{ g m}^{-2} \text{ d}^{-1}$. The IPSAS 0 – 8 mol.% simulant loaded glasses did not reach a steady dissolution rate for the duration of the experiment, experiencing an apparent rate increase between days 14 and 28. The IPSAS 25 mol.% ceria glass-ceramic experienced a plateau of overall mass loss between days 21 and 28, indicating that the small quantity of soluble surface species had been fully dissolved or a passivating layer had formed on the powder particles [53–55]. The SIP wasteforms performed the best during the 28-day study. While also considering cerium releases, the SIP 25 mol.% simulant loaded sample was the most durable. With the lower measured actual cerium

content of the SIP series, this was expected. The durability was substantially decreased with the IPSAS melt series for loadings up to 8 mol.% ceria, attributed to the refractory oxide additions to the batch. However, the IPSAS 25 mol.% simulant sample retained a greater quantity of ceria than its SIP series counterpart, while maintaining a comparable chemical durability.

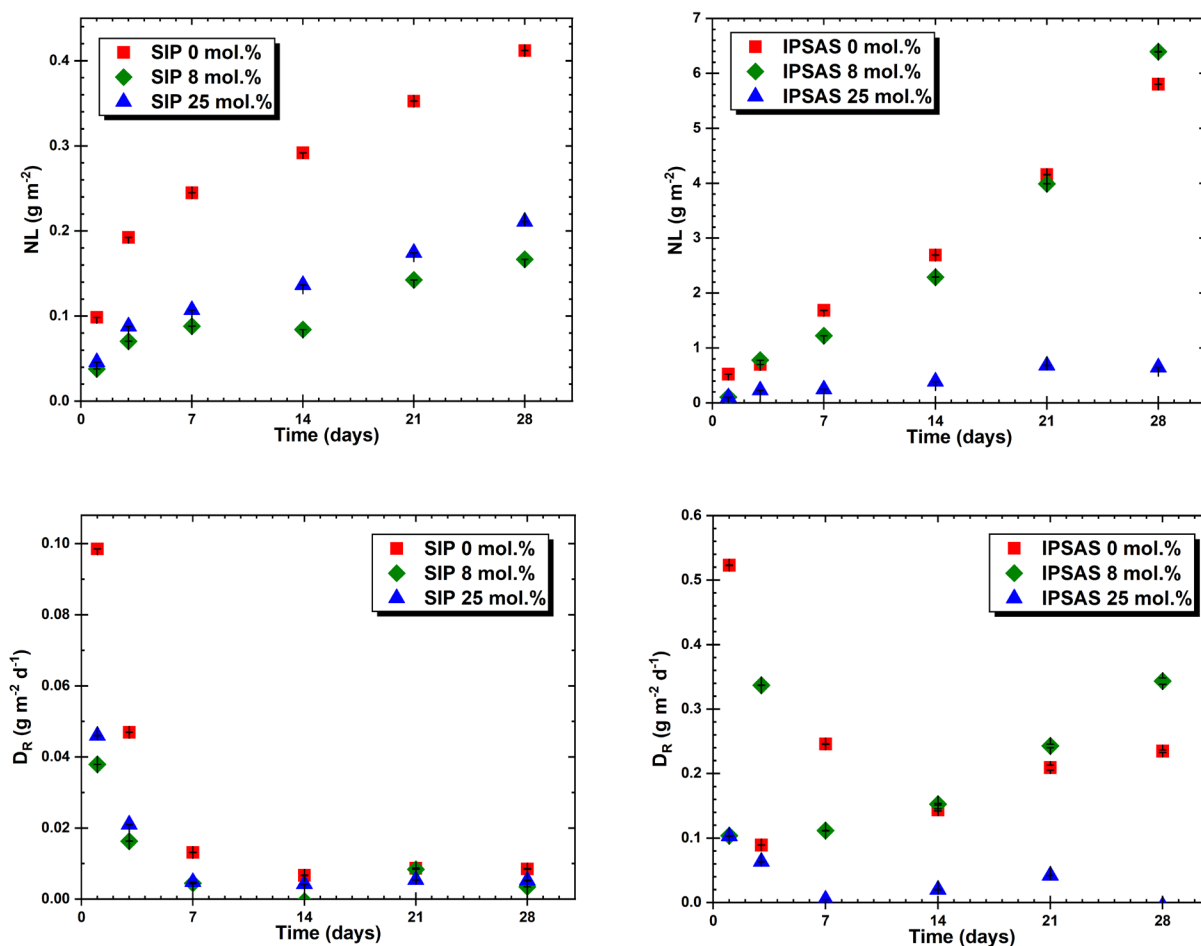


Figure 4.10.E – Plots showing overall normalised mass loss for SIP (top left) and IPSAS (top right) samples, with the derived instantaneous dissolution rates for SIP (bottom left) and IPSAS (bottom right) samples.

4.11 Conclusions and further work

Additions of refractory oxides for the IPSAS series reduced the aggressive melt characteristics such as foaming seen with SIP glass melts, with greater overall solubility for simulant waste. SIP glass melted with more aggressive self-stirring during the generation of ammonia, leading to a degree of breakdown of the alumina crucibles and leaching of aluminium into the glass melt. IPSAS base glass was found to have a narrower temperature range between the glass transition onset and the crystallisation temperature, with the SIP base glass having a lower measured glass transition onset.

SIP series wastefoms developed the most porosity at high waste loadings, but all melt series were found to result in low density, high porosity products beyond 43 – 45 mol.% batched simulant waste loading. The onset of crystallisation typically occurred for loadings within the range of 16 – 25 mol.% batched ceria additions, though the SIP 1450 °C series melts were more aggressive, generating slag which was poorly incorporated and crystalline content was found at loadings as low as 4 mol.% simulant additions. Molar volume of wastefoms appeared to increase with an approximately exponential trend following the onset of crystallisation, even at the highest simulant waste loadings, primarily due to the development of significant porosity and a lower-than-expected measured content of ceria in the wastefoms.

Glass ceramic materials developed in all melt series, with sodium iron phosphate-based glass as the primary matrix phase, doped with cerium and aluminium. IPSAS series glasses additionally featured small quantities of batched silicon in the glass phase. The primary crystalline phase was cerium monazite as $\text{Ce}(\text{PO}_4)$, with some secondary crystalline sodium iron phosphate as $\text{NaFe}(\text{P}_2\text{O}_7)$ developing and undigested simulant waste as CeO_2 retained at higher loadings. The IPSAS 1250 – 1350 °C melt series remained amorphous up to loadings of 16 mol.% batched simulant.

The bulk compositions of prototypical wastefoms, as measured EDX, were found to contain significantly less cerium than was expected from the batched content. With the aggressive conditions of the melts, more refractory batch content such as ceria may have evolved into a slag which was deposited on the crucible during casting. In addition, the high relative density of ceria may have caused a significant proportion to sink to the base of the melt. The separation of larger crystals of monazite from the bulk material was observed, while effort was made to ensure representative EDX sampling, there still may have been regions of agglomerated crystallites not accounted for, below the polished monolith surface. Only the highly porous glass ceramic samples contained in excess of 15 mol.% ceria in the bulk material. The highest retained simulant waste loadings were above 20 mol.% as measured for SIP 45 mol.% batched samples melted at 1250 °C and 1450 °C, with IPSAS 43 mol.% simulant sample melted at 1450 °C. The more corrosive SIP melts were found to contain more aluminium in the bulk material, indicating that the crucibles had

significantly degraded during the melting process, as it was not accounted for with the batched reagents. Greater simulant waste additions as ceria appears to further passivate the melting conditions, as it is itself a refractory addition. Without annealing, crystallisation occurred and some dendritic formation of AlPO_4 developed. The cerium monazite phase was found form a typical core-shell type microstructure around grains of ceria, in effect encapsulating the simulant waste. The growth of sodium iron phosphate crystallites was confirmed with electron microscopy, with few local regions containing small sodium aluminium iron phosphates. The degree of porosity development was also verified, and observations were made of monazite forming dendritic cruciform crystallites at the onset of crystallisation. Beyond the crystallisation point, rather than a glass solubility limit being reached, cerium partitioning favoured the crystalline monazite phase, leaving a glass matrix partially depleted of simulant waste. Use of the image based quantitative phase analysis technique yielded comparable results with a spike Rietveld method, while improving the throughput, removing the need for an internal spike standard improved flexibility for analysis of samples containing unknown phases. Phase analysis showed that at the highest simulant waste loadings for the IPSAS series, the majority phases by volume were crystalline, indicating that a sintered glass ceramic wastefrom could be made with batch contents to only produce enough glass for bonding the ceramic phases. However, the image-based analysis method did not account for very small quantities of crystalline sodium iron phosphate, detected as minor reflections by pXRD in the IPSAS 34 mol.% simulant sample melted at 1250 °C.

Mössbauer fits with four Lorentzian doublets for each iron valence yielded results showing a trend of increasing Fe(II) content with increased waste loading, suggesting reduced aqueous durability [56]. The less aggressive melting conditions associated with the samples batched with more simulant material may provide an environment whereby a greater proportion of free iron ions can be reduced. However, the XAS results did not wholly agree with this trend, the SIP series materials were measured to follow the slight increase of redox potential, though XAS data indicated a slight decrease of Fe(II) content with increased batch loading of simulant waste, meaning more non-bridging bonds with iron, as it behaves as less of a network former with increasing Fe(II) content. The iron redox behaviour as assessed via Mössbauer spectroscopy, was comparable for SIP and IPSAS series wastefroms, although the IPSAS series, particularly the 25 mol.% loaded material melted at 1350 °C had a greater measured bulk cerium content than the SIP counterparts. Fe-K edge X-ray absorption spectroscopy showed an edge shift and pre-edge feature transformation between the SIP and IPSAS series indicating a configurational change associated with the iron redox behaviour. The fitting method found iron valence with a comparable range to that of Mössbauer analyses, with an overall greater Fe(II) proportion with the IPSAS series, though the aforementioned difference in trend. It is noted that a greater distribution of datapoints will be required in order to conclude a trend of redox behaviour with high confidence. Fe-K edge EXAFS

analyses provided an insight into the coordination behaviour and local structure of the glass series, with respect to iron as a central absorber. Bond valence sums produced iron redox values that agreed well with Mössbauer and pre-edge analyses. The SIP 0 – 25 mol.% loaded wastefoms melted at 1350 °C exhibited a first shell of oxygen atoms bonding in a more tetrahedral coordination. While the overall IPSAS series was also found to demonstrate a slightly tetrahedral coordination of oxygen about the iron centres, the IPSAS 0 mol.% simulant glass melted at 1350 °C had a slightly octahedral coordination environment. As such disordered configurations are not typically associated with iron retention in a crystalline phase, the EXAFS findings indicate that iron is bonding in the glass phase, likely substituting for some phosphorous atoms in P – O – P chains.

28 day accelerated chemical durability testing indicated that the SIP series was overall more resistant to dissolution than the IPSAS counterparts, whereby hydrolysis of the poorly durable phosphorous in the glass phase P – O – P bridges occurs, leading to generation of highly acidic species in the dissolution media. This low pH environment can further interfere with the electrochemical crosslinking between phosphate chains in the glass matrix [3], leading to further dissolution. The highest simulant loaded wastefoms tested performed the best under leaching conditions, with the presence of a highly durable [57] crystalline monazite phase, and less cerium present in the lower durability glass phase. Dissolution behaviour during the experimental duration was congruent with respect to glass network and modifier elements, indicating uniform degradation of the glass. As a greater Fe(III) content of a phosphate glass is typically indicative of improved chemical durability properties [7,42], this was reflected in the SIP series glasses, for which iron was present in a greater proportion of Fe(III). However, the difference of iron valence for SIP and IPSAS series is slight, so a significantly poorer overall durability is more likely due to the presence of silicon as a modifier in the glass network and a greater proportion of cerium retained in the glass phase. The exception is for the IPSAS 25 mol.% simulant loaded wastefom melted at 1350 °C with a chemical durability comparable to that of the SIP counterparts, while a significantly greater proportion of simulant waste was retained in the final wastefom. Here a passivating layer may have formed on the particle surfaces, reducing the loss rates to near undetectable values. With a greater proportion of cerium retained in chemically resistant crystalline phases, the cerium loss rates for this sample were also approaching undetectable levels.

With the studied compositions and melting conditions, the IPSAS 25 mol.% waste loading sample melted at 1350 °C is considered to have the most optimal properties for potential actinide disposition. The IPSAS waste forms have superior melting behaviour and retention of simulant waste, the 25 mol.% series exhibited high density and molar volume. Spectroscopic analyses also showed substitution of iron for phosphorous in phosphate bridges, with iron redox trending to Fe(III) for IPSAS series materials. While the 0 – 8 mol.% simulant loaded IPSAS wastefoms did not perform as well as the other series under accelerated leaching conditions, the

proposed 25 mol.% simulant IPSAS variant retained cerium in durable phases and was found to have a lower overall dissolution rate. As mentioned in **Section 4.3**, the use of ceria as a simulant for UO_2 has some caveats with reference to density (lower with ceria) and redox behaviour. The increased density of UO_2 would likely mean that even more is retained in the crucible during melting, unless stirring is implemented. While ceria surrogates are also redox active, like UO_2 , the redox couples and behaviour is not equivalent. The formation of U(V) and U(VI) and the effects of these redox couples would require further analysis with depleted surrogates.

Further proposed work includes thermal analyses of the waste loaded glasses and of glass compositions as batched, allowing for a study of the pre-melting behaviour and evolution of ammonia at low temperatures, additionally viscosity measurements could be used to assess how the glass melt at scale might perform. Glass preparation variables such as manual stirring, melting times, and use of other phosphate reagent sources should be reviewed with the compositions in this work, as this may alter the redox behaviour of iron and simulant waste cation in the wasteform. The effect of other modifier additions such as zirconia and magnesium oxide could also be studied as possible inclusions with Magnox and zircaloy clad fuels, though alternatively addition of size reduced pieces of chromium stainless steel and such cladding alloys may provide a more representative simulant. A simulated spent fuel composition with depleted uranium oxide and simulated fission products could provide a more accurate analogue, while still reducing worker hazard during investigations.

Verification of product composition via X-ray fluorescence measurements should provide more reliable data than the EDX analysis method used, a technique such as electron probe microanalysis could be used to aid in verification of chemistry and identity of small crystallites. Further XAS studies could utilise principal component analysis and linear combination fitting to allow for fingerprinting analysis against known standards. While Ce-L₃, Ce-L₂ and fluorescence measurements were carried out as part of this work, it was not possible to resolve a realistic first shell coordination and structural environment due to the presence of cerium in highly crystalline and amorphous phases. EXAFS data for cerium also featured a significant multiple electron excitation feature which interfered with structural analyses. Further study should consider a suite of micro analytical techniques for studying the crystalline phases separately from the glass matrix. Structural information could be further supported by techniques such as laser Raman spectroscopy. Alteration layers on the dissolution glass powders could not be observed using SEM, high resolution microscopy could be utilised, or an accelerated vapor hydration test could be employed to permit study of alteration and gel layers. Longer dissolution experiments with alkaline groundwater solutions would help develop an improved understanding of the geochemical behaviour of these wasteforms, while use of ICP with a mass spectrometer could aid in measuring the very low cerium and iron concentrations as found for some aliquots.

Chapter 4 references

- [1] Heysham 2 and Torness end dates brought forward by EDF, World Nucl. News. (2022). <https://www.world-nuclear-news.org/Articles/EDF-confirms-earlier-end-date-for-Heysham-2-and-To>.
- [2] D. Hambley, Storage of thermal reactor fuels – Implications for the back end of the fuel cycle in the UK, EPJ Nucl. Sci. Technol. 2 (2016) 21. <https://doi.org/10.1051/EPJN/2016014>.
- [3] B.C. Bunker, G.W. Arnold, J.A. Wilder, Phosphate glass dissolution in aqueous solutions, J. Non. Cryst. Solids. 64 (1984) 291–316. [https://doi.org/10.1016/0022-3093\(84\)90184-4](https://doi.org/10.1016/0022-3093(84)90184-4).
- [4] C.H. Booth, P.G. Allen, J.J. Bucher, N.M. Edelstein, D.K. Shuh, G.K. Marasinghe, M. Karabulut, C.S. Ray, D.E. Day, Oxygen and phosphorus coordination around iron in crystalline ferric ferrous pyrophosphate and iron-phosphate glasses with UO₂ or Na₂O, J. Mater. Res. 14 (1999) 2628–2639. <https://doi.org/10.1557/JMR.1999.0352>.
- [5] A. Bohre, K. Avasthi, V.I. Pet'kov, Vitreous and crystalline phosphate high level waste matrices: Present status and future challenges, J. Ind. Eng. Chem. 50 (2017) 1–14. <https://doi.org/10.1016/j.jiec.2017.01.032>.
- [6] R. Gresch, W. Müller-Warmuth, H. Dutz, X-ray photoelectron spectroscopy of sodium phosphate glasses, J. Non. Cryst. Solids. 34 (1979) 127–136. [https://doi.org/10.1016/0022-3093\(79\)90012-7](https://doi.org/10.1016/0022-3093(79)90012-7).
- [7] C.W. Kim, C.S. Ray, D. Zhu, D.E. Day, D. Gombert, A. Aloy, A. Mogaš-Milanković, M. Karabulut, Chemically durable iron phosphate glasses for vitrifying sodium bearing waste (SBW) using conventional and cold crucible induction melting (CCIM) techniques, J. Nucl. Mater. 322 (2003) 152–164. [https://doi.org/10.1016/S0022-3115\(03\)00325-8](https://doi.org/10.1016/S0022-3115(03)00325-8).
- [8] D. Russo, D. Rodriguez, N. Grumbaum, C. Gonzalez Oliver, High temperature oxidation and crystallization behavior of phosphate glass compositions, (2003). https://inis.iaea.org/collection/NCLCollectionStore/_Public/35/103/35103669.pdf?r=1.
- [9] D.O. Russo, D.S. Rodríguez, J.M. Rincón L., M. Romero, C.J.R. González Oliver, Thermal properties and crystallization of iron phosphate glasses containing up to 25 wt% additions of Si-, Al-, Na- and U-oxides, J. Non. Cryst. Solids. 354 (2008) 1541–1548. <https://doi.org/10.1016/J.JNONCRY SOL.2007.08.044>.
- [10] S.V. Stefanovsky, O.I. Stefanovsky, S.S. Danilov, M.I. Kadyko, Phosphate-based glasses and glass ceramics for immobilization of lanthanides and actinides, Ceram. Int. 45 (2019) 9331–9338. <https://doi.org/10.1016/J.CERAMINT.2018.06.208>.
- [11] M.C. Stennett, C.L. Corkhill, L.A. Marshall, N.C. Hyatt, Preparation, characterisation and dissolution of a CeO₂ analogue for UO₂ nuclear fuel, J. Nucl. Mater. 432 (2013) 182–188. <https://doi.org/10.1016/J.JNUCMAT.2012.07.038>.
- [12] P.A. Bingham, R.J. Hand, M.C. Stennett, N.C. Hyatt, M.T. Harrison, The use of surrogates in waste immobilization studies: A case study of plutonium, Mater. Res. Soc. Symp. Proc. 1107 (2008) 421–428. <https://doi.org/10.1557/proc-1107-421>.
- [13] P.A. Bingham, R.J. Hand, S.D. Forder, Doping of iron phosphate glasses with Al₂O₃, SiO₂ or B₂O₃ for improved thermal stability, Mater. Res. Bull. 41 (2006) 1622–1630. <https://doi.org/10.1016/J.MATERRESBULL.2006.02.029>.

- [14] S.S. Danilov, S. V. Stefanovsky, O.I. Stefanovskaya, S.E. Vinokurov, B.F. Myasoedov, Y.A. Teterin, Aluminum (Iron) Phosphate Glasses Containing Rare Earth and Transuranium Elements: Phase Composition, Oxidation State of Np and Pu, and Hydrolytic Durability, *Radiochem.* 2018 604. 60 (2018) 434–439.
<https://doi.org/10.1134/S1066362218040136>.
- [15] B.C. Sales, L.A. Boatner, Physical and chemical characteristics of lead-iron phosphate nuclear waste glasses, *J. Non. Cryst. Solids.* 79 (1986) 83–116.
[https://doi.org/10.1016/0022-3093\(86\)90040-2](https://doi.org/10.1016/0022-3093(86)90040-2).
- [16] T. Honma, A. Sato, N. Ito, T. Togashi, K. Shinozaki, T. Komatsu, Crystallization behavior of sodium iron phosphate glass $\text{Na}_2 - \text{XFe}_1 + 0.5\text{xP}_2\text{O}_7$ for sodium ion batteries, *J. Non. Cryst. Solids.* 404 (2014) 26–31. <https://doi.org/10.1016/j.jnoncrsol.2014.07.028>.
- [17] K. Joseph, M.C. Stennett, N.C. Hyatt, R. Asuvathraman, C.L. Dube, A.S. Gandy, K. V. Govindan Kutty, K. Jolley, P.R. Vasudeva Rao, R. Smith, Iron phosphate glasses: Bulk properties and atomic scale structure, *J. Nucl. Mater.* 494 (2017) 342–353.
<https://doi.org/10.1016/j.jnucmat.2017.07.015>.
- [18] Y. Ma, Y. Ma, G. Giuli, H. Euchner, A. Groß, G. Orazio Lepore, D. Geiger, J. Biskupek, U. Kaiser, H.M. Schütz, A. Carlsson, T. Diemant, R. Jürgen Behm, M. Kuenzel, S. Passerini, D. Bresser, H. Euchner, A. Groß, G.O. Lepore, D. Geiger, J. Biskupek, U. Kaiser, A. Carlsson, T. Diemant, R.J. Behm, Y. Ma, Y. Ma, H.M. Schütz, M. Kuenzel, S. Passerini, D. Bresser, G. Giuli, Introducing Highly Redox-Active Atomic Centers into Insertion-Type Electrodes for Lithium-Ion Batteries, *Adv. Energy Mater.* 10 (2020) 2000783.
<https://doi.org/10.1002/AENM.202000783>.
- [19] M.M. Zaman, S.M. Antao, A Possible Radiation-Induced Transition from Monazite-(Ce) to Xenotime-(Y), *Miner.* 2021, Vol. 11, Page 16. 11 (2020) 16.
<https://doi.org/10.3390/MIN11010016>.
- [20] S. Gates-Rector, T. Blanton, The Powder Diffraction File: a quality materials characterization database, *Powder Diffr.* 34 (2019) 352–360.
<https://doi.org/10.1017/S0885715619000812>.
- [21] F. W Jones, The measurement of particle size by the X-ray method, 1938.
<https://doi.org/10.1098/rspa.1938.0079>.
- [22] A.L. Patterson, The Scherrer Formula for X-Ray Particle Size Determination, *Phys. Rev.* 56 (1939) 978. <https://doi.org/10.1103/PhysRev.56.978>.
- [23] H. Klug, L. Alexander, *X-ray Diffraction Procedures: For Polycrystalline and Amorphous Materials*, 2nd Edition, 1974. <https://doi.org/https://doi.org/10.1002/xrs.1300040415>.
- [24] Yunxiang Ni, J.M. Hughes, A.N. Mariano, Crystal chemistry of the monazite and xenotime structures, *Am. Mineral.* 80 (1995) 21–26. <https://doi.org/10.2138/am-1995-1-203>.
- [25] Y. Ma, Y. Ma, G. Giuli, H. Euchner, A. Groß, G.O. Lepore, F. D’Acapito, D. Geiger, J. Biskupek, U. Kaiser, H.M. Schütz, A. Carlsson, T. Diemant, R.J. Behm, M. Kuenzel, S. Passerini, D. Bresser, Introducing Highly Redox-Active Atomic Centers into Insertion-Type Electrodes for Lithium-Ion Batteries, *Adv. Energy Mater.* 10 (2020).
<https://doi.org/10.1002/AENM.202000783>.

- [26] C.H. Chen, T. Aizawa, N. Iyi, A. Sato, S. Otani, Structural refinement and thermal expansion of hexaborides, *J. Alloys Compd.* 366 (2004). [https://doi.org/10.1016/S0925-8388\(03\)00735-7](https://doi.org/10.1016/S0925-8388(03)00735-7).
- [27] I.C. Madsen, N.V.Y. Scarlett, L.M.D. Cranswick, T. Lwin, Outcomes of the International Union of Crystallography Commission on Powder Diffraction round robin on quantitative phase analysis: Samples 1a to 1h, *J. Appl. Crystallogr.* 34 (2001) 409–426. <https://doi.org/10.1107/S0021889801007476>.
- [28] N.V.Y. Scarlett, I.C. Madsen, L.M.D. Cranswick, T. Lwin, E. Groleau, G. Stephenson, M. Aylmore, N. Agron-Olshina, Outcomes of the International Union of Crystallography Commission on Powder Diffraction round robin on quantitative phase analysis: Samples 2, 3, 4, synthetic bauxite, natural granodiorite and pharmaceuticals, *J. Appl. Crystallogr.* 35 (2002) 383–400. <https://doi.org/10.1107/S0021889802008798>.
- [29] I.C. Madsen, N.V.Y. Scarlett, N.A.S. Webster, Quantitative phase analysis, *NATO Sci. Peace Secur. Ser. B Phys. Biophys.* (2012) 207–218. https://doi.org/10.1007/978-94-007-5580-2_19.
- [30] A.E. Ringwood, S.E. Kesson, N.G. Ware, W. Hibberson, A. Major, Immobilisation of high level nuclear reactor wastes in SYNROC, *Nature.* 278 (1979) 219–223. <https://doi.org/10.1038/278219a0>.
- [31] A.K. Varshneya, J.C. Mauro, *Inorganic Glasses*, 2019.
- [32] H.D. Schreiber, The chemistry of uranium in glass-forming melts: Redox interactions of U(VI)-U(V)-U(IV) with cerium in aluminosilicates, *J. Non. Cryst. Solids.* 49 (1982) 189–200. [https://doi.org/10.1016/0022-3093\(82\)90118-1](https://doi.org/10.1016/0022-3093(82)90118-1).
- [33] A. V. Luzhetskyy, V.A. Petrov, S. V. Yudinsev, V.I. Malkovsky, M.I. Ojovan, M.S. Nickolsky, A.A. Shiryaev, S.S. Danilov, E.E. Ostashkina, Effect of Gamma Irradiation on Structural Features and Dissolution of Nuclear Waste Na–Al–P Glasses in Water, *Sustain.* 2020, Vol. 12, Page 4137. 12 (2020) 4137. <https://doi.org/10.3390/SU12104137>.
- [34] D. Rancourt, K. Lagarec, *Recoil - Mössbauer Spectral Analysis Software for Windows*, (1998). <https://denisrancourt.ca/Recoil-Manual.pdf>.
- [35] M.D. Dyar, D.G. Agresti, M.W. Schaefer, C.A. Grant, E.C. Sklute, Mössbauer spectroscopy of Earth and planetary materials, *Annu. Rev. Earth Planet. Sci.* 34 (2006) 83–125. <https://doi.org/10.1146/annurev.earth.34.031405.125049>.
- [36] G.L. Williams, *⁵⁷Fe Mossbauer studies of phosphate-based glass systems*, 1990. <http://shura.shu.ac.uk/20542/>.
- [37] S.T. Reis, A. Moguš-Milanković, V. Ličina, J.B. Yang, M. Karabulut, D.E. Day, R.K. Brow, Iron redox equilibrium, structure and properties of zinc iron phosphate glasses, *J. Non. Cryst. Solids.* 353 (2007) 151–158. <https://doi.org/10.1016/J.JNONCRY SOL.2006.10.002>.
- [38] P.A. Bingham, R.J. Hand, O.M. Hannant, S.D. Forder, S.H. Kilcoyne, Effects of modifier additions on the thermal properties, chemical durability, oxidation state and structure of iron phosphate glasses, *J. Non. Cryst. Solids.* 355 (2009) 1526–1538. <https://doi.org/10.1016/J.JNONCRY SOL.2009.03.008>.

- [39] P.A. Bingham, R.J. Hand, Vitrified metal finishing wastes: I. Composition, density and chemical durability, *J. Hazard. Mater.* 119 (2005) 125–133. <https://doi.org/10.1016/J.JHAZMAT.2004.11.014>.
- [40] P.A. Bingham, S.D. Forder, R.J. Hand, A. Lavaysierre, Mössbauer studies of phosphate glasses for the immobilisation of toxic and nuclear wastes, (n.d.). <https://doi.org/10.1007/s10751-006-9256-y>.
- [41] D. Day, C. Ray, K. Marasinghe, K. Mevlut, X. Fang, An Alternative Host Matrix Based on Iron Phosphate Glasses for the Vitrification of Specialized Waste Forms, Rolla, MO, 2000. <https://www.osti.gov/servlets/purl/827407/>.
- [42] S.T. Reis, M. Karabulut, D.E. Day, Chemical durability and structure of zinc-iron phosphate glasses, *J. Non. Cryst. Solids.* 292 (2001) 150–157. [https://doi.org/10.1016/S0022-3093\(01\)00880-8](https://doi.org/10.1016/S0022-3093(01)00880-8).
- [43] M. Wilke, F. Farges, P.E. Petit, G.E. Brown, F. Martin, Oxidation state and coordination of Fe in minerals: An Fe K-XANES spectroscopic study, *Am. Mineral.* 86 (2001) 714–730. <https://doi.org/10.2138/am-2001-5-612>.
- [44] G.J. Redhammer, G. Amthauer, G. Roth, G. Tippelt, W. Lottermoser, Single-crystal X-ray diffraction and temperature dependent ⁵⁷Fe Mössbauer spectroscopy on the hedenbergite-aegirine (Ca,Na)(Fe²⁺,Fe³⁺)Si₂O₆ solid solution, *Am. Mineral.* 91 (2006) 1271–1292. <https://doi.org/10.2138/AM.2006.2173/MACHINEREAADABLECITATION/RIS>.
- [45] F.J. Harris, On the Use of Windows for Harmonic Analysis with the Discrete Fourier Transform, *Proc. IEEE.* 66 (1978) 51–83. <https://doi.org/10.1109/PROC.1978.10837>.
- [46] M. Newville, Using Bond Valence sums as restraints in XAFS analysis, *Phys. Scr. T.* T115 (2005) 159–161. <https://doi.org/10.1238/PHYSICA.TOPICAL.115A00159/XML>.
- [47] I.D. Brown, The chemical bond in inorganic chemistry : the bond valence model, (2006) 278. <https://archive.org/details/chemicalbondinin0000brow/page/n9/mode/2up>.
- [48] M. Karabulut, G.K. Marasinghe, C.S. Ray, G.D. Waddill, D.E. Day, Y.S. Badyal, M.-L. Saboungi, S. Shastri, D. Haeffner, A high energy x-ray and neutron scattering study of iron phosphate glasses containing uranium, *J. Appl. Phys.* 87 (2000) 2185. <https://doi.org/10.1063/1.372160>.
- [49] X. Fang, C.S. Ray, A. Mogu S-Milankovi, D.E. Day, Iron redox equilibrium, structure and properties of iron phosphate glasses, *J. Non. Cryst. Solids.* 283 (2001) 162–172. [https://doi.org/10.1016/S0022-3093\(01\)00416-1](https://doi.org/10.1016/S0022-3093(01)00416-1).
- [50] Y. Deng, Q. Liao, F. Wang, H. Zhu, Synthesis and characterization of cerium containing iron phosphate based glass-ceramics, *J. Nucl. Mater.* 499 (2018) 410–418. <https://doi.org/10.1016/J.JNUCMAT.2017.12.001>.
- [51] K. Xu, P. Hrma, W. Um, J. Heo, Iron phosphate glass for immobilization of ⁹⁹Tc, *J. Nucl. Mater.* 441 (2013) 262–266. <https://doi.org/10.1016/j.jnucmat.2013.06.008>.
- [52] M.T. Harrison, C.R. Scales, Durability of borosilicate glass compositions for the immobilisation of the UK's separated plutonium stocks, in: *Mater. Res. Soc. Symp. Proc.*, 2008: pp. 429–436. <https://doi.org/10.1557/proc-1107-429>.

- [53] P. Frugier, S. Gin, Y. Minet, T. Chave, B. Bonin, N. Godon, J.E. Lartigue, P. Jollivet, A. Ayral, L. De Windt, G. Santarini, SON68 nuclear glass dissolution kinetics: Current state of knowledge and basis of the new GRAAL model, *J. Nucl. Mater.* 380 (2008) 8–21. <https://doi.org/10.1016/J.JNUCMAT.2008.06.044>.
- [54] H. Zhang, C.L. Corkhill, P.G. Heath, R.J. Hand, M.C. Stennett, N.C. Hyatt, Effect of Zn- and Ca-oxides on the structure and chemical durability of simulant alkali borosilicate glasses for immobilisation of UK high level wastes, *J. Nucl. Mater.* 462 (2015) 321–328. <https://doi.org/10.1016/J.JNUCMAT.2015.04.016>.
- [55] A. Doret, N. Pellerin, M. Allix, S. Pellerin, V. Léna, K. Perrigaud, D. Massiot, Influence of Alteration Solutions on the Chemical Durability of the Zerodur® Glass-Ceramic: Structural Investigation, *Int. J. Appl. Ceram. Technol.* 12 (2015) 811–822. <https://doi.org/10.1111/IJAC.12270>.
- [56] X. Yu, D.E. Day, G.J. Long, R.K. Brow, Properties and structure of sodium-iron phosphate glasses, *J. Non. Cryst. Solids.* 215 (1997) 21–31. [https://doi.org/10.1016/S0022-3093\(97\)00022-7](https://doi.org/10.1016/S0022-3093(97)00022-7).
- [57] N. Clavier, R. Podor, N. Dacheux, Crystal chemistry of the monazite structure, *J. Eur. Ceram. Soc.* 31 (2011) 941–976. <https://doi.org/10.1016/J.JEURCERAMSOC.2010.12.019>.

5. Aluminosilicate Glass-Ceramic Materials for Treatment of Spent Radionuclide Ion Exchange Media

Summary

Orphan nuclear materials are not confined only to the fuel inventory, secondary waste such as spent ion exchange media must also be considered. A review of the literature for thermally treated spent ion specific media (ISM) wastefoms was undertaken, assessing media alongside the UK SIXEP compositions. The relatively novel method of spark plasma sintering was selected as a processing methodology. Mapping of such inorganic ion exchange residues was made to aluminosilicate glass ceramics Initial trials from earlier work on simulant inorganic ion exchange material, including parametrisation of processing parameters and wastefom prototype characterisation [1], informed optimum process conditions to be carried through to further study. A larger volume of simulant waste was prepared and sintered in preparation for a 28-day PCT-B chemical durability study. Characterisation before and after the dissolution experiments, indicated that the majority of initially exchanged caesium was retained in high durability feldspar phases, and subject to scale-up considerations, provides a robust multiphase host environment for spent ion exchange material. The undertaking of this project also served, as part of joint UK-Japanese research to support Fukushima Daiichi decommissioning efforts and optioneering for treatment of spent adsorbents, delivered as an external article output in a special edition of the Journal of Nuclear Science and Technology [2].

5.1 Ion specific media and treatment options

5.1.1 Fukushima Daiichi disaster

The historic 9.0 Mw (moment magnitude scale) [3,4] East-Japan earthquake on March 11th 2011, caused immediate widespread devastation to the populated cities and infrastructure on the main island of Honshu. Despite targeted construction regulations and citizen preparedness drills following previous historical tremors – a catastrophe of this scale, and the events that followed, were completely unprecedented.

Following shortly after the initial seismic activity, the first of a series of extremely destructive tidal waves reached the coastal regions of Japan, inundating entire ports, towns, and industrial districts. One such facility was the Fukushima Daiichi NPP, which had automatically initiated SCRAM shutdown immediately after the earthquake warning had been issued. Although AC grid power was disconnected during the quake, emergency diesel generators in site basements activated, operating nominally to power emergency cooling systems. However, the tsunami surpassed 15 m at the coast of the site, overwhelming the existing 10 m seawall and flooding the control and generator buildings [5,6]. Severe damage to the emergency generators led to the loss of cooling, hydrogen explosions and partial meltdown of Units 1, 2 and 3 at the Fukushima Daiichi NPP, in what has been rated a combined Level 7 severity nuclear accident on the international nuclear event scale (INES), equivalent rating to that at Chernobyl NPP – 1986 [7].

Although early efforts to restore emergency power and cooling were hampered by devastated infrastructure, contaminated debris and high radiation levels, extensive sea and fresh-water injection eventually allowed for the attainment of cold shutdown conditions (officially declared on 16th December 2011) [8].

5.1.2 Commercial ion-exchange materials

Extensive decommissioning activities have been carried out since the accident and are still underway. The flow of groundwater as well as continual pumping of sea and fresh-water into Units 1-3 to maintain cold shutdown, has led to the generation of 216 – 300 m³ of contaminated water per day [9,10]. One of the first major undertakings at the site to manage these large volumes of highly contaminated coolant, was the establishment of water treatment facilities such as advanced liquid processing system (ALPS) to reduce the activity and volume of contaminated effluent. The primary action by which these facilities function is using the mechanisms of a range of selective ISMs, wherein microporosity and complimentary inorganic/organic structures allow for the preferential adsorption of radionuclides onto the exchange media. One effluent contaminant present in large concentrations is the ¹³⁷Cs radionuclide (fission product Caesium-137 with a half-life of 30.08 y) [11]. The cumulative volume of water treated by the Cs adsorption apparatus to date is

2,112,460 m³ [9], which has produced 4,408 spent vessels, filters and containers of waste exchange material.

The NURES[®], *Fortum*, system is a key operational component of ALPS, which uses a cyanoferrate ISM, CsTreat[®]: hydrous hexacyanoferrate resin, K₂[CoFe(CN)₆] \cdot xH₂O [12]. This media has a high efficiency for caesium exchange over a broad pH range (1-13), with a preference for caesium interchange with potassium [13]. Current solutions for management of spent CsTreat[®] include shielding of entire exchange columns and cementitious encapsulation for interim storage facilities, leading to a large volume increase of the wastefrom and limited lifetime durability. In the UK small amounts of CsTreat[®] has been vacuum dried, temporarily stored in steel baskets [14] as well as some stored with a vinyl ester styrene polymer buffer in steel drums [15].

In the Simplified Active water Retrieval and Recovery (SARRY) treatment facility, another material used for caesium ion exchange is IONSIV[™], *Universal Oil Products- Honeywell*, a crystalline silico-titanate (CST), Na₂Ti₂O₃(SiO₄) \cdot xH₂O - synthesised with small niobium additions. IONSIV[™] has preferential exchange for caesium at high pH, and can also remove cobalt and strontium radionuclides from contaminated effluents [16]. The porous channel structures of IONSIV[™] allow exchange to take place between sodium cations and caesium radionuclides [17]. Encapsulation of spent CST waste in blast furnace slag (BFS) cements has been considered as this will reduce the exchange of caesium to hydrous phases in ordinary Portland cement (OPC) and disposal environment ground-waters [18].

The KURION ion-exchange plant was initially set up to remove ¹³⁷Cs from the water circuit using a variety of engineered inorganic zeolites based on a type of aluminosilicate called chabazite. This material has up to seven specific structural sites with varying degrees of exchange affinity, proportional to the arrangements of alkaline cations within the 8-ring subunit trigonal structure, [Na,Ca,K(AlSi₄O₁₂ \cdot xH₂O)]. Chabazite has been demonstrated for most effective cation exchange in low salinity solutions with a pH of 7-8 [19]. Investigations into a variety of waste treatment techniques have been carried out such as encapsulation using OPC and calcium aluminate cement with fly-ash (CAC-SF), though caesium poorly partitions into solid phases due to large ionic radius and wastefroms have had impracticable leach rates of up to 20% of immobilised Cs (7 days with DI water at 50 °C) [20]. Further study of this material is also attractive because of its similar composition to SIXEP zeolite, clinoptilolite [21].

Other undertakings for remediation and decommissioning of the NPP site included the construction of sea-side and land-side impermeable walls (completed 2015 and 2016 respectively) to restrict the contamination of ground and sea-water [22]. Installation of protective covers, caps and shields has allowed for complete removal of fuel from the storage pond of Unit 4 (reactor defueled at the time of the accident), investigatory surveys of damaged cores and commencement of spent fuel retrieval from Unit 3 [23].

5.1.3 Thermal treatment options for spent ion-exchange materials

When caesium has been complexed into salts and mineral mixtures, significant volatilisation and loss of simulant radionuclides has been observed experimentally at temperatures exceeding 1050 °C [24], which precludes the use of many well established high-temperature incineration [25] and vitrification technologies. In addition to this, organic ISMs such as CsTreat[®] can thermally decompose to produce harmful volatile organic compounds (VOCs) such as gaseous hydrogen cyanide. Nevertheless, studies have been piloted for the use of metallic oxide catalysts and low-temperature gasification or pyrolysis to suppress the generation of volatiles [26–28]. A trial thermal treatment plant for simulating fluidised-bed gasification of municipal and low-intermediate level carbonaceous wastes has had promising success by the state technical research centre (VTT), Finland [29,30] – though most current pilot designs necessitate vast off-gas treatment apparatus.

HIP or hot isostatic pressing, is a thermal consolidation technique which uses simultaneous isostatic pressurisation with inert gas and heating to achieve high porosity reduction of material within a weld-sealed waste container – thereby reducing risk factors for volatilisation. The high-temperature volatility of adsorbed caesium would also apply to inorganics such as the silico-titanate IONSIV[™], though use of HIP has been demonstrated to significantly improve volume reduction and long-timescale chemical durability of potential spent CST wasteforms [31,32]. HIP has been explored for optimisation of intermediate-high level waste processing over the past several decades, although the large majority of this work has been confined to the immobilisation of inactive surrogate wastes [33,34].

For zeolites such as KURION's chabazite, several other studies were conducted with sintering of ceramic matrices [35] and lead borosilicate glass encapsulation [36], although neither had reasonable consideration made for: volume reduction, possible volatilisation of caesium or the chemical durability of the wasteform. Work for a recent student project has trialled the thermal processing of Cs-exchanged chabazite by HIP, with an evaluation of the chemical durability properties indicating a suitably robust wasteform [37]. The project in question however did not attempt to address: the simplification/removal of pre-processing steps; optimisation of pressure-temperature processing conditions; the improvement of a sub-optimal throughput rate of HIP waste products; the scalability for processing large volumes of spent inorganic ISM.

An earlier report project [1] considered the relatively novel thermal treatment method of spark plasma sintering, also known as field-assisted sintering. This technique utilises a high applied direct-current with combined uniaxial dynamic compression to generate a joule-heating effect in a non-conductive sample, providing rapid heating rates, good mass transport, improved grain growth and potential for high volume reduction to near-theoretical sintered densities [38]. The processing time was notably shorter than that of HIP, the only pre-treatment steps were calcination to remove free water and loading of the conductive graphite die.

5.2 Synthesis and characterisation

5.2.1 *As-received material and ion-exchange*

The following provides a brief summary of the sample preparation technique used, more comprehensive accounts can be found in the aforementioned report and subsequent paper [1,2]. A natural source of chabazite from an agricultural stream was used as the simulant of KURIONs exchange material; its composition was 70 ± 2 wt.% Chabazite (Verdi - Zeover), 18 ± 5 wt.% volcanic glass with auxiliary components (< 5 wt.% each) of feldspar, pyroxenes, biotite and philpsite. The material was exchanged with a $0.1 \text{ M } ^{133}\text{CsNO}_3$ solution (Arcos 99%) in a teflon vessel for 24 hours, turned continuously using a roller-mill. After rinsing, filtration and removal of the subsequent liquor, the exchanged material was dried for 24 hours at $95 \text{ }^\circ\text{C}$ in air, **Section 3.1.3**.

5.2.2 *Spark plasma sintering*

After a calcination step at $300 \text{ }^\circ\text{C}$ in air, 3 g pellets of exchanged material were made by loading into a graphite die (20 mm annulus) lined with graphite sheeting, then consolidated under 50 MPa of uniaxial pressure for 10 minutes at $1000 \text{ }^\circ\text{C}$ using a HP-D 25 SPS system, *FCT Systeme GmbH*, under argon flow, **Section 3.1.4.c**. After cooling and removal from the die, remnant graphite liner material was removed using SiC abrasive. The sintering conditions of: 50 MPa, $1000 \text{ }^\circ\text{C}$ for a 10-minute dwell, were selected following the parametric cold-press and sintering trial [1].

5.2.3 *Bulk characterisation*

Helium gas pycnometry was used to measure sample density and was used as an accompanying analysis to identify any changes in density following the exchange process. A slight increase was found, with the as-received material had an average density of $2.4411 \pm 0.0015 \text{ g cm}^{-3}$ and the ion-exchanged tuff with a density of $2.4679 \pm 0.0017 \text{ g cm}^{-3}$. The increase here is again attributed to the larger atomic mass of caesium over other exchange cations. Semi-quantitative SEM/EDX confirmed the phase assemblages, particle sizes, morphologies and partitioning of Cs into the chabazite particles, with some minor exchange with cations in the phillipsite framework.

Following the thermal treatment of samples by SPS, it was found through pXRD, that all zeolite structures were successfully reacted into feldspar, $\text{K}[\text{AlSi}_3\text{O}_8]$; anorthite, $\text{Ca}[\text{Al}_2\text{Si}_2\text{O}_8]$; pyroxene, $\text{Fe}_{0.07}\text{Na}_{0.16}\text{Ca}_{0.84}\text{Mg}_{0.94}[\text{Si}_2\text{O}_6]$ and amorphous-phases (observed diffuse scattering at $20 - 30^\circ 2\theta$), **Figure 5.2.A** [2]. XRF analysis confirmed approximate retention of exchanged caesium during the sintering process, though average results were presented with a large error, $2.09 \pm 0.20 \text{ wt.}\% \text{ Cs}_2\text{O}$.

Semi-quantitative local chemical analysis by SEM/EDX, **Figure 5.2.B**, showed that caesium had primarily partitioned into a dispersed, globular, feldspar-type phase with maximum loading of 13.7 ± 4.2 wt.% Cs, with an approximate determined stoichiometry of $\text{Cs}_{0.9}\text{Ca}_{0.5}\text{K}_{1.1}[\text{Al}_3\text{Si}_8\text{O}_{22}]$. The final selected processing parameters, **Section 5.3.2**, yielded material with density by gas pycnometry of 2.7314 ± 0.0017 g cm⁻³. Additional detail relating to the characterisation of SPS and pre-SPS samples is included in the journal article, see **Appendix 5**.

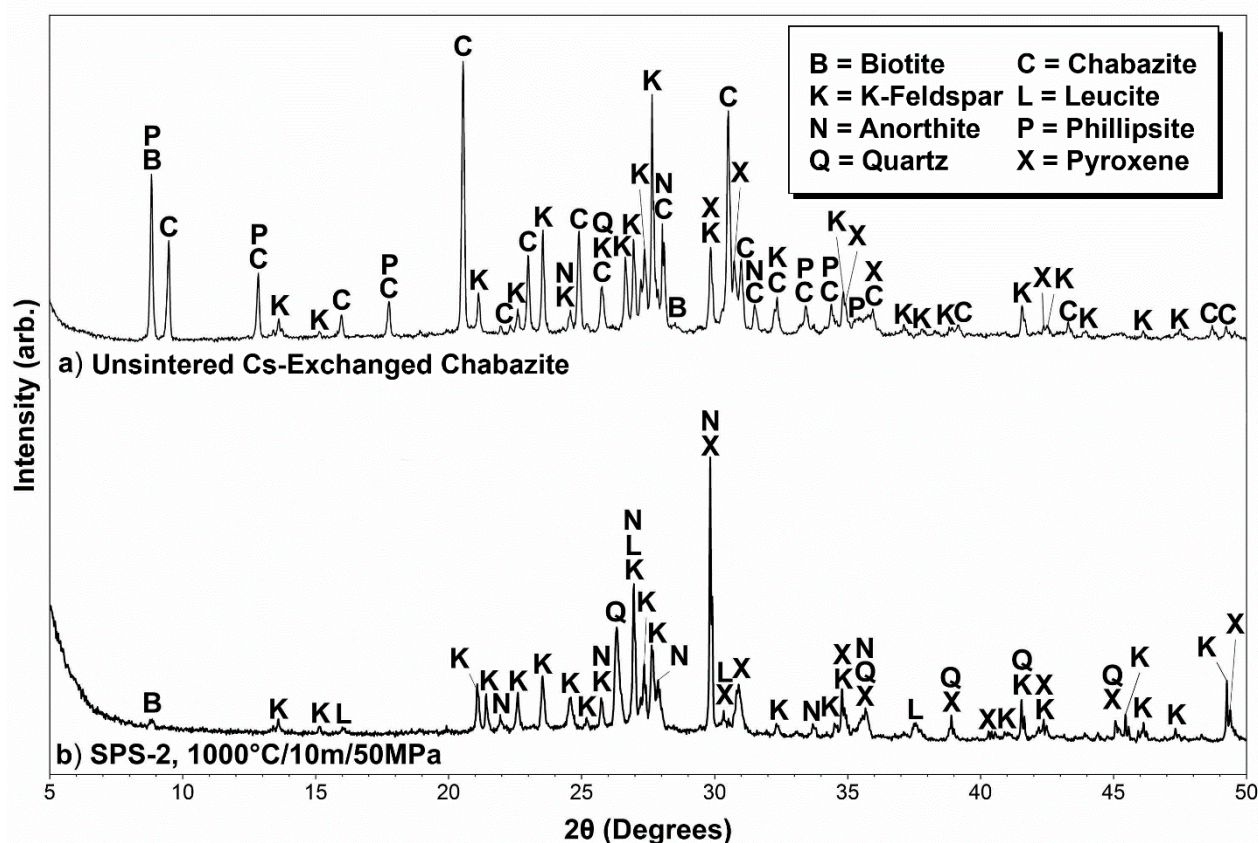


Figure 5.2.A – pXRD patterns for Cs- exchanged chabazite processed by SPS at 1000 °C for 10 minutes under 50 MPa applied pressure – blue/dotted line represents pre-dissolution at day 0, and black line shows SPS wasteform powder sampled after 28 days of PCT-B dissolution adapted from *Harnett et al.* [2].

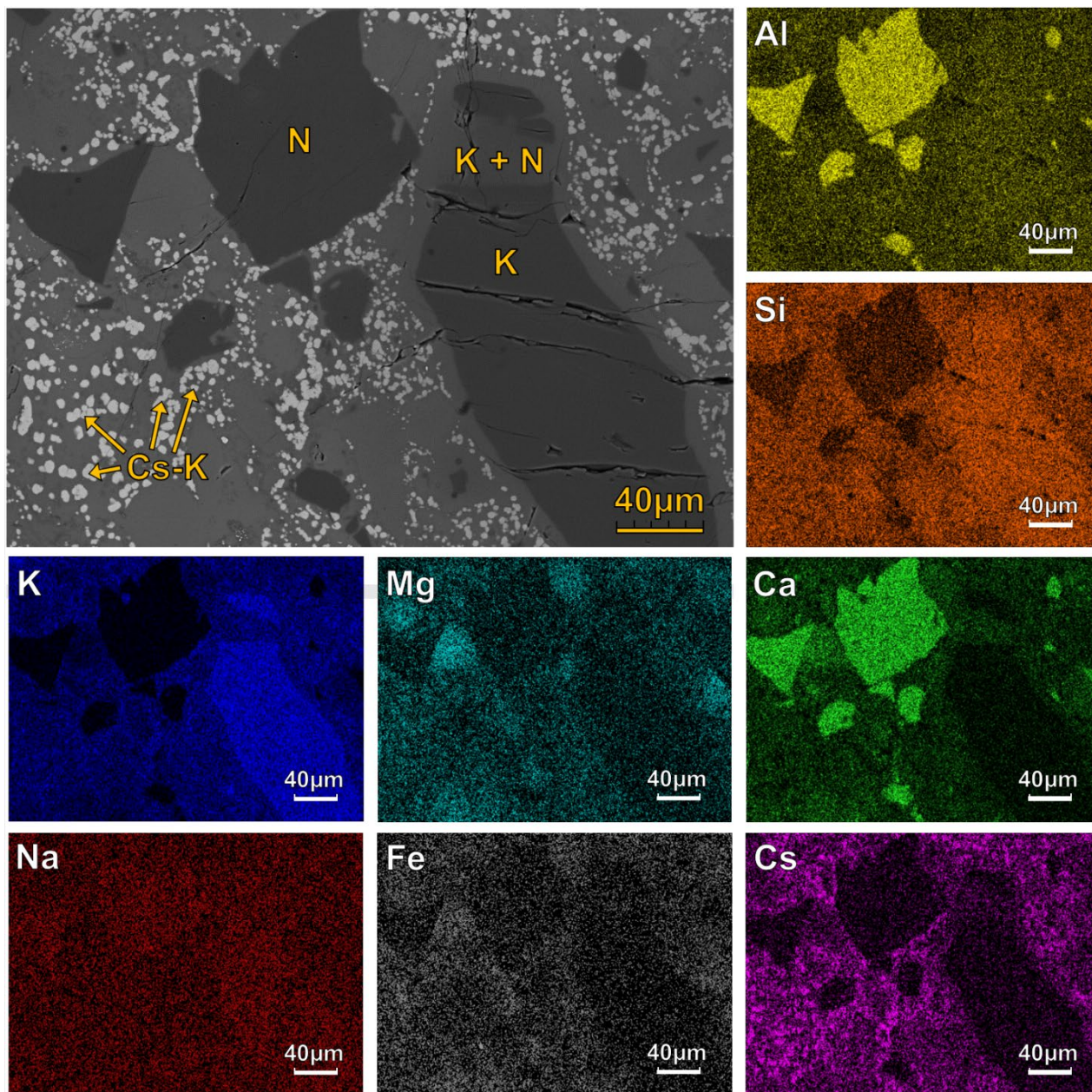


Figure 5.2.B – A combined BSE micrograph and EDX maps for a monolithic SPS wasteform prior to preparation for PCT-B dissolution (N = anorthite, K = potassium feldspar, x-K = ‘x’ doped potassium feldspar), from *Harnett et al.* [2].

5.3 Chemical durability testing

After >10 g of sintered material was generated by SPS under conditions of: 50 MPa, 1000 °C for a 10-minute dwell, powders with particle size fraction of between 75-150 µm were prepared as per **Section 3.10.1**. This allowed for the geometric assumption of sample surface area / volume of solution ratio as 1200 m⁻¹.

5.3.1 PCT-B testing

The durability study was undertaken using approximately 1 g of chabazite SPS powder with 9 mL of UHQ water as a leachate. Three sample vessels and two blanks for each time duration (1, 3, 7, 14, 21 and 28 days) were held at 90 °C in an oven to accelerate chemical alteration. Leachate aliquot analysis by ICP-OES was followed with measurements of Cs content by ion chromatography (Thermo Scientific ICS 1100). Measured pH of sample solutions remained largely consistent with an overall average of pH 10.6 ± 0.2, signifying that the initial dissolution has buffered to a basic condition, see **Figure 5.3.A**.

5.3.2 ICP-OES and ion chromatography analysis

The results from leachate analysis by ICP-OES are presented in **Figure 5.3.A**, showing the overall and normalised losses of the most significant dissolution components: Si, Cs, Al, K, Ca, and Na (g m⁻²). The opening dissolution rate is artificially elevated by the presence of remnant particles of size < 75 µm, where it is common for some to still adhere to the larger particles despite the intensive propan-2-ol washing and ultrasonic cleaning method. The slight positive correlation between the loss rates of silicon, caesium, and potassium, for days 0 – 21, may indicate the dissolution of a glass phase, though with the presence of all three of these ionic species in multiple phases of the wastefrom is prohibitive for assignment to a single discrete crystalline or amorphous structure. It should be noted that significant evaporative losses were observed for day 28, resulting in more concentrated aliquot and anomalous loss values (some omitted negative values). For days 1 – 21, the calculated initial dissolution rate for silicon was found to be $1.1 \times 10^{-3} \text{ g m}^{-2} \text{ d}^{-1}$, almost an order of magnitude improvement over the silicon loss rate of $\sim 8 \times 10^{-3} \text{ g m}^{-2} \text{ d}^{-1}$ for a HLW borosilicate glass composition [39]. The normalised losses of aluminium, calcium and sodium, all show a steady or reducing residual rate before day 14, this is comparable to similar behaviour observed with a longer durability study on international simple glass (ISG), although dissolution of material in a 0.25 M NaOH leachate started to resume following an initial decline, at day 20 [40].

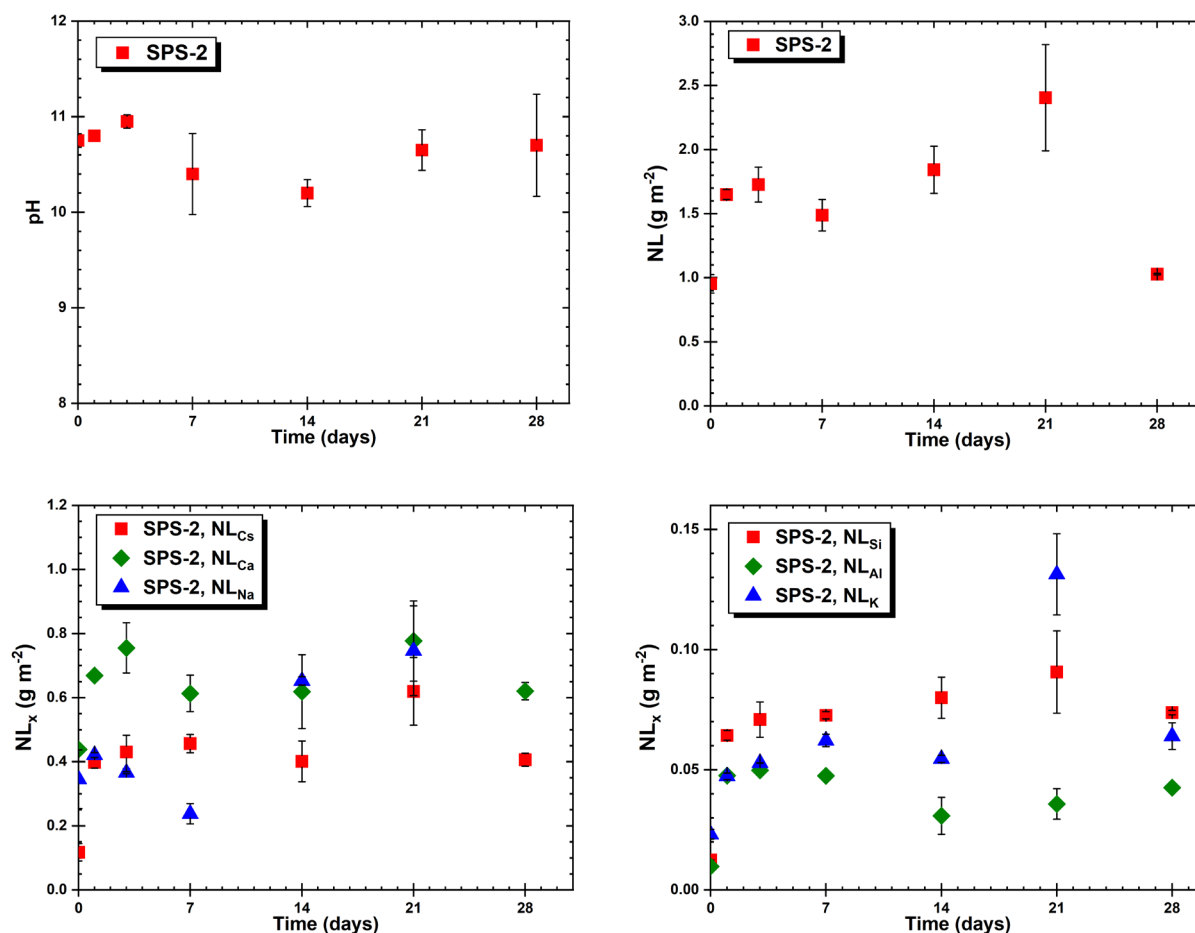


Figure 5.3.A - Normalised loss rates for 28-day PCT-B durability study with SPS Cs-exchanged chabazite, some negative values and day 28 for Na are anomalous and omitted from analysis. Plots of pH (top left); total sample mass loss (top right); normalised losses of caesium, calcium, and sodium (bottom left); normalised losses of silicon, aluminium, and potassium (bottom right), adapted from data obtained for *Harnett et al.* [2].

5.3.3 Post dissolution powder characterisation

Powder samples from some time points, especially day 28 at the end of the study, were further characterised, first by pXRD, **Section 3.3.1**, to allow for phase analysis and comparison to as-sintered samples. Powder samples were mounted in epoxy resin, by first combing a small quantity of uncured resin with the powder and loading into a mount supporting clasp, before pouring the remaining volume of resin. Though a typical grinding and polishing regime followed, a key precaution was avoidance of using any aqueous carriers or water, to avoid any interaction with soluble layers and precipitates. Assessments of particle size, morphology, alteration layers and local chemical composition were conducted using SEM and semi-quantitative EDX spectroscopy **Section 3.8.2**. Typical working distances used were 7.4 ± 0.1 mm. Local chemical compositions were calculated using an average of 10 EDX points per phase feature, normalising against inferred oxygen chemistry for charge balancing.

Diffraction patterns from analysis of Cs-chabazite SPS powders by pXRD before and after the 28-day chemical durability experiment can be seen in **Figure 5.3.B**. The inventory of aluminosilicate phases is almost completely retained, although some variation in peak intensity was observed, particularly for the $(20\bar{2})$ anorthite peak at $\sim 27.8^\circ 2\theta$, $\text{Ca}[\text{Al}_2\text{Si}_2\text{O}_8]$ (PDF #89–1461) and the pyroxene $(22\bar{1})$ and feldspar (113) peaks at $\sim 30.0^\circ$, $49.4^\circ 2\theta$; $\text{Fe}_{0.1}\text{Na}_{0.2}\text{Ca}_{0.8}\text{Mg}[\text{Si}_2\text{O}_6]$ (PDF #86–0005) and $\text{K}[\text{AlSi}_3\text{O}_8]$ (PDF #83–1657) and respectively. These deviations could be attributed to preferential leaching of the potassium feldspar phase, as the majority of remaining peaks for the feldspar reduce in intensity between the two measurements. The single (100) peak corresponding to biotite at $\sim 9.0^\circ 2\theta$ $\text{KMg}_3[\text{AlSi}_3\text{O}_{10}]$ (PDF #73–1661), was characteristic of the chabazite tuff precursor, while still present in the as processed (SPS) sample, the intensity for material before dissolution was relatively minor. Without further surface and chemical analysis, the intensity shift is ascribed to the result of preferred orientation effects [42].

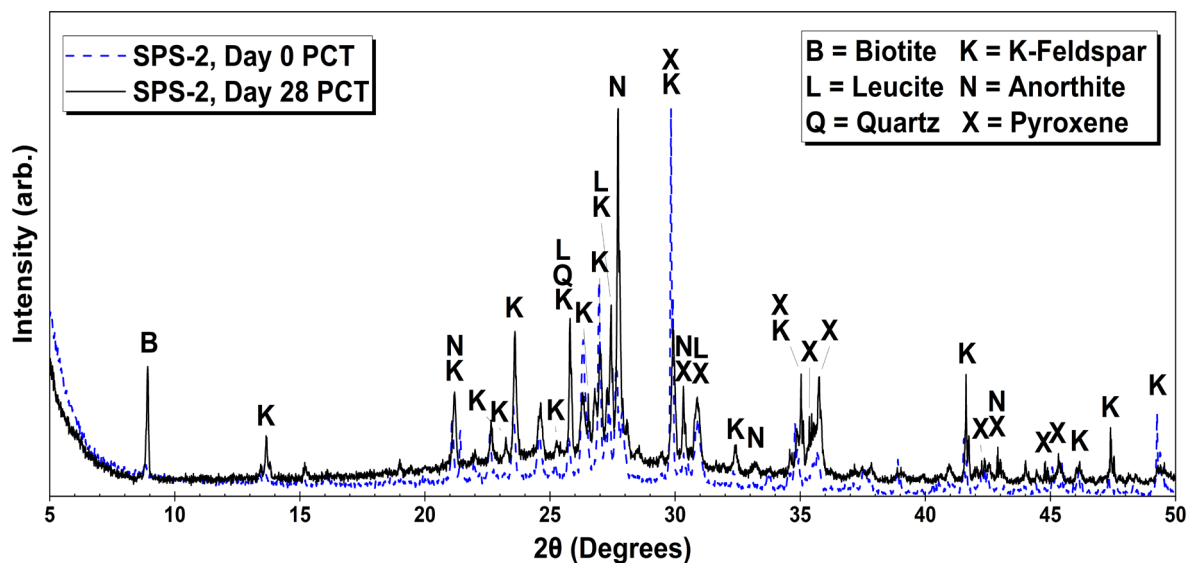


Figure 5.3.B – pXRD patterns for Cs- exchanged chabazite processed by SPS at 1000 °C for 10 minutes under 50 MPa applied pressure – blue/dotted line represents pre-dissolution at day 0, and black line shows SPS wastefrom powder sampled after 28 days of PCT-B dissolution, adapted from *Harnett et al.* [2].

Individual dissolution particles were observed by SEM after mounting in resin, sectioning the individual grains through the action of surface polishing. High magnifications were used under the same observation conditions to determine any possible alteration layer thicknesses and the relative chemical composition. A powder grain from day 28, approximately 80 – 100 μm diameter was found containing three distinct different phases, see **Figure 5.4.C**. The darker, more angular region was observed by EDX to have elevated Ca and slightly increased Al content. Following semi-quantitative analysis calculations, it was determined to have a stoichiometry of $\text{Ca}_{0.9}[\text{Al}_{1.6}\text{Si}_2\text{O}_8]$, corresponding to retained anorthite (N). The porous region covering approximately half of the particle was found to have a large potassium content and an approximate composition of $\text{Na}_{0.2}\text{Mg}_{0.4}\text{Ca}_{0.2}\text{Fe}_{0.2}\text{K}_{2.0}[\text{Al}_{3.3}\text{Si}_8\text{O}_{22}]$, a deficient alkali feldspar (K), which while observed in the day 0 samples – had appeared to develop substantially more porosity after the 28 days of dissolution, indicating a moderate degree of degradation. The low degree of porosity can be noted in **Figure 5.2.B**. The lighter, high-density phase which can also be seen in the adjacent particles of the micrograph, had a relatively higher intensity of detected caesium, and following average compositional calculations, was found to be a largely unaltered Cs-feldspar with a composition of $\text{Cs}_{0.3}\text{Mg}_{0.4}\text{Ca}_{0.6}\text{K}_{0.9}[\text{Al}_{3.4}\text{Si}_8\text{O}_{22}]$, (K –Cs). It is unlikely that the low caesium feldspar (K) region is providing a passivation effect, as the surrounding particles in the micrograph (K –Cs phases) do not appear to have any alteration or dissolution induced porosity.

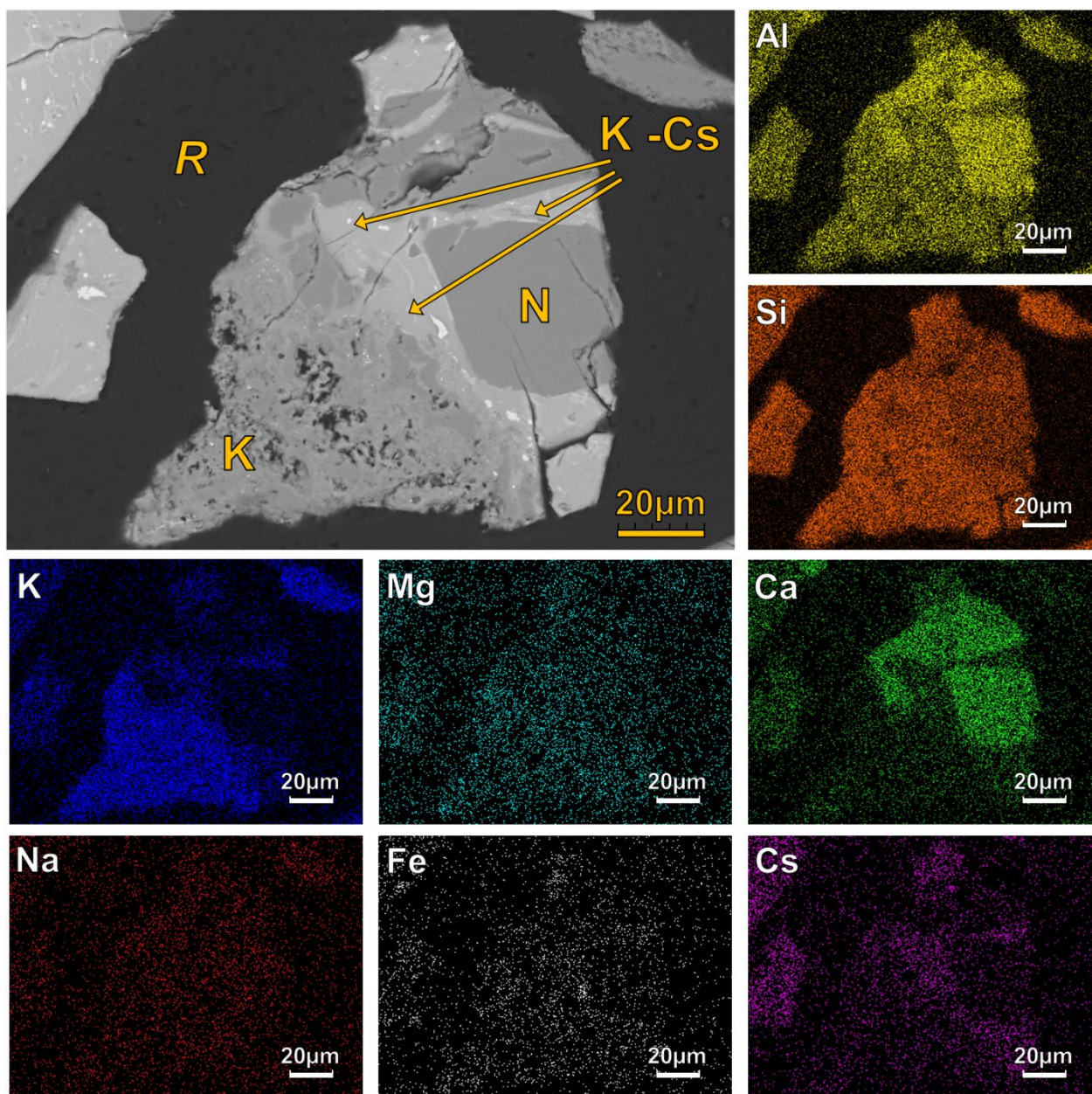


Figure 5.4.C – A combined BSE micrograph and EDX maps for a particle of SPS wasteform powder sampled after 28 days of PCT-B dissolution (*R* = mounting resin, *N* = anorthite, *K* -*x* = ‘*x*’ doped potassium feldspar), from *Harnett et al.* [2].

The edge of another particle was observed demonstrating some surface damage as well as three phases aligning to those seen in the as-thermally treated monolith microstructures, **Figure 5.4.D**. The heavily fractured light grey region with high magnesium and iron content was found to have an average composition of $\text{Fe}_{0.4}\text{Al}_{0.1}\text{Mg}_{1.1}\text{Ca}_{0.9}[\text{Si}_2\text{O}_6]$, indicative of a pyroxene (**X**), though the apparent delamination at the particle surface and depletion of calcium could indicate a minor degree of preferential alteration approximately 4 – 5 μm into the powder grain. A darker grey phase with a diameter of approximately 20 – 30 μm appeared to be relatively dense but deficient in caesium –

average composition was found to be $\text{Cs}_{0.1}\text{K}_{0.9}[\text{AlSi}_3\text{O}_8]$, an unaltered low- Cs doped feldspar phase (**K –Cs**). A surrounding region with white globular precipitates of 5 – 10 μm , was calculated to have a high potassium, calcium, and caesium content, with a composition of $\text{Cs}_{0.2}\text{K}_{0.3}\text{Ca}_{0.3}[\text{AlSi}_3\text{O}_8]$ (**K –Cs + N**). This phase was also found in the day 0 sample and appeared to have no morphological or significant chemical changes that would have indicated a dissolution reaction.

Attribution of some chemical alteration can be made into the potassium feldspar and pyroxene components of the wasteform, though a larger array of particles will have to be studied to determine other significant contributors to the dissolution. The linear increase of normalised silicon loss is characteristic of an under-saturation of dissolution leachate/liquor, with respect to Si, supported by some preliminary pH Redox Equilibrium in C-language (PHREEQC, WATEQ4F database) simulations [41] of dissolution saturation behaviour with raw ICP data. Negative saturation indices generated for anorthitic/silicate species was consistent with under-saturation, however further work should be conducted to elucidate any further attributions to hydrated silicate and amorphous silica phases. It should be noted that a linear rate was only observed after day 0 and before day 28 due to evaporative losses, as such it was only referenced as a residual rate, the steady dissolution following rapid breakdown of fines with ion exchange and initial hydrolysis of the glass network. It cannot be ascertained whether the dissolution is genuinely congruent or incongruent because the contribution to the dissolution behaviour of each silicon containing glass and mineral phase is not known. Resolution for congruency would require additional spatially resolved investigations such as tomographic or ex-situ interferometry study.

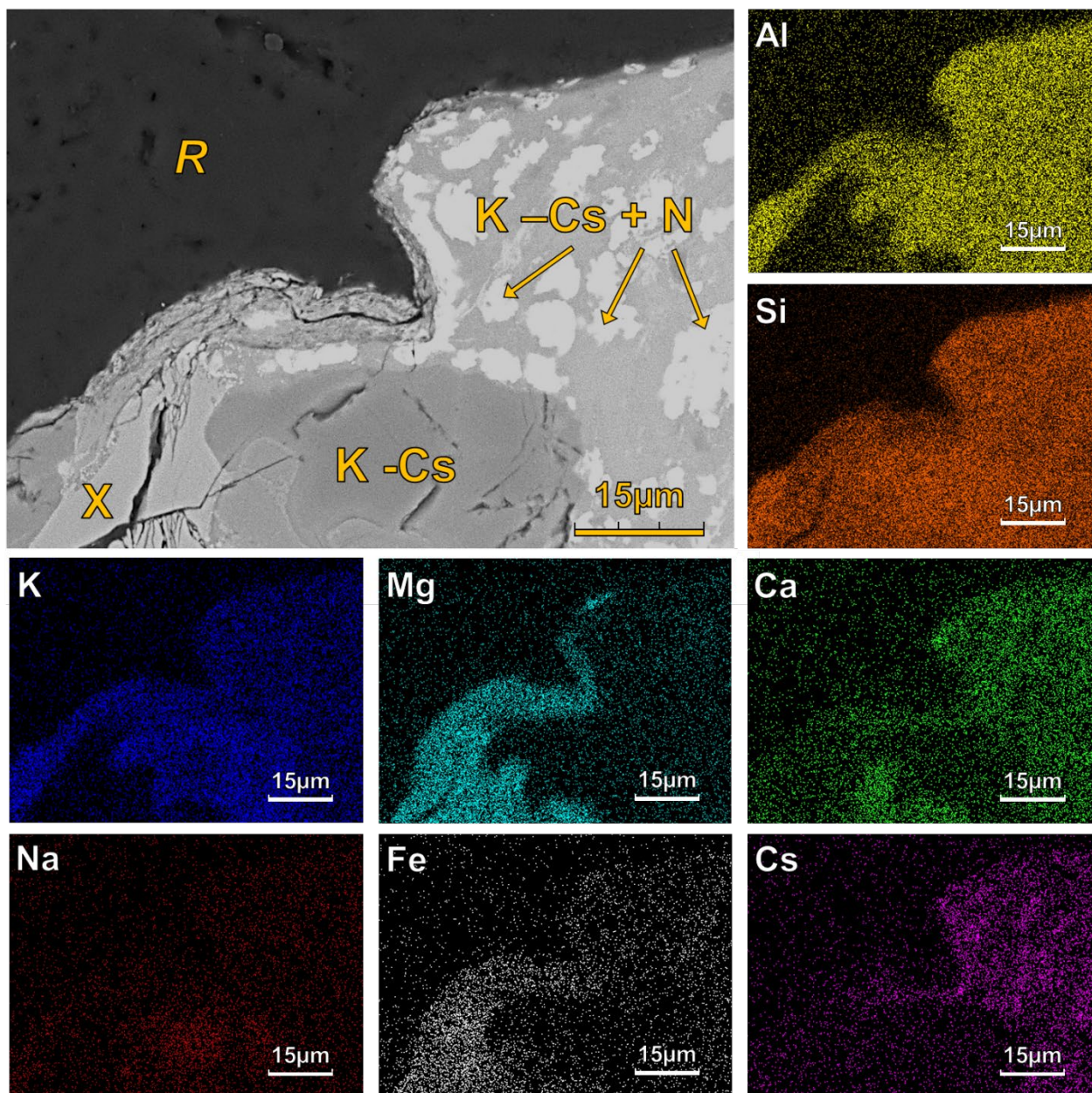


Figure 5.3.D – A combined BSE micrograph and EDX maps for particle edge of SPS wastefrom powder sampled after 28 days of PCT-B dissolution (R = mounting resin, X = pyroxene, N = anorthite, K - Cs [+ N] = caesium doped potassium feldspar [and anorthite]), *unpublished*.

5.4 Conclusions and further work

The 28 day PCT-B durability study of Cs-exchanged chabazite processed by SPS, demonstrated that silicon species dissolution behaviour is similar to that of borosilicate based glass wastefoms used for processing of UK HLW [39]. However, this is with only use of the small snapshot of dissolution behaviour that the 28-day PCT durability study provides. While some minor to moderate dissolution of pyroxene containing and low caesium containing feldspar phases was observed by an electron microscopy study, assignment, or weighting of dissolution to specific phases is prohibited by the similar aluminosilicate compositions of the 6 – 7 detected phases in the SPS material. The aqueous species and dilution simulation code PHREEQC was used to determine saturation of the leachate solution by Si, additional use could provide further insight into the solubility limits associated with the leachate volume and dissolved species. An alternative statistical method for selection of particles for SEM/EDX observations may be used to provide a more accurate overview of the wastefom phases experiencing alteration under PCT conditions. Application of quantitative phase analysis of sintered SPS products could incorporate spiked Rietveld X-ray diffraction or image-analysis methods, as outlined in **Section 3.9.2**. Further work including the ex situ monitoring of local dissolution and atomic force microscopy (AFM) [42] may allow for a resolution of this, and longer term wastefom behaviour could be assessed using a harsher chemical durability testing methodology such as single pass flow through (SPFT) [43] or aggressive acid dissolution. Spark plasma sintering of aluminosilicate ISM has been demonstrated, providing a robust wastefom resistant to leach resistance on the laboratory scale, but further work hopes to assess the effect of short-term irradiation on structural and chemical durability. This may be achieved using rapid irradiation experiments with gamma dosing from a ^{60}Co or ^{137}Cs irradiator, and alpha irradiation from a helium ion accelerator such as that available for research applications at the Dalton Cumbrian Facility [44]. In addition to use of neutron counting and gamma spectroscopy characterisations for activated species following irradiation, application of structural analysis could concern both basic x-ray diffraction and more nuanced study with sub-sampling of major crystalline and amorphous phases before ^{27}Al and ^{29}Si magic angle spinning nuclear magnetic resonance spectroscopy (MAS-NMR) [44].

Chapter 5 References

- [1] L.C. Harnett, *Conditioning of Spent Ion Exchange Materials at the Fukushima Daiichi NPP Site*, The University of Sheffield, 2017.
- [2] L.C. Harnett, L.J. Gardner, S.-K. Sun, C. Mann, N.C. Hyatt, Reactive spark plasma sintering of Cs-exchanged chabazite: characterisation and durability assessment for Fukushima Daiichi NPP clean-up, *J. Nucl. Sci. Technol.* (2019) 1–11. <https://doi.org/10.1080/00223131.2019.1602484>.
- [3] F. Diao, X. Xiong, Y. Zheng, Static slip model of the M w 9.0 Tohoku (Japan) earthquake: Results from joint inversion of terrestrial GPS data and seafloor GPS/acoustic data, *Chinese Sci. Bull.* 57 (2012) 1990–1997. <https://doi.org/10.1007/s11434-012-5014-5>.
- [4] B. Podili, S.T.G. Raghukanth, Ground Motion Parameters for the 2011 Great Japan Tohoku Earthquake, *J. Earthq. Eng.* 23 (2019) 688–723. <https://doi.org/10.1080/13632469.2017.1342292>.
- [5] M. Kazama, T. Noda, Damage statistics (Summary of the 2011 off the Pacific Coast of Tohoku Earthquake damage), *Soils Found.* 52 (2012) 780–792. <https://doi.org/10.1016/J.SANDF.2012.11.003>.
- [6] TEPCO, *The Great East Japan Earthquake and Current Status of Nuclear Power Stations*, 2012. http://www.tepco.co.jp/en/nu/fukushima-np/f1/images/f12np-gaiyou_e_1.pdf.
- [7] IAEA, *Fukushima Nuclear Accident Update Log*, (2011) IAEA. <https://www.iaea.org/newscenter/news/fukushima-nuclear-accident-update-log-15>.
- [8] G. Brumfiel, Fukushima reaches cold shutdown, *Nature*. (2011). <https://doi.org/10.1038/nature.2011.9674>.
- [9] TEPCO, *Situation of Storage and Treatment of Accumulated Water including Highly Concentrated Radioactive Materials at Fukushima Daiichi Nuclear Power Station (407th Release)*, 2019. https://www7.tepco.co.jp/wp-content/uploads/handouts_190624_02-e.pdf.
- [10] TEPCO, *Major Initiatives for Water Management*, (2014). https://www7.tepco.co.jp/responsibility/decommissioning/action/w_management/index-e.html.
- [11] E. Browne, J.K. Tuli, Nuclear Data Sheets for A = 137, *Nucl. Data Sheets.* 108 (2007) 2198. <https://doi.org/10.1016/J.NDS.2007.09.002>.
- [12] J. Lehto, S. Haukka, R. Harjula, M. Blomberg, Mechanism of caesium ion exchange on potassium cobalt hexacyanoferrates(II), *J. Chem. Soc. Dalt. Trans.* (1990) 1007. <https://doi.org/10.1039/dt9900001007>.
- [13] E. Tusa, R. Harjula, P. Yarnell, Fifteen Years of Operation with Inorganic Highly Selective Ion Exchange Materials, *WM'07 Conf.* (2007). [https://web.archive.org/web/20170809103727/https://www.fortum.com/SiteCollectionDocuments/Products and services/WM07_15years_7025.pdf](https://web.archive.org/web/20170809103727/https://www.fortum.com/SiteCollectionDocuments/Products%20and%20services/WM07_15years_7025.pdf).
- [14] NDA, *Waste Stream: Magnox-Secondary Ion Exchange Resin (Cs-Treat)*, 2016. <https://ukinventory.nda.gov.uk/wp-content/uploads/sites/18/2017/03/9B85.pdf>.
- [15] S. Doudou, J. Mcteer, S. Wickham, R. Thied, R. Woodcock, T. Turner, C. Hamblin, M. Buckley, *Optimised Management of Orphan Wastes in the UK*, (2013). <https://doi.org/10.1115/ICEM2013-96330>.

- [16] R.G. Anthony, R.G. Dosch, C.V. Philip, Method of using novel silico-titanates, 1994. <https://patents.google.com/patent/US6110378>.
- [17] D.M. Poojary, R.A. Cahill, A. Clearfield, Synthesis, Crystal Structures, and Ion-Exchange Properties of a Novel Porous Titanosilicate, *Chem. Mater.* 6 (1994) 2364–2368. <https://doi.org/10.1021/cm00048a024>.
- [18] A. Jenni, N.C. Hyatt, Encapsulation of caesium-loaded Ionsiv in cement, *Cem. Concr. Res.* 40 (2010) 1271–1277. <https://doi.org/10.1016/J.CEMCONRES.2009.10.015>.
- [19] D. Novembre, B. Di Sabatino, D. Gimeno, M. Garcia-Vallès, S. Martínez-Manent, Synthesis of Na–X zeolites from tripolaceous deposits (Crotone, Italy) and volcanic zeolitised rocks (Vico volcano, Italy), *Microporous Mesoporous Mater.* 75 (2004) 1–11. <https://doi.org/10.1016/J.MICROMESO.2004.06.022>.
- [20] H. Fryda, G. Vetter, R. Ollitrault-Fichet, P. Boch, A. Capmast, Formation of chabazite in mixes of calcium aluminate cement and silica fume used for caesium immobilization, 1996. <https://www.icevirtuallibrary.com/doi/pdf/10.1680/adcr.1996.8.29.29>.
- [21] A. Braun, Application of Ion Exchange Processes for the Treatment of Radioactive Waste and Management of Spent Ion Exchangers, 2002. https://www-pub.iaea.org/MTCD/Publications/PDF/TRS408_scr.pdf.
- [22] TEPCO, Completion of Seaside Impermeable Wall Closure at Fukushima Daiichi Nuclear Power Station, 2016. https://www7.tepco.co.jp/wp-content/uploads/hd03-02-03-002-005-handouts_151026_01-e.pdf.
- [23] TEPCO, Fukushima Daiichi Nuclear Power Station Phase 2 freezing of Landside Impermeable Wall starts, 2016. https://www7.tepco.co.jp/wp-content/uploads/hd03-02-03-002-004-handouts_160606_01-e.pdf.
- [24] B.P. Spalding, Volatilization of Cesium-137 from Soil with Chloride Amendments during Heating and Vitrification, *Environ. Sci. Technol.* 28 (1994) 1116–1123. <https://doi.org/10.1021/es00055a022>.
- [25] B.D. Amiro, S.C. Sheppard, F.L. Johnston, W.G. Evenden, D.R. Harris, Burning radionuclide question: What happens to iodine, cesium and chlorine in biomass fires?, *Sci. Total Environ.* 187 (1996) 93–103. [https://doi.org/10.1016/0048-9697\(96\)05125-X](https://doi.org/10.1016/0048-9697(96)05125-X).
- [26] M. Matsuda, K. Funabashi, H. Yusa, Effect of Metallic Impurities on Oxidation Reaction of Ion Exchange Resin, (I), *J. Nucl. Sci. Technol.* 23 (1986) 244–252. <https://doi.org/10.1080/18811248.1986.9734977>.
- [27] K. Kinoshita, M. Hirata, T. Yahata, Treatment of Ion-Exchange Resins by Fluidized Bed Incinerator Equipped with Copper Oxide Catalyst Fundamental Studies, *J. Nucl. Sci. Technol.* 28 (1991) 228–238. <https://doi.org/10.1080/18811248.1991.9731348>.
- [28] R.-S. Juang, T.-S. Lee, Oxidative pyrolysis of organic ion exchange resins in the presence of metal oxide catalysts, *J. Hazard. Mater.* 92 (2002) 301–314. [https://doi.org/10.1016/S0304-3894\(02\)00025-0](https://doi.org/10.1016/S0304-3894(02)00025-0).
- [29] S. Ciuta, D. Tsiamis, M.J. Castaldi, *Gasification of Waste Materials*, Elsevier, 2018. <https://doi.org/10.1016/C2015-0-06162-7>.
- [30] Theramin, Thermal treatment for radioactive waste minimisation and hazard reduction Title: Gasification based waste treatment, 2019. http://www.theramin-h2020.eu/downloads/THERAMIN_D3_4_Gasification_based_waste_treatment.pdf.

- [31] T.-Y. Chen, J.A. Hriljac, A.S. Gandy, M.C. Stennett, N.C. Hyatt, E.R. Maddrell, Thermal Conversion of Cs-exchanged IONSIV IE-911 into a Novel Caesium Ceramic Wasteform by Hot Isostatic Pressing, *MRS Proc.* 1518 (2013) 67–72. <https://doi.org/10.1557/opl.2013.202>.
- [32] T.-Y. Chen, E.R. Maddrell, N.C. Hyatt, A.S. Gandy, M.C. Stennett, J.A. Hriljac, Transformation of Cs-IONSIV® into a ceramic wasteform by hot isostatic pressing, *J. Nucl. Mater.* 498 (2018) 33–43. <https://doi.org/10.1016/J.JNUCMAT.2017.10.011>.
- [33] E. Maddrell, Hot isostatically pressed wasteforms for future nuclear fuel cycles, *Chem. Eng. Res. Des.* 91 (2013) 735–741. <https://doi.org/10.1016/J.CHERD.2012.11.004>.
- [34] M.W. Stewart, L. Heights, A.A. Sam Moricca, A. Tina Eddowes, A. Yingjie Zhang, A.R. Eric Vance, A.R. Gregory Lumpkin, M. Dowson, M. James, *The Use of Hot Isostatic Pressing to Process Nuclear Waste Forms*, 2009. <https://proceedings.asmedigitalcollection.asme.org>.
- [35] P. Cappelletti, G. Rapisardo, B. de Gennaro, A. Colella, A. Langella, S.F. Graziano, D.L. Bish, M. de Gennaro, Immobilization of Cs and Sr in aluminosilicate matrices derived from natural zeolites, *J. Nucl. Mater.* 414 (2011) 451–457. <https://doi.org/10.1016/J.JNUCMAT.2011.05.032>.
- [36] D. Pletser, R.K. Chinnam, M. Kamoshida, W.E. Lee, Immobilisation process for contaminated zeolitic ion exchangers from Fukushima, *MRS Adv.* 1 (2016) 4089–4094. <https://doi.org/10.1557/adv.2017.194>.
- [37] J.J. Hartley, *A Dissolution Study of Thermally Treated Chabazite by Hot Isostatic Pressing*, The University of Sheffield, 2019.
- [38] Z.A. Munir, U. Anselmi-Tamburini, M. Ohyanagi, The effect of electric field and pressure on the synthesis and consolidation of materials: A review of the spark plasma sintering method, *J. Mater. Sci.* 41 (2006) 763–777. <https://doi.org/10.1007/s10853-006-6555-2>.
- [39] M.T. Harrison, C.R. Scales, Durability of borosilicate glass compositions for the immobilisation of the UK's separated plutonium stocks, in: *Mater. Res. Soc. Symp. Proc.*, 2008: pp. 429–436. <https://doi.org/10.1557/proc-1107-429>.
- [40] M. Fournier, P. Frugier, S. Gin, Resumption of Alteration at High Temperature and pH: Rates Measurements and Comparison with Initial Rates, *Procedia Mater. Sci.* 7 (2014) 202–208. <https://doi.org/10.1016/J.MSPRO.2014.10.026>.
- [41] D.L. Parkhurst, C.A.J. Appelo, Description of input and examples for PHREEQC version 3: a computer program for speciation, batch-reaction, one-dimensional transport, and inverse geochemical calculations, *Tech. Methods.* (2013). <https://doi.org/10.3133/TM6A43>.
- [42] J. Cama, L. Zhang, J.M. Soler, G. De Giudici, R.S. Arvidson, A. Lüttge, Fluorite dissolution at acidic pH: In situ AFM and ex situ VSI experiments and Monte Carlo simulations, *Geochim. Cosmochim. Acta.* 74 (2010) 4298–4311. <https://doi.org/10.1016/J.GCA.2010.04.067>.
- [43] ASTM, Standard Practice for Measurement of the Glass Dissolution Rate Using the Single-Pass Flow-Through Test Method 1, 2018. <https://doi.org/10.1520/C1662-18>.
- [44] M. Herbas, *Ion Exchange to cope with decommissioning*, University of Manchester, 2018. https://www.research.manchester.ac.uk/portal/files/78646962/FULL_TEXT.PDF.

6. Further discussion and conclusions

6.1 Conclusions

Through a review of the UK inventory of orphan nuclear materials and non-reprocessable wastes, arisings from legacy development and degraded spent fuel were determined to primarily consist of AGR (uranium oxide clad with stainless steel); LWR (uranium and plutonium oxide clad with zirconium alloy); Magnox (uranium metal clad with magnesium-aluminium alloy). There are also materials arising from prototype reactor breeder blanket components, novel cladding alloys and designs as well as a host of inorganic and organic selective ion exchange media from effluent decontamination.

A set of pre-processing steps were considered to prepare orphan nuclear materials for thermal treatment. From mechanical separation and de-cladding of solid components to separation and chemical dissolution of fuel containing materials, the proposed pre-processing methods aim to homogenise waste feeds prior to further treatment. Where fuel can be separated from its cladding, storage basket and any backfill material, it is preferential to treat this as an individual actinide and fission product rich feed, where elements from cladding alloys may decrease wastefrom loading and long-term durability in storage. Material feeds rich in magnesium, iron, zirconium, uranium, plutonium, fission products were proposed as the homogeneous waste streams for the most significant proportion of the orphan nuclear inventory. Vitrification and hot-pressing thermal treatment methods were reviewed and considered in relationship to the feed chemistry and potential host matrices. Glass-ceramics were selected as a primary route, due to very high chemical durability and self-irradiation resistance of crystalline phases, while maintaining the chemical flexibility and bonding of a glass phase. HIP, HUP and SPS were also considered for some glass-ceramic and ceramic host matrices, SPS can offer rapid sintering at lower equivalent temperatures than would be required for low pressure sintering. Multi-phase SYNROC-type ceramic assemblages were also considered for treatment of concentrated and separated spent oxide fuel, as there is potential for high waste loading, retention of fission products and possible processing under hermetically sealed conditions.

A sodium iron phosphate glass-ceramic composition was selected for potential treatment of iron-rich spent fuel waste streams. A SIP base glass was synthesised and doped with small additions of alumina and silica (IPSAS) in order to study the passivation of melt behaviour, phase assemblage and wastefrom performance. Fluorite structured cerium oxide was used as a waste simulant, loading the glass ceramic compositions at up to 45 mol.%. For SIP and IPSAS series, the onset of crystallisation was found with samples loaded with more

than 16 – 25 mol.% waste, where the primary phase developments were cerium monazite and sodium iron phosphate. In cases of higher loadings, an increase in porosity development was observed and some undigested cerium oxide was retained in the wasteform. Melts performed at 1250 – 1450 °C showed that at high temperatures, a greater quantity of aluminium is dissolved from the alumina crucible into the glass, with further additions of simulant waste appearing to passivate this effect. Cerium monazite crystallised in a characteristic core-shell morphology, forming around partially digested grains of cerium oxide. At the melt solubility point of 16 – 25 mol.% monazite microstructure was also observed as a distributed arrangement of dendritic cruciform micro-crystallites. Retention of batched quantities of simulant oxide waste was measured to be substantially lower than targeted with the initial batch. While this may be attributed to phase separation during the melt and casting stages of synthesis, the method used to quantify glass bulk composition, EDX, is semi-quantitative and further compositional analysis of bulk and individual phases may be required.

Spectroscopic studies were utilised to assess the redox environment of iron, as this may inform chemical durability performance and glass structure local to iron centres. Results showed that the bulk wasteforms contained approximately 30% Fe(II), reflective of previous phosphate glass studies. There was an apparent trend of slight increase of Fe(II) content with greater simulant loading in SIP wasteforms, while the IPSAS series indicated that greater loading slightly decreases Fe(II) content. An X-ray absorption spectroscopy investigation suggested that the proportion of Fe(II) in the glass ceramic materials was slightly higher, than as measured by Mössbauer spectroscopy. Further work with consideration for a temperature-dependant study, is required in order to generate an accurate value for recoil-free fraction, which for this project was determined from a literature review of similar sodium iron phosphate compositions. The oxygen coordination environment for iron centres demonstrated iron-oxygen bonding in near-tetrahedral configuration for all wasteforms, with the exception of IPSAS 0 mol.% simulant glass melted at 1350 °C, which was determined to be more octahedrally coordinated. With further spectroscopic work, the confirmation of iron as a substituting atom for phosphorous in P – O – P linkages should show its position as a network modifier, and how the structure relates to more hydrolytically stable iron species.

A 28-day accelerated dissolution experiment for a matrix of SIP and IPSAS series samples, showed the deleterious effect of small refractory additions to precursor batches, with IPSAS 0 – 8 mol.% simulant wasteforms degrading at a significantly faster rate than that of the SIP series. The 0 mol.% waste counterparts achieved the highest congruent releases of glass network elements, and the 25 mol.% simulant materials had the lowest losses, indicating

that the addition of cerium oxide as a simulant waste increases the chemical durability. While the SIP series was overall more chemically durable, the IPSAS 25 mol.% simulant sample achieved comparable leaching rates, while having retained more of the batched cerium oxide in the bulk wasteform.

These findings indicated that with the formation of cerium monazite crystals, mobile cerium in the glass melt migrates from the glass phase, preferentially forming more highly durable monazite. With a lower durability glass phase depleted in cerium, a greater proportion remains sequestered in a crystalline phase. Under accelerated leaching conditions, the SIP wasteforms and IPSAS 25 mol.% simulant sample performed comparably to UK borosilicate glasses for treatment of HLW and to other cerium phosphate compositions.

A quantitative phase analysis code was iterated for rapid measurement of multi-phase wasteforms. Several features were implemented and adjusted to improve efficiency and usability with various different assemblages. The key advantage over more traditional methods, often requiring several hours per sample, is the data collection and processing time of image based QPA. Including image acquisition times, results comparable to an internal-standard Rietveld method were achieved in a total of 8 minutes for a 10 BSE set, increasing to 20 minutes for a 25 image set. The technique does, however, have an inherent limitation with difficulty processing images containing phases with similar BSE grey contrast, as such, it would be unable to distinguish between two phases with exactly the same mean atomic number. The open nature of this platform will allow for ease of additional control, modification and integration with microscopes featuring motorised or computer-controlled stages. Other heterogeneous multi-phase materials may be measured using this method, such as those studied by researchers in the fields of cultural heritage and archaeology. Such a technique may be applied to images acquired through other micro-analysis techniques such as optical and Raman spectroscopy; however, due care will be required to ensure defined contrast of both amorphous and crystalline phases, with minimum resolvable feature size constrained to the diffraction limit with light-based analyses.

An inorganic ion exchange material was selected, analogous to those used at the SIXEP and Fukushima waste effluent treatment plants for decontamination of radionuclides. As a secondary orphan material, once spent, this type of exchange media is considered waste. Exchanged resin was prepared using a simulant caesium contaminated solution, before drying and thermally treating using a high-throughput SPS technique. The simulant waste compacts formed an aluminosilicate glass-ceramic under the hot-pressing conditions, with higher concentrations of caesium partitioning into a feldspar phase. Six individual crystalline phases

were identified in the wastefrom with a small quantity of bonding glass matrix. Due to the heterogenous assemblage of the wastefrom, conclusive underpinning of the source of particular elemental releases is limited under accelerated conditions with only a 28-day study. A short term residual silicon loss rate was found to be comparable to that of UK HLW borosilicate glass waste streams. While this aluminosilicate composition may provide a suitable wastefrom for treatment for immobilisation of ion exchange media, consideration should be made for process scale-up and further work is required to determine the precise dissolution mechanisms for such a wastefrom.

6.1 Future work

A significant aspect of treating the inventory of orphan nuclear materials, is for the use of hot isostatic pressing and multi-phase ceramic matrices. Some initial project work related to prototyping SYNROC ceramic materials for immobilisation of orphan waste is featured in a research output, see **Appendix 1**. Solubility of the matrix for simulant oxide fuel was promising, although a high degree of porosity developed under the atmospheric pressure sintering conditions. Further work could apply the use of hot pressing to thermal treatment and densification of such materials.

Thermal behaviour of SIP and IPSAS glass melts could be studied using viscosity measurements and a wider gamut of Differential Scanning Calorimetry (DSC) and DTA methods, including an assessment of the low temperature reactions of batched reagents before softening and melting occurs. Alternation of phosphate source to phosphoric acid may provide a more passive melt without the generation of ammonia. Spectroscopic and microprobe techniques could be employed to study the composition of the glass phase in highly crystalline glass-ceramic samples, while aiding in the confirmation of crystallite composition. Use of depleted uranium oxide or simulated-fuel-fission product compositions with other additives such as chromium may also aid in simulating a stainless steel contaminated fuel feed. Laser Raman spectroscopy would support further X-ray absorption spectroscopy investigation of the local structure of the glass phases, while hot-stage microscopy could allow for an in-situ study of crystallisation. ICP-mass spectrometry could be employed to accurately quantify the lower concentrations of iron and cerium in some samples, while a vapour hydration test of a glass coupon would permit study of glass alteration and gel layers.

Further developments to the image analysis code are required to improve accessibility, portability, and ease of use. The quantification methodology has been demonstrated in the phosphate glasses project work, a small-scale experiment with barium containing ceramics, and a zirconolite glass ceramic loaded with plutonium (unpublished). Integration of microscope stage remote control by software may permit more rapid and repeatable automated analysis. Scale-up for SPS based immobilisation should be trialled, and application of a thermodynamic modelling study would inform the limitations of thickness and for waste feeds containing less resistive elements. Irradiation testing would aid in performance characterisation for high heat generating waste and for judgment of amorphisation resistance. Monitoring of SPS off-gasses would progress the understanding of temperature dependant releases of volatiles during sintering.

Appendix 1. Development of phosphate glass and multi-phase titanate ceramic compositions for thermal treatment of irradiated nuclear fuel residues

This publication formed part of a contribution to the European Commission THERmal treatment for RAdioactive waste MINimisation and reduction (THERAMIN) project. It features some early results from iron phosphate glass trials before processing conditions had been optimised. This article also discusses some of the SYNROC-F type titanate ceramic work and development of methodologies for precursor preparation prior to atmospheric pressure sintering experiments.

PAPER • OPEN ACCESS

Development of phosphate glass and multi-phase titanate ceramic compositions for thermal treatment of irradiated nuclear fuel residues

To cite this article: L Harnett *et al* 2020 *IOP Conf. Ser.: Mater. Sci. Eng.* **818** 012012

View the [article online](#) for updates and enhancements.

Development of phosphate glass and multi-phase titanate ceramic compositions for thermal treatment of irradiated nuclear fuel residues

L Harnett¹, M C Stennett¹, E R Maddrell² and N C Hyatt^{1*}

¹Department of Materials Science & Engineering, The University of Sheffield, Mappin Street, Sheffield, S1 3JD.

²National Nuclear Laboratory, Sellafield, Seascale, Cumbria, CA20 1PG, UK

*n.c.hyatt@sheffield.ac.uk

Abstract. The highly heterogeneous nature of UK legacy damaged and degraded spent nuclear fuels and so called, ‘orphan fuels’, prohibits the use of standard conditioning methods. An inventory of UK residual fuels yielded an account for three main fuel types: Magnox, AGR (advanced gas-cooled reactor) and MOx (mixed oxides). A series of glass and ceramic type host systems have been investigated for potential conditioning of these high uranium content spent fuel materials. Electron microscopy and powder X-ray diffraction techniques were used to characterise the prototypical wastefuels. Two sets of low-melt temperature phosphate glass compositions were trialled with additions of CeO₂ to simulate the fluorite structure and large ionic radius of U in oxide fuels. Evolution of monazite-type phases at simulant oxide fuel loadings above 15 wt.% highlighted a potential development into a glass-ceramic hybrid assemblage. Investigation into the use of an alkoxide nitrate synthesis route for SYNROC-F type ceramic precursors has allowed for the demonstration of a sintered host pyrochlore phase containing up to ~40 wt.% fuel simulant CeO₂. Gas evolution has led to increased porosity at higher temperatures and longer sintering times, this may be mitigated by higher pre-calcination temperatures.

1. Introduction

After operation in a nuclear reactor, spent fuel is retained in a storage medium, typically water, to allow for the shielding of workers from the high radiation doses and cooling of decay heat. The UK uniquely differentiates between ‘damaged nuclear fuel’ and ‘failed’ fuels: a moderate failure refers to a breach of the fuel element (such as a pinhole), whereas a damaged fuel element has a significant deviation from the typical fuel pin geometry (bent or fractured element). The severity of damaged fuel may confer conditions that can lead to processing and manipulation problems. Failed AGR (Advanced Gas cooled Reactor) fuel has historically been packed into containment using reactor-site facilities, to allow transport to ThORP (Thermal Oxide Reprocessing Plant). Pond storage of some spent fuel has led to degradation and non-conformable cladding geometry; some of this material was still reprocessed with a slightly different procedure, but the stability and integrity of a significant quantity of damaged SNF (Spent Nuclear Fuel) negates use of standard conditioning methods. In 2009, an IAEA working group



defined damaged spent fuel as “*any SNF that requires non-standard handling to demonstrate compliance with applicable safety, regulatory or operational requirements*” [1]. Through a review of reactor-fuel specific literature and a collaborative liaison with a National Nuclear Laboratory spent fuel management team, a taxonomy of UK degraded spent fuel and fuel residues of interest was constructed. The major contributors by tons of heavy metal are: Magnox type with some Dounreay Fast Reactor breeder blanket material; low-enrichment type MOx (Mixed Oxide) fuel, steel clad AGR fuel; and a small quantity of experimental carbide fuels.

Many of the spent fuel materials in the UK inventory cannot be processed by the ThORP separation facilities, since activities terminated in 2018, and may be unsuitable for Magnox reprocessing at Sellafield before the end of its operational lifetime in 2020 [2]. Much of this legacy spent fuel is unsuitable for typical vitrification treatments due to volatile content, damage to the fuel pins, contamination through corrosion of containment, novel assembly design, experimental fuel compositions and inclusion of cutting debris [3–6]. The UK is currently considering long term disposal solutions for high activity materials in a mined Geological Disposal Facility (GDF), although very deep boreholes may prove a viable alternative [7].

2. Existing thermal treatment methods

The vast majority of studied and applied vitrification techniques focus on the addition or development of borosilicate glass (either through loading of frit or glass precursors), which can provide high chemical durability and moderate waste loading for ILW (Intermediate Level Waste) streams. However, borosilicate may be unsuitable for some HLW (High Level Waste) and orphan fuels: the poor actinide loading capability may lead to large volume increases of waste, high temperature melts could cause volatilisation of fission products, and the chemical durability may fall short for the particularly long-lived radionuclides [8]. Phosphate glasses were first investigated by the US and Germany during the 1960s, as an alternative to borosilicate: attractive for the low melt temperature and solubility of sulfates and molybdates [9]. Despite these advantages, research slowed as early phosphate glass compositions were unsuitable for waste vitrification due to: highly corrosive melts (therefore propensity to damage melters and refractories); crystallisation during annealing (nucleation of NaPO₄ crystallites) [10]; and devitrification at higher temperatures, leading to poor chemical durability [11]. Over the past several decades, research has returned to improving phosphate glasses for actinide waste disposition; additions of Na, Al and Fe oxides are a focus of this work since they may confer better dissolution behaviour when compared to typical borosilicate glass, with complete loading of UO₂ of at least ~12 wt.%, and melting at 1150°C [12]. This research aims to partly build upon recent work that highlighted some chemically durable SAP and SAIP (sodium-aluminium phosphate and sodium-aluminium-iron phosphate) glass compositions that are capable of ~49 wt.% UO₃ waste loading. Although annealing did increase crystalline development for the SAIP composition, the leach rate of U was demonstrated to be below 10 g m⁻² d⁻¹, under PCT-B (Product Consistency Test) conditions [13].

Extensive research and development work has been carried out concerning the use of crystalline ceramic materials for the immobilisation of radioactive waste. A multiphase titanate ceramic, SYNROC (synthetic rock), has been investigated by several nuclear science institutions, in collaboration with international nuclear materials research groups [14]. One compositional variant, known as SYNROC-F was specifically designed for high UO₂ loading to directly immobilise spent fuel. The main components of this formulation are: 95 wt.% cubic U-pyrochlore type similar to betafite (CaUTi₂O₇) [15] for disposition of U, rare earths and Sr; up to 5 wt.% hollandite [Ba(Al,Ti)₂Ti₆O₁₆] [16] for immobilisation of large ionic radius radionuclides like ¹³⁷Cs; up to 5 wt.% tetragonal rutile or titanium dioxide (TiO₂) [17]. While synthesis has been carried out using combinations of oxides, precursors generated using sol-gel methods and proprietary techniques, further improvements could be made to streamline the preparation and improve the reactivity of SYNROC precursors, facilitating incorporation of dissolved waste and liquors.

3. Experimental methodology

3.1. Phosphate glass wasteform

The phosphate glass systems explored were based on two Fe-phosphate compositions: one with small oxide additions of Si, Al and Na, and another only with Na additions. Herein, these compositions will be referred to as IPSAS and SIP, respectively. Oxide and organic constituents were batched and homogenised with the main phosphate base as $\text{NH}_4\text{H}_2\text{PO}_4$ (98% ACS, Alfa Aesar) and Fe_2O_3 (96%, Sigma Aldrich), SiO_2 (99.5%, Alfa), Na_2CO_3 (98%, Alfa), Al_2O_3 (99%, Alfa) and CeO_2 (99.5%, Alfa). CeO_2 additions were used as an inactive simulant for UO_2 , as its fluorite structure can provide suitable analogue behaviour prior to approval of active material trials. Batches were homogenised with between 0 – 20 wt.% CeO_2 as simulated spent fuel. The oxide constituents were held for 6 hours at 200°C before 2 hours at a melt temperature of 1250°C under air in an alumina crucible. Glass samples were poured onto a preheated casting plate before annealing for 4 hours at 550°C and slow cooled to room temperature. Samples from the glass coupons were ball-milled for pXRD (powder X-ray diffraction) using a Bruker D2 PHASER diffractometer with a LynxEye detector ($\text{Cu K}\alpha$, $\lambda = 1.5418 \text{ \AA}$ radiation). Diffraction patterns were collected in fluorescence mode between $10^\circ < 2\theta < 70^\circ$ with a step size of $0.02^\circ 2\theta$ and dwell time of 3 s per step. Sections of the coupons were also mounted in resin before polishing to a $1 \mu\text{m}$ mirror finish and coated with a layer of carbon for observation by SEM (scanning electron microscopy). A Hitachi TM3030 electron microscope was coupled with a Bruker Quantax 70 EDX (energy dispersive X-ray) spectroscopy system for chemical analysis.

3.2. Multi-phase titanate wasteform

An alkoxide-nitrate synthesis method was used to generate the reactive titanate precursors. Reagents were sourced from the following: $\text{Ca}(\text{NO}_3)_2 \cdot 4\text{H}_2\text{O}$ (99%, Acros Organics); $\text{Ba}(\text{NO}_3)_2$ (99%, Fluorochem); $\text{Ce}(\text{NO}_3)_3 \cdot 6\text{H}_2\text{O}$ (99%, Sigma); $\text{Al}(\text{OH})_3$ (98%, Acros); and $\text{C}_{12}\text{H}_{28}\text{O}_4\text{Ti}$ (96%, Fluorochem). Nitrate components were dissolved in an excess of warm de-ionised water, with the simulant waste added as $\text{Ce}(\text{NO}_3)_3 \cdot 6\text{H}_2\text{O}$ for co-precipitation and ease of homogenisation. Separately, a mixture of isopropyl alcohol and aluminium hydroxide were agitated before complexing with an equal volume of titanium isopropoxide. The resulting complex was then shear mixed with the dissolved nitrates to ensure rapid and homogenous precipitation. The slurry was dried before calcining for 12 hours at 600°C , the resulting powder was ball milled to increase reactivity before uniaxial compression into pellets and sintering for 1 hour at a range of temperatures $1000^\circ\text{C} - 1300^\circ\text{C}$. Samples were analysed by pXRD using the same instrument as in Section 3.1 but with adjustment of the detector energy discriminator for rejection of the $\text{Fe K}\alpha$ fluorescence emission from the sample for reduced background, collecting patterns between $10^\circ < 2\theta < 55^\circ$ with a step size of $0.02^\circ 2\theta$ and dwell time of 1 s per step. SEM/EDX was also conducted on the specimens using an identical method as in Section 3.1.

4. Results and discussions

4.1. Phosphate glass wasteform

All glasses had a high viscosity during pouring and flowed from upturned crucibles, slowing at a rate proportional to that of the increasing CeO_2 content. A coupon was successfully cast for each composition, and promptly annealed; only the 20 wt.% CeO_2 Na-Fe-phosphate glass fractured in a brittle mode after annealing. Figure 1 shows the X-ray diffraction patterns for IPSAS up to 20 wt.% CeO_2 . All of the pXRD patterns demonstrated consistent diffuse scattering for $10^\circ < 2\theta < 40^\circ$ in both systems, indicating a disordered amorphous glass structure. At simulated fuel loadings above 10 wt.% CeO_2 , minor developments of crystalline monazite (CePO_4 , COD 9001646) [18] and cristobalite (SiO_2 , COD 1010944) [19] were identified. Figure 2 is an SEM/EDX map of a SIP glass sample batched with 15 wt.% CeO_2 . Light grey angular particles with diameters between 5 - 30 μm show elevated Ce detections and inclusion of P surrounding unreacted pure CeO_2 . Bulk sample surfaces analysed were largely pristine, with only sporadic inclusion of partially reacted simulant waste and crystallised monazite. The glass matrices of SIP samples had an apparent saturation point for dissolution of Ce, in

the case of 15 wt.% waste SIP glass, the bulk composition by EDX had an average saturated Ce content of 9.8 ± 0.1 wt.%. However, the glass matrix local to monazite and CeO_2 crystals revealed a significantly lower average Ce component of 4.8 ± 0.5 wt.%. The bulk glass content for SIP batched with 20 wt.% CeO_2 similarly was found to have a saturated Ce component at 8.9 ± 0.1 wt.%. The waste loadings for IPSAS were not sufficient to confirm a Ce saturation point, although for the IPSAS sample batched with 20 wt.% simulant oxide waste, an average bulk glass composition of 13.1 ± 0.4 wt.% Ce was determined. Further SEM observations on this sample found comparatively less frequent instances of undigested oxide and monazite (as compared to SIP with the same waste loading).

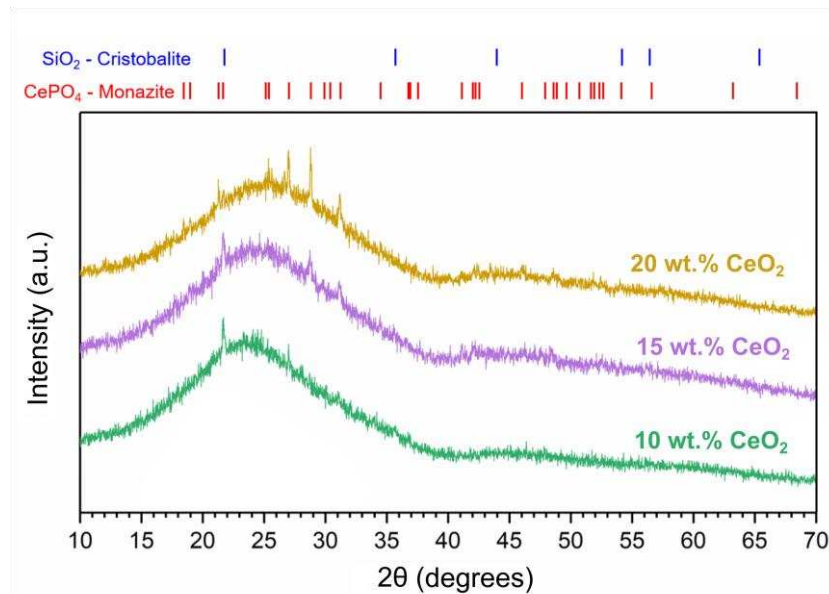


Figure 1. pXRD of IPSAS glasses 10-20 wt.% CeO_2 batches including stick patterns.

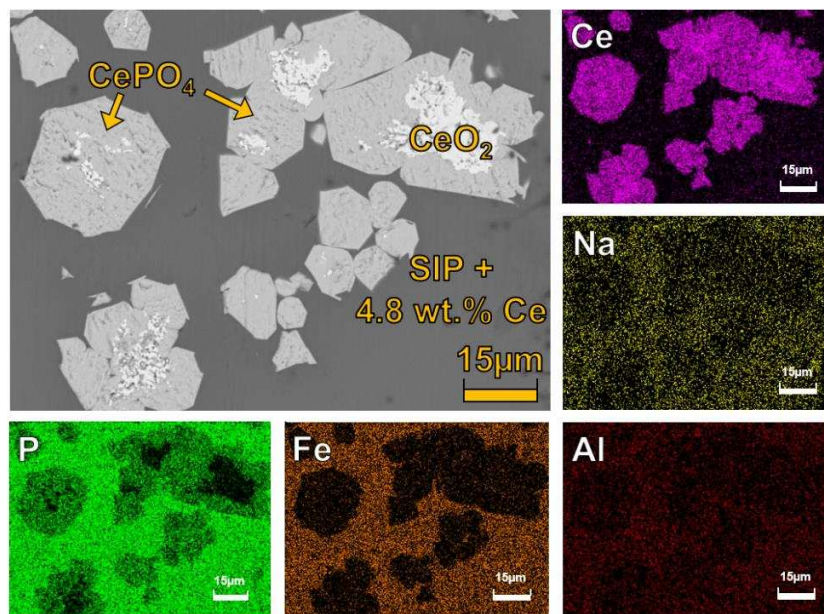


Figure 2. SEM/EDX of IPSAS glass batched with 15 wt.% CeO_2 , scale-bars are 15 μm .

4.2. Multi-phase titanate wasteform

Sintering of the titanate ceramic material afforded significant pellet stability improvements, with increasing apparent hardness and darkening of colour correlating with raising the hold temperature. Figure 3 shows the pXRD patterns for the sintered pellets including data from the 600°C calcined material. The slight diffusivity of the calcined precursor indicates a moderate degree of miscibility and the presence of crystallised CeO₂ (JCPDS 78-0694) is observed. After sintering the material becomes highly crystalline, with a majority pyrochlore phase with peak positions almost identical to the U-containing equivalent pyrochlore (Ca,Ce)₂Ti₂O₇ ([Ca,U]₂Ti₂O₇, JCPDS 45-1477). A minor balance of crystalline rutile has formed and was detected for material sintered between 1000°C - 1200°C (TiO₂, JCPDS 89-0555); over the same temperature range a concomitant decrease in the relative intensity of TiO₂ and CeO₂ reflections is also evident as the phase assemblage tends towards an apparent equilibrium. However, the diffraction pattern for sample material sintered at 1300°C exhibited what appeared to be some CeO₂ reflections, a minor reflection corresponding to rutile at 40.62° 2θ, and severely diminished reflections for the pyrochlore phase. Figure 4 is a micrograph showing SEM/EDX data for the sample sintered at 1300°C. It was evident here and when analysing the bulk sample, that the light grey contrasted region with a Ce pyrochlore composition is still present as a majority primary phase. This would suggest that the titanate structure has undergone a phase transformation, to that of a new structure-type, with evolution of a gas that has led to the further development of 10 - 20 μm pores. Semi-quantitative analysis using EDX yielded an average pyrochlore composition of (Ca_{0.57}, Ce_{0.43})₂Ti₂O₇ (± 0.02 f.u.). Accounting for the oxygen from the CeO₂ incorporated into the structure, the approximate waste loading of this phase is ~40 wt.%. Rutile was also found (dark grey region) as a minor phase with globular morphologies.

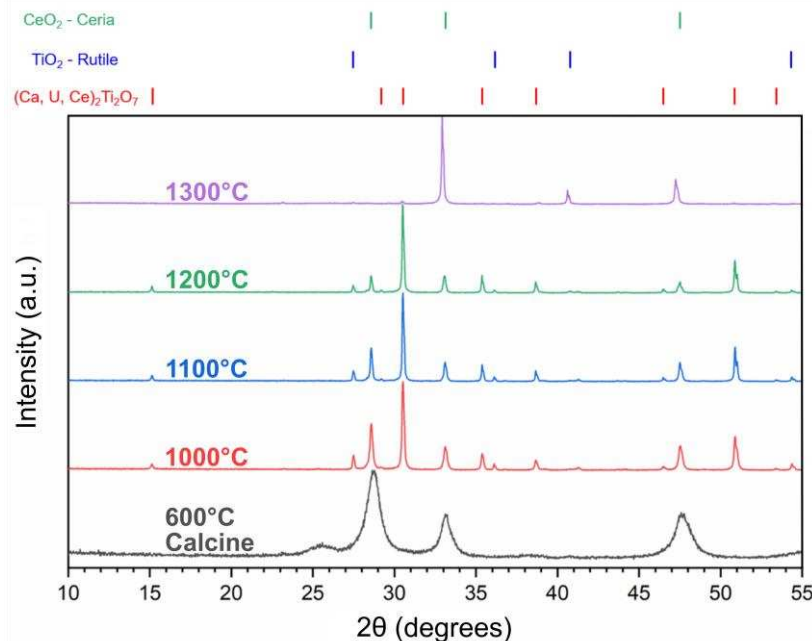


Figure 3. pXRD of co-precipitated multi-phase ceramics, as-calcined and sintered at their respective temperatures, with phase representative stick patterns.

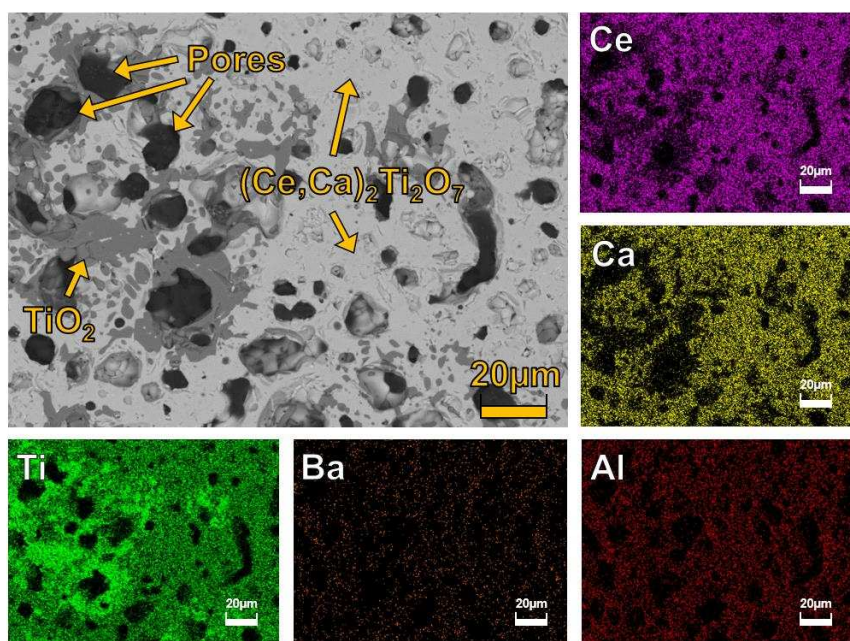


Figure 4. SEM/EDX of SYNROC-F type material cold pressed and sintered at 1300°C for 1 hour. Note Ti, Ba and Ca maps differ from Figure 2, scale-bars are 20 µm.

5. Conclusions and further work

The work conducted was able to successfully demonstrate the incorporation of CeO₂ as a waste simulant up to 13.1 ± 0.4 wt.% in a phosphate glass matrix with a quantity retained in a durable crystalline monazite phase. Further study is necessary to determine the effect of changing melt conditions, such as pressure and temperature, durability assessment by dissolution, and the coordination of Ce and Fe using XAS (X-ray absorption spectroscopy). Up to ~40 wt.% simulant CeO₂ waste was also immobilised into a pyrochlore host phase; further work will be directed at understanding structure evolution above 1200°C, generation of a hollandite secondary phase for minor actinide uptake, and durability of the wasteform.

6. References

- [1] IAEA 2009 *Management of damaged spent nuclear fuel No. NF-T-3.6 Guides*
- [2] Thompson G R 2014 *Radiological risk at nuclear fuel reprocessing plants*
- [3] Jensen S E and Nonbol E 1998 *Description of the Magnox type of gas cooled reactor*
- [4] Godfrey H 2017 *Latest understanding of corrosion of Magnox, aluminium and uranium metal wastes in cement*
- [5] POST 2000 *Parliam. Off. Sci. Technol.* 1–8
- [6] NDA 2011 *Exotic fuels-Dounreay Fast Reactor (DFR) breeder*
- [7] NIEA 2009 *Geological disposal facilities on land for solid radioactive wastes guidance on requirements for authorisation*
- [8] Sales B C and Boatner L A 1986 *J. Non. Cryst. Solids* **79** 83–116
- [9] Terai R, Eguchi K and Yamanaka H 1979 *Cer. in Nucl. Wst. Mgmt.* (USDOE) pp 62–5
- [10] Minaev A, Oziraner S and Prokhorova N 1979 *Cer. in Nucl. Wst. Mgmt.* (USDOE) pp 229–32
- [11] Jantzen C M 1986 *J. Non. Cryst. Solids* **84** 215.
- [12] Mesko M and Day D 1999 *J. Nucl. Mater.* **273** 27.
- [13] Stefanovsky S V, Stefanovsky O I, Danilov S S and Kadyko M I 2019 *Ceram. Int.* **45** 9331.
- [14] Ringwood A E, Kesson S E, Ware N G, Hibberson W and Major A 1979 *Nature* **278** 219.

- [15] Iwata S and Cenxual K 2016 $Ca_{1.25}U_{0.75}Ti_2O_7$ ($CaUTi_2O_7$) crystal structure.
- [16] Anthony W, Bideaux R, Bladh K and Nichols M 2005 *Handbook of mineralogy - Hollandite*.
- [17] Anthony W, Bideaux R, Bladh K and Nichols M 2005 *Handbook of mineralogy - Rutile*.
- [18] Yunxiang Ni, Hughes J M and Mariano A N 1995 *Am. Mineral.* **80** 21.
- [19] Wyckoff R W G 1925 *Zeitschrift für Krist. - Cryst. Mater.* **62** 1.

Acknowledgement

LH is grateful to EPSRC and the Nuclear Decommissioning Authority for award of a PhD studentship. This research utilised the HADES / MIDAS Facility, established with financial support from the UK Department for Business, Energy and Industrial Strategy and EPSRC under grant reference EP/T011424/1. This research was sponsored in part by EPSRC under grant references EP/P013600/1, and EP/S01019X/1, and conducted in part under the auspices of the IAEA co-ordinated Research Programme on Management of Severely Damaged Spent Fuel and Corium (T13015) for which support is gratefully acknowledged. Statement from the authors: This paper reflects only the author's view and the European Commission is not responsible for any use that may be made of it. No potential conflict of interest was reported by the authors.

Appendix 2. Characterisation of sodium iron phosphate glass loaded with simulant nuclear fuel

This report denotes the outcome of part of a series of beamline experiments at the KEK-Photon Factory synchrotron, Tskuba Japan. Three temperature series of IPSAS glass compositions were measured in transmission mode and iron redox was determined using a pre-edge fitting method. Data from the NSLS-II, Brookhaven NY, USA synchrotron was used in this thesis as the beamline used achieved featured an improved X-ray brilliance and fine adjustment monochromators allowed for more optimal energy resolution.

Characterisation of sodium iron phosphate glass loaded with simulant nuclear fuel

Liam Harnett*, Martin Stennett, and Neil Hyatt

Immobilisation Science Laboratory, Department of Materials and Science Engineering, The University of Sheffield, Sheffield, S1 3JD, UK

1 Introduction

The UK holds a significant quantity of degraded nuclear fuel from research and decommissioning activities. Approximately 200 teHM of this inventory is clad with or stored using stainless-steel materials, in many cases degradation would prevent de-cladding prior to processing of the actinide components [1], [2]. A relatively novel method for immobilization of such materials, details the total chemical dissolution of degraded fuel using a similar chemistry to that of the PUREX process [3], followed by a pre-calcination step and vitrification with a sodium-iron phosphate glass composition.

The relation of iron oxidation state to chemical durability in aqueous environments has been well established in literature [4]. Optimal redox behaviour describes speciation of Fe^{3+} ions to facilitate substitution of poor durability P-O-P bonding structures with the higher durability P-O-Fe counterparts.

2 Experiment

Sodium iron phosphate glass was batched with a base composition of ~61/18/9/7/5 mol.% of $\text{P}_2\text{O}_5/\text{Fe}_2\text{O}_3/\text{Na}_2\text{O}/\text{SiO}_2/\text{Al}_2\text{O}_3$, using reagent grade oxides as precursors and $(\text{NH}_4)_2\text{H}_2\text{PO}_4$ as a phosphate source. This base glass will be further represented as IPSAS (iron phosphate sodium iron silicate). 0-16 mol.% CeO_2 was added to each base composition as the fuel simulant, followed by homogenisation, 6 hrs pre-calcination at 600 °C, followed by melting at a range of temperatures between 1250 - 1450 °C, casting and annealing at 550°C for 4 hrs – all under an air atmosphere.

Pulverised samples of annealed glass were diluted with PEG with addition masses selected for the relative cross-section at the Fe-K edge. XANES spectra were collected in transmission mode at BL-27B. Standards of Fe_3O_4 , $\text{Fe}_3(\text{P}_2\text{O}_7)_2$, $\text{Fe}_3(\text{PO}_4)_2$ were also prepared and measured. The Athena software package was used to correct and align data, before use of a Lorentzian fitting function to integrate the area under the pre-edge features and determine the centroid position.

3 Results and Discussion

Figure 1 shows the result from integration of the pre-edge features for the IPSAS glass compositions with 0 mol.% CeO_2 melted at two different temperatures. A significant variation in the higher 1450 °C melt sample is the larger contribution at a slightly lower energy, shifting the centroid position, indicating a change in iron oxidation state. Figure 2 details the centroid positions for IPSAS samples melted between 0 – 15mol.% CeO_2 at

temperatures of 1250 – 1450 °C, with reference compounds used to delineate Fe^{2+} and Fe^{3+} speciation. A clear correlation shows a decrease of average oxidation state with increasing melt temperature.

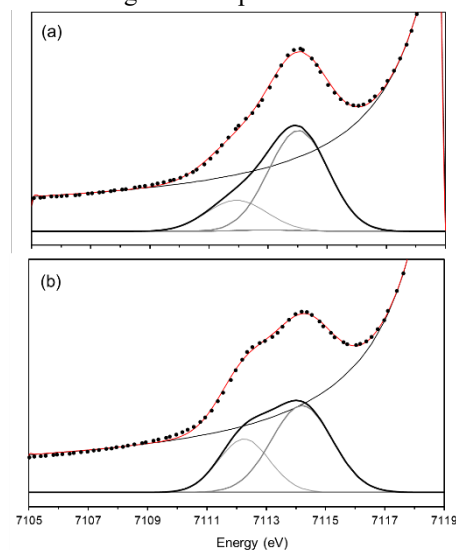


Fig. 1: Pre-edge features of the Fe-K edge data for IPSAS melted at 1350 °C (a) and 1450 °C (b).

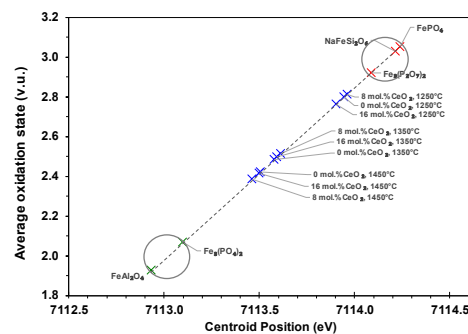


Fig. 2: Average oxidation state of IPSAS glass samples plotted with Fe (II) and Fe (III) reference standards

References

- [1] H. Godfrey, *NNL, UK* (2017).
- [2] M. Mignanelli and T. Shaw, *NNL, UK* (2009).
- [3] W. B. Lanham and T. C. Runion, *Oak Ridge, Tennessee* (1949).
- [4] P. A. Bingham, R. J. Hand, O. M. Hannant, S. D. Forder, and S. H. Kilcoyne, *J. Non. Cryst. Solids*, vol. 355, no. 28–30, pp. 1526–1538, Aug. (2009), doi: 10.1016/J.JNONCRY SOL.2009.03.008.

* lcharnett1@sheffield.ac.uk

Appendix 3. Characterisation of glass-ceramic wasteforms using quantitative image analysis of electron micrographs

This short publication discusses some of the motivations for development of the image analysis code and revises the early development and results. The work here concerns analysis of a smaller group of images than that reported in this thesis. Smaller image sets cover a less representative region of the sample surfaces, so values vary slightly when compared with analysis of larger image sets.



Characterisation of glass ceramic wasteforms using quantitative image analysis of electron micrographs

L. Harnett¹ · M. Stennett¹ · E. Maddrell² · N. Hyatt¹

Received: 3 December 2021 / Accepted: 31 January 2022 / Published online: 9 February 2022
© The Author(s) 2022

Abstract

Multi-phase material systems make up a significant proportion of the currently proposed and researched wasteforms for sequestration of heterogeneous nuclear material feeds. Quantification of the components for such multi-phase assemblages is typically performed using diffraction-based Rietveld methods, many of which necessitate long measurement times of several hours. Furthermore, careful additions of an internal standard are typically required, to facilitate inclusion of amorphous phases in the quantification. The application of an image analysis method has been investigated, using the z-contrast greyscale of back-scattered electron micrographs to determine the relative quantities of component phases in a suite of monolithic phosphate glass ceramic wasteforms. This work demonstrates an alternate methodology for accelerated quantification which could be applied to other heterogeneous wasteforms and multi-phase materials.

Introduction

Quantitative phase analysis is key to the development of glass ceramic nuclear wasteforms. In addition to presenting us with relative phase ratios, it can allow us to infer properties of the material as a sum of its constituent crystalline and glassy phases. Some of the most regularly implemented phase quantification techniques have centred around X-ray diffraction-based Rietveld and pattern refinement methods. While these can provide useful additional information on material structure and phase assemblage, there are some inherent limitations such as the necessity to use an internal standard to quantify amorphous phases. Moreover, many refinement techniques require a starting model and structural understanding of the material [1, 2]. Micrographic image analysis is not an uncommon technique to research areas such as cementitious materials, as it can be particularly well utilised to measure pore sizes efficiently and determine aggregate size distribution [3]. Quantitative phase analysis by electron micrograph thresholding across contrast regions

has been observed in the literature, though in this example, the technique was facilitated by proprietary-hard-coded microscope software with limited flexibility and user parametrisation [4]. This work aims to provide an open-source, fast and lightweight image analysis tool to complement common characterisation techniques for glass ceramics.

Materials and methods

The prototypical glass ceramic wasteform material used in this study was from a suite of sodium-iron-phosphate compositions, with additions of alumina and silica to melts and loading of cerium oxide as a fluorite surrogate for spent fuel. The composition used for initial tests consisted of component oxides and ammonium dihydrogen phosphate, loaded with 40 wt% CeO₂ and melted at 1250 °C before casting and annealing for 4 h at 550 °C, henceforth, identified as IPSAS 40 wt% CeO₂, 1250 °C. Glass ceramic monolithic samples were sectioned, cold resin mounted and polished to a 1 µm mirror finish and carbon coated to reduce surface charge. BSEs (Back scattered electron micrographs) were collected using a Hitachi TM3030 instrument, with a tungsten filament and an accelerating voltage of 15 kV. Concurrent analysis by pXRD (powder X-ray Diffraction) and EDX (Energy Dispersive X-ray) allowed for confirmation of phase assemblage [5]. Image acquisition parameters were set to medium brightness and high contrast, with fine adjustments

✉ L. Harnett
Lcharnett1@sheffield.ac.uk

¹ Immobilisation Science Laboratory, Department of Materials Science and Engineering, University of Sheffield, Sheffield S1 3JD, UK

² National Nuclear Laboratory, Workington CA20 1PG, Cumbria, UK

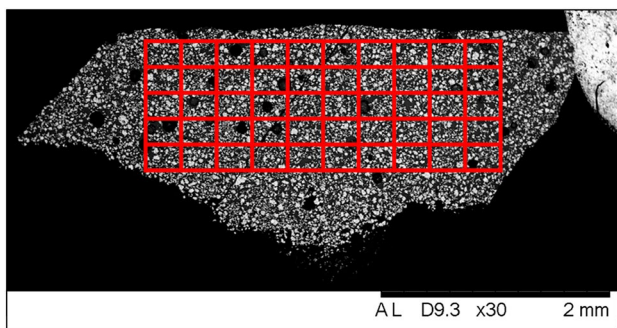


Fig. 1 Broad-overview BSE of IPSAS 40 wt% CeO₂, 1250 °C, with coordinate grid overlay

made, per sample, to maximise the contrast in grey values between the individual phases. The phase proportions can be delineated, as delimited by regions with different grey values, or BSE contrast, a factor influenced by the atomic number of the species in each phase. The free, open-source image processing software ImageJ, was used as a base platform in the Fiji package [6]. The package utilises JavaScript-based functions and macros to assist with automation of various post-processing tasks. This work concerns a script of approximately ~350 lines of code which will facilitate a quantitative-phase analysis methodology. An initial routine uses sample surface BSEs collected at a range of magnifications, measuring particle size to pixel count ratios and smallest-feature statistics. The routine is followed by selection of an optimum magnification, such that small crystallites (> 5 μm) are properly resolved. A low-magnification broad micrograph of the material surface was collected, allowing overlay of a coordinate grid, a pseudo-random number

generator was then used to select cells of the grid to collect sample micrographs at the desired magnification, Fig. 1.

During following stages of the code progression, image-scale calibration was unnecessary, as phase quantities were determined by ratio of pixel counts. The script analyses a histogram of grey values represented in the sample BSE, then calculating the points at which minima of intensity can be found. The peak intensities between such points were then used to represent the discrete phases, the areas for which were determined by thresholding between pairs of minima and counting the number of pixels remaining, Fig. 2a. Ratios of these areas were then used to infer relative phase quantities. Following the processing of a first BSE, the remaining image set from a sample can be quickly processed to strengthen the measurement statistics. The user is given option to manually exclude mis-identified phases such as mounting material or pores Fig. 2b and can also generate a representative figure to accompany phase quantity statistics for publication. At the time of writing, the script can delineate 2–6 individual phases.

Results

Following the measurement of an initial sample BSE, the remaining image set is loaded by the script as a stack, so results are supplied as an indirect volume percentage, as the direct measurements made to individual BSEs result in area percentage values. The test sample, IPSAS 40 wt% CeO₂, 1250 °C, was measured to collect statistics over a range of 10 BSEs, with the script identifying with 99.9% confidence: 61.9 ± 2.3 vol% glass, 34.9 ± 2.0 vol% CePO₄ and 3.2 ± 0.5 vol% CeO₂ (darkest to lightest contrast, respectively), Fig. 3a. Another test sample, with a base

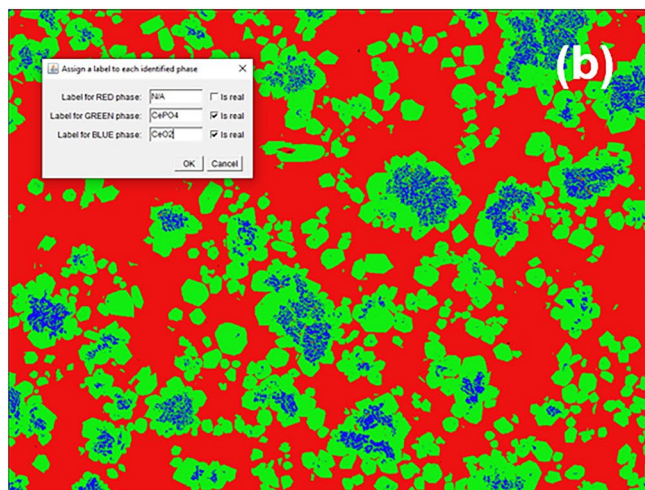
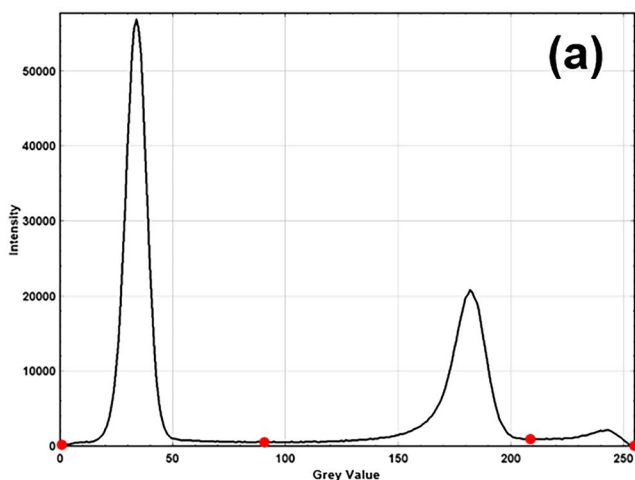


Fig. 2 Grey value histogram for IPSAS 40 wt% CeO₂, 1250 °C (a), phase labelling and exclusion (b)

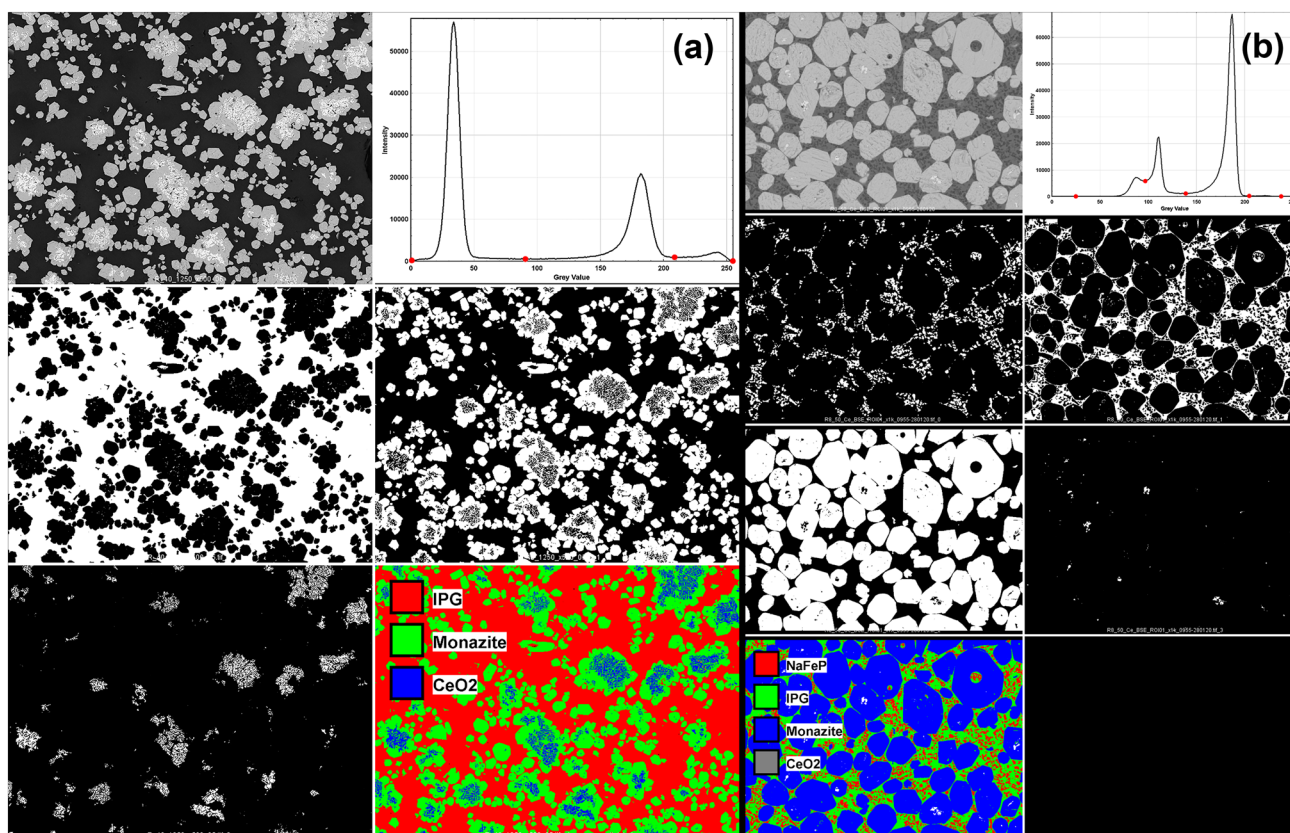


Fig. 3 Representative measurement summaries for 3-phase IPSAS 40 wt% CeO₂, 1250 °C (a) and 4-phase IPSAS 50 wt% CeO₂, 1450 °C (b)

sodium-iron-phosphate glass composition with 50 wt% CeO₂ melted at 1450 °C, was also measured using the same method over 10 BSEs, with 99.9% confidence: 22.0 ± 1.7 vol% glass, 8.7 ± 0.4 vol% crystalline sodium-iron-phosphate, 68.5 ± 2.9 vol% CePO₄, 0.8 ± 0.2 vol% CeO₂ (darkest to lightest contrast, respectively), Fig. 3b. Each image was collected in about 30 s, with another 15 for adjustment and stage movement. Image sets of stack size 10 were measured by the script in approximately 30 s (as verified by a counting function), on a moderately equipped workstation built in 2018.

Discussion

The results presented here, demonstrate how the script can be used to analyse micrographs of samples with varying phase assemblages and with different phase morphologies. Some preliminary tests with a SYNROC-F type multi-phase ceramic [7] and a barium phosphate multi-phase system [8] have indicated that adjustable sensitivity will be a necessary feature to modify the minima-detecting algorithm, as some ceramic phases have surfaces with very well-defined contrast, such that the histogram of grey values presents with

sharp peaks and phases with very similar contrast, such that overlap can occur. Implementation of sensitivity adjustment is underway to facilitate measurement of such phase assemblages. The technique does, however, have an inherent limitation with difficulty processing images containing phases with similar BSE grey contrast, as such, it would be unable to distinguish between two phases with exactly the same mean atomic number. A high degree of precision was achieved with the sodium-iron-phosphate glass ceramic materials, with error comparable to Rietveld-type analyses [2]; further improvements have been shown with larger samples of 20–25 BSEs. The key concluding advantage over more traditional methods often requiring several hours per sample is the data collection and processing time of image-based QPA, represented as 8 min for a 10 BSE set, up to 20 min for a 25 image set. The open nature of this platform will allow for ease of additional control, modification and integration with microscopes featuring motorised or computer-controlled stages. Other heterogeneous multi-phase materials may be measured using this method, such as those studied by researchers in the fields of cultural heritage and archaeology. Such a technique may be applied to images acquired through other micro-analysis techniques such as optical and Raman spectroscopy; however, due care will be

required to ensure defined contrast of both amorphous and crystalline phases, with minimum resolvable feature size constrained to the diffraction limit with light-based analyses. Further planned work includes measurement of samples of a zirconolite glass ceramic composition, use of a rapid X-ray diffraction-based quantification method to verify the performance and accuracy of the image method [9], improvements to portability of the analysis package—including greater compatibility through Linux and macOS platforms with their respective filesystems.

Acknowledgments This research utilised the HADES/MIDAS facility at the University of Sheffield established with financial support from EPSRC and BEIS, under Grant EP/T011424/1. The author would like to send their immeasurable gratitude to The EPSRC and Nuclear Decommissioning Authority for the award of a PhD studentship and appreciations to Professor Neil Hyatt and Dr Martin Stennett for their excellent support and supervision, particularly during the global pandemic.

Data availability The datasets generated during the current study are not publicly available due to active continued work and refinement of the methodology at the time of writing, subject to further publication but are available from the corresponding author on reasonable request.

Declarations

Conflict of interest No potential conflict of interest was reported by the authors.

Open Access This article is licensed under a Creative Commons Attribution 4.0 International License, which permits use, sharing, adaptation, distribution and reproduction in any medium or format, as long as you give appropriate credit to the original author(s) and the source, provide a link to the Creative Commons licence, and indicate if changes were made. The images or other third party material in this article are included in the article's Creative Commons licence, unless indicated otherwise in a credit line to the material. If material is not included in the article's Creative Commons licence and your intended use is not permitted by statutory regulation or exceeds the permitted use, you will need to obtain permission directly from the copyright holder. To view a copy of this licence, visit <http://creativecommons.org/licenses/by/4.0/>.

References

1. X. Orlhac et al., *J. Appl. Crystallogr.* **34**, 114–118 (2001)
2. S. Kemethmüller et al., *J. Am. Ceram. Soc.* **89**, 2632–2637 (2006)
3. M.A. Saghiri et al., *Eur. Endod. J.* **5**, 128–133 (2020)
4. J. Crum et al., *J. Nucl. Mater.* **444**, 481–492 (2014)
5. N.C. Hyatt et al., *IOP Conf. Ser. Mater. Sci. Eng.* **818**, 012022 (2020)
6. J. Schindelin et al., *Nat. Methods* **9**, 676–682 (2012)
7. L. Harnett et al., *IOP Conf. Ser. Mater. Sci. Eng.* **818**, 012012 (2020)
8. K. Popa et al., *J. Solid State Chem.* **180**, 2346–2355 (2007)
9. H.P. Klug and L.E. Alexander, *X-Ray Diffraction Procedures: For Polycrystalline and Amorphous Materials*, 2nd ed. (Wiley, New York, 1974) pp. 531–565

Appendix 4. Quantitative image analysis source code

Current version of the image analysis code (please do not re-distribute). The code operates using an ImageJ macro language similar to JavaScript. Sample images stored in a specific folder, much of the set-up can be configured with user prompts or is managed automatically. Detailed instructions for specific use-cases can be provided.

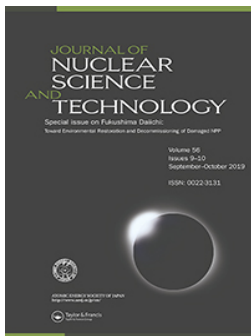
[https://drive.google.com/drive/folders/1fpwyegxcBLRd1uoXjkh1z-O85bNETG7D?usp=share link](https://drive.google.com/drive/folders/1fpwyegxcBLRd1uoXjkh1z-O85bNETG7D?usp=share_link)

OR

See accompanying files (**PAGIS**).

Appendix 5. Reactive spark plasma sintering of Cs-exchanged chabazite: characterisation and durability assessment for Fukushima Daiichi NPP clean-up

This article summarises the findings of the aluminosilicate wasteform produced by thermally treating simulant ion exchange material with SPS. The parametric study of processing parameters is discussed, with exchanged and sintered material characterised. The study culminated in a short term accelerated dissolution experiment.



Reactive spark plasma sintering of Cs-exchanged chabazite: characterisation and durability assessment for Fukushima Daiichi NPP clean-up

Liam. C. Harnett, Laura. J. Gardner, Shi-Kuan Sun, Colleen Mann & Neil. C. Hyatt

To cite this article: Liam. C. Harnett, Laura. J. Gardner, Shi-Kuan Sun, Colleen Mann & Neil. C. Hyatt (2019) Reactive spark plasma sintering of Cs-exchanged chabazite: characterisation and durability assessment for Fukushima Daiichi NPP clean-up, Journal of Nuclear Science and Technology, 56:9-10, 891-901, DOI: [10.1080/00223131.2019.1602484](https://doi.org/10.1080/00223131.2019.1602484)

To link to this article: <https://doi.org/10.1080/00223131.2019.1602484>



© 2019 The Author(s). Published by Informa UK Limited, trading as Taylor & Francis Group.



Published online: 14 Apr 2019.



[Submit your article to this journal](#)



Article views: 1843



[View related articles](#)






[View Crossmark data](#)



Citing articles: 13 [View citing articles](#)

Reactive spark plasma sintering of Cs-exchanged chabazite: characterisation and durability assessment for Fukushima Daiichi NPP clean-up

Liam. C. Harnett , Laura. J. Gardner , Shi-Kuan Sun , Colleen Mann  and Neil. C. Hyatt 

Immobilisation Science Laboratory, Department of Materials Science and Engineering, University of Sheffield, Sheffield, UK

ABSTRACT

Ion-specific media (ISM) have played an integral role in the clean-up and remediation efforts at the Fukushima Dai-ichi disaster site, through the processing of contaminated wastewaters. The use of these materials generates a secondary nuclear waste stream, presenting its own series of engineering problems arising from stringent handling and long-term storage requirements. A reactive spark plasma sintering (SPS) method was investigated for conditioning of the spent cesium exchanged zeolite, chabazite. A natural form of the zeolite was used as an analogue to the engineered ISM used at the Fukushima NPP site. Simulant wasteforms were sintered using different temperature and pressure parameters followed by analysis of phase assemblage, density, and durability (using the product consistency test (PCT)). The results indicated that zeolite structure had collapsed completely, with the exchanged cesium partitioned primarily into a durable feldspar to assure stability of the sintered material for passively safe storage or geological disposal.

ARTICLE HISTORY

Received 21 November 2018
Accepted 23 March 2019

KEYWORDS

Chabazite; zeolite; cesium; reactive spark plasma sintering; Fukushima Daiichi NPP; ion exchange; radioactive waste management

1. Introduction

The March 2011 earthquake and tsunami led to a series of serious coolant loss incidents at the Fukushima Daiichi nuclear power plant (NPP) [1]. Three reactor units experienced partial core meltdowns, but reactor water levels were eventually stabilised by the pumping of sea water and fresh water, achieving cold shutdown conditions. Cesium-137 is a high yield fission product ($t_{1/2} = 31.17$ yr) and, consequently, it is present at high concentrations in the NPP wastewater. Due to the radiotoxicity of Cs-137 and other radionuclides present in these effluents, treatment is necessary before the used cooling water can be reused or released.

One method of effluent treatment is the use of ion exchange materials, such as zeolites. These microporous aluminosilicates are available commercially as mineral or synthetic materials, finding common usage in ion exchange as adsorbents. The individually unique structures of these media result in both high selectivity and specificity for ion exchange. To facilitate Cs removal from the contaminated coolant water, one of the main effluent treatment facilities installed on the Fukushima Daiichi NPP site is the KURION ion exchange plant, using engineered Na-chabazite as an exchange medium [2]. The high porosity of this material, based on a ~ 3.8 Å diameter “8-ring” framework structure, provides a large surface area for exchange with high selectivity for Cs [3,4]. As of October 2018, this facility has treated a cumulative Cs-contaminated water volume of

391,870 m³, producing 771 large exchange columns of spent material [5]. Conditioning of the large volumes of spent zeolite waste is one of the more demanding unsolved engineering issues as part of the clean-up effort, with strict acceptance criteria and constraints [6] that must be followed: limited space at potential disposal sites necessitates a high reduction in volume of wasteforms, minimal leaching, and corrosion of containment and long-term chemical stability. Vitrification using borosilicate glasses has been considered but volatilisation of cesium at high processing temperatures (up to 1300°C) poses a potential challenge [7]. Encapsulation of ion exchange materials using standard cementitious compositions has been studied [8–10,11], though systems such as ordinary Portland cement (OPC) may necessitate particle size reduction of zeolites, and degradation of the ion exchange framework, as a result of the internal pH, releases the incorporated radiocesium. Cement encapsulation is also expected to result in a relative volume increase for the final wasteform.

Spark plasma sintering (SPS) is a relatively novel sintering technique that operates on the principle of a Joule heating effect via a very high applied current coupled with uniaxial pressure, which facilitates mass-transport and grain growth. Rapid heating rates and the application of pressure allow near-theoretical densities to be achieved in the final pellet product using relatively low temperatures [12], with the potential for high wasteform volume reduction. This work demonstrates the viability of spark plasma sintering as a method for the thermal

treatment of spent chabazite ion exchange materials and evaluates the wastefrom chemical durability using the ASTM Product Consistency Test (PCT-B).

2. Experimental methods

2.1 Material synthesis

The chabazite used in this study was a natural source, supplied from Verdi S.p.A as “Zeover.” The reported manufacturer data were as follows: the particle size range of 0.1–0.7 mm, a cation exchange capacity (CEC) of 2.2 ± 0.2 meq/g, and a reported composition of $(\text{Na}_{0.14}\text{K}_{1.03}\text{Ca}_{1.00}\text{Mg}_{0.17})[\text{Al}_{3.46}\text{Si}_{8.53}\text{O}_{24}]\cdot 9.7\text{H}_2\text{O}$ [13]. This constituted a mineral composition of 70 ± 2 wt.% chabazite with minor constituents at: 18 ± 5 wt.% obsidian glass, 5 ± 2 wt.% potassium feldspars, 3 ± 1 wt.% pyroxenes, 2 ± 1 wt.% biotite, and 2 ± 1 wt.% phillipsite [10]. Chabazite was exchanged in a 0.1 M CsNO_3 (Arcos Organics, 99% purity) solution using UHQ water (18.2 M Ω). The chabazite was agitated on a roller mill for 24 h at room temperature. The exchanged material was rinsed twice with 1 L of distilled H_2O , filtered, and dried at 95°C for 24 h.

The Cs-chabazite was calcined in air at 300°C for 12 h to remove remnant water. 3 g of the dried Cs-chabazite was pressed into a 20 mm graphite die and consolidated using a HP-D 25 SPS system (FCT Systeme GmbH). The average measured apparent density of green-body pressed pellets was 1.556 ± 0.041 g/cm³. Samples were consolidated according to the method used by Sun *et al.* [14], at 1000°C or 1100°C at 50°C/min under an argon atmosphere with a dwell time of 10 min, under a uniaxial pressure of 15 MPa or 50 MPa. Sintered samples were allowed to cool naturally to ambient temperature. Residual graphite foil was removed by manual grinding using SiC paper. The total processing time per sample, including die loading, was 60 min.

2.2 Characterisation

The phase assemblage of the as-received, exchanged, and SPS samples was determined by powder X-ray diffraction (XRD) on a Bruker D2 PHASER diffractometer with a LynxEye detector utilising $\text{Cu K}\alpha$ ($\lambda = 1.5418$ Å) radiation, a Ni foil was used to filter the $\text{K}\beta$ radiation. Diffraction patterns were collected between $5^\circ < 2\theta < 50^\circ$ with a step size of $0.02^\circ 2\theta$ and dwell time of 1 s per step. X-ray fluorescence (XRF) analysis was used to quantify the bulk oxide constituents of the as-received, Cs-exchanged, and SPS samples. XRF beads were prepared using a lithium tetraborate flux (Sigma Aldrich, 99.995% purity) at a 1:10 sample-to-flux ratio and analysed using a PANalytical Zetium spectrometer under vacuum with a Rh tube operating at 50 kV and 30 mA (Table 1). Microstructures were observed using a Hitachi TM3030 scanning electron microscope (SEM) coupled with

Table 1. Results for compositional analysis by X-ray fluorescence, including calculated values for approximate water loss on ignition and standard deviations for all averaged data.

Compound	As-Received Average (wt.%)	Cs-Exchanged Average (wt.%)	SPS-2 Average (wt.%)
SiO_2	52.10 ± 0.23	50.82 ± 0.02	55.55 ± 0.21
Al_2O_3	18.90 ± 0.03	18.40 ± 0.08	20.45 ± 0.07
K_2O	6.87 ± 0.05	6.60 ± 0.05	7.44 ± 0.03
CaO	6.13 ± 0.01	5.30 ± 0.09	5.46 ± 0.02
Fe_2O_3	5.48 ± 0.02	4.73 ± 0.02	4.28 ± 0.04
MgO	1.98 ± 0.01	1.86 ± 0.02	1.77 ± 0.03
Cs_2O	*	1.96 ± 0.02	2.09 ± 0.20
Na_2O	1.14 ± 0.02	0.73 ± 0.02	0.85 ± 0.03
TiO_2	0.69 ± 0.01	0.62 ± 0.01	0.60 ± 0.01
I	0.44 ± 0.01	0.45 ± 0.01	0.33 ± 0.10
SrO	0.23 ± 0.01	0.20 ± 0.01	0.25 ± 0.05
H_2O **	5.30 ± 0.22	7.76 ± 0.24	*
Total	$99.25^{\dagger\dagger}$	$99.45^{\dagger\dagger}$	$99.07^{\dagger\dagger}$

*Below the detection limit

** Determined by mass loss of structural water upon ignition

†† Less than 100% of the composition is reported as the trace components were discounted.

a Bruker Quantax 70 energy dispersive X-ray spectroscopy system (EDX) at a working distance of 7.4 ± 0.1 mm using a silicon drift detector. Samples were resin mounted, polished to a 1 μm finish, and carbon coated. The approximate stoichiometry was determined on the average composition of 10 EDX data points per microstructural feature. Semi-quantitative phase analysis assumed oxygen stoichiometry required for charge neutrality. Density measurements were conducted using a Micrometrics AccuPyc II 1340 gas pycnometer with a 1 cm³ sample cell (chabazite samples) and a 0.1 cm³ cell for the SPS powder for proof of concept studies. The density of the SPS fragments was determined using a Mettler Toledo Archimedes balance (Table 2).

The chemical durability assessment (sample SPS-2 only) was performed in duplicate using the Product Consistency Test (PCT-B, ASTM methodology C1285-14 [15]). Powdered samples (75–150 μm) were prepared and washed using IPA. Tests were carried out at 90°C in a 15 mL PTFE vessel with 9 mL of leachate (UHQ water, 18.2 M Ω) to give a surface area-to-volume ratio of 1200 m⁻¹, based on geometrical assumptions. Sacrificial samples were taken at time points: 1, 3, 7, 14, 21, and 28 days, aliquots were passed through a 0.2 μm filter, pH measured using a Mettler Toledo pH meter, and acidified with nitric acid (Ultrapure NORMATOM 67–69%, VWR). The leachates were analysed using inductively coupled plasma-optical emission spectroscopy (ICP-OES) (Thermo Fisher iCAPDuo 6300) and ion chromatography (IC) (Thermo Scientific ICS-1100) using the cation column for cesium analysis.

3. Results and discussion

3.1 Exchanged material characterisation

The phase assemblages of the as-received and Cs-exchanged materials were determined by powder XRD (Figure 1). The observed major phases present were

Table 2. The density and phase assemblage reference matrix for all samples in this study.

Sample	Processing Conditions	XRD Phases*		Main Cs bearing Phase (EDX Formula)	Main Phase Cs (wt.%)	Average Density Archimedes (g/cm ³)	Average Density Gas Pycnometry (g/cm ³)
		Major	Minor				
As-received	–	C	B, K, N, P, Q, X	Ca _{1.5} K _{1.0} [Al ₃ Si ₈ O ₂₄].12H ₂ O**	–	††	2.4411 ± 0.0015
Cs-exchanged	Cs-exchange	C	B, K, N, P, Q, X	Cs _{0.5} Ca _{0.9} K _{1.2} [Al ₄ Si ₈ O ₂₄].12H ₂ O**	7.2 ± 3.1	††	2.4679 ± 0.0017
SPS-1	SPS, 1000°C, 10 min, 15MPa	K	B, L, N, Q, X	Cs _{0.7} Ca _{0.5} K _{1.1} [Al ₃ Si ₈ O ₂₂]	11.0 ± 2.8	2.658 ± 0.004	2.6657 ± 0.0038
SPS-2	SPS, 1000°C, 10 min, 50MPa	K	B, L, N, Q, X	Cs _{0.9} Ca _{0.5} K _{1.1} [Al ₃ Si ₈ O ₂₂]	13.7 ± 4.2	2.658 ± 0.003	2.7314 ± 0.0017
SPS-3	SPS, 1100°C, 10 min, 15MPa	K	L, Q, X	Cs _{0.5} Ca _{0.3} K _{1.6} [Al ₃ Si ₈ O ₂₄]	8.4 ± 3.3	2.588 ± 0.003	2.6050 ± 0.0059

* Where: **B** = biotite KMg₃[AlSi₃O₁₀], **C** = chabazite Ca₂[Al₄Si₈O₂₄].12H₂O, **K** = K-feldspars K[AlSi₃O₈], **L** = leucite K[FeSi₂O₆], **N** = anorthite Ca[Al₂Si₂O₈], **P** = phillipsite Na₂[Al₂Si₆O₆].H₂O, **Q** = quartz [SiO₂], and **X** = pyroxene Fe_{0.07}Na_{0.16}Ca_{0.84}Mg_{0.94}[Si₂O₆]

** Assuming complete hydration to 12H₂O

†† Not measured as there was only granular sample

chabazite, Ca₂[Al₄Si₈O₂₄].12H₂O (JCPDS-ICDD, Powder Diffraction File, PDF #34–0137), the K-feldspars K[AlSi₃O₈]; sanidine (PDF #71–0992) with microcline (PDF #83–1604), and pyroxene, Fe_{0.07}Na_{0.16}Ca_{0.84}Mg_{0.94}[Si₂O₆] (PDF #86–0005). Several less intense reflections were found to correspond to biotite, KMg₃[AlSi₃O₁₀] (PDF #73–1661), phillipsite, Na₂[Al₂Si₆O₆].12H₂O (PDF #12–0195), quartz, [SiO₂] (PDF #81–1665), and anorthite, Ca[Al₂Si₂O₈] (PDF #89–1461). There were only very slight differences between the two diffraction patterns, post Cs-exchange, such as the relative intensities of the low angle reflections for phillipsite, biotite, and chabazite (2θ < 20°), due to Cs ion exchange and preferred orientation effects associated with the biotite mica (where preferred orientation refers to the crystallographic phenomenon of some crystallites having a tendency to pack in favour of a particular direction, influencing the diffraction pattern).

Elemental compositions of the as-received and Cs-exchanged materials were determined using XRF spectroscopy. Table 1 shows the compositions of the pre- and post-exchange samples, by relative average weight percent of oxide components. The water losses, as calculated by the sample mass lost on ignition, had the largest degree of variability, likely resulting from residual water from the exchange process. The large size of the Cs⁺ cation means that there is a preferential exchange to the sites of wide ~7Å aperture “8-ring” structure within the chabazite framework [3,4]. XRD and XRF analysis confirm that the bulk mineral and chemical composition is consistent with reference to the manufacturer data sheet.

A BSE micrograph and EDX maps of the Cs-exchanged sample provided a survey of individual particle morphologies and compositions. In Figure 2, a particle with high porosity and grain sizes ranging between 200 and 300 μm was characteristic of a chabazite, and semi-quantitative analysis of a region yielded a composition of Cs_{0.5}Ca_{0.9}K_{1.2}[Al₄Si₈O₂₄].12H₂O, demonstrating the exchange and cation

variation on the primary Ca-chabazite (C) phase detected by XRD. This corresponds to a Cs loading of 7.2 ± 3.1 wt.% for individual chabazite particles, this is comparable to the Cs-exchange achieved by Du *et al.* for pure chabazite – 6.4 wt.% [16]. A series of angular, low porosity particles were also found, corresponding to K-feldspar (K) K_{0.8}[AlSi₃O₈], pyroxene (X) Fe_{0.2}Al_{0.2}Mg_{0.8}Ca_{1.1}[Si₂O₆], and a silica/quartz (Q) SiO₂. In addition, spherical particles associated with the 18 wt. % ± 5% obsidian glass present within the chabazite source material [13] were observed in the analysis of microstructure, although not apparent in Figure 2 (see Supporting Info 3).

The density of the as-received chabazite (2.4411 ± 0.0015 g/cm³) was observed to increase after Cs-exchange to 2.4679 ± 0.0017 g/cm³ (Table 2). This increase is associated with the incorporation of Cs within the chabazite structure, displacing the cation occupancy at the sodium or potassium sites, and increasing the cation atomic mass by ~3–5 fold.

3.2 Characterisation of reactive spark plasma sintered material

Phase assemblages for each of the SPS pellets (SPS-1–3) were determined by powder XRD. The reflections associated with chabazite were entirely absent from the diffraction patterns (Figure 3). This demonstrated that a complete collapse of the zeolite structure was achieved using SPS as a thermal treatment method for ion exchange materials, forming known mineral crystalline phases. The major phases present in all SPS samples were K-feldspars, K[AlSi₃O₈] in the form of sanidine (PDF #83–1657), orthoclase (PDF #83–1253), and microcline (PDF #83–1604), with minor reflections corresponding to anorthite, Ca[Al₂Si₂O₈] (PDF #12–0301) and pyroxene, Fe_{0.07}Na_{0.16}Ca_{0.84}Mg_{0.94}[Si₂O₆] (PDF #86–0005).

Although the SPS-1 (1000°C, 10 min, 15 MPa) and SPS-2 (1000°C, 10 min, 50 MPa) samples had consistent phase assemblages based on the minerals

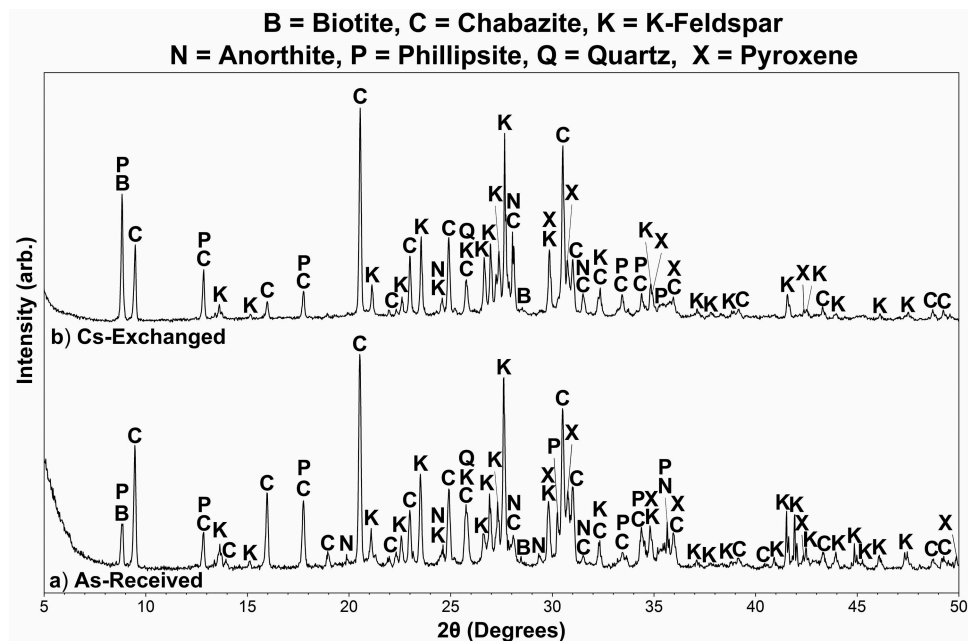


Figure 1. XRD patterns for the (a) as-received and (b) Cs-exchanged samples.

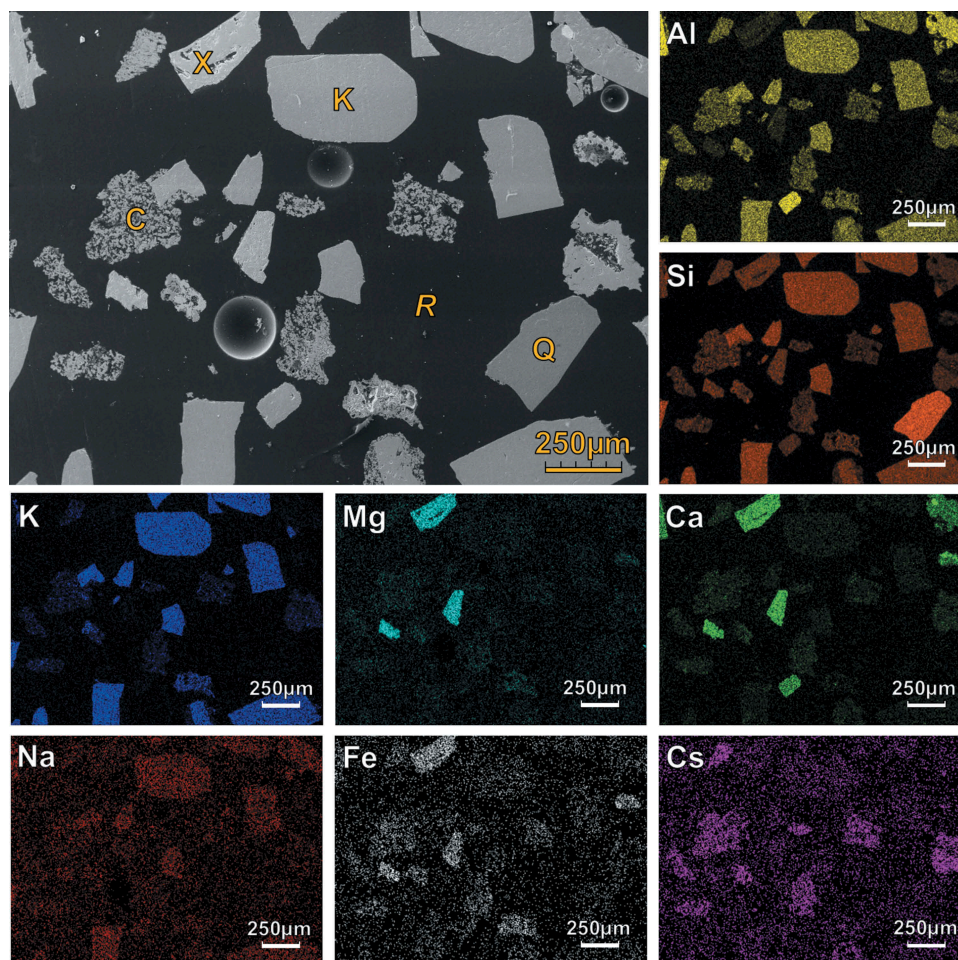


Figure 2. SEM/EDX micrographs of the Cs-exchanged chabazite, where labelled phases correspond to (C) chabazite, (K) potassium feldspar, (Q) quartz, (R) resin, and (X) pyroxene.

present, there were, however, subtle differences in the relative intensities observed. For example, the reflection at $2\theta \approx 27.7^\circ$, corresponding to sanidine feldspar (K), was observed with a significantly higher relative

intensity in the SPS-1 sample, compared to that of the SPS-2. Conversely, the peak at $2\theta \approx 29.3^\circ$ assigned to anorthite and pyroxene phases (N/X) had a significantly lower relative intensity in SPS-1.

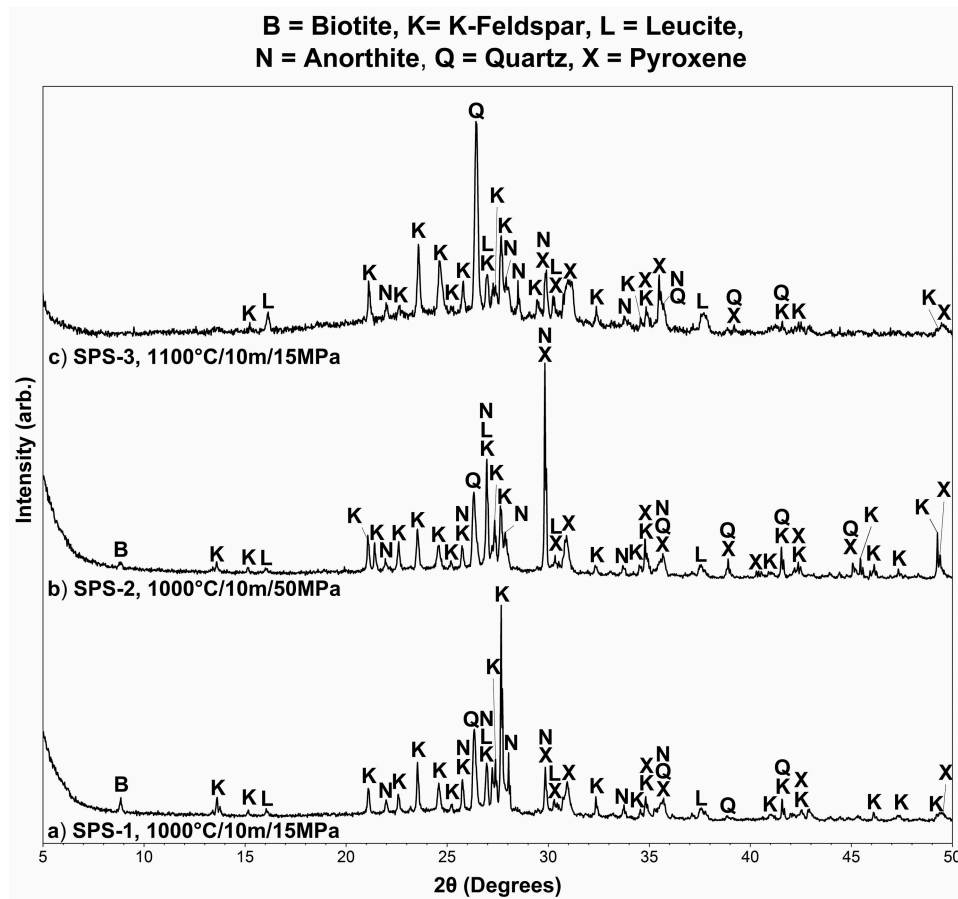


Figure 3. XRD patterns for powdered SPS samples: (a) 1000°C, 10 min, 15 MPa, (b) 1000°C, 10 min, 50 MPa, and (c) 1100°C, 10 min, 15 MPa.

Compared to SPS-1, the effect of an increased processing temperature (SPS-3, 1100°C, 10 min, 15 MPa) resulted in quartz (Q) having the highest relative intensity rather than the K-feldspar. Also observed was the emergence of diffuse scattering between $17.5^\circ < 2\theta < 37.5^\circ$. These features are consistent with vitrification mechanisms and amorphous glass phases formed after the complete breakdown of aluminosilicate frameworks [17,18]. Therefore, it is possible to state that for the SPS-processing conditions investigated, the effect of pressure had little impact on the phase assemblage (only the proportion), which was juxtaposed to the effect of temperature. The absence of pollucite ($\text{CsAlSi}_2\text{O}_6$) was due to the molar ratio of alkali:aluminium:silicon in the SPS composite (approximately 1:2:4.7 – as derived from Table 1), which is closer to the ideal ratio of the feldspar observed in the microstructure (1:1:3) than to that of pollucite (or leucite, the K-counterpart (1: 1: 2)) [19]. The Cs was resultantly taken into the feldspar solid solution during melt crystallisation. The normalised Cs_2O content of the ion exchanged material immediately before and after SPS treatment (i.e. accounting for the loss of water in the calcination pre-treatment step) was determined by XRF analysis to be 2.14 ± 0.02 and 2.11 ± 0.18 wt.%, respectively. No measurable change in the Cs_2O content was determined, within the precision of the analysis, and thus the full inventory of Cs_2O was

retained. This is likely due to the very short processing time combined with uniaxial pressure. Further work is required to demonstrate which SPS-processing temperature for waste management of Cs-ion exchange materials is optimal, based on microstructure, chemical stability, and radiation tolerance.

Microstructure and semi-quantitative analysis was undertaken for the SPS pellets, shown in Figures 4–5. The SPS-1 microstructure was observed to contain several distinct phases, all with very low apparent visible porosity. A dark, angular particle with a width of $90 \mu\text{m}$ had a high calcium intensity with the absence of potassium, EDX quantification provided a composition of $\text{Ca}_{0.8}[\text{Al}_{1.7}\text{Si}_2\text{O}_8]$, corresponding to anorthite (N). In Figure 4, A magnesium-calcium rich region yielded a more complex EDX composition of $\text{Fe}_{0.2}\text{Al}_{0.2}\text{Mg}_{0.8}\text{Ca}_{0.9}[\text{Si}_2\text{O}_6]$, indicating a diopsidian pyroxene with incorporation of small amounts of iron and aluminium, associated with the XRD phase match for pyroxene (X).

The bulk matrix phase encapsulating the crystal grains within the sample was reviewed, with EDX maps over two regions showing evenly distributed intensities for potassium and calcium as well as a high detection of aluminosilicate constituents. A bright globular $5\text{--}10 \mu\text{m}$ precipitate phase was abundant in the matrix and appeared to have a high Cs content. This matrix-precipitate complex appeared to have an

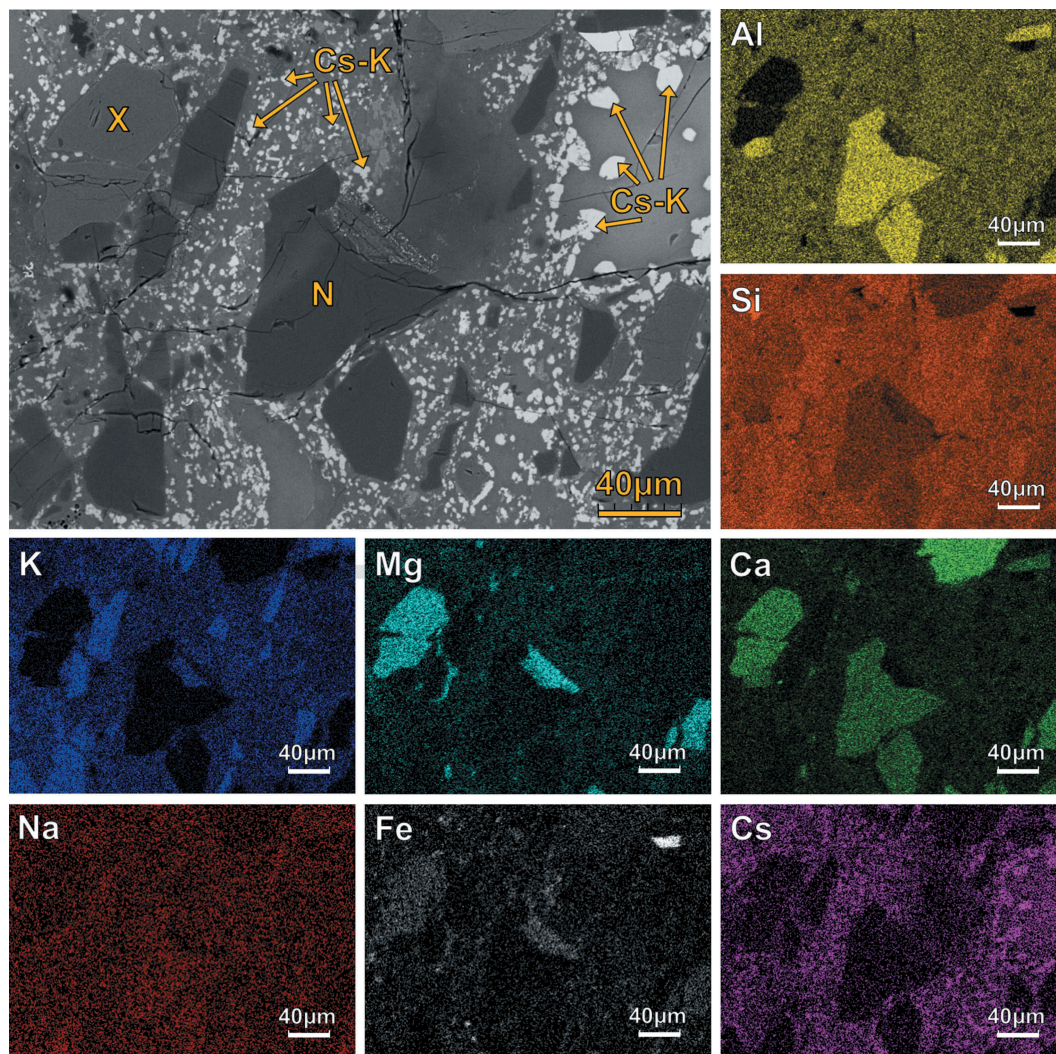


Figure 4. SEM/EDX micrographs of SPS-1 (1000°C, 10 min, 15 MPa), where labelled phases correspond to (N) anorthite, (X) pyroxene, and (Cs-K) cesium–potassium feldspars dispersed in anorthitic matrices.

intermediate potassium and plagioclase feldspar composition of $\text{Cs}_{0.7}\text{Ca}_{0.5}\text{K}_{1.1}[\text{Al}_3\text{Si}_8\text{O}_{22}]$, equating to a Cs waste-loading of 11.0 ± 2.8 wt.%. A breakdown of the cesium containing zeolite structure appears to have formed a combined matrix of the lower free energy alkali feldspars (K type and Cs type) [20] and anorthite, for which only limited powder diffraction reference data were available. Analysis of SPS-2 (Supporting Info 4) displays very similar features to the 15 MPa microstructure: namely a mixed feldspar-plagioclase composition of $\text{Cs}_{0.9}\text{Ca}_{0.5}\text{K}_{1.1}[\text{Al}_3\text{Si}_8\text{O}_{22}]$, corresponding to a Cs waste-loading capacity of 13.7 ± 4.2 wt.%. This indicated that pressure had little effect on the microstructure and local chemistry of the sintered wasteform.

In Figure 5, the higher temperature SPS-3 sample (1100°C) resulted in a noticeably sparser distribution of distinctive phase regions. The Cs-rich matrix (white precipitate) demonstrated the lowest cesium loading of the three SPS wasteforms, with a calculated composition of $\text{Cs}_{0.5}\text{Ca}_{0.3}\text{K}_{1.6}[\text{Al}_3\text{Si}_8\text{O}_{24}]$, which corresponds to a Cs waste-loading capability of 8.4 ± 3.3 wt.%. This

could be indicative of a greater abundance of this phase or Cs incorporation into other phases (e.g. the vitreous phase). The remaining features of SPS-3 corresponding to a ~ 100 μm diameter dark, angular anorthite (N) particle with a formula $\text{Ca}_{0.8}[\text{Al}_{1.7}\text{Si}_2\text{O}_8]$ continue to remain out of the solid solution. The elongated particle with apparent delamination can be observed reacting with the matrix phase, where the bulk particle had an EDX quantified chemistry of $\text{K}_{0.8}[\text{AlSi}_3\text{O}_8]$, a K-feldspar (K), and that of the reaction-rim was $\text{Ca}_{0.2}\text{K}_{0.5}[\text{AlSi}_3\text{O}_8]$, a combination of plagioclase and K-feldspar (K + N).

Density balance measurements, Table 2, indicated that lower temperature sintering conditions (1000°C) gave the best density values, 2.658 ± 0.004 g/cm^3 for SPS-1 and 2.658 ± 0.003 g/cm^3 for SPS-2. The poorest density balance results were those of the SPS-3 sample, with an average of 2.588 ± 0.003 g/cm^3 . The results for gas pycnometry of SPS samples were in agreement with the Archimedes balance data, showing that the optimum density was achieved with the lower sintering temperature of 1000°C and higher

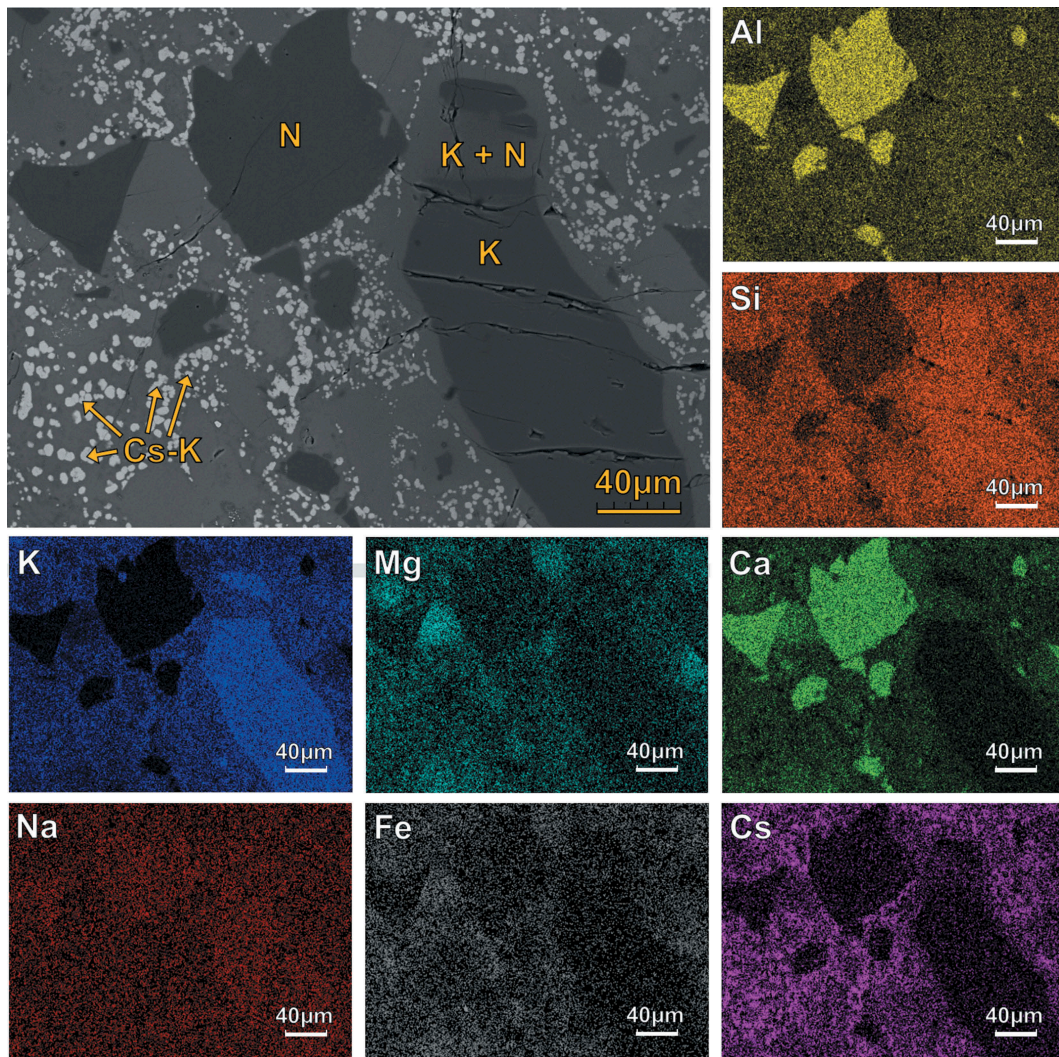


Figure 5. SEM/EDX micrographs of SPS-3 (1100°C, 10 min, 15 MPa), where labelled phases correspond to (K) potassium feldspar, (N) anorthite, and (Cs-K) cesium–potassium feldspars dispersed in anorthitic matrices.

pressure of 50 MPa, with $2.7314 \pm 0.0017 \text{ g/cm}^3$. This corresponded to a 10.7% increase from the Cs-exchanged source material. The ground material from the SPS-3 pellet achieved poorer densities compared to the low temperature counterparts, which may have been due to a microstructural bloating effect resulting from the evolution of water [21]. Considering the measured average apparent density (see material synthesis) and the gas pycnometry results, the wastefrom volume reductions achieved for SPS-1, 2 and 3 were $41.6 \pm 1.0\%$, $43.0 \pm 1.0\%$ and $40.3 \pm 1.0\%$, respectively. With the highest density and volume reduction, the SPS-2 material was selected as an optimal candidate for a 28-day chemical durability study.

3.3 Durability study of reactive spark plasma sintered material

The short-term chemical durability of Cs-chabazite processed as SPS-2 (1000°C/50 MPa) was performed using ASTM PCT-B methodology [15]. Figure 6

describes the normalised mass loss of elements as detected by ICP-OES (IC for Cs, standard deviations were obtained from duplicate samples). The average pH (day 0–28, 7 time points) during testing was observed to be $\text{pH } 10.64 \pm 0.24$, and this low standard deviation indicated that the sample naturally buffered during experiment initialisation. In Figure 6, there was a high initial elemental release rate observed between day 0 and day 1, especially prominent for Si, Al, and Cs. This behaviour is associated with the rapid dissolution of residual fines within the sample, even though due care was taken to remove fines during sample preparation by washing with IPA until clear.

In Figure 6, the Si concentration (present at SiO_2 55.6 wt.%, Table 1) was observed to increase commensurate with experiment duration, indicative of accelerated dissolution for the SPS-2 sample. The normalised release rate for Si was calculated as $1.13 \pm 0.12 \times 10^{-3} \text{ g m}^{-2} \text{ d}^{-1}$, day 28 was excluded due to significant evaporation of the leaching solution. In comparison, clinoptilolite simulant converted into NaAlO_2 and NaB_4O_7 -based glasses (via hot isostatic pressing) resulted in Si release

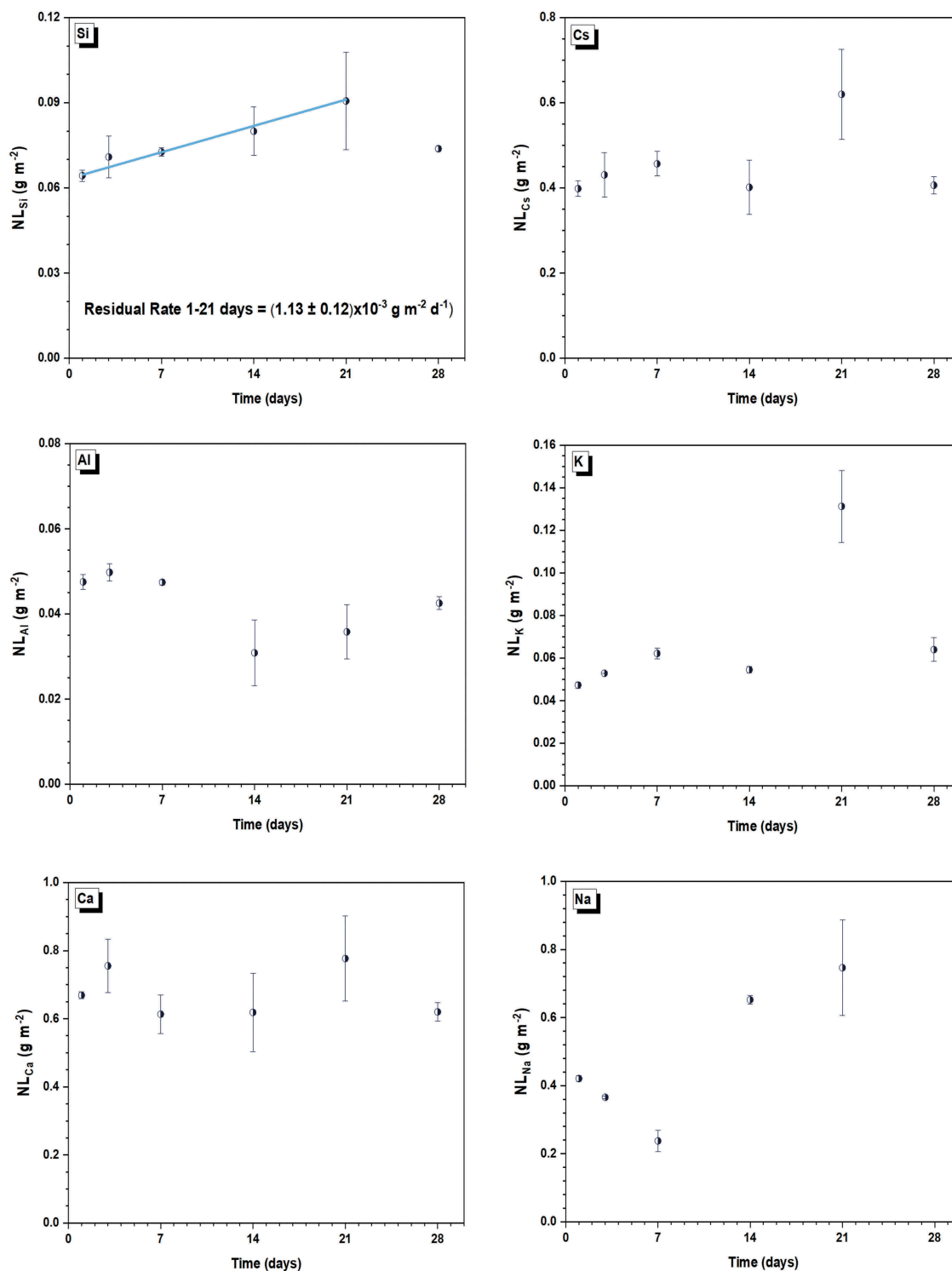


Figure 6. Normalised elemental mass loss of SPS-2 (1000°C, 10 min, 50 MPa) from PCT-B experiments performed at 90°C in 18.2 MΩ water.

rates of $4.21 \times 10^{-4} \text{ g m}^{-2} \text{ d}^{-1}$ and $6.80 \times 10^{-4} \text{ g m}^{-2} \text{ d}^{-1}$, respectively [22]. Prototype fast reactor (PFR) raffinate immobilised in a barium borosilicate glass achieved a Si release rate of $7.19 \times 10^{-3} \text{ g m}^{-2} \text{ d}^{-1}$ [23]. The durability of SPS-2 is therefore comparable to proposed thermal treatment options for two different UK ILW waste streams; however, it should be noted that the cited examples were performed at a higher SA/V ratio (2000 m^{-1}) than this study. The Cs-chabazite immobilised in SPS-2

resulted in a multi-phase matrix with Si present in all of the crystalline phases (K-feldspar, leucite, anorthite, and pyroxene) and the vitreous phase, which makes it difficult to assign dissolution to a specific phase within the sample.

A general trend was observed for the dissolution behaviour of Al, Ca, Cs, and K (Figure 6), where the concentrations appeared to remain steady throughout the duration (within error). This would suggest the

B = Biotite, K = K-Feldspar, L = Leucite, N = Anorthite, Q = Quartz, X = Pyroxene

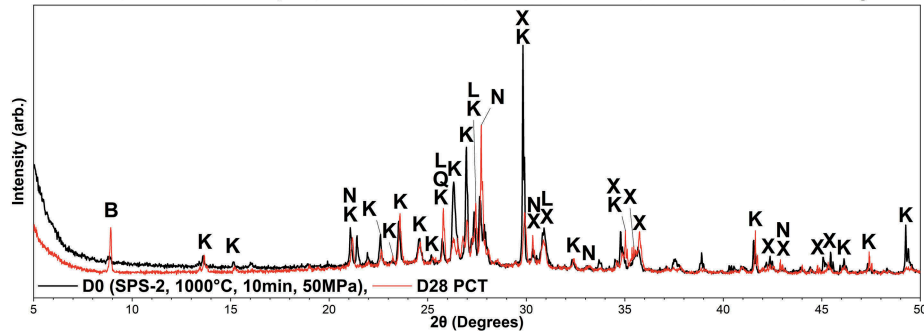


Figure 7. XRD pattern for the SPS-2 (1000°C, 10 min, 50 MPa) before and post-dissolution at day 0 and 28.

sample underwent congruent/constant dissolution. It is considered that the elemental loss spikes observed at day 21 could be associated with the evaporative loss resulting in artificially increased concentrations. XRD performed post-dissolution (Figure 7) revealed that the relative intensity of K-feldspar reflections significantly reduced compared to those for anorthite. The relative intensity of the biotite reflection at $\sim 9^\circ$ 2θ increased compared to the SPS-2 before dissolution (Figure 3). As no further thermal treatment process occurred to this sample, it could be assumed that the overall degree of crystallinity decreased as a result of the experiment rather than an increased presence of biotite.

Analysis of the Cs-chabazite SPS-2 particles post-dissolution by SEM/EDX (Figure 8) demonstrates that the dissolution of the material occurs heterogeneously, with preferential alteration of some phases. Within the central particle, regions rich in Ca, Al, and Si are representative of anorthite concurring with the XRD (Figure 3) for the continued presence of anorthite. The micro-cracks observed across several particles are from sample preparation rather than dissolution effects, shown in Figures 4 and 5.

The greyscale differences in the central particle elucidate the presence of two Cs-bearing K-feldspar regions with differing behaviour under dissolution conditions. The first K-feldspar can be assigned to the light grey region (surrounding the anorthite grain and left-hand side particles), where no dissolution effects were observed. The composition of this region was determined to be $\text{Cs}_{0.3}\text{Mg}_{0.4}\text{Ca}_{0.6}\text{K}_{0.9}[\text{Al}_{3.4}\text{Si}_8\text{O}_{22}]$, with a Cs concentration of 5.8 ± 1.8 wt.%. In contrast, the development of pitting/visible porosity was observed within the darker grey region (central particle, bottom left) suggestive of preferential dissolution. The calculated composition post-dissolution was $\text{Cs}_{0.1}\text{Na}_{0.2}\text{Mg}_{0.4}\text{Ca}_{0.2}\text{Fe}_{0.2}\text{K}_{2.0}[\text{Al}_{3.3}\text{Si}_8\text{O}_{22}]$, with a Cs concentration of 1.0 ± 0.4 wt.%. Due to the complex nature of a multi-phase wastefrom, future work to observe the retreat rate of the component phases by vertical scanning interferometry (VSI) and perform micro-analysis techniques to

identify the phases would help to determine the driving mechanism behind the dissolution behaviour observed in this study.

4. Conclusions

Microstructural characterisation and phase assemblage revealed the diverse mineral composition of a natural chabazite source used as a simulant for spent ion exchange media arising on the Fukushima NPP site. A proof of concept study demonstrated the efficacy of SPS for conditioning of such aluminosilicate zeolite wastes. Conceptual wastefroms were successfully produced using different SPS conditions, where the collapse of the porous zeolite framework led to an increase in absolute density. The highest Cs waste loading (in the main Cs-bearing phase) was obtained at sintering conditions of 1000°C/50 MPa. The uniaxial application of pressure and high temperature for 10 min provides a combination of parameters, which was ideal for ensuring collapse of the chabazite framework with partitioning of the exchanged Cs into a feldspar phase. The long-term durability of the SPS-2 sample is challenging to understand due to the heterogeneous nature of the sample and requires further work to understand the contributions of the component phases to the overall dissolution behaviour. Although use of this technology for waste conditioning is at a stage of relative infancy and Technology Readiness Level of 2–3, SPS has the potential for high volume reduction of wastes, providing a significant advantage over cement encapsulation, due to the anticipated waste volume increase and potential waste / encapsulant reaction. The process is the markedly faster and less energy intensive than hot isostatic pressing, at comparable lab scale. Some limited scalability studies for ceramic-metal type functionally graded materials were reported by Gullion *et al.* and Tokita who demonstrated capability for homogenous consolidation of disc-shaped samples with up to 100 mm diameter and 40 mm thickness [24–26]. Clearly, considerable additional research would be required to translate the conceptual approach developed here to application at full scale for

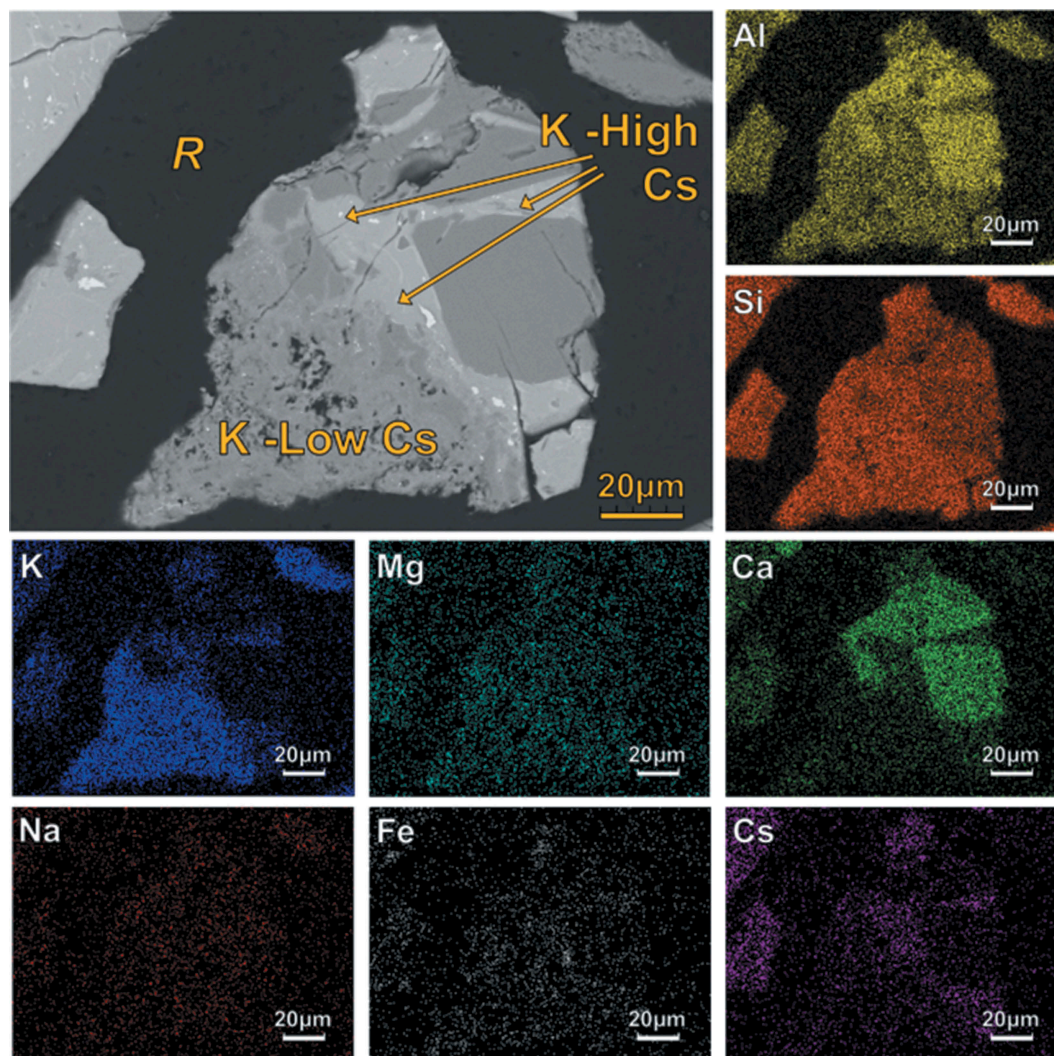


Figure 8. SEM/EDX micrographs of SPS-2 (1000°C, 10 min, 50 MPa) post-dissolution at day 28.

conditioning of inorganic ion exchange materials. Nevertheless, the full retention of the Cs_2O inventory in processing and durability experiments achieved in this conceptual study provide a compelling case for such future research. Although the product geometry, in the form of large sintered discs, might be considered a limitation, such geometry would offer the potential to control the thermal characteristics of the waste package by separating such discs with thermally conductive materials. Future work should use a more realistic simulant to allow for more accurate modelling and characterisation, and the radiation stability of the wasteforms should then be assessed.

Acknowledgments

The authors are grateful to the EPSRC for sponsorship of this research, under grants EP/N017617/1, EP/P013600/1, EP/S01019X/1, and EP/N017870/1. LH is grateful to EPSRC and the Nuclear Decommissioning Authority for award of a PhD studentship. This research was performed in part at the MIDAS Facility, at the University of Sheffield, which was established with support from the Department of Energy and Climate Change.

Disclosure statement

No potential conflict of interest was reported by the authors.

Funding

This work was supported by the Engineering and Physical Sciences and Research Council (EPSRC) [EP/N017617/1, EP/P013600/1, EP/S01019X/1, EP/N017870/1].

ORCID

Liam. C. Harnett <http://orcid.org/0000-0002-9296-1145>
 Laura. J. Gardner <http://orcid.org/0000-0003-3126-2583>
 Shi-Kuan Sun <http://orcid.org/0000-0002-1688-5072>
 Colleen Mann <http://orcid.org/0000-0002-8781-1652>
 Neil. C. Hyatt <http://orcid.org/0000-0002-2491-3897>

References

- [1] Tokyo Electric Power Company. Fukushima nuclear accident analysis report. Toyko, Japan: Tokyo Electric Power Company Holdings, Inc.; 2012.

- [2] Denton MS, Mertz JL, Bostick WD, editors. Fukushima nuclear crisis recovery: a modular water treatment system deployed in seven weeks. AZ, USA: Waste Management; 2012 Feb 26 - March 1.
- [3] Baek W, Ha S, Hong S, et al. Cation exchange of cesium and cation selectivity of natural zeolites: chabazite, stilbite, and heulandite. *Microporous Mesoporous Mater.* 2018;264:159–166.
- [4] Calligaris M, Mezzetti A, Nardin G, et al. Crystal structures of the hydrated and dehydrated forms of a partially cesium-exchanged chabazite. *Zeolites.* 1986;6(2):137–141.
- [5] Tokyo Electric Power Company. Situation of storage and treatment of accumulated water including highly concentrated radioactive materials and Fukushima Daiichi nuclear power station (372nd release) - October 4th, 2018. Toyko, Japan: Tokyo Electric Power Company Holdings, Inc; 2018.
- [6] International Atomic Energy Agency. Application of ion exchange processes for the treatment of radioactive waste and management of spent ion exchangers. Technical reports series no. 408. Vienna, Austria: International Atomic Energy Agency; 2002.
- [7] Kimura R, Inagaki Y, Idemitsu K, et al. Vitrification processes of simulated cesium sorbing zeolite waste. *Prog Nucl Energy.* 2018;108:497–502.
- [8] Gordon LE, Milestone NB, Angus MJ, editors. The immobilisation of clinoptilolite within cementitious systems. *Materials Research Symposium*; Boston, USA. 2008.
- [9] Sharp JH, Milestone NB, Hill J, et al., editors. Cementitious systems for encapsulation of intermediate level waste. The 9th International Conference on Radioactive Waste Management and Environmental Remediation; 2003 Sept 21-25; Oxford, UK.
- [10] Milestone NB. Reactions in cement encapsulated nuclear wastes: need for toolbox of different cement types. *Adv Appl Ceram.* 2006;105(1):13–20.
- [11] Jenni A, Hyatt NC. Encapsulation of caesium-loaded ions in cement. *Cem Conc Res.* 2010;40:1271–1277. <https://doi.org/10.1016/j.cemconres.2009.10.015>
- [12] Munir ZA, Anselmi-Tamburini U, Ohyanagi M. The effect of electric field and pressure on the synthesis and consolidation of materials: A review of the spark plasma sintering method. *J Mater Sci.* 2006;41(3):763–777.
- [13] Verdi SPA. Zeover data sheet. Torrino, Italy: Verdi S.p.A; 2015.
- [14] Sun S-K, Stennett MC, Corkhill CL, et al. Reactive spark plasma synthesis of $\text{CaZrTi}_2\text{O}_7$ zirconolite ceramics for plutonium disposition. *J Nucl Mater.* 2018;500:11–14.
- [15] ASTM International. C 1285 – 02 (Reapproved 2008) standard test methods for determining chemical durability of nuclear, hazardous, and mixed waste glasses and multiphase glass ceramics: the Product Consistency Test (PCT). USA.
- [16] Du T, Fang X, Wei Y, et al. Synthesis of nanocontainer chabazites from fly ash with a template- and fluoride-free process for cesium ion adsorption. *Energy Fuels.* 2017;31(4):4301–4307.
- [17] Greaves GN, Meneau F, Kargl F, et al. Zeolite collapse and polyamorphism. *J Phys.* 2007;19(41):415102.
- [18] Belviso C. EMT-type zeolite synthesized from obsidian. *Microporous Mesoporous Mater.* 2016;226:325–330.
- [19] Schairer JF, Bowen NL. Melting relations in the systems $\text{Na}_2\text{O}-\text{Al}_2\text{O}_3-\text{SiO}_2$ and $\text{K}_2\text{O}-\text{Al}_2\text{O}_3-\text{SiO}_2$. *Am J Sci.* 1947;245(4):199–201.
- [20] Rajib M, Sasaki T, Kobayashi T, et al. Analysis of sorption behavior of cesium and iodide ions on pumice tuff. *J Nucl Sci Technol.* 2011;48(6):950–957.
- [21] De Gennaro R, Cappelletti P, Cerri G, et al. Zeolitic tuffs as raw materials for lightweight aggregates. *Appl Clay Sci.* 2004;25(1):71–81.
- [22] Heath PG. Alternative processing methods for the thermal treatment of radioactive wastes [PhD Thesis]. Sheffield: The University of Sheffield; 2015.
- [23] Heath PG, Corkhill CL, Stennett MC, et al. Whales KM and Hyatt NC. Immobilisation of prototype fast reactor raffinate using barium silicate ILW glasses. *J Nucl Mater.* 2018;508:203–211.
- [24] Tokita M. Development of large-size ceramic/metal bulk FGM fabricated by spark plasma sintering. *Proc 1998 5th Int Symp Functionally Graded Mat.* 1999;308-311:83–88.
- [25] Tokita M. Large-size WC/Co functionally graded materials fabricated by spark plasma sintering (SPS) method. *Proc Seventh Int Symp Functionally Graded Mat.* 2003;423-425:39–44.
- [26] Guillon O, Gonzalez-Julian J, Dargatz B, et al. Field-assisted sintering technology/spark plasma sintering: mechanisms, materials, and technology developments. *Adv Eng Mater.* 2014;16(7):830–849.